

UNIVERSITY OF CALIFORNIA  
Santa Barbara

# Modeling Solution Growth of Inorganic Crystals

A Dissertation submitted in partial satisfaction  
of the requirements for the degree of

Doctor of Philosophy

in

Chemical Engineering

by

Preshit Dandekar

Committee in Charge:

Professor Michael F. Doherty, Chair

Professor Bradley F. Chmelka

Professor Baron Peters

Professor Ram Seshadri

September 2014

The Dissertation of  
Preshit Dandekar is approved:

---

Professor Bradley F. Chmelka

---

Professor Baron Peters

---

Professor Ram Seshadri

---

Professor Michael F. Doherty, Committee Chair

August 2014

Modeling Solution Growth of Inorganic Crystals

Copyright © 2014

by

Preshit Dandekar

*To my parents, Prakash and Deepa Dandekar*

## Acknowledgements

There are several people who made significant contributions to my pursuit of a doctoral degree, and I thank all of them. Regrettably, only some of them are mentioned here.

To quote Warren Buffet - “I won the fetus lottery”. My parents Deepa and Prakash, who are engineers themselves, instilled in me a scientific mind, and persevered throughout my childhood to teach me the importance of hard work and humility. My brother Pranav has been a great source of encouragement and intellectual support, always asking me the tough questions. My uncle Hemant helped me prioritize academics during my undergraduate education, and was instrumental in me developing pride and fondness for the chemical engineering discipline.

My advisor Mike Doherty has been a great source of knowledge as well as wisdom. He has been the perfect guide, stepping out to give me the time and the freedom to pursue a research problem, and coming back into the thick of things whenever his help was needed. Through his senior design class, he helped sustain my dream of being a good chemical engineer. I am infinitely grateful and proud to have worked with him for these five years. I must thank my committee members, who provided valuable comments and suggestions that helped me better shape the course of my doctoral research. I want to thank all my co-workers within the Doherty group, specifically, Drs. Mike Lovette, Zubin Kuvadia, Seung Ha Kim and Thomas Vetter, for their help and support in some of my projects. Working with such incredibly intelligent and fun-loving people has been a great learning experience.

Meeting my wife Vedavati was certainly the best thing that happened to me in Santa Barbara. Though not from an engineering background, she has shown tremendous patience in listening to all my work stories/ideas. I cannot thank her enough for her love, emotional support and understanding.

# Curriculum Vitæ

Preshit Dandekar

## Education

Ph.D. Chemical Engineering, University of California Santa Barbara 2014

B.Tech. & M.Tech. Chemical Engineering, Silver medal recipient for graduating top of the class, Indian Institute of Technology Bombay, India 2009

## Publications

Preshit Dandekar and Michael F. Doherty, “Prediction of Growth Morphology of Aragonite Crystals using Spiral Growth Model”, (*manuscript in preparation*).

Preshit Dandekar and Michael F. Doherty, “A Mechanistic Growth Model for Inorganic Crystals: Solid-State Interactions”, *AIChE J.*, **2014**, (*in press*).

Preshit Dandekar and Michael F. Doherty, “A Mechanistic Growth Model for Inorganic Crystals: Growth Mechanism”, *AIChE J.*, **2014**, (*in press*).

Shailendra Bordawekar, Zubin B. Kuvadia, Preshit Dandekar, Samrat Mukherjee and Michael F. Doherty, “Interesting Morphological Behavior of Organic Salt Choline Fenofibrate: Effect of Supersaturation and Polymeric Impurity”, *Cryst. Growth Des.*, **2014**, *14*, 3800-3812.

Preshit Dandekar and Michael F. Doherty, “Imaging Crystallization”, *Science*, **2014**, *344*, 705–706.

Seung Ha Kim, Preshit Dandekar, Michael A. Lovette and Michael F. Doherty, “Kink Rate Model for the General Case of Organic Molecular Crystals”, *Cryst. Growth Des.*, **2014**, *14*, 2460–2467.

Preshit Dandekar, Zubin B. Kuvadia and Michael F. Doherty, “Engineering Crystal Morphology”, *Annu. Rev. Mater. Res.*, **2013**, *43*, 359–386.

Preshit Dandekar, Chandra Venkataraman and Anurag Mehra, “Pulmonary Targeting of Nanoparticle Drug Matrices”, *J. Aerosol Med. Pulm. D.*, **2010**, *23*, 343–353.

## Conference Presentations

Preshit Dandekar and Michael F. Doherty, “A Mechanistic Model for Crystal Growth of Calcite”, AIChE Annual Meeting, San Francisco, November 2013.

Preshit Dandekar, “Engineering Growth Shapes of Inorganic Crystals”, 6th Annual Amgen-Clorox Graduate Student Symposium, Department of Chemical Engineering, University of California Santa Barbara, October 2013.

Preshit Dandekar and Michael F. Doherty, “Growth, Dissolution and Stabilization of Polar Oxide Surfaces”, AIChE Annual Meeting, Pittsburgh, November 2012.

Michael F. Doherty and Preshit Dandekar, “Molecular Design Rules for Blast-Resistant Honeycomb Structures”, European Conference on Composite Materials (ECCM15), Venice Italy, June 2012.

Preshit Dandekar and Michael F. Doherty, “A Mechanistic Growth Model for Ionic Crystals”, AIChE Annual Meeting, Minneapolis, October 2011.

### **Awards and Honors**

Dow Discovery Fellowship supported by The Dow Chemical Co. for pursuing fundamental research in Chemical Engineering, **2012-14**.

Best Poster, 4th Annual Amgen-Clorox Graduate Student Symposium, **2011**.

Outstanding Teaching Assistant Award, Dept. of Chemical Engineering, UCSB, **2011**.

Institute Academic Prize for best annual performance in the Department of Chemical Engineering, IIT Bombay, **2007-2008**.

## Abstract

# Modeling Solution Growth of Inorganic Crystals

Preshit Dandekar

Crystallization of inorganic solids from solution is of interest in several areas such as biomineralization, carbon sequestration, catalysis, photovoltaics, etc. The end-use functionality in some of the industrial applications is determined by the growth morphology of the inorganic crystals. A mechanistic understanding of the growth process will enable the design of functionally desirable inorganic crystalline solids.

The kinetics of crystal growth is governed primarily by the intermolecular interactions between the growth units on crystal surfaces and across the solid-solution interface. Therefore, this modeling effort is focused on the solid-state as well as the solution phase chemistry. The challenges associated with the solid-state chemistry of inorganic crystals, including long-range electrostatic interactions, stoichiometry, electronic structure of surface growth units, etc., were resolved within an easy-to-implement framework. The importance of the solution structure information (from experiments or molecular simulations) has been highlighted appropriately.

This dissertation presents a spiral growth model that predicts the morphology of solution grown crystals (e.g.,  $\text{CaCO}_3$ ) at ambient conditions. The model also provides quantitative insights into the kinetics of hydrothermal synthesis of inorganic oxides, such as  $\text{TiO}_2$  and  $\text{ZnO}$ , using the periodic bond chain (PBC) theory.

This mechanistic model could be extended to identify suitable growth modifiers for a wide range of inorganic crystals such as salts and oxides. The ultimate goal is to develop a predictive tool that helps engineer the synthesis of inorganic solids with desired functionality.

# Contents

<b>Acknowledgments</b>	<b>v</b>
<b>Vitæ</b>	<b>vii</b>
<b>Abstract</b>	<b>ix</b>
<b>List of Figures</b>	<b>xiv</b>
<b>List of Tables</b>	<b>xxi</b>
<b>1 Introduction</b>	<b>1</b>
1.1 Motivation . . . . .	1
1.2 Background . . . . .	3
1.3 Mechanistic Growth Models . . . . .	9
1.4 Dissertation Outline . . . . .	15
<b>Bibliography</b>	<b>17</b>
<b>2 Solid-State Interactions in Inorganic Crystals</b>	<b>20</b>
2.1 Introduction . . . . .	20
2.2 Periodic Bond Chains (PBCs) in Inorganic Crystals . . . . .	22
2.2.1 Building Unit of the PBC . . . . .	24
2.2.2 Step Edges from Building Units and PBCs . . . . .	28
2.2.3 PBCs in Bulk Calcite . . . . .	31
2.3 Surface Effects on Solid-State Interactions . . . . .	38
2.3.1 Bond Valence Model . . . . .	40
2.3.2 PBC Energies on (10 $\bar{1}$ 4) Surface of Calcite . . . . .	48
2.4 Kink Site Energies . . . . .	49
2.4.1 Space Partitioning . . . . .	50
2.4.2 Kink Site Energies on (10 $\bar{1}$ 4) Surface of Calcite . . . . .	56
2.5 Discussion . . . . .	58

2.6	Conclusions . . . . .	60
<b>Bibliography</b>		<b>62</b>
<b>3</b>	<b>Spiral Growth of Inorganic Crystals</b>	<b>67</b>
3.1	Introduction . . . . .	67
3.2	Growth Mechanism . . . . .	70
3.3	Kink Density Calculation . . . . .	73
3.4	Kink Rate for Inorganic Crystals . . . . .	77
3.4.1	New Kink Rate Model . . . . .	78
3.4.2	Expressions for Attachment and Detachment Fluxes . . . . .	82
3.5	Step Velocity Predictions on (10 $\bar{1}$ 4) Surface of Calcite . . . . .	91
3.6	Critical Length of a Spiral Edge . . . . .	97
3.6.1	Morphology of Calcite Crystals . . . . .	103
3.7	Conclusions . . . . .	104
<b>Bibliography</b>		<b>106</b>
<b>4</b>	<b>Crystal Growth and Morphology Prediction of Aragonite</b>	<b>111</b>
4.1	Introduction . . . . .	111
4.2	Periodic Bond Chains in Aragonite Crystals . . . . .	112
4.3	Step Velocity of Edges with Multiple Structures . . . . .	121
4.4	Space Partitioning in Aragonite Crystals . . . . .	126
4.5	Spiral Growth Calculations . . . . .	131
4.6	Conclusions . . . . .	135
<b>Bibliography</b>		<b>137</b>
<b>5</b>	<b>Crystal Growth of Anatase from Hydrothermal Synthesis</b>	<b>139</b>
5.1	Introduction . . . . .	139
5.1.1	Growth Unit for Anatase Crystal Growth . . . . .	140
5.2	Periodic Bond Chains in Anatase Crystals . . . . .	141
5.3	Hydrothermal Synthesis . . . . .	147
5.3.1	Synthesis Procedure . . . . .	148
5.3.2	Characterization . . . . .	149
5.4	Discussion . . . . .	153
5.5	Conclusions . . . . .	156
<b>Bibliography</b>		<b>158</b>
<b>6</b>	<b>Stabilization and Growth of Polar Crystal Surfaces</b>	<b>161</b>
6.1	Introduction . . . . .	161
6.2	Crystal Structure of Wurtzite Zinc Oxide . . . . .	164

6.3	Building Unit and PBCs in Zinc Oxide Crystals . . . . .	167
6.4	Stabilization of Polar {0002} ZnO surfaces . . . . .	174
6.5	Conclusions . . . . .	179
<b>Bibliography</b>		<b>181</b>
<b>7</b>	<b>Conclusions and Future Work</b>	<b>185</b>
7.1	Overview and Summary . . . . .	185
7.2	Directions for Future Work . . . . .	187
7.2.1	Modeling . . . . .	187
7.2.2	Experiments . . . . .	192
<b>Bibliography</b>		<b>194</b>
<b>Appendices</b>		<b>197</b>
<b>A</b>	<b>Step-by-step Methodology for Crystal Morphology Prediction of Inorganic Solids</b>	<b>197</b>
<b>Bibliography</b>		<b>208</b>
<b>B</b>	<b>Detailed Expression for the Kink Rate</b>	<b>209</b>
<b>Bibliography</b>		<b>214</b>
<b>C</b>	<b>Time Scale Comparison between Edge Rearrangement and Kink Incorporation</b>	<b>215</b>
<b>Bibliography</b>		<b>220</b>
<b>D</b>	<b>Modification of Surface Charges for Polarity Stabilization</b>	<b>221</b>
<b>Bibliography</b>		<b>226</b>
<b>E</b>	<b>Force Field Parameters for Some Inorganic Crystals</b>	<b>227</b>
<b>Bibliography</b>		<b>229</b>

# List of Figures

1.1	(a) 3D model of Pd nanocrystals (golden) grown on a SrTiO <sub>3</sub> (001) substrate (green) in an ultrahigh vacuum environment. (b) shows the evolution of the height and length of the Pd nanocrystals. The dashed line indicates the equilibrium shape while the different markers for the datapoints indicate different nucleation temperatures. Reprinted with permission from Silly et al [12]. Copyright ©2005, The American Physical Society. . . . .	5
1.2	Predicted shape evolution of ibuprofen from a spherical seed (a-d) ( $\Delta\xi = 0.025$ ) and experimental steady-state shape (e). Parts (a-d) not drawn to scale. Reprinted with permission from Lovette et al [17]. Copyright ©2008, American Chemical Society. . . . .	7
1.3	The sequence of events associated with the incorporation of solute growth units into the kink sites (orange) present on a crystal surface. The incoming solute growth unit (dark grey cube) has the same chemical composition and structure as the other growth units in the crystal (light grey cubes). Processes 3 (desolvation) and 5 (release of latent heat) have not been illustrated for the sake of brevity. . . . .	10
1.4	Schematic of step edges at 0 °K (a) and above 0 °K (b and c). The grey squares in (b) represent kink sites separated by an average distance of $x_0$ . Image (c) is a schematic of layered growth of the $\{hkl\}$ face growing at a perpendicular growth rate, $G_{hkl}$ , through the lateral spreading of steps separated by an interstep distance, $y$ , with a height, $h$ , at a step velocity of $v$ . Adapted with permission from Lovette et al [17]. Copyright ©2008, American Chemical Society. . . . .	11

1.5	Growth mechanisms as a function of supersaturation. The solid line is the growth rate in each regime of supersaturation. The short dashed lines are the growth rates if 2D nucleation is continued to be dominant below its applicable supersaturation range. The long dashed line is the growth rate if spiral growth were the persistent mechanism above its applicable supersaturation range. Reprinted with permission from Lovette et al [17]. Copyright ©2008, American Chemical Society. . . . .	12
2.1	A view along the b axis of the barite ( $\text{BaSO}_4$ ) unit cell. The broken black rectangles show the building unit for PBCs in barite crystals. The solid black rectangle shows the edges of the unit cell. Barium atoms are represented by green spheres and sulfate growth unit by yellow (S) and red (O) capped sticks. Note that in this view, the fourth oxygen atom of the sulfate group overlaps with one of the other oxygen atoms and is therefore not visible. . . . .	26
2.2	Crystal packing on the (210) barite surface. The broken black rectangles form building units and the solid red rectangle shows the step edge along the [120] direction. The [120] step edge consists of half of the building unit arrangement while the other half forms part of another step edge parallel to the first one. . . . .	30
2.3	Calcite unit cell with the Ca atoms (green sphere) and $\text{CO}_3$ groups (grey and red capped sticks). The contents of the asymmetric unit of the unit cell are labeled in cyan. . . . .	32
2.4	The two building units (enclosed within the broken black and blue rectangles) in calcite crystal and the arrangement of $\text{Ca}^{2+}$ and $\text{CO}_3^{2-}$ ions within each building unit. The two building units are related to each other by a $2_1$ screw axis. . . . .	33
2.5	The packing of a calcite unit cell with building units (enclosed within broken blue and black ellipses). . . . .	33
2.6	Crystal packing on the (10 $\bar{1}$ 4) surface of calcite. The broken black rectangles form building units and the solid red parallelogram shows the step edge along the [48 $\bar{1}$ ] direction. The [48 $\bar{1}$ ] step edge consists of half of the building unit contents while the other half forms part of another step edge parallel to the first one. . . . .	34
2.7	Step edges along various PBC directions on the (10 $\bar{1}$ 4) surface of calcite. The ‘straight’ bond chains [441] and [48 $\bar{1}$ ] are shown in solid red and blue lines, respectively. The ‘sawtooth’ bond chains [010] and [42 $\bar{1}$ ] are shown in broken green and broken purple lines, respectively. . . . .	35
2.8	AFM image of a growth spiral on the (10 $\bar{1}$ 4) surface of calcite. The image size is $3 \times 3 \mu\text{m}$ . Adapted with permission from Davis et al. [29]. Copyright ©2004, Mineralogical Society of America. . . . .	38

2.9	Side view of the $[\bar{4}41]$ edge on the $(10\bar{1}4)$ surface of calcite. The $[\bar{4}41]_+$ and $[\bar{4}41]_-$ edges have been shown in (a) and (b), respectively, with the angle between the edge and the terrace being obtuse for the former and acute for the latter edge. . . . .	39
2.10	A representation of the electrostatic field in the $(1\bar{1}0)$ face of rutile ( $\text{TiO}_2$ ). The light lines represent the electrostatic field lines and the thick lines show the zero-flux boundary that partitions space into bond regions. Adapted with permission from Preiser et al. [33]. Copyright ©1999, International Union of Crystallography. . . . .	42
2.11	A side view of the $(10\bar{1}4)$ surface of calcite showing the two different orientations of carbonate groups in the surface layer. The two orientations are colored black and blue; the oxygen atoms (A, X and B) within each group are also labeled. . . . .	47
2.12	Partition of 3D orthogonal space into octants (white and grey cubes), quadrants (blue squares) and axes (red lines). . . . .	52
2.13	Classification of the 13 crystalline partitions around a kink site (white cube) on the $[100]$ edge of the $(001)$ Kossel crystal surface. The partitions are colored corresponding to their classification listed in Table 2.8. . . . .	52
2.14	A plan view of the $(10\bar{1}4)$ surface of calcite showing the two orientations a) $\mathcal{E}$ and b) $\mathcal{W}$ of Ca kink sites on the $[48\bar{1}]$ obtuse edge. The kink site Ca atoms are enclosed within the red circles. . . . .	57
3.1	A representative rearrangement of a Ca and a $\text{CO}_3$ growth unit (within the black circle) from a straight $[48\bar{1}]$ edge on $(10\bar{1}4)$ surface of calcite to form four kink sites (red circles). The water molecules surrounding the edge and kink sites have not been shown. . . . .	74
3.2	The two orientations ( $\mathcal{E}$ and $\mathcal{W}$ ) of kink sites on the $[48\bar{1}]$ edge on $(10\bar{1}4)$ surface of calcite. . . . .	76
3.3	Representative arrangement of multiple types of kink sites along the edge of an AB-type ionic crystal surface. There are two types of A (cyan) and B (orange) kink sites each that are repeated by symmetry along the edge. The arrow indicates the direction of the growth of the step. . . . .	79
3.4	Transition between A and B kink sites based on the attachment or detachment of A and B growth units and the fluxes associated with these transitions. . . . .	80
3.5	Representative energy landscape during attachment and detachment from kink sites. The reactant state is the growth unit attached in the kink site. The product state is the unattached kink site and fully solvated growth unit in the solution. $k^+$ and $k^-$ are the rate constants for the attachment and detachment processes, respectively. . . . .	83

3.6	Illustration of the detachment process of an A type kink site that results in the formation of a B type kink site. The change in the potential energy of the system in this process is given by the kink detachment work $\Delta W$ . The solvent molecules around the edge are not shown for clarity. . . . .	90
3.7	Comparison of model predictions of the step velocities of obtuse and acute spiral edges with AFM measurements reported by Teng et al. [48] at $r = 1.04$ . . . . .	92
3.8	Sensitivity of the kink detachment work $\Delta W$ to variations ( $\pm 5\%$ ) in the interaction energies between the kink site ions and the surrounding water molecules for the kink sites with $\mathcal{E}$ orientation on the $[\bar{4}41]$ obtuse edge on the $(10\bar{1}4)$ surface of calcite. . . . .	94
3.9	In situ AFM images of growth spirals on the $(10\bar{1}4)$ surface of calcite crystal. The activity ratio of $\text{Ca}^{2+}$ to $\text{CO}_3^{2-}$ ions increases from panels (a) to (c). Adapted with permission from Stack and Grantham 2010 [39]. Copyright ©2010, American Chemical Society. . . . .	95
3.10	Comparison of the variation of the step velocities of obtuse and acute spiral edges with increasing activity ratio of $\text{Ca}^{2+}$ to $\text{CO}_3^{2-}$ measured by Stack and Grantham [39] with the model predictions. The experiments and the model predictions are at a constant supersaturation of $S = 1.58$ . . . . .	96
3.11	(a) 1D nucleation of a new edge and the creation of new surface area (colored in red). (b) $\Delta G$ variation with length of the edge for a hypothetical centrosymmetric molecular crystal. . . . .	98
3.12	Structure of 1D nucleated edge along $[48\bar{1}]$ direction on the $(10\bar{1}4)$ surface of calcite as a function of length of the edge. . . . .	100
3.13	(a) and (b) $\Delta G$ variation with the length of the $[48\bar{1}]$ obtuse spiral edge on the $(10\bar{1}4)$ surface of calcite crystals at $S = 1.5$ . The edge begins with a Ca ion ( $i = 1$ , see Figure 3.12a).(b) shows an enlarged version of the inset within the red rectangle in (a). The black dashed line in (b) signifies $\Delta G = 0$ while the red vertical arrow shows the value of the critical length $l_{1,c} = 76.8$ nm. . . . .	101
3.14	(a) The predicted morphology of calcite crystals dominated by the $\{10\bar{1}4\}$ family of faces. (b) Morphology of the Icelandic Spar calcite crystal on exhibition at the National Museum of Natural History in Washington, DC. . . . .	103
4.1	Aragonite unit cell with the Ca atoms (green sphere) and $\text{CO}_3$ groups (grey and red capped sticks). The contents of the asymmetric unit of the unit cell are labeled in blue. . . . .	113
4.2	A view of the crystal packing in aragonite along the $[100]$ direction with building units enclosed within cyan and black ellipses. Each building unit consists of two Ca and two $\text{CO}_3$ groups. . . . .	114

4.3	A view of the crystal packing in aragonite along the [001] direction with the boundaries of a (020) slice shown with broken black lines. The blue and black ellipses represent the contents of the two types of building units.	115
4.4	A plan view of the (020) slice of aragonite crystal. (a) shows the periodic bond chains along the [001] direction (purple). (b) shows the periodic bond chains along [201] (red) and $\bar{[201]}$ (mustard) directions.	116
4.5	A plan view of the (110) slice of aragonite crystal. (a) shows the arrangement of the building units (black and cyan ellipses). (b) shows the periodic bond chains along the $\bar{[111]}$ (blue) and $[1\bar{1}1]$ (brown) directions.	117
4.6	Plan views of the (a) (002) and (b) (011) slice of aragonite crystals.	117
4.7	(a) View along the [001] direction of (110) and $\bar{(110)}$ slices of aragonite crystals. (b) Step edges along the $\langle 111 \rangle$ family of PBCs passing through the Ca atom labeled in red. The shared intermolecular interactions are highlighted using black circles.	120
4.8	View of aragonite crystal packing along (a) $\bar{[111]}$ and (b) $\bar{[3\bar{1}0]}$ lattice directions highlighting the two different structures (cyan and magenta) of the $\bar{[111]}$ PBC edge.	122
4.9	Plan view of a hypothetical crystal face with two types for edge 1. The growth units along the two types of edge structures are represented by red ( <i>I</i> ) and green ( <i>II</i> ) circles.	123
4.10	Predicted morphology of aragonite crystals grown from aqueous solution at $S = 1.2$ and $r = 1.0$ . The crystal shape is needle-like with an aspect ratio $\gg 100$ .	133
5.1	(a) Anatase ( $\text{TiO}_2$ ) unit cell with the contents of the asymmetric unit labeled in blue. Ti and O atoms are represented by silver and red spheres respectively. (b) Packing of the coordination octahedra ( $\text{TiO}_6$ ) within the unit cell.	142
5.2	View along (a) [100] and (b) [010] lattice directions of the crystal packing around the anatase unit cell with building units enclosed within cyan ellipses.	143
5.3	Plan view of the (101) anatase crystal surface. (a) shows the packing of the surface with building units (cyan ellipses). (b) shows the periodic bond chains along the [010] (green) and $\bar{[1\bar{1}1]}$ (blue) step edges.	144
5.4	(a) View of anatase crystal packing along the $\bar{[100]}$ direction showing the boundaries of the (004) slice and the inversion centers (black circles). (b) Plan view of the (004) anatase crystal surface showing the periodic bond chains along [010] and [100] (green) edges.	145
5.5	(a) Predicted morphology of anatase crystals using the attachment energy model. (b) A typical morphology of anatase crystals grown by hydrothermal synthesis. Adapted with permission from Deng et al. [17]. Copyright ©2009 Elsevier B.V.	147

5.6	X-ray diffraction patterns of $\text{TiO}_2$ crystals synthesized using the hydrothermal synthesis technique reported by Deng et al [17]. . . . .	150
5.7	SEM images of hydrothermally grown anatase crystals. (a) and (b) are samples from batch 1, (c) and (d) are samples from batch 2, and (e) and (f) are samples from batch 3. The scale bar on all the figures except (d) is $1 \mu\text{m}$ . The scale bar on (d) is 200 nm. . . . .	151
5.8	<i>Ex situ</i> AFM images of hydrothermally grown anatase crystal surfaces of a sample taken from batch 2. (a) shows a part of an anatase crystal in the background. The object in the foreground could be another anatase crystal. (b) and (d) are amplitude images from an area shown within white rectangle in (a). (c) and (e) are the height profiles of the black lines in (b) and (d). . . . .	152
5.9	Side view of the (101) slice of anatase crystals. The height of monomolecular steps on the (101) surface is equal to the slice thickness, $d_{101} = 3.516 \text{ \AA}$ . . . . .	153
6.1	The classification of ionic crystal surfaces based on the value of the electrostatic dipole moment perpendicular to the crystal surface (denoted by the black horizontal line). The contents of the repeat unit for the crystal packing perpendicular to the surface are enclosed within broken black rectangles. The three crystal surfaces with different ionic arrangements are labeled based on Tasker's classification [3]. . . . .	162
6.2	(a) Asymmetric shape of an $\alpha$ -resorcinol crystal grown from aqueous solution. Scale bar is $10 \mu\text{m}$ . Adapted with permission from Srinivasan et al [11]. Copyright ©2005, American Chemical Society. (b) Asymmetric shapes of urea crystals grown from methanol. Adapted with permission from Piana et al [14]. Copyright ©2005, Nature Publishing Group. . . .	164
6.3	The crystallographic unit cell of wurtzite zinc oxide structure with the contents of the asymmetric unit labeled in blue. Zn and O atoms are represented by the blue-grey and the red spheres, respectively. . . . .	165
6.4	A view of the crystal packing in wurtzite ZnO along the $b$ lattice direction. The dashed lines indicate the (0002) and (000 $\bar{2}$ ) planes that terminate with Zn and O atoms, respectively. . . . .	167
6.5	View of wurtzite zinc oxide crystal packing along (a) $b$ and (b) $c$ lattice directions showing the arrangement of Zn and O atoms in the layers of the non-polar crystal surfaces - (10 $\bar{1}$ 0) and (11 $\bar{2}$ 0). . . . .	167
6.6	Two choices for the building unit of PBCs in ZnO wurtzite crystals. $I$ and $II$ have radii of gyration equal to $1.887 \text{ \AA}$ and $1.633 \text{ \AA}$ , respectively. . . . .	169

6.7	(a) A view of the crystal packing in wurtzite ZnO along the [010] direction. The dashed lines indicate the boundaries of the (0002) slice. The green rectangles show the contents of the building unit for wurtzite ZnO crystals. (b) Plan view of the (0002) face showing the periodic bond chains along the [100] and [010] directions. The solid-state growth units (ZnO) are shown within the black rectangles. . . . .	170
6.8	Plan view of the (a) (10 $\bar{1}$ 0) and (b) (11 $\bar{2}$ 0) faces on ZnO wurtzite crystals. The solid-state growth units ZnO are shown within black rectangles. The PBCs on the (10 $\bar{1}$ 0) face are [010] and [001], while the PBCs on the (11 $\bar{2}$ 0) face are parallel to the $[\bar{1}$ 10 and [001] directions. . . . .	171
6.9	(a) Morphology of ZnO wurtzite crystals predicted under vacuum growth using the attachment energy model. (b) SEM images showing the morphology of ZnO crystals grown from zinc nitrate and hexamethylenetetramine (HMT). Adapted with permission from McPeak and Baxter [31]. Copyright ©2009, American Chemical Society. . . . .	173
6.10	Scanning tunneling microscopy (STM) images of triangular islands and pits formed on clean Zn-terminated (0002) ZnO surface under UHV conditions. (a) Adapted with permission from Dulub et al [38]. Copyright ©2002 Elsevier Science B.V. Image size is 50 nm $\times$ 50 nm. (b) Adapted with permission from Onsten et al [43]. Copyright ©2010, American Chemical Society. Image size is 30 nm $\times$ 30 nm. . . . .	176
6.11	A hypothetical structure of a triangular island on the (0002) surface of wurtzite zinc oxide crystals. The edges of the triangular island are parallel to the [100], [010] and [110] directions. There are 28 O atoms and 21 Zn atoms within the island. . . . .	177
7.1	An illustrative representation of the following molecular processes occurring near a step edge of a crystal surface - (1) edge rearrangement, (2) kink incorporation, and (3) 1D nucleation. . . . .	190
C.1	Representative rearrangement of a straight edge on a crystal surface that involves the detachment of an edge growth unit to a step adatom position.	216
C.2	The ratio of characteristic time scales of edge rearrangement ( $\tau_{rea}$ ) to kink incorporation ( $\tau_{inc}$ ) at different $S$ and $\Delta W$ values. . . . .	218
D.1	The electric field and potential at a point P at a distance $r$ from an infinitely long flat plane with a uniform surface charge per unit area, $+\sigma$ .	222
D.2	A simplified view of the arrangement of ions in the layers beneath a Tasker type 3 ionic crystal surface [1]. (a) shows the crystal surface with native charge density ( $\sigma$ ) on the ionic layers. (b) shows the crystal surface with modified charge densities ( $\sigma'$ ) on the two outermost layers. Green and blue lines represent layers containing negative and positive charged ions, respectively. . . . .	223

# List of Tables

2.1	PBC interaction energies in bulk calcite crystal . . . . .	36
2.2	Bond valence parameters and bond valences for the atom pairs in bulk calcite . . . . .	45
2.3	Bond valence parameters and the bond valences for the O-H pairs in liquid water . . . . .	45
2.4	Partial charges of the calcium atoms in calcite at different lattice positions	46
2.5	Partial charges of the atoms of the carbonate growth unit in calcite at various lattice positions . . . . .	47
2.6	PBC interaction energies ( $E_{PBC}$ ) in kcal/mol along the spiral edges on the $(10\bar{1}4)$ surface of calcite crystal in contact with water . . . . .	48
2.7	List of octants, quadrants and axes in the 3D orthogonal coordinate system with their mathematical notations . . . . .	51
2.8	Classification of the 13 crystalline partitions of space around a kink site along the $[100]$ edge on the $(001)$ surface of a Kossel crystal . . . . .	53
2.9	Kink site potential energy ( $U_{kink}$ ) in kcal/mol for the 32 kink sites on the $(10\bar{1}4)$ surface of calcite . . . . .	58
3.1	Density of kink sites ( $\rho$ ) on the $[48\bar{1}]$ spiral edges of $(10\bar{1}4)$ face of calcite	76
3.2	Kink detachment work ( $\Delta W$ ) values in kcal/mol for the kink sites on the $[48\bar{1}]$ spiral edges of a $(10\bar{1}4)$ face of calcite . . . . .	90
3.3	Critical lengths ( $l_c$ ) in nm of the $[48\bar{1}]$ spiral edges on the $(10\bar{1}4)$ face of calcite crystals at $S = 1.5$ . . . . .	101
4.1	$E^{att}$ and $E_{PBC}$ values for the F-faces on aragonite crystal surface . . . . .	121
4.2	The cardinal directions used for space partitioning on aragonite crystal faces . . . . .	127
4.3	$\Delta W$ values (in kcal/mol) for the 112 types of kink sites on the spiral edges of aragonite crystal surfaces . . . . .	130
4.4	Results of spiral growth calculations on the edges of aragonite crystal surfaces at $S = 1.2$ , $r = 1.0$ . . . . .	132

5.1	$E_{PBC}$ values for the F-faces on the anatase crystal surface . . . . .	146
6.1	$E_{PBC}$ values for the periodic bond chains on the ZnO wurtzite crystal surfaces . . . . .	173
E.1	Force field parameters for calcite and aragonite crystals [1] . . . . .	227
E.2	Force field parameters for anatase crystals [4] . . . . .	228
E.3	Force field parameters for ZnO wurtzite crystals [5] . . . . .	228

# Chapter 1

## Introduction

Reproduced in part with permission from: Dandekar, P.; Kuvadia, Z.B.; Doherty, M.F. Engineering Crystal Morphology. *Annual Reviews of Materials Research*, **2013**, *43*, 359-386.

### 1.1 Motivation

Crystallization is both a widely observed natural phenomenon and a common industrial process. It pervades several scientific disciplines from geology, atmospheric chemistry, marine biology to pharmaceuticals, catalysis, electronics, etc. The versatility of crystallization is evident from its use either as a separation technique to remove certain undesired crystalline impurities, or its application as a materials synthesis process for high purity crystalline products. The total value of crystalline solids manufactured worldwide is several trillion dollars per year. Therefore, systematic improvements in either function or processing of these crystalline products have the potential for significant beneficial impact.

The crystallization process and operating parameters govern several fundamental properties of the resulting crystalline materials including chemical purity profile, polymorphic state, crystal size and shape distributions, etc. Crystal shape or morphology significantly influences the end-use efficacy of solid products (e.g., bioavailability for pharmaceutical compounds [1], reactivity for catalysts [2]), as well as the downstream performance of the entire process (e.g., by affecting filtering and drying times [1]).

The desired morphology of a crystalline material is strongly dependent on its application. A particular crystal shape may be desirable in one industrial process and may be completely undesired in another. For example, nanowires or needle-like shaped ZnO crystals significantly increase the absorption efficiency of dye-sensitized solar cells [3], whereas needles of any crystalline active pharmaceutical product (API) are troublesome in downstream processing [1] and should be avoided [4]. In other applications, the preferred shape is based upon a desired or undesired crystal face. For example, the {100} family of faces of Ag nanocrystals exhibit higher catalytic activity for ethylene epoxidation reactions than the {111} family [5], which is the more prominent face on the equilibrium morphology [6].

Several design parameters such as the choice of solvent, temperature, pH, additives or growth modifiers, etc., may govern the crystallization process and the end use performance of the crystalline product. As a result, the experimental design space is very large, so trial-and-error approaches may not be efficient for synthesis of crystalline materials with desired functionality. To meet the challenge of scientifically engineering the shape

of crystalline solids, there have been significant theoretical efforts undertaken in recent decades to model the growth process and to understand the underlying crystal growth mechanisms. This doctoral dissertation was undertaken to understand the growth process of inorganic crystals and to provide a predictive framework for designing inorganic crystalline solid particles.

## 1.2 Background

In some situations, crystals will achieve their equilibrium shape (although this is much less common than one might imagine). The equilibrium criteria for the shape of interfaces dividing solid and fluid phases were first developed by Gibbs [7]. He showed that the equilibrium shape of a solid crystal would be such that the total surface energy,  $\sum_i \gamma_i A_i$ , be a minimum for a fixed crystal volume, where  $A_i$  is the area of face  $i$  and  $\gamma_i$  is the surface energy per unit area of face  $i$ . Wulff later developed a geometric approach for determining the shapes of faceted crystals (at constant temperature and pressure) with anisotropic surface free energies that conforms to the criterion of Gibbs. This is known as the Wulff construction [8, 9]. The Wulff construction is determined by connecting the end points of vectors, each having a specific magnitude  $H_i$  and a common origin, to planes that are perpendicular to each vector. The magnitude,  $H_i$ , is proportional to the corresponding surface free energy,  $\gamma_i$  of the respective surface; thus the Wulff construction

has the form [10, 11]

$$\frac{\gamma_1}{H_1} = \frac{\gamma_2}{H_2} = \dots = \frac{\gamma_i}{H_i} = \dots = \frac{\gamma_N}{H_N} \quad (1.1)$$

where  $N$  is the number of faces on the crystal surface. This equation is valid only at equilibrium and defines the Gibbs-Wulff shape of the crystal. However, Gibbs had the following footnoted remark about his equilibrium condition, “On the whole it seems not improbable that the form of very minute crystals in equilibrium with solvents is principally determined by the condition that  $(\sum_i \gamma_i A_i)$  shall be a minimum for the volume of the crystal, but as they grow larger (in a solvent no more supersaturated than is necessary to make them grow at all), the deposition of new matter on the different surfaces will be determined more by the orientation of the surfaces and less by their size and relations to the surrounding surfaces. As a final result, a large crystal, will generally be bounded by those surfaces alone on which the deposit of new matter takes place least readily. But the relative development of the different kinds of sides will not be such as to make  $(\sum_i \gamma_i A_i)$  a minimum.” (Gibbs, Collected Works [7], pp. 325-326). In other words, Gibbs expected that crystal surfaces would be dominated by the slow growing faces and that the shapes of the resulting crystals would be their “growth shapes” not their equilibrium shapes. It took until approximately 1960 to discover the corresponding conditions for determining the growth shapes of crystals (Equation 1.2).

An impressive demonstration of Gibbs’ speculation was published by Silly et al. [12] and is shown in Figure 1.1. The “hut-like” nanocrystals of palladium were grown on a SrTiO<sub>3</sub>(001) substrate and achieved their equilibrium shape at sizes below approximately

10nm (i.e., they lie on the equilibrium dashed line in the figure) but at larger sizes the crystals fall on a different line corresponding to the non-equilibrium growth shape. This behavior recurs for both “hexagons” and “truncated pyramids” that grow under different experimental conditions.

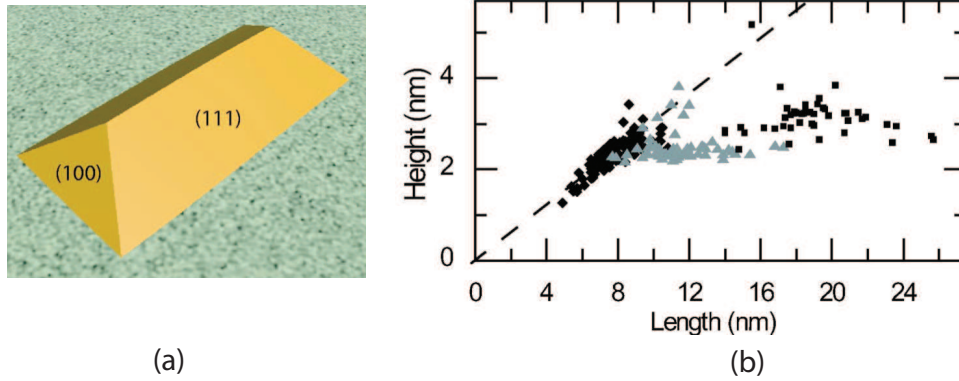


**Figure 1.1:** (a) 3D model of Pd nanocrystals (golden) grown on a SrTiO<sub>3</sub>(001) substrate (green) in an ultrahigh vacuum environment. (b) shows the evolution of the height and length of the Pd nanocrystals. The dashed line indicates the equilibrium shape while the different markers for the datapoints indicate different nucleation temperatures. Reprinted with permission from Silly et al [12]. Copyright ©2005, The American Physical Society.

Frank [13] and Chernov [14] were the first to develop dynamic models for evolving crystal shapes and to find the condition which determines their steady-state growth shape. The Frank-Chernov condition for faceted crystals consisting of  $N$  faces on the crystal surface is

$$\frac{G_1}{H_1} = \frac{G_2}{H_2} = \dots = \frac{G_i}{H_i} = \dots = \frac{G_N}{H_N} \quad (1.2)$$

where  $H_i$  is the perpendicular distance of face  $i$  from an origin inside the crystal (e.g., in units of nm),  $G_i$  is the absolute normal growth rate of face  $i$  (e.g., in units of nm/s). This

is similar to the Wulff construction for equilibrium shapes but with the specific surface energy ( $\gamma$ ) of the face replaced by its normal growth rate ( $G$ ).

Under growth conditions (e.g., positive supersaturation, usually measured in terms of the chemical potential driving force represented by  $\Delta\mu > 0$ , where  $\Delta\mu$  is the difference between the chemical potentials of the growth medium and the solute crystal) most crystals spontaneously grow as faceted particles [15, 16]. Although the size of a growing crystal does depend on the absolute values of the growth rate ( $G$ ), the steady-state shape of a growing crystal is determined only by the relative growth rates of the faces exposed on the crystal surface. This is demonstrated by a simple rearrangement of Equation 1.2 as follows

$$\frac{R_1}{x_1} = \frac{R_2}{x_2} = \dots = \frac{R_i}{x_i} = \dots = \frac{R_{N-1}}{x_{N-1}} = 1 \quad (1.3)$$

where  $R_i$  is the growth rate of face  $i$  relative to a reference face,  $R_i = G_i/G_{ref}$ . Similarly,  $x_i$  is the perpendicular distance of face  $i$  from an origin normalized with the perpendicular distance of the reference face from the origin,  $x_i = H_i/H_{ref}$ . In Equation 1.3, face  $N$  is assumed to be the reference face. In crystal growth models, the slowest growing face is usually chosen as the reference face so that  $R_{ref} = 1$  and the other faces have a relative growth rate  $\geq 1$ .

The Frank-Chernov condition validates Gibbs' assertion that the surface structure of large crystals is dominated by the slow growing planes and that faster moving faces "grow out" of the crystal surface and are not present on the steady-state growth shape.

Figure 1.2 shows the computed shape evolution of an ibuprofen crystal grown in aqueous solution from a spherical seed to its final faceted steady-state shape.

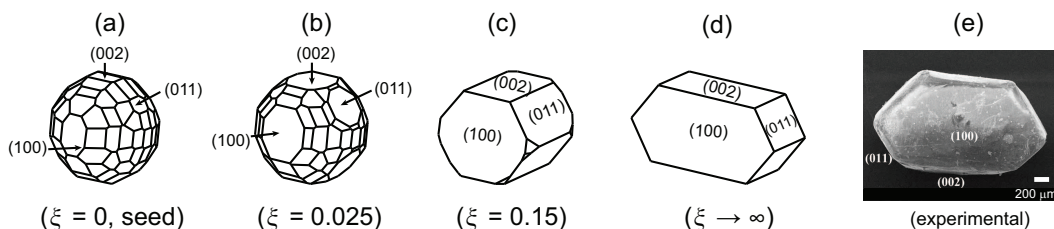


**Figure 1.2:** Predicted shape evolution of ibuprofen from a spherical seed (a-d) ( $\Delta\xi = 0.025$ ) and experimental steady-state shape (e). Parts (a-d) not drawn to scale. Reprinted with permission from Lovette et al [17]. Copyright ©2008, American Chemical Society.

Most of the faces disappear during the shape evolution because they grow too fast relative to their neighbors. Once the steady-state shape is achieved the crystal continues to grow and increase its size with a self-similar shape. The slow growing planes are normally the crystal faces with low values of the Miller indices and these are the ones that most commonly appear on crystal surfaces. In contrast, under dissolution conditions (e.g., undersaturation,  $\Delta\mu < 0$ ) faces that dissolve faster are more prominent on the crystal surface, and these tend to be the high Miller index faces. The faces exposed on the surface of a growing crystal will be different than those on a dissolving crystal and thus they will have different shapes. Additional shapes can be engineered by placing the crystal in a thermal cycling environment whereby in one part of the cycle the crystal grows and in the next it partially dissolves [18, 19].

The first approaches for predicting the growth rate of crystal faces were based exclusively on the structure and interactions within the crystal. Bravais [20] proposed a quantitative relationship for predicting crystal growth rates, based on crystal structure,

supported by the later observations of Friedel [21]. The Bravais relationship is given as

$$G_{hkl} \propto \frac{1}{d_{hkl}} \quad (1.4)$$

where  $G_{hkl}$  and  $d_{hkl}$  are the perpendicular growth rate and interplanar spacing, respectively, of the face specified by the Miller index  $hkl$ . This model (which is referred to as the Bravais-Friedel-Donnay-Harker or BFDH model [22]) is the most easily implemented method for shape prediction because it requires only knowledge of the crystallography of the solid.

A different approach from the BFDH model was the attachment energy model, developed by Hartman and Perdok [23, 24], and Hartman and Bennema [25], who took into account the energetics of crystal interactions in addition to the crystal geometry. They assumed that the time needed for the formation of a bond decreases with increasing bond energy. Defining the attachment energy,  $E_{hkl}^{att}$ , as “the bond energy released when one building unit is attached to the surface of a crystal face,” this assumption leads to the perpendicular growth rate of a crystal face increasing with increased attachment energy,

$$G_{hkl} \propto E_{hkl}^{att} \quad (1.5)$$

These early models did not attempt to capture the exact microscopic mechanism of growth, but instead tried to construct the shape by relating growth rates of faces to either the structure or the energy of the crystal. As a result they often fail to give reliable predictions. However, these models have been widely used in the literature and still persist in modified and improved forms. The effect of the solvent on crystal

growth is accounted by a modified attachment energy model [26–28] that uses molecular simulations to calculate an effective  $E_{hkl}^{att}$  that includes the solid-solvent interactions on the ( $hkl$ ) crystal surface.

In order to account for growth behavior of crystals in different solvents, at various supersaturations and in the presence of additives/imposters, it becomes essential to embrace high fidelity mechanistic models that are devised on sound microscopic principles and as a result are more reliable and accurate.

### 1.3 Mechanistic Growth Models

Mechanistic growth models predict growth rates for crystal faces by kinetic considerations of the sequence of events by which growth units incorporate into crystal lattices. During growth of a crystal face from solution the following processes occur (Figure 1.3):

- (1) Solute molecules are transported from the bulk solution towards the face by convection and diffusion (bulk transport).
- (2) Solute molecules diffuse on the terrace of the crystal surface (surface diffusion).
- (3) Solute molecules and kink sites shed their surrounding solvent molecules (desolvate).
- (4) Solute molecules incorporate into kink sites (surface integration).
- (5) The latent heat of crystallization is released and transported to the crystal and solution.

Surface integration of solute molecules onto the surface is the rate limiting step compared to diffusion or bulk transport mechanisms for almost all molecular organic (and

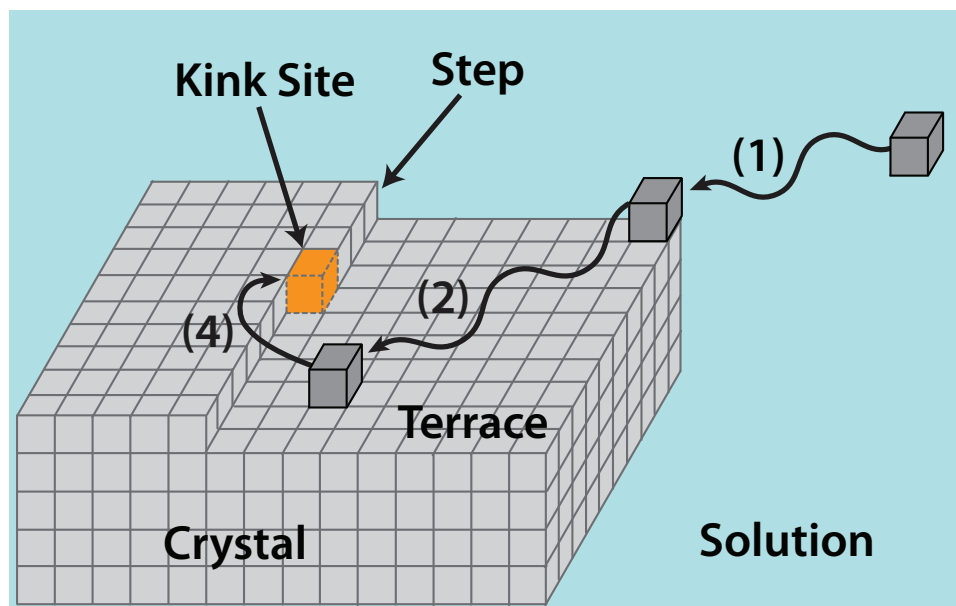


**Figure 1.3:** The sequence of events associated with the incorporation of solute growth units into the kink sites (orange) present on a crystal surface. The incoming solute growth unit (dark grey cube) has the same chemical composition and structure as the other growth units in the crystal (light grey cubes). Processes 3 (desolvation) and 5 (release of latent heat) have not been illustrated for the sake of brevity.

several inorganic) crystals grown from solution. Under surface integration-limited growth, a crystal grows by the flow of steps across the crystal surface. These steps may result from either the formation of 2D nuclei or screw dislocations emerging on the surface. Correspondingly, 2D nucleation and spiral growth are two types of mechanisms for layered growth. According to theory developed by Frenkel [29] and extended by Burton et al., [30] at any temperature higher than 0 °K, steps will contain kink sites (Figure 1.4a and b). The density of kink sites on the step depends on the strength of intermolecular attractions.

On exposure to a supersaturated environment, solute molecules adsorb on the face, diffuse and incorporate into kink sites, causing the layer to spread laterally across the

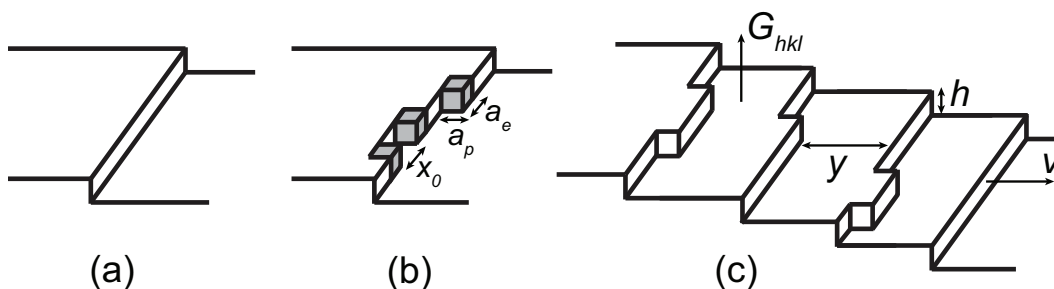


**Figure 1.4:** Schematic of step edges at 0 °K (a) and above 0 °K (b and c). The grey squares in (b) represent kink sites separated by an average distance of  $x_0$ . Image (c) is a schematic of layered growth of the  $\{hkl\}$  face growing at a perpendicular growth rate,  $G_{hkl}$ , through the lateral spreading of steps separated by an interstep distance,  $y$ , with a height,  $h$ , at a step velocity of  $v$ . Adapted with permission from Lovette et al [17]. Copyright ©2008, American Chemical Society.

face. As the layer spreads laterally, new layers are formed on top of it either by new 2D nuclei formation or by shifting of the dislocation source to a layer above (spiral growth). This process repeats, resulting in the perpendicular growth of the crystal face (Figure 1.4c). Generally, a face will grow by whichever process or mechanism enables the fastest growth rate for a defined set of the environmental variables. Organic crystals are grown mainly at low supersaturations to achieve a high degree of purity and control over the entire crystallization process and ensure stable, uniformly distributed well-faceted crystals. Under conditions of low supersaturation, clusters of molecules are not able to cross the thermodynamic free-energy barrier to form stable 2D nuclei and hence such nuclei are unable to form and grow on crystal surfaces. At such conditions, crystal growth occurs by the spiral mechanism, first postulated by Frank in 1949 and developed in detail by Burton, Cabrera and Frank (BCF) in their classic 1951 paper. Crystals expose surface imperfections in the form of screw dislocations that trigger growth spirals on the crystal

surface under the influence of supersaturation resulting in the growth of the surface in its normal direction. Hence, the spiral growth mechanism is the prevalent mechanism at low supersaturations whereas 2D nucleation becomes the rate controlling mechanism at higher supersaturations, since 2D clusters are then able to cross the thermodynamic barrier and once formed, grow more rapidly than spirals [17, 31] (Figure 1.5).

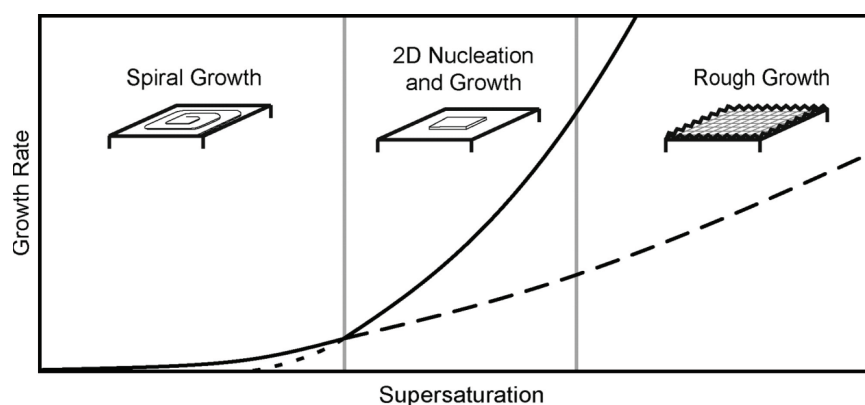


**Figure 1.5:** Growth mechanisms as a function of supersaturation. The solid line is the growth rate in each regime of supersaturation. The short dashed lines are the growth rates if 2D nucleation is continued to be dominant below its applicable supersaturation range. The long dashed line is the growth rate if spiral growth were the persistent mechanism above its applicable supersaturation range. Reprinted with permission from Lovette et al [17]. Copyright ©2008, American Chemical Society.

The relative growth rates remain fairly constant over the range of supersaturations where the spiral growth model applies. Changes in relative growth rates with variation in supersaturation are generally an indication of a change in growth mechanism [32]. An attempt at predictive modeling of supersaturation-dependent crystal shapes was carried out by Lovette and Doherty [33] by identifying the ranges of supersaturation in which the spiral growth and 2D nucleation mechanisms would be dominant.

According to the BCF model, the growth rate of a crystal face that is growing by the spiral mechanism can be expressed as

$$G = \frac{h\mathbf{v}}{y} \quad (1.6)$$

where  $h$  is the height of the step,  $\mathbf{v}$  is the step velocity and  $y$  is the interstep distance on the particular face (Figure 1.4c). The BCF model describes the step fronts or edges that form spirals as being composed of multiple kink sites, which are the favorable sites for the incorporation of solute growth units, based on the bonding structure that they expose to the incoming solute growth units from the solution. The step velocity is dependent on the number density of kink sites on each step, which in turn is a function of the the work required to form the kink sites from a straight step (this quantity is also known as the kink energy). The step height is simply given by geometry (a factor or multiple of interplanar spacing) whereas the interstep distance,  $y$ , is a function of energetics and supersaturation. It has been established beyond doubt in the literature by several theories and experiments that a step edge  $i$  begins to flow outwards, due to incorporation of growth units into kink sites, with a constant step velocity  $\mathbf{v}_i$  only when a spiral edge reaches a critical length  $l_{i,c}$ . This critical length depends on the energetic interactions within the edge itself and on supersaturation. When the spiral side  $i$  moves, it exposes a new edge  $i + 1$  which will start moving in its normal direction when it reaches its critical length. The supplementary section of Rimer et al. [34] contains a video capture of an actual growth spiral of L-cystine that can serve as a basic visualization of this growth phenomenon.

Several notable modifications and extensions of the BCF model such as the work by Chernov [35], and by the Doherty group [36] attempt to mechanistically predict crystal morphologies. The traditional approach of assuming a Kossel crystal lattice, a simple cubic lattice with all equal bonds, made it applicable to centrosymmetric molecules only. Non-centrosymmetric molecules form complex intermolecular bonding structures which pose a set of unique challenges such as multiple types of growth units and kink types resulting in a non-isotropic driving force on edges in different directions. For about five decades after the BCF model was published, the step velocity was always assumed to be only a function of the number density of kink sites. In the last fifteen years, there have been several important developments in the field of non-Kossel crystal growth. Zhang and Nancollas worked on the step movement on the surface of AB-type ionic crystals [37]. For the first time they introduced the concept of kink rate to account for the non-isotropic driving force and reasoned that the step velocity must be directly proportional to the kink rate in addition to the kink density. Kink rate is the net rate of incorporation of solute growth units into different types of kink sites on a particular edge [32, 35] and is an essential calculation for acentric growth units. Chernov et al [38, 39] also derived expressions for the step velocity of non-Kossel crystals, mainly addressing the surface physics and extended the concept to a system with three types of kink sites in series. Recently, Kuvadia and Doherty [32] developed a master equation that can be solved to yield kink rate for any number of kink sites in series, thus extending the concept to all organic molecular crystals.

Another key concept useful to understand crystal growth of real-complexity systems is the theory of stable and unstable edges [32]. The non-centric nature of the bonding on a crystal surface often results in a combination of stable and unstable edges. The concept of unstable edges in some PBC directions also explains the asymmetric growth spirals on surfaces that are a characteristic of non-centrosymmetric growth units. The layers of unstable edges lead to a modified kink rate expression as described in the Kuvadia and Doherty model. The entire approach gave excellent agreement of predicted crystal shapes with experimental shapes for systems of real complexity such as paracetamol and lovastatin.

## **1.4 Dissertation Outline**

The remaining chapters of this dissertation provide a mechanistic framework for modeling inorganic crystallization processes, and demonstrate how the understanding of the solid-state interactions and the growth mechanism can be used to predict and modify crystal shapes. The chapters of this dissertation were written separately and each chapter can be approached on its own. However, if read together this dissertation aims to provide a contiguous story demonstrating the various causalities present in ionic crystal growth from solution.

In an attempt to introduce the concepts discussed throughout this dissertation in a tractable manner, Chapter 2 provides a new method to model the solid-state interactions of inorganic crystal growth. In Chapter 3, a spiral growth model is proposed that

utilizes the calculation of solid-solid and solid-solvent interaction energies that govern the kinetics of surface integration-limited growth. Together, these two chapters provide a first-principles methodology that can be applied to study crystal growth and predict the steady-state morphology of solution grown inorganic crystals. These concepts were applied to study the growth of calcite ( $\text{CaCO}_3$ ) crystals grown in an aqueous solution.

Aragonite is a metastable polymorph of calcium carbonate with lower lattice symmetry than calcite. Chapter 4 discusses a special case of the space partitioning method developed in Chapter 2 for the calculation of kink site energetics of aragonite crystals. The mechanistic concepts covered in Chapters 2 and 3 are used to predict the steady-state morphology of aragonite crystals grown from water.

Several inorganic crystals such as  $\text{CaCO}_3$ ,  $\text{BaSO}_4$ ,  $\text{KH}_2\text{PO}_4$ , etc. are grown from aqueous solution at room temperatures. However, many industrially relevant inorganic crystals such as  $\text{TiO}_2$ ,  $\text{ZnO}$ ,  $\text{SiO}_2$  (quartz), etc. have poor solubility in water at room temperature. Hydrothermal processes are commonly used synthesis techniques for crystal growth of such inorganic crystals. Chapter 5 presents both experimental and theoretical efforts undertaken to study hydrothermal synthesis of anatase ( $\text{TiO}_2$ ). Chapter 6 discusses growth and stabilization of  $\text{ZnO}$  wurtzite, which is a polar crystal structure. The mechanism(s) responsible for the stabilization of polar crystal surfaces have not completely revealed their mystery yet.

Finally, Chapter 7 summarizes this dissertation and provides insights into relevant avenues for future research.

# Bibliography

- [1] N. Variankaval, A. S. Cote, and M. F. Doherty. From form to function: Crystallization of active pharmaceutical ingredients. *AIChE J.*, 54:1682–1688, 2008.
- [2] H. G. Yang, C. H. Sun, S. Z. Qiao, J. Zou, G. Liu, S. C. Smith, H. M. Cheng, and G. Q. Lu. Anatase TiO<sub>2</sub> single crystals with a large percentage of reactive facets. *Nature*, 453:638–641, 2008.
- [3] M. Law, L. E. Greene, J. C. Johnson, R. Saykally, and P. Yang. Nanowire dye-sensitized solar cells. *Nat. Mater.*, 4:455–459, 2005.
- [4] M. A. Lovette and M. F. Doherty. Needle-shaped crystals: Causality and solvent selection guidance based on periodic bond chains. *Cryst. Growth Des.*, 13:3341–3352, 2013.
- [5] P. Christopher and S. Linic. Shape- and size-specific chemistry of Ag nanostructures in catalytic ethylene epoxidation. *ChemCatChem*, 2:78–83, 2010.
- [6] Y. Xia, Y. Xiong, B. Lim, and S. E. Skrabalak. Shape-controlled synthesis of metal nanocrystals: Simple chemistry meets complex physics? *Angew. Chem. Int. Ed.*, 48:60–103, 2009.
- [7] J. W. Gibbs. *The Collected Works of J. Willard Gibbs*. New Haven: Yale University Press, 1957.
- [8] G. Wulff. Zur frage der geschwindigkeit des wachsthums und der auflösung der krystallflächen. *Z. Kristallogr.*, 34:449, 1901.
- [9] C. Herring. Some theorems on the free energies of crystal surfaces. *Phys. Rev.*, 82:87–93, 1951.
- [10] B. Mutaftschiev. *Handbook of Crystal Growth, 1a Fundamentals–Thermodynamics and Kinetics*, chapter Nucleation Theory, pages 187–247. Amsterdam: North-Holland, 1993.
- [11] R. Kern. *Morphology of Crystals: Part A*, chapter The Equilibrium Form of a Crystal, pages 77–206. Tokyo: Terra Scientific Publishing Company, 1987.

- [12] F. Silly, A. C. Powell, M. G. Martin, and M. R. Castell. Growth shapes of supported Pd nanocrystals on SrTiO<sub>3</sub>(001). *Phys. Rev. B*, 72:165403, 2005.
- [13] F. C. Frank. *Growth and Perfection of Crystals*, chapter On the Kinematic Theory of Crystal Growth and Dissolution Processes, pages 411–419. New York: Wiley, 1958.
- [14] A. A. Chernov. The kinetics of the growth forms of crystals. *Sov. Phys. Cryst.*, 7:728–730, 1963.
- [15] G. Liu, K. Chen, H. Zhou, J. Tian, C. Pereira, and J. M. F. Ferreira. Fast shape evolution of tin microcrystals in combustion synthesis. *Cryst. Growth Des.*, 6:2404–2411, 2006.
- [16] K. Jackson, D. Uhlmann, and J. Hunt. On the nature of crystal growth from the melt. *J. Cryst. Growth*, 1:1 – 36, 1967.
- [17] M. A. Lovette, A. R. Browning, D. W. Griffin, J. P. Sizemore, R. C. Snyder, and M. F. Doherty. Crystal shape engineering. *Ind. Eng. Chem. Res.*, 47:9812–9833, 2008.
- [18] R. C. Snyder and M. F. Doherty. Faceted crystal shape evolution during dissolution or growth. *AIChE J.*, 53:1337–1348, 2007.
- [19] M. A. Lovette, M. Muratore, and M. F. Doherty. Crystal shape modification through cycles of dissolution and growth: Attainable regions and experimental validation. *AIChE J.*, 58:1465–1474, 2012.
- [20] A. Bravais. *Études Crystallographiques*. Paris: Gauthier-Villars, 1866.
- [21] M. G. Friedel. Études sur la loi de Bravais. *Bull. Soc. Franc. Miner.*, 9:326, 1907.
- [22] J. D. H. Donnay and D. Harker. A new law of crystal morphology extending the law of bravais. *Amer. Min.*, 22:446, 1937.
- [23] P. Hartman and W. G. Perdok. On the relations between structure and morphology of crystals. I. *Acta Crystallogr.*, 8:49–52, 1955.
- [24] P. Hartman and W. G. Perdok. On the relations between structure and morphology of crystals. II. *Acta Crystallogr.*, 8:521–524, 1955.
- [25] P. Hartman and P. Bennema. The attachment energy as a habit controlling factor : I. Theoretical considerations. *J. Cryst. Growth*, 49:145–156, 1980.
- [26] J. J. Lu and J. Ulrich. An improved prediction model of morphological modifications of organic crystals induced by additives. *Cryst. Res. Technol.*, 38:63–73, 2003.

- [27] R. B. Hammond, K. Pencheva, V. Ramachandran, and K. J. Roberts. Application of grid-based molecular methods for modeling solvent-dependent crystal growth morphology: Aspirin crystallized from aqueous ethanolic solution. *Cryst. Growth Des.*, 7:1571–1574, 2007.
- [28] J. Chen and B. L. Trout. Computer-aided solvent selection for improving the morphology of needle-like crystals: A case study of 2,6-dihydroxybenzoic acid. *Cryst. Growth Des.*, 10:4379–4388, 2010.
- [29] J. Frenkel. On the surface motion of particles in crystals and the natural roughness of crystalline faces. *J. Phys. U.S.S.R.*, 9:392, 1945.
- [30] W. K. Burton, N. Cabrera, and F. C. Frank. The growth of crystals and the equilibrium structure of their surfaces. *Phil. Trans. Roy. Soc. A*, 243:299–358, 1951.
- [31] M. Ohara and R. C. Reid. *Modeling Crystal Growth Rates from Solution*. New Jersey: Prentice-Hall, Inc., 1973.
- [32] Z. B. Kuvadia and M. F. Doherty. Spiral growth model for faceted crystals of non-centrosymmetric organic molecules grown from solution. *Cryst. Growth Des.*, 11:2780–2802, 2011.
- [33] M. A. Lovette and M. F. Doherty. Predictive modeling of supersaturation-dependent crystal shapes. *Cryst. Growth Des.*, 12:656–669, 2012.
- [34] J. D. Rimer, Z. An, Z. Zhu, M. H. Lee, D. S. Goldfarb, J. A. Wesson, and M. D. Ward. Crystal Growth Inhibitors for the Prevention of L-Cystine Kidney Stones Through Molecular Design. *Science*, 330:337–341, 2010.
- [35] A. A. Chernov. *Modern Crystallography III. Crystal Growth*. Berlin: Springer-Verlag, 1984.
- [36] R. C. Snyder and M. F. Doherty. Predicting crystal growth by spiral motion. *Proc. R. Soc. A*, 465:1145–1171, 2009.
- [37] J. Zhang and G. H. Nancollas. Kink density and rate of step movement during growth and dissolution of an AB crystal in a nonstoichiometric solution. *J. Colloid Interface Sci.*, 200:131 – 145, 1998.
- [38] A. Chernov, L. Rashkovich, and P. Vekilov. Steps in solution growth: dynamics of kinks, bunching and turbulence. *J. Cryst. Growth*, 275:1–18, 2005.
- [39] L. Rashkovich, E. Petrova, T. Chernevich, O. Shustin, and A. Chernov. Non-kossel crystals: Calcium and magnesium oxalates. *Crystallogr. Rep.*, 50:S78–S81, 2005.

## Chapter 2

# Solid-State Interactions in Inorganic Crystals

Reproduced in part with permission from: Dandekar, P.; Doherty, M.F. A Mechanistic Growth Model for Inorganic Crystals: Solid-State Interactions. *AIChE Journal*, **2014**, (*in press*).

### 2.1 Introduction

The steady-state morphology achieved by a growing crystal depends on the growth kinetics of all the crystal faces [1, 2]. When the surface integration of growth units is rate limiting, the crystal grows by the flow of steps across its surface. The growth units attach into special sites, known as kink sites, along these steps. A kink site on the crystal surface is defined as the lattice position of a growth unit in which it is surrounded by exactly half of the solid-state neighbors as in the bulk crystal (also known as the half-crystal position) [3]. The rate of crystal growth is fundamentally linked to the work done in adding a growth unit into the kink site [4]. Therefore, the solid-state interactions in

the crystal must be studied in detail to create a mechanistic growth model for inorganic crystals.

Inorganic crystals are often composed of highly electropositive and electronegative atoms, so the solid-state intermolecular interactions are dominated by the electrostatic interactions. Normally, the long-range electrostatic interactions within ionic crystals are accounted for by using the Madelung constant, which is the ratio of the overall electrostatic interaction energy inside the bulk crystal relative to the nearest-neighbor electrostatic interaction energy [5, 6]. However, this approach only captures the interactions in the bulk solid and does not consider the variation in the electronic structure at the growth surfaces. The goal here is to develop an engineering model suitable for product and process design that combines the concepts of bulk electrostatic interactions developed by Madelung [5] and Ewald [6] with the effect of the surface structure on the electronic properties of surface atoms of inorganic crystals. The partial charges of atoms in the bulk crystal differ from those on the surface and both differ from the classical valence charge or oxidation state. Quantum mechanical calculations and density functional theory can be used to calculate accurately the partial charges of bulk atoms as well as the surface atoms but it is impractical to perform these calculations on every face of every inorganic crystal. We find that for crystal growth models, the alternative approach provided by the bond valence model [7, 8] delivers sufficiently accurate values of the partial charges of atoms on inorganic crystal surfaces without the need for electron density calculations.

This chapter presents a general method to identify the lattice directions along the strongest intermolecular interactions within inorganic crystals. Identifying these directions, also known as periodic bond chain (PBC) vectors [9], is key to predicting the structure of the step edges and the shapes of growth spirals formed on crystal surfaces. The PBC directions on the cleavage plane of the calcite polymorph of calcium carbonate are identified, and the asymmetric shape of the growth spiral is attributed to the asymmetric structure of the step edges on the  $(10\bar{1}4)$  calcite surface. The classical bond valence theory based on Pauling's rules for ionic bonding [10] is applied here to calculate the partial charges of surface ions as a function of their atomic surroundings. The potential energies of growth units situated in the kink sites along the edges of growth spirals can be calculated for inorganic crystals using a space partitioning method. This method, when applied to the kink sites on the  $(10\bar{1}4)$  surface of calcite crystals, shows the quantitative basis for the asymmetry of the growth spirals and paves the way for a general mechanistic growth model to predict the crystal growth rates and morphologies of inorganic solids, including those with technological importance.

## **2.2 Periodic Bond Chains (PBCs) in Inorganic Crystals**

Hartman and Perdok [9] proposed the concept of periodic bond chains (PBCs) as the key link between the solid-state interactions and the kinetics of crystal growth. PBCs are

chains of strong intermolecular interactions between growth units along a lattice direction which is called the PBC vector. These strong interactions are formed between the growth units (molecules/ions) during the crystallization process and therefore exclude any intra-growth-unit interactions. According to Hartman and Perdok [9, 11], periodic bond chains must satisfy certain rules as listed below

1. A periodic bond chain must consist of uninterrupted chains of strong intermolecular interactions so that the crystal would grow in the direction of the PBC.
2. There must be a fundamental arrangement of growth units within the chain, also known as the structural period of the PBC, that is repeated by lattice translations along the PBC vector to obtain the entire periodic bond chain.
3. An intermolecular interaction between a pair of growth units cannot be shared by two PBCs in the same face of a crystal. An interaction may be shared between two PBCs that are not within the same crystal face.
4. The arrangement of growth units along a PBC direction must have the same stoichiometry as the overall stoichiometry of the crystal.
5. For non-polar crystal structures (wherein the net dipole moment of the crystallographic unit cell is zero), the component of the electrostatic dipole moment perpendicular to the PBC vector must be zero.

The perpendicular dipole moment property can be related to the stability of non-polar crystal surfaces. Tasker proposed a stability criterion for ionic crystal surfaces

based on the absence of a dipole moment perpendicular to the surface [12]. Since a stable surface layer contains two or more PBCs, a net dipole moment perpendicular to the PBC vector results in a nonzero dipole moment perpendicular to the surface and will therefore destabilize the surface. Therefore, Tasker's criterion and the PBC property are self-consistent.

If there is a polar axis present in the unit cell, all the periodic bond chains in the crystal may have a net perpendicular dipole moment that is parallel to the polar axis direction. The surfaces of such crystals undergo reconstruction to stabilize the dipole moment perpendicular to the surface and the growth mechanisms of these polar surfaces are still debated [13, 14]. However, the growth of polar crystals is not considered in this chapter.

### **2.2.1 Building Unit of the PBC**

A systematic method to identify the PBCs in inorganic crystals must enforce the Hartman-Perdok rules discussed above, including the stoichiometry and perpendicular dipole moment properties. Inorganic crystals consist of ions as the growth units that are individually non-stoichiometric. Therefore, the PBCs must consist of stoichiometric groups of ions that are repeated throughout the crystal. We use the concept of a building unit of the PBC that has been used earlier for studying the PBCs in calcite ( $\text{CaCO}_3$ ) [15, 16]. The building unit of a PBC is defined as a stoichiometric arrangement of ions such that its rotation and translation along the PBC vector direction will yield the entire

bond chain. Thus, the dipole moment of the building unit must be zero if a single building unit has to yield all the PBCs in the crystal while satisfying the perpendicular dipole moment property for each individual PBC.

The building unit of a PBC must not be confused with the growth unit, the asymmetric unit, or the crystallographic unit cell. The growth unit is the solute species that is present in the growth environment (solution, vapor, etc.) and attaches into the kink sites on the crystal surface. A growth unit may be a molecule (e.g., for a paracetamol crystal), ion (e.g., for a calcium carbonate crystal) or a dimer (e.g., for an  $\alpha$ -glycine crystal). Therefore, a growth unit may not always be stoichiometric. A building unit is the fundamental unit of the PBCs in inorganic crystals and will typically consist of multiple growth units. Figure 2.1 shows the arrangement of  $\text{Ba}^{2+}$  and  $\text{SO}_4^{2-}$  growth units within the building unit, as well as in the crystallographic unit cell of barite ( $\text{BaSO}_4$ ). The building unit for barite consists of two barium and two sulfate growth units and has zero dipole moment. The unit cell consists of four barium and four sulfate growth units while the asymmetric unit consists of one Ba, one S and three O atoms [17]. The conventional notation for the ionic growth units with their oxidation states as superscripts is written here with the understanding that these may not be the actual partial charges of these ions. The calculation of the actual partial charges on the ionic growth units will be discussed in the next section.

There may be several combinations of atoms (or ions) within a crystal structure that satisfy the stoichiometry and zero dipole moment properties. A set of guidelines are listed

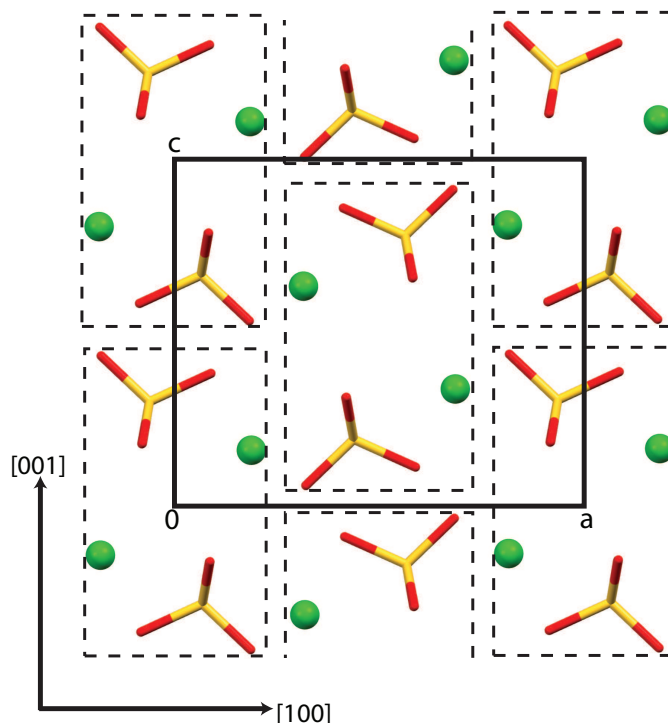


**Figure 2.1:** A view along the  $b$  axis of the barite ( $\text{BaSO}_4$ ) unit cell. The broken black rectangles show the building unit for PBCs in barite crystals. The solid black rectangle shows the edges of the unit cell. Barium atoms are represented by green spheres and sulfate growth unit by yellow (S) and red (O) capped sticks. Note that in this view, the fourth oxygen atom of the sulfate group overlaps with one of the other oxygen atoms and is therefore not visible.

below that may assist in the identification of the most suitable arrangement of atoms within the building unit of a crystal.

- The stoichiometric arrangement of atoms with zero dipole moment must have the **fewest possible number of atoms**. A level of coarse graining (atoms to building units) is required for the identification of PBC directions from chains of building units. Therefore, the identified PBC directions will be more accurate if the number of atoms within the building unit is smaller.

- Among all the candidate building units with same number of atoms, a building unit with the **smallest size or length** is preferred. This follows from the same argument about coarse graining. Radius of gyration may be a convenient measure of the typical length scale of a building unit.
- All possible building units that are not related to each other by the symmetry operators allowed within a particular space group are called independent building units. Two building units (A and B) are symmetrically dependent if there exists a symmetry operator (that belongs to the list of all allowed symmetry operators in that space group), such that applying this operator on every atom within building unit A yields the corresponding atom within building unit B. If no such symmetry operation relates building units A and B, they are called independent building units.
- The contents of the asymmetric unit of the space group can provide a useful check for symmetry dependence between building units. The asymmetric unit is defined as the set of atoms within the unit cell such that the application of all the symmetry operators on these atoms yields all the other atoms within the unit cell. If all the atoms within the asymmetric unit are contained inside a single building unit, then by definition of the asymmetric unit, the lattice symmetry operators can be applied on this particular building unit to obtain all other building units. Therefore, there is only one independent building unit within the crystal structure.

Once all the independent building units are identified based on the aforementioned properties, the symmetry operators of the unit cell are used to pack the crystal with building units. Uninterrupted chains joining these building units can be identified as the PBC directions. Since the building unit is stoichiometric and has a zero dipole moment, the PBCs thus formed will satisfy the Hartman-Perdok rules.

### **2.2.2 Step Edges from Building Units and PBCs**

From a crystal growth perspective, the PBCs are important because the steps of a growth spiral or 2D nucleus on the crystal surface are parallel to the PBC vectors. Knowledge of all the PBC directions on any crystal surface will give the directions of the edges of a growth spiral and help predict its shape. The building unit and its arrangement along a PBC vector must eventually identify the structure of the step edges parallel to that PBC vector.

A step edge is the fundamental feature of a growth step on a crystal surface. Above absolute zero temperature, a straight step edge constantly rearranges under thermal fluctuations to a more favorable configuration such that there is always a finite density of kink sites along the step edge. A growth step moves by the incorporation of growth units into these kink sites present along the edge. Thus, the thickness of a step edge in the growth direction depends on the dimensions of the kink site which is usually 1 growth unit in thickness.

The arrangement of building units along the PBC direction may not give the exact step edge structure since the building unit usually consists of more than one growth unit. For example, Figure 2.2 shows that the arrangement of the building units along the  $[120]$  direction on the  $(210)$  surface of barite does not give the structure of the actual step edge that grows in the  $[001]$  direction. The arrangement of all the building units along a specific PBC direction must be decomposed into individual growth units and an arrangement of growth units along this specific PBC direction must be identified such that three conditions are satisfied - the resulting arrangement must (a) be stoichiometric, (b) have zero dipole moment perpendicular to the specific PBC vector and (c) have dimensions  $\sim 1$  growth unit thickness in the direction of the step motion. Figure 2.2 shows that the step edge structure along the  $[120]$  edge can be constructed from half of the contents of the arrangement of the building units along the  $[120]$  direction. A similar decomposition of the arrangement of the building units must be done for every PBC direction to correctly identify the structure of the step edge. In some cases, this decomposition can be more complicated as the exact step edge structure may be formed out of chains of building units along two different PBC directions. This will be shown later in the chapter for the step edges on calcite surfaces.

Once the structure of the step edges along all the PBC directions is identified, the interaction energy along these edges is calculated to obtain the energy required to create kink sites from a straight step edge [18]. Electrostatic interactions dominate the lattice energy of inorganic crystals so the contribution of the long-range interactions in the PBC

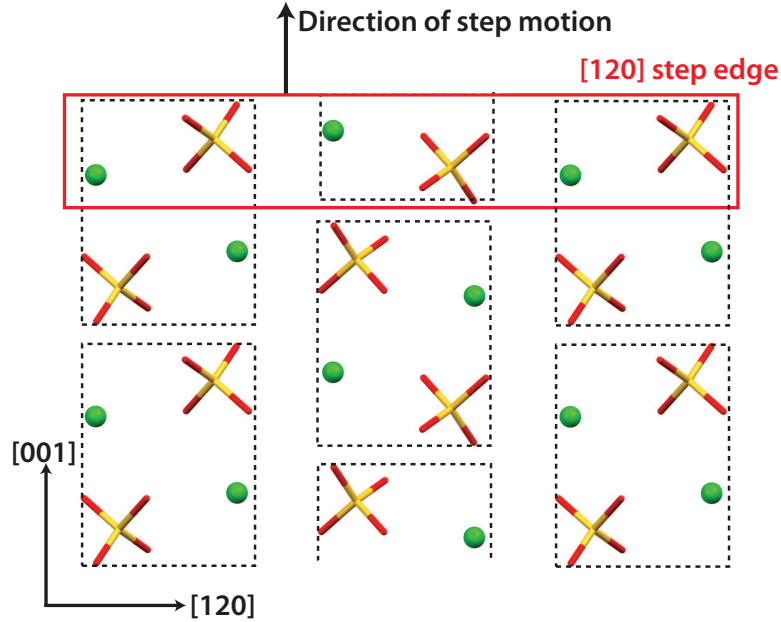


**Figure 2.2:** Crystal packing on the (210) barite surface. The broken black rectangles form building units and the solid red rectangle shows the step edge along the [120] direction. The [120] step edge consists of half of the building unit arrangement while the other half forms part of another step edge parallel to the first one.

interaction energies must be calculated. For example, the ratio of the total interaction energy along the [100] PBC direction to the nearest-neighbor interaction energy for rock salt NaCl crystal is equal to  $2\ln 2 = 1.386$  [19]. The magnitude of the long-range (beyond nearest neighbor) interaction energy accounts for about 44% of the total interaction energy along the [100] PBC chain of rock salt NaCl crystals. Therefore, the energy calculations for inorganic crystals must never be limited to only nearest-neighbor interactions. The interaction energy for a growth unit along the PBC vector  $\vec{v}$  direction is given by

$$E_{PBC, \vec{v}} = \frac{1}{2} \sum_{i=1}^{\infty} \left( \sum_{j=1}^{N_{GU}} U_{i,j} \right) \quad (2.1)$$

$$U_{i,j} = \sum_{k=1}^{N_{GU,i}} \left( \frac{q_j q_k}{4\pi\epsilon_0 r_{jk}} + U_{j,k}^{sr} \right) \quad (2.2)$$

where  $N_{GU}$  is the number of atoms in the central growth unit,  $N_{GU,i}$  is the number of atoms in the growth unit  $i$  along the PBC vector  $\vec{v}$ .  $U^{sr}$  is the short-range interaction energy. A Buckingham potential is used to model the short-range interactions for most inorganic crystals [20, 21].

The framework developed here for identifying the building units, PBC directions and step edge structures is completely general and can be applied to any inorganic crystal. The model requires the crystallographic unit cell data, the partial charges on the atoms of each growth unit in the bulk solid (obtained from quantum mechanical calculations), and a suitable short-range intermolecular force field as inputs to identify the PBC directions in the crystal and calculate the interaction energy  $E_{PBC}$  along each PBC vector. We discuss the PBCs on calcite ( $\text{CaCO}_3$ ) as an example in the following sections.

### 2.2.3 PBCs in Bulk Calcite

At ambient conditions, calcite is the most stable polymorph of crystalline calcium carbonate. It is ubiquitous in nature in the form of sedimentary and metamorphic rocks, cave formations, shells of marine organisms, etc. Crystal growth of calcite has been of special interest from a biomineralization perspective [22]. Pure calcite crystals occur in rhombohedral shape dominated by the  $\{10\bar{1}4\}$  family of cleavage planes [23]. Calcite crystallizes in the  $R\bar{3}c$  space group in the trigonal crystal system. The unit cell parameters for calcite are  $a = b = 4.988 \text{ \AA}$ ,  $c = 17.061 \text{ \AA}$ ,  $\alpha = \beta = 90^\circ$ ,  $\gamma = 120^\circ$  [24]. Figure 2.3 shows the calcite unit cell with the arrangement of the Ca and  $\text{CO}_3$  groups. The atoms

within the asymmetric unit (which consists of one atom each of Ca, C and O) are also labeled in Figure 2.3. The two orientations of the carbonate group in the calcite unit cell are related to each other by a  $2_1$  screw axis.

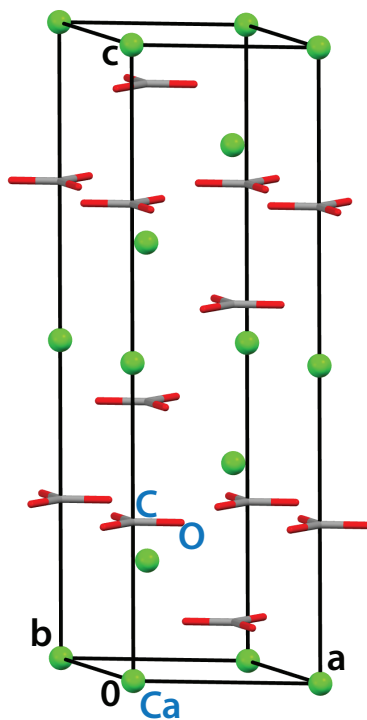


**Figure 2.3:** Calcite unit cell with the Ca atoms (green sphere) and CO<sub>3</sub> groups (grey and red capped sticks). The contents of the asymmetric unit of the unit cell are labeled in cyan.

The building unit of the PBCs in calcite crystals was identified using the properties discussed previously. Figure 2.4 shows the arrangement of Ca<sup>2+</sup> and CO<sub>3</sub><sup>2-</sup> ions within the building units. The two building units shown are related by a  $2_1$  screw axis and are therefore the same building unit with the composition Ca<sub>2</sub>C<sub>2</sub>O<sub>6</sub>. Thus, a single building unit can be used to create all the PBCs in calcite using the symmetry operators present

in the crystallographic unit cell. Figure 2.5 shows the packing of the entire unit cell with building units.

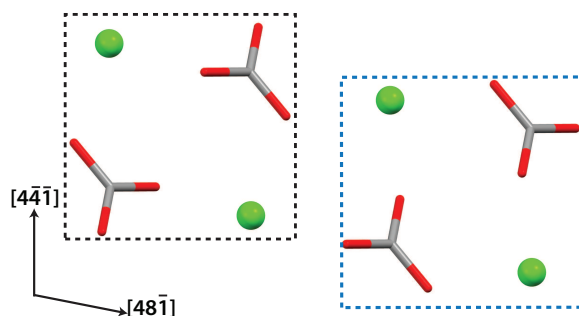


**Figure 2.4:** The two building units (enclosed within the broken black and blue rectangles) in calcite crystal and the arrangement of  $\text{Ca}^{2+}$  and  $\text{CO}_3^{2-}$  ions within each building unit. The two building units are related to each other by a  $2_1$  screw axis.

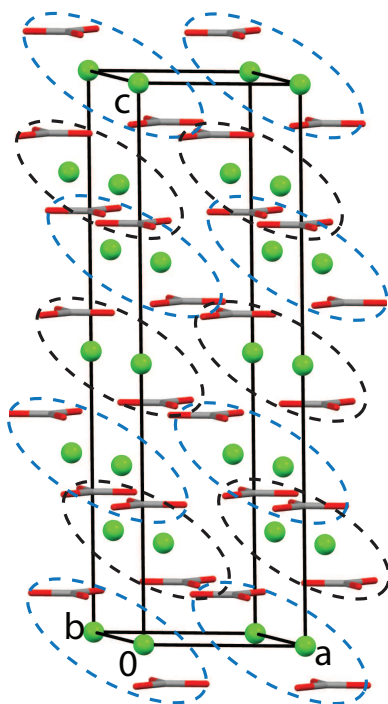


**Figure 2.5:** The packing of a calcite unit cell with building units (enclosed within broken blue and black ellipses).

The packing of the building units on the  $(10\bar{1}4)$  cleavage surface of calcite allows the identification of four PBC directions -  $[\bar{4}41]$ ,  $[48\bar{1}]$ ,  $[42\bar{1}]$  and  $[010]$ . The structure of the step edges on the  $\{10\bar{1}4\}$  calcite surface can be identified from the arrangement of the building units in each of these four PBC directions. The step edge in the  $[48\bar{1}]$  direction contains only half of the contents of the building units, as shown in Figure 2.6. The same is true for the step edge structure in the  $[\bar{4}41]$  direction.

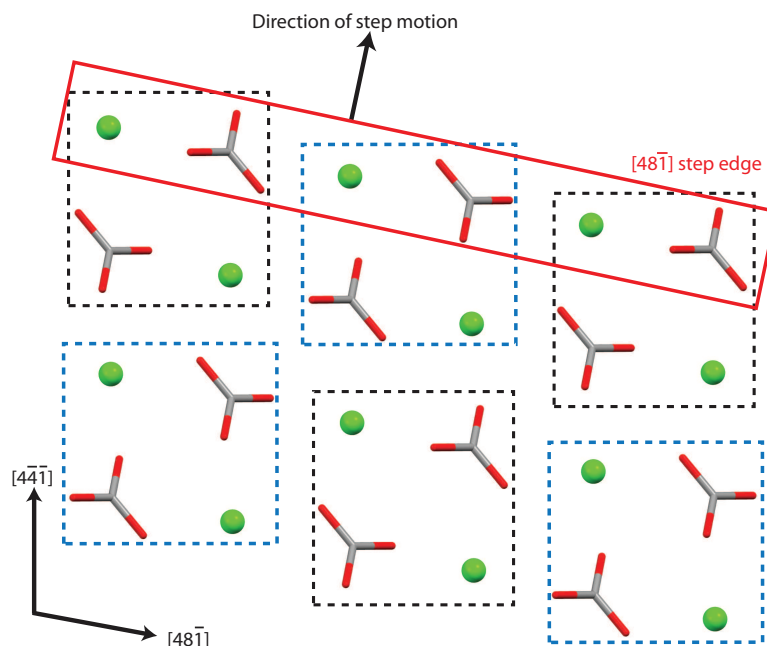


**Figure 2.6:** Crystal packing on the  $(10\bar{1}4)$  surface of calcite. The broken black rectangles form building units and the solid red parallelogram shows the step edge along the  $[48\bar{1}]$  direction. The  $[48\bar{1}]$  step edge consists of half of the building unit contents while the other half forms part of another step edge parallel to the first one.

Figure 2.7 shows the step edge structures for the four PBCs on the  $(10\bar{1}4)$  surface of calcite. The step edges in both the  $[\bar{4}41]$  and  $[48\bar{1}]$  directions are stoichiometric and have zero dipole moment perpendicular to the edge direction. There are two sawtooth-shaped step edges,  $[010]$  and  $[42\bar{1}]$ , that also possess these properties. However, the arrangement

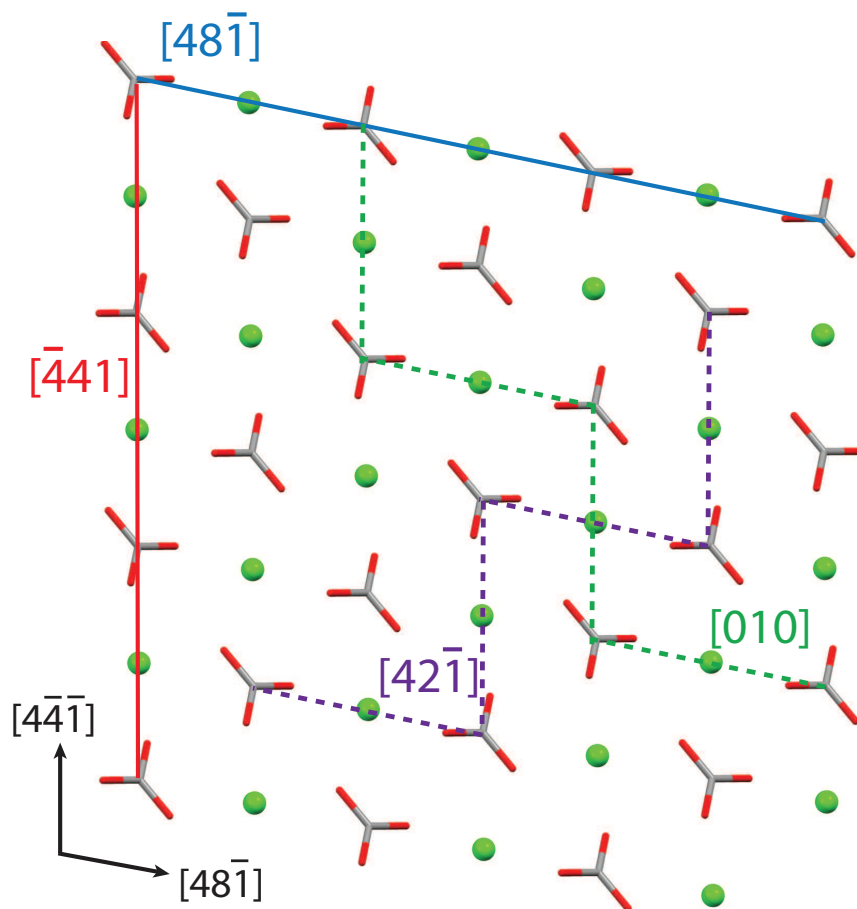


**Figure 2.7:** Step edges along various PBC directions on the  $(10\bar{1}4)$  surface of calcite. The ‘straight’ bond chains  $[\bar{4}41]$  and  $[48\bar{1}]$  are shown in solid red and blue lines, respectively. The ‘sawtooth’ bond chains  $[010]$  and  $[42\bar{1}]$  are shown in broken green and broken purple lines, respectively.

of growth units along the latter pair of PBCs are combinations of the chains in the  $[\bar{4}41]$  and  $[48\bar{1}]$  directions (since some of the interactions between the growth units along the  $[010]$  and  $[42\bar{1}]$  step edges are shared with the growth units along the  $[\bar{4}41]$  and  $[48\bar{1}]$  directions). Hence, there are only two independent PBCs on the  $(10\bar{1}4)$  surface of calcite. It is also evident that the structure of the PBCs in the  $[\bar{4}41]$  and  $[48\bar{1}]$  directions is identical. In fact, there are three families of symmetrically equivalent PBCs present

**Table 2.1:** PBC interaction energies in bulk calcite crystal

PBC vector	$E_{PBC}$ (kcal/mol of growth unit)
$[\bar{4}41]$ , $[48\bar{1}]$ , $[841]$	-140.7
$[010]$ , $[100]$ , $[110]$	-115.3
$[42\bar{1}]$ , $[241]$ , $[2\bar{2}1]$	-96.5

in calcite crystal and they have been listed in Table 2.1. The average interaction energy ( $E_{PBC}$ ) of a growth unit along each of these PBCs in the bulk crystal is also listed in Table 2.1. The interaction energies for the  $[010]$  and  $[42\bar{1}]$  families of PBCs are calculated fully counting the shared interactions with the  $[\bar{4}41]$  family of PBCs (i.e., as though the  $[\bar{4}41]$  family did not exist). The force field parameters including Buckingham potential parameters and partial charges were obtained from Raiteri et al. [25]. A rigid model for the carbonate growth unit is used, which reproduces the bulk structural properties and the water interface equally well as compared to a flexible carbonate model [26].

The lattice energy of calcite was calculated using the same force field parameters [25]. A Madelung sum was carried out for the electrostatic interactions, and the lattice energy remained constant with increasing supercell size beyond  $60 \times 60 \times 20$ . A 10 Å cutoff was applied for the short-range interactions. The lattice energy was calculated as -671.7 kcal/mol for calcium carbonate, which matches very well with the reported value of -670.2 kcal/mol calculated from a Born-Fajans-Haber thermodynamic cycle [27]. The lattice energy of most inorganic crystals is an order of magnitude higher than that of most organic molecular crystals [28] and this difference is also manifested in the values of  $E_{PBC}$  for calcite.

There are four types of growth units in series along each of these edges – two  $\text{Ca}^{2+}$  and two  $\text{CO}_3^{2-}$  ions. The  $E_{PBC}$  values were calculated by averaging the interaction energies of all four growth units with all the other growth units along the semi-infinite chain parallel to the PBC vector direction. The  $E_{PBC}$  values in Table 2.1 show that the  $[\bar{4}41]$  family is the strongest family of PBCs in the calcite crystal. As discussed above, there are only two independent PBCs on the  $(10\bar{1}4)$  surface of calcite, therefore the periodic bond chains along the  $[\bar{4}41]$  and  $[48\bar{1}]$  directions will be the two PBCs present on this surface. This result is consistent with the earlier calculations of interaction energies of adjacent pairs of  $\text{Ca}^{2+}$  and  $\text{CO}_3^{2-}$  ions with the other ions in a semi-infinite chain along the PBC vector directions on the  $(10\bar{1}4)$  surface of calcite [16]. Since the  $[010]$  and  $[42\bar{1}]$  families of PBCs contain intermolecular interactions shared with the  $[\bar{4}41]$  and  $[48\bar{1}]$  PBCs, these two families of PBCs will not be considered further in this work. Figure 2.8 shows the shape of the growth spirals observed from atomic force microscopy (AFM) measurements on the  $(10\bar{1}4)$  surface of calcite [29]. The four-sided growth spiral is formed by the  $[\bar{4}41]$  and  $[48\bar{1}]$  step edges as predicted by the model.

From Figure 2.8, the growth spiral is asymmetric, such that the two opposite edges parallel to the  $[\bar{4}41]$  PBC vector grow at different step velocities [30]. The same is true for the step velocities of the two edges parallel to the  $[48\bar{1}]$  direction. However, the interaction energy values,  $E_{PBC}$ , reported in Table 2.1 are the same for both the opposite edges, denoted as  $[\bar{4}41]_+$  and  $[\bar{4}41]_-$ . Therefore, the presence of asymmetric

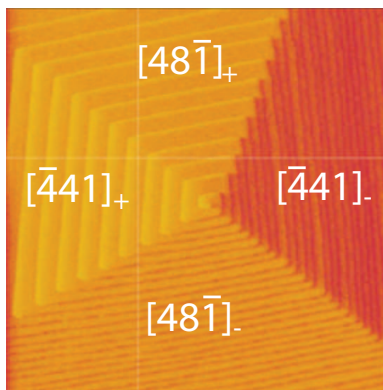


**Figure 2.8:** AFM image of a growth spiral on the  $(10\bar{1}4)$  surface of calcite. The image size is  $3 \times 3 \mu\text{m}$ . Adapted with permission from Davis et al. [29]. Copyright ©2004, Mineralogical Society of America.

growth spirals on the  $(10\bar{1}4)$  surface of calcite cannot be explained on the basis of the PBC interaction energies in bulk calcite.

It has been postulated that the asymmetry of the growth spirals stems from the difference in the structure of the  $[\bar{4}41]_+$  and  $[\bar{4}41]_-$  edges [31]. The surface energies of these As shown in Figure 2.9, the  $[\bar{4}41]_+$  and  $[\bar{4}41]_-$  edges form obtuse and acute angles, respectively with the terrace plane. These edges are also referred to as the obtuse and acute edges, respectively.

## 2.3 Surface Effects on Solid-State Interactions

The hypothesis here is that the asymmetric structure of the opposite step edges on the  $(10\bar{1}4)$  calcite surface and the resulting difference in the electronic properties of the atoms along these edges must result in a difference in the solid-state interactions between the growth units present along the  $[\bar{4}41]_-$  acute and  $[\bar{4}41]_+$  obtuse edges. This variation

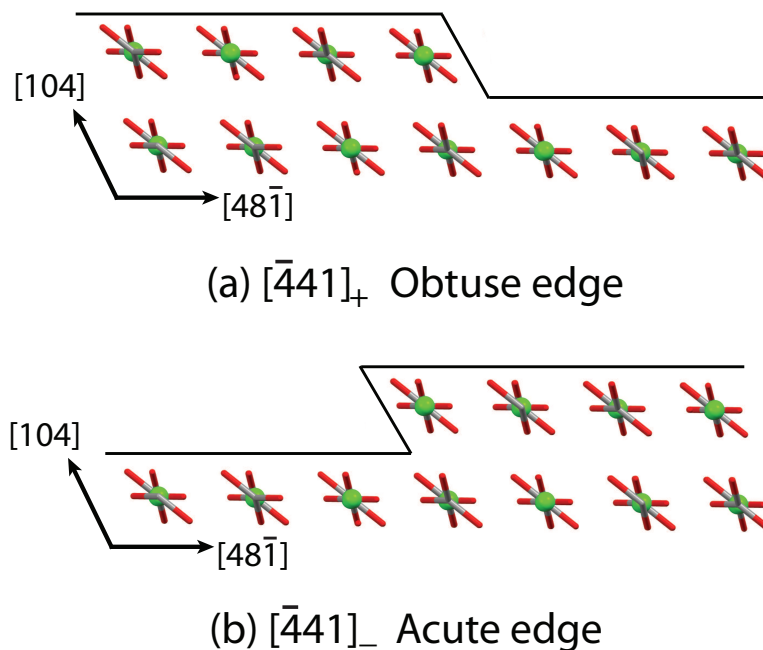


**Figure 2.9:** Side view of the  $[\bar{4}41]$  edge on the  $(10\bar{1}4)$  surface of calcite. The  $[\bar{4}41]_+$  and  $[\bar{4}41]_-$  edges have been shown in (a) and (b), respectively, with the angle between the edge and the terrace being obtuse for the former and acute for the latter edge.

in the interaction energies will result in asymmetric step velocities for the acute and obtuse spiral edges on the  $(10\bar{1}4)$  surface of calcite. A quantitative relationship between the environment of an atom and its partial charge is required to capture the difference in electronic properties of atoms between the obtuse and acute edges.

In the field of condensed matter physics, it is well known that the electronic structure (and hence the partial charge) of an atom is strongly related to the number and types of surrounding atoms and their distances from the central atom [19]. Knowledge of an atom's surroundings in the solid state has been one of the foundations of the ionic model of chemical bonding. Pauling proposed a set of five rules in 1929 that relate the crystal structure of an ionic solid to the properties of the constituent atoms [10]. These rules have

been used to predict the crystal structure of ionic solids if the ionic radii and coordination numbers for the ions within the solid are known. One of the five rules relates the atomic charge on an anion,  $q_i$ , with the strength of the electrostatic bond  $S_{ij}$  that the anion  $i$  shares with its neighboring cation  $j$  in the solid [10].

$$q_i = - \sum_{j=1}^{CN_i} \left( \frac{q_j}{CN_j} \right) = - \sum_{j=1}^{CN_i} S_{ij} \quad (2.3)$$

where  $CN_i$  and  $CN_j$  are the coordination numbers of the anion  $i$  and cation  $j$ , respectively.  $q_j$  is the charge on cation  $j$ , and  $S_{ij}$  has units of electronic charge (Coulombs) and is always positive. The negative sign is introduced in equation 2.3 only to ensure that the charge  $q_i$  on anion  $i$  is always negative. For any ion in general, the charge is given by the summation of the bond strengths shared with its neighbors and the appropriate sign is affixed to the value of the summation depending on whether the ion is less or more electronegative than its neighbors (positive and negative signs, respectively).

Pauling's definition of the bond strength  $S$  can be used to calculate the partial charge of an ion only if the crystal structure has high symmetry such that all the bond strengths that a cation shares with its neighboring anions are equal (e.g., all nearest anionic neighbors are equidistant from the cation). This definition also does not account for the asymmetry in electrostatic bond strengths resulting from the relaxation of surface layers.

### 2.3.1 Bond Valence Model

A realistic quantification of the bond strength between atoms in inorganic crystals was made possible in the early 1970s when Donnay and Allmann proposed empirical

relationships between the electrostatic bond strength  $s$  and the interionic distance [32]. Brown and Shannon [7] verified the generality of two Donnan and Allmann correlations between the bond strength  $s_{ij}$  and the interatomic distance  $r_{ij}$  between atoms  $i$  and  $j$

$$\left(\frac{s_{ij}}{e}\right) = \exp\left(\frac{R_0 - r_{ij}}{B}\right) \quad (2.4)$$

$$\left(\frac{s_{ij}}{e}\right) = \left(\frac{r_{ij}}{R_0}\right)^{-N} \quad (2.5)$$

where  $R_0$ ,  $B$  and  $N$  are parameters for each  $(i, j)$  pair and  $e$  is the elementary charge. These empirical correlations are robust such that the same parameter values work well for any inorganic solid containing the same pair of atoms [8]. Although both the correlations work well, equation 2.4 is preferred because it reflects the repulsive potential between atoms and also because it is a well-behaved mathematical function at very small interatomic distances. To avoid confusion with Pauling's definition of bond strength, the quantity  $s_{ij}$  calculated from equation 2.4 is termed the *bond valence* between atoms  $i$  and  $j$ . This method is therefore called the bond valence model. Note that when all atomic neighbors in the coordination shell have the same charge and are all equidistant from the central ion,  $s_{ij} = S_{ij}$ .

The physical significance of the bond valence model and its applicability to quantify electrostatic interactions in inorganic solids has been studied in some detail [33]. The electrostatic field lines between two atoms in any inorganic solid can be added up using Gauss' law to calculate the total electrostatic flux (normalized by the permittivity of free space  $\epsilon_0$ ) between the two atoms. Figure 2.10 shows an example of the electrostatic field lines in the  $(1\bar{1}0)$  plane of rutile ( $\text{TiO}_2$ ). For most inorganic crystals, the root

mean squared error between the bond valences calculated from the interatomic distances (Equation 2.4) and the total electrostatic flux calculated from Gauss' law was found to be less than  $0.1e$  [33]. This shows that the bond valence method accurately estimates the electrostatic interactions between two atoms in the solid state and therefore can be used to calculate the partial charges of atoms in inorganic crystals.

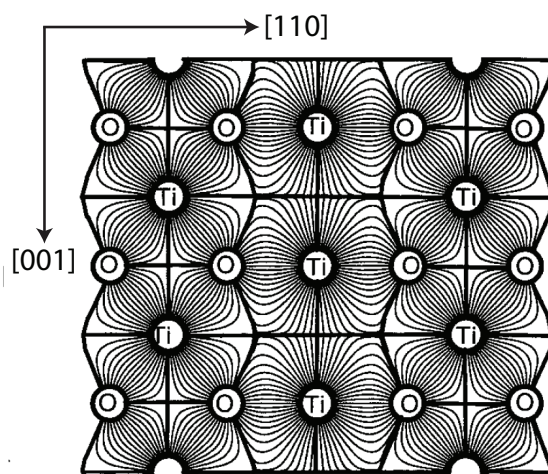


**Figure 2.10:** A representation of the electrostatic field in the  $(1\bar{1}0)$  face of rutile ( $\text{TiO}_2$ ). The light lines represent the electrostatic field lines and the thick lines show the zero-flux boundary that partitions space into bond regions. Adapted with permission from Preiser et al. [33]. Copyright ©1999, International Union of Crystallography.

The bond valence method assumes the fully ionic model for chemical bonding in inorganic crystals such that the partial charge of an atom obtained from the summation of its bond valences in the bulk is equal to its oxidation state. However, it is well known that most inorganic solids are not fully ionic. There is always some sharing of the electron density between the less electronegative and more electronegative atoms in the solid. Therefore, the actual atomic charge may not be equal to the oxidation state of the atom. Quantum mechanical calculations of bulk solids provide the accurate

electron density distribution within the solid. Mulliken population analysis [34] and Bader charge partitioning [35] are two of the most widely used methods to partition the electron density between the atomic nuclei so that each atom can be assigned a partial charge. It is important to avoid the use of classical oxidation states on atoms in inorganic crystals since those charges overestimate the lattice energies.

The bond valence model can still be used to calculate the partial charges of surface atoms, provided the actual partial charges on the atoms in the bulk solid are known (e.g., from DFT calculations). The individual bond valences  $s_{ij}$  calculated from interatomic distances (e.g., from equation 2.4) must be scaled by the ratio of actual charge  $q_{i,actual}$  to the oxidation state  $q_{i,OS}$  of the atom  $i$  to give a normalized bond valence value  $s'_{ij}$  given by

$$s'_{ij} = s_{ij} \left( \frac{q_{i,actual}}{q_{i,OS}} \right) \quad (2.6)$$

where  $q_{i,OS} = \sum_{j=1}^{CN_i} s_{ij}$  (i.e., equation 2.3) and  $q_{i,actual} = \sum_{j=1}^{CN_i} s'_{ij}$ . The normalized bond valence  $s'_{ij}$  should be used to calculate the actual partial charge  $q_{i,surf}$  of atom  $i$  on the surface with coordination number  $CN_{i,surf}$  as follows

$$q_{i,surf} = \sum_{j=1}^{CN_{i,surf}} s'_{ij} \quad (2.7)$$

Thus, the bond valence model can be used to calculate the actual partial charges on the surface atoms of any inorganic crystal if the interatomic distances between the surface atoms and their neighbors are known. Although this method may not be as accurate as

quantum mechanical calculations on a crystal surface, it is much simpler and faster, and it has been found to be well suited to predicting crystal growth of inorganic solids.

Accurate information about the structure of both the surface and the growth medium close to the surface is required to calculate the surface charges using the bond valence model. Usually, surfaces of inorganic solids undergo relaxation and sometimes even reconstruct [19]. Experimental measurements of surface relaxation using diffraction-based methods such as low-energy electron diffraction (LEED) can provide the positions of surface atoms and can be used to calculate the new distances between these atoms and their neighbors. Similarly, accurate information about the structure of solvent molecules around the surface atoms is needed to calculate the bond valence between the surface atoms and the solvent species. Experiments such as X-ray reflectivity measurements [36, 37] and molecular simulations [25, 38–40] can provide the distances between the surface or edge atoms and the solvent molecules. These inputs are required to accurately calculate the partial charges of atoms on inorganic crystal surfaces.

For bulk calcite crystal, the partial charges for atoms in the bulk were obtained from Raiteri et al. [25]. They fitted the force field parameters including the partial charges against the measured structural and mechanical properties of calcite crystal, as well as, against the experimental free energy change ( $\Delta G$ ) of phase transition between calcite and aragonite. The reported values of the bulk partial charges for Ca, C and O are +2, +1.123 and -1.041, respectively. The bond valence parameters for the two atom pairs (Ca-O and C-O) were obtained from a list of bond valence parameters hosted online

**Table 2.2:** Bond valence parameters and bond valences for the atom pairs in bulk calcite

Atom pair	$R_0$ (Å)	$B$ (Å)	$r_{ij}$ (Å)	$s'_{ij}$ ( $e$ )
Ca and O	1.967	0.37	2.360	0.333
C and O	1.390	0.37	1.280	0.374

**Table 2.3:** Bond valence parameters and the bond valences for the O-H pairs in liquid water

Atom pair	$R_0$ (Å)	$b$ (Å)	$r_{ij}$ (Å)	$s'_{ij}$ ( $e$ )
O and H (covalent)	0.907	0.28	0.9572	0.323
O and H (hydrogen bond)	0.569	0.94	1.9	0.094

by Ian David Brown. Table 2.2 lists the bond valence parameters for the two pairs of atoms along with the interatomic distances in bulk calcite and bond valences scaled by their oxidation states. Calcite crystal structure has high symmetry such that each Ca atom is surrounded by 6 equidistant oxygen atoms and each C atom is surrounded by 3 equidistant oxygen atoms.

The bond valences for the O-H atom pair and their partial charges in liquid water were obtained from Brown [8] and the TIP3P model [41], respectively, and are tabulated in Table 2.3. The structure of liquid water is assumed to be such that a tetrahedrally coordinated O atom shares covalent bonds with two H atoms and hydrogen bonds with the other two H atoms [8]. The distances between the O atom and the two sets of H atoms are 0.9572 Å and 1.9 Å, respectively. The partial charges for O and H atoms were obtained from the TIP3P model as  $-0.834e$  and  $+0.417e$ , respectively [41].

The distribution of water molecules around different surface species on calcite ( $10\bar{1}4$ ) surface was obtained from the MD simulations performed by Wolthers et al. [38]. They reported average distances between the water molecules near the surface and the calcite

**Table 2.4:** Partial charges of the calcium atoms in calcite at different lattice positions

Lattice Position	Partial Charge ( $e$ )
Bulk Ca	+2.0
Terrace Ca	+1.917
Edge (Acute or Obtuse) Ca	+1.833
Kink Ca	+1.750

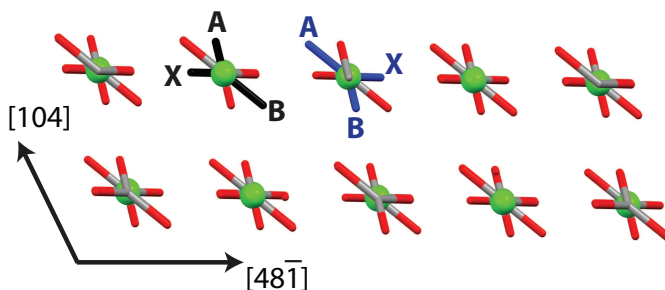
growth units in different surface positions (terrace/step/kink). The partial charges of Ca, C and O atoms in different surface positions were calculated using these interatomic distances and the bond valence model. Table 2.4 lists the partial charges of Ca atoms in different lattice positions on the calcite ( $10\bar{1}4$ ) surface, and in the bulk. The partial charge on a Ca atom decreases as its location varies from inside the bulk solid to a kink site on a crystal surface. Although these charge values are calculated in the presence of water molecules, yet their presence does not fully compensate for the loss of solid-state coordination for surface species. The partial charge on the carbon atoms remains constant (+1.135) at every lattice position (bulk and surface) since it is always surrounded by its three neighboring oxygen atoms. The partial charges on the oxygen atoms in different lattice positions are tabulated in the supplementary information (Table S2).

The partial charges on the three oxygen atoms of the carbonate growth unit in different lattice positions are reported in Table 2.5. The oxygen atoms of the carbonate group are labeled as A, X or B depending on their orientation (Figure 2.11). This notation is consistent with that used by Wolthers et al<sup>3</sup>. In Table 2.5, the partial charges of each O atom are listed for both carbonate orientations (blue and black from Figure 2.11) on the  $[\bar{4}41]$  edges. If the partial charge of an O atom is the same for both orientations, there

**Table 2.5:** Partial charges of the atoms of the carbonate growth unit in calcite at various lattice positions

Lattice Position	Partial Charges of O atoms and CO <sub>3</sub> ion ( <i>e</i> )			
	O (A)	O (X)	O (B)	CO <sub>3</sub>
Bulk	-1.045	-1.045	-1.045	-2.0
Terrace	-0.962	-1.045	-1.045	-1.917
$[\bar{4}41]$ Obtuse edge	-0.962	-0.962,-1.045	-1.045,-0.962	-1.833
$[\bar{4}\bar{4}1]$ Acute edge	-0.878,-0.962	-1.045,-0.962	-1.045	-1.833
$[\bar{4}41]$ Obtuse $\mathscr{W}$ kinks	-0.962	-0.962	-0.962	-1.750
$[\bar{4}41]$ Obtuse $\mathscr{E}$ kinks	-0.962,-0.878	-0.878,-1.045	-1.045,-0.962	-1.750
$[\bar{4}\bar{4}1]$ Acute $\mathscr{W}$ kinks	-0.878	-0.962	-1.045	-1.750
$[\bar{4}\bar{4}1]$ Acute $\mathscr{E}$ kinks	-0.878, -0.962	-1.045,-0.878	-0.962,-1.045	-1.750

is only one entry for that O atom. Otherwise, the first entry is the partial charge of O atom in the blue orientation and the second entry is for the black orientation.

**Figure 2.11:** A side view of the (10 $\bar{1}$ 4) surface of calcite showing the two different orientations of carbonate groups in the surface layer. The two orientations are colored black and blue; the oxygen atoms (A, X and B) within each group are also labeled.

The partial charges for the analogous lattice positions on the [48 $\bar{1}$ ] edges can be calculated by swapping the partial charge values between the blue and black orientations. For kink site carbonate growth units, one must also swap the kink orientation from  $\mathscr{E}$  to  $\mathscr{W}$  and vice versa to get the partial charges on the kink sites of the [48 $\bar{1}$ ] edges.

**Table 2.6:** PBC interaction energies ( $E_{PBC}$ ) in kcal/mol along the spiral edges on the  $(10\bar{1}4)$  surface of calcite crystal in contact with water

Spiral Edge	Ca (1)	CO <sub>3</sub> (2)	Ca (3)	CO <sub>3</sub> (4)	Average
$[\bar{4}41]$ Obtuse	-104.9	-138.5	-104.9	-138.5	-121.7
$[\bar{4}41]$ Acute	-104.9	-139.6	-104.9	-137.4	-121.7
$[48\bar{1}]$ Obtuse	-104.9	-138.5	-104.9	-138.5	-121.7
$[48\bar{1}]$ Acute	-104.9	-139.6	-104.9	-137.4	-121.7

### 2.3.2 PBC Energies on $(10\bar{1}4)$ Surface of Calcite

The interaction energies along the PBC directions on the  $(10\bar{1}4)$  calcite surface will govern the density of kink sites along the spiral step edges and ultimately affect the growth kinetics of the spiral edges. The PBC interaction energies of growth units on calcite surface in contact with water are calculated from equations 2.1 and 2.2 using the partial charges listed in Tables 2.4 and S2. Since the partial charges of oxygen atoms on obtuse and acute edges are different, the interaction energies are calculated separately for both types of edges and reported in Table 2.6. There are four growth units (two Ca and two CO<sub>3</sub>) along each of the four spiral edges on the  $(10\bar{1}4)$  surface of calcite, and the interaction energy for each growth unit is reported along with the average interaction energy per growth unit for each edge.

For both the acute and obtuse edges in either  $[\bar{4}41]$  or  $[48\bar{1}]$  directions, the average interaction energy along the edge is exactly the same, similar to that in the bulk crystal. However, the individual interaction energies of the growth units differ between the acute and obtuse edges. Thus, different values of surface partial charges on the oxygen atoms of CO<sub>3</sub> groups on acute and obtuse edges (Table S2) result in the interaction energies

being different on acute and obtuse edges for each of the four growth units. The value of  $E_{PBC}$  determines the work done to create kink sites from thermal rearrangement of a straight step edge [42], therefore, the density of kink sites is expected to be different on obtuse and acute edges. The step velocity of a growing spiral edge depends on the density of kink sites along the edge [42] so this difference in  $E_{PBC}$  partially explains the asymmetric shape of growth spirals on the  $(10\bar{1}4)$  surface of calcite. The step velocity also depends on the kinetics of incorporation into kink sites which is governed by the energetics of the kink site growth units, as discussed in Chapter 3.

## 2.4 Kink Site Energies

The kinetics of crystal growth are governed by the energetics of the kink site position on the crystal surface [3, 43]. The rate of attachment/detachment of growth units from the kink sites depends on the work done to attach/detach a growth unit from the kink site [4]. The work done in addition/removal of a growth unit to/from a kink site depends on the potential energy of the growth unit in the kink site, which is determined by the local structure of the crystalline solid as well as the growth medium. For organic crystals, the potential energies of growth units in the kink site positions on the crystal surface can be calculated by the addition of the nearest neighbor PBC interaction energies [42]. However, this method will not work for inorganic crystals since the electrostatic interactions contribute almost entirely to the lattice energy and there are strong interactions from non-nearest neighboring ions with like charge, which by definition cannot form PBCs.

Therefore, such repulsive interactions are not accounted for when considering the PBC interaction energies and summing up only the PBC interaction energies will overestimate the magnitude of the potential energy of a kink site growth unit.

The potential energy of a growth unit in the kink site must be calculated by summing up all the atom-atom interactions over the entire three dimensional crystal. However, using a brute-force summation of the coulombic interactions will be computationally prohibitive and will be repeated for every kink site along each edge on each crystal face. The Ewald summation method [6, 44] has been applied to systems with uniform geometries and charges [45, 46], but it cannot be applied here since the partial charges on the atoms in the surface layer and along the step edge are different from the partial charges on atoms in the bulk. Therefore, the concept of space partitioning is used to calculate the kink site potential energies for inorganic crystals. The basic concept behind this method has been used successfully in the literature to calculate the surface Madelung constants for some inorganic crystals [47, 48].

### **2.4.1 Space Partitioning**

Three dimensional space can be partitioned into three types of components - axes, quadrants and octants, which are one, two and three dimensional objects, respectively. Figure 2.12 shows the partitioning of the orthogonal coordinate system into these three types of objects. The 26 partitions in the 3D orthogonal coordinate system and their mathematical notations have been listed in Table 2.7.

**Table 2.7:** List of octants, quadrants and axes in the 3D orthogonal coordinate system with their mathematical notations

Type	Mathematical Notation	
Octant	$X < 0, Y < 0, Z < 0$	$X < 0, Y < 0, Z > 0$
	$X < 0, Y > 0, Z < 0$	$X < 0, Y > 0, Z > 0$
	$X > 0, Y < 0, Z < 0$	$X > 0, Y < 0, Z > 0$
	$X > 0, Y > 0, Z < 0$	$X > 0, Y > 0, Z > 0$
Quadrant	$X < 0, Y < 0, Z = 0$	$X < 0, Y > 0, Z = 0$
	$X > 0, Y < 0, Z = 0$	$X > 0, Y > 0, Z = 0$
	$X = 0, Y < 0, Z < 0$	$X = 0, Y < 0, Z > 0$
	$X = 0, Y > 0, Z < 0$	$X = 0, Y > 0, Z > 0$
	$X < 0, Y = 0, Z < 0$	$X < 0, Y = 0, Z > 0$
	$X > 0, Y = 0, Z < 0$	$X > 0, Y = 0, Z > 0$
Axis	$X < 0, Y = 0, Z = 0$	$X > 0, Y = 0, Z = 0$
	$X = 0, Y < 0, Z = 0$	$X = 0, Y > 0, Z = 0$
	$X = 0, Y = 0, Z < 0$	$X = 0, Y = 0, Z > 0$

For a Kossel crystal with a growth unit at the center of the crystal and at the origin of the orthogonal coordinate system, the neighboring growth units in the solid state can be grouped into each of the 26 partitions of the 3D space. The potential energy of the central growth unit can be divided into the additive contributions from growth units in each of those 26 partitions. This method assumes that the potential energy can be written as the sum of pairwise interaction energies alone and that the contribution of the three-body interactions is negligible.

Let us consider a kink site on the [100] edge of the (001) Kossel crystal surface (Figure 2.13). The growth unit in the kink site is at the origin of the coordinate system. By definition, the growth unit is in the half-crystal position [3] and is thus surrounded by exactly half of its solid-state neighbors in the bulk, i.e., 13 partitions. The other 13 par-

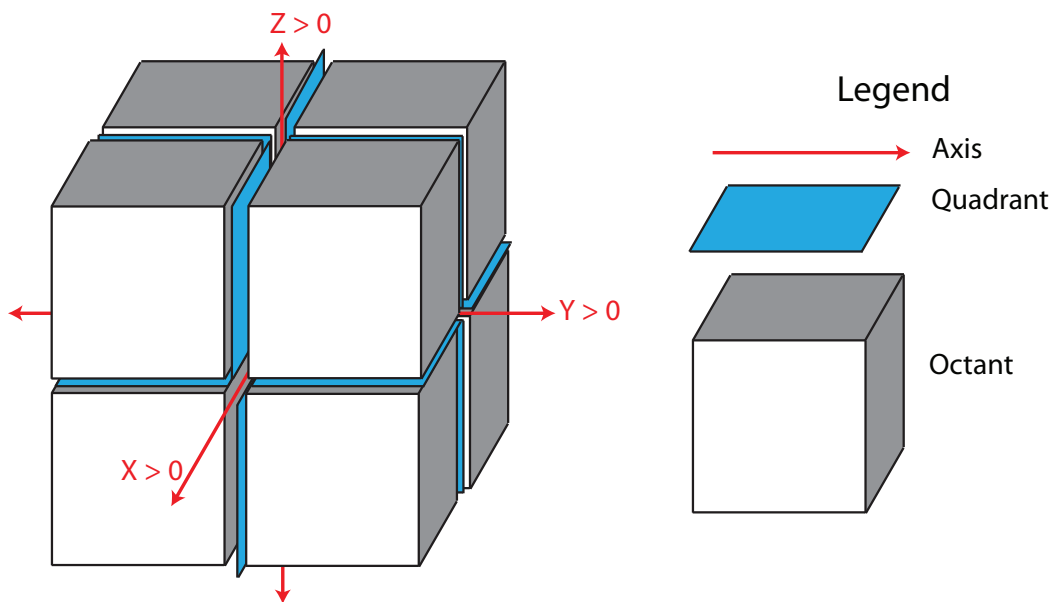


**Figure 2.12:** Partition of 3D orthogonal space into octants (white and grey cubes), quadrants (blue squares) and axes (red lines).

titions of space form the growth medium and the interactions between the solvent species present in those partitions with the central growth unit will be calculated separately.

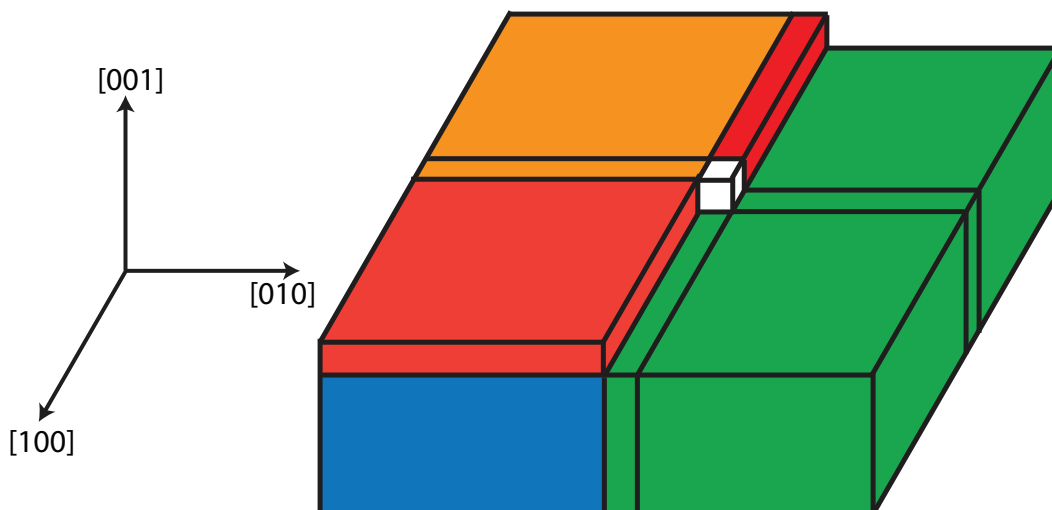


**Figure 2.13:** Classification of the 13 crystalline partitions around a kink site (white cube) on the  $[100]$  edge of the  $(001)$  Kossel crystal surface. The partitions are colored corresponding to their classification listed in Table 2.8.

**Table 2.8:** Classification of the 13 crystalline partitions of space around a kink site along the [100] edge on the (001) surface of a Kossel crystal

Partition Type	Notation			Classification
	X	Y	Z	
Octant	< 0	< 0	< 0	<b>Bulk Solid</b>
Octant	> 0	< 0	< 0	
Quadrant	= 0	< 0	< 0	
Quadrant	< 0	= 0	< 0	
Axis	= 0	= 0	< 0	
Octant	> 0	> 0	< 0	<b>Bulk + Surface</b>
Octant	< 0	> 0	< 0	
Quadrant	= 0	> 0	< 0	
Quadrant	> 0	= 0	< 0	
Quadrant	< 0	< 0	= 0	<b>Surface</b>
Axis	= 0	< 0	= 0	
Quadrant	> 0	< 0	= 0	<b>Surface+Edge</b>
Axis	< 0	= 0	= 0	<b>Edge</b>

Table 2.8 lists the 13 partitions that form the solid-state neighbors of the growth unit in the kink site shown in Figure 2.13. Each of the growth units belonging to these 13 partitions contributes additively to the potential energy of the growth unit in the kink site. To calculate the energy contributions of each partition of space, it is necessary to classify each of the 13 partitions based on the effect of its location within the crystal on the partial charges of the atoms within the partition. The crystal surface or the terrace is assumed to be only a single atomic layer in thickness so that every layer below it is considered as bulk crystal. An octant can be either a part of the bulk crystal, or a part of the terrace and bulk crystal such that the top layer of the octant is part of the terrace and the rest behaves as bulk crystal. Similarly, a quadrant can be a part of bulk

solid, bulk + terrace, only terrace, or terrace + step edge, depending on its location in the crystal. Finally, an axis could be part of the bulk solid, terrace or edge. This classification makes it easier to quantify the electronic structure of atoms belonging to each part of the crystal. The partial charges of all the atoms in all possible crystal positions (bulk, terrace, step edge, kink, etc.) are calculated using the bond valence method. Table 2.8 lists the classification of the 13 solid-state partitions surrounding the kink site on the (001) Kossel crystal surface.

Once the atoms in each of the 13 solid-state partitions of space are grouped, the crystal packing in each of these partitions is generated and each atom within a partition is assigned the appropriate partial charge. The positions of the atoms in the surface layer and at edge positions are obtained from the amount of surface relaxation in presence of solvent that is obtained from either *in situ* diffraction experiments [49] or molecular simulations [38]. The interaction energies of all the atoms in the crystal with the atoms of the central growth unit can thus be calculated one partition at a time. The interaction energies from each partition of space, when they are part of the bulk crystal, can be calculated only once and stored to speed up calculations. These energy values can then be reused for any kink site depending on which partitions of space form part of the bulk crystal for that particular kink site. For crystallographic unit cells with a high degree of symmetry, many of these partitions of space will be symmetrically equivalent and will contribute equally to the kink site potential energy. This symmetry equivalence should be exploited to further save computational efforts.

This analysis works well with minor modifications for a non-orthogonal crystal structure. The lattice spacing or the interaction energies along the three cardinal directions need not be symmetric. This method can be applied to any crystal structure once the three strongest PBC directions are identified. Placing the three cardinal directions ( $X, Y, Z$  in the Kossel crystal example) along the three strongest PBC directions of the crystal will simplify the kink site energy calculations as the step edges of growth spirals will be aligned with these cardinal directions. The classification of the 13 partitions of space that form the crystal will thus be straightforward.

If there are some intermolecular interactions shared between two PBCs that are present in two different F-faces, the choice of the cardinal directions may not be unique for the entire crystal. For example, if the PBCs in  $X$  and  $Z$  directions share a common bond, then the space partitioning for the face containing  $X$  and  $Y$  PBCs cannot be carried out with  $Z$  as the third cardinal direction. In such cases, the three cardinal directions are chosen separately for each F-face to ensure that a PBC with shared interactions is not a part of the space partitioning analysis. Some of the PBCs in aragonite crystals share some intermolecular interactions and Chapter 4 addresses the challenge of space partitioning for such a crystal in detail.

The interactions between the species of the growth medium and the kink site growth unit cannot be calculated using this space partitioning method. Since the growth medium or solvent does not have a periodic structure, it is impossible to calculate the long-range electrostatic interaction energies between kink site growth unit and the solvent molecules

without performing a molecular dynamics simulation to determine the solvent structure around the kink site. If the solvent molecules near the crystal surface are assumed to screen the kink site growth unit, the interaction energy with solvent molecules can be calculated once their distribution near the kink site is known [38].

### 2.4.2 Kink Site Energies on $(10\bar{1}4)$ Surface of Calcite

The three PBC directions in the  $[\bar{4}41]$  family with the strongest PBC interaction energy in bulk calcite (Table 2.1) were chosen as the three cardinal directions to apply the space partitioning method to calculate kink site energies on calcite crystal surfaces. Table 2.9 shows the kink site potential energies,  $U_{kink}$ , for all the kink sites on the spiral edges of the  $(10\bar{1}4)$  face of calcite. There are two edge directions  $[\bar{4}41]$  and  $[48\bar{1}]$  on the  $(10\bar{1}4)$  surface and each edge has an obtuse and acute orientation. There are four types of growth units on each of these edges (2 Ca and 2  $\text{CO}_3$ ). There are two orientations of a kink site on any spiral edge (obtuse or acute). Figure 2.14 shows these two orientations ( $\mathcal{E}$  and  $\mathcal{W}$ ) of a Ca kink site along the  $[48\bar{1}]$  obtuse edge. When the edge grows in the North direction, a kink site in the  $\mathcal{E}$  orientation faces the East direction while the kink site in the  $\mathcal{W}$  orientation faces the West direction. Therefore, there are a total of 32 types of kink sites on the  $(10\bar{1}4)$  surface of calcite.

The symmetry equivalence between the kink sites on the  $[\bar{4}41]$  and  $[48\bar{1}]$  edges is apparent from the kink site potential energies reported in Table 2.9. The potential energy of the Ca (1) kink site ( $\mathcal{E}$  orientation) on the  $[\bar{4}41]$  obtuse edge is exactly equal

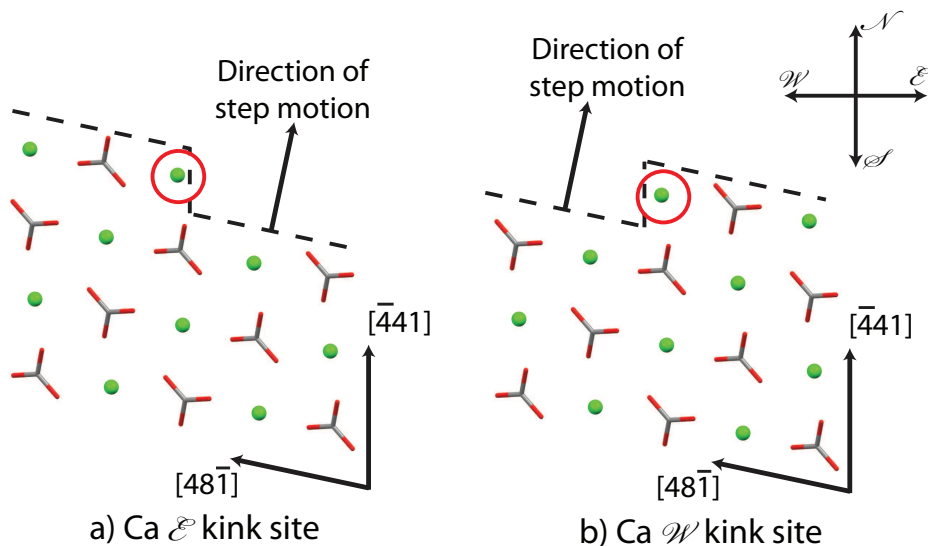


**Figure 2.14:** A plan view of the  $(10\bar{1}4)$  surface of calcite showing the two orientations a)  $\mathcal{E}$  and b)  $\mathcal{W}$  of Ca kink sites on the  $[48\bar{1}]$  obtuse edge. The kink site Ca atoms are enclosed within the red circles.

to that of the Ca (3) kink site ( $\mathcal{W}$  orientation) on the  $[48\bar{1}]$  obtuse edge and so on. The kink site potential energies  $U_{kink}$  calculated for the obtuse and acute edges of the growth spirals on calcite  $(10\bar{1}4)$  surface are not equal to each other as shown in Table 2.9. Since the attachment/detachment rate from the kink sites and the step velocity depends on the kink site potential energy [42, 50], the  $U_{kink}$  values suggest that the step velocities of obtuse and acute edges should be different. Therefore, the difference in the solid-state interaction energies in the kink sites between acute and obtuse spiral edges provides a quantitative explanation for the presence of asymmetric growth spirals on the  $(10\bar{1}4)$  surface of calcite.

**Table 2.9:** Kink site potential energy ( $U_{kink}$ ) in kcal/mol for the 32 kink sites on the (10 $\bar{1}$ 4) surface of calcite

Edge Type	Ca (1)	CO <sub>3</sub> (2)	Ca (3)	CO <sub>3</sub> (4)
[ $\bar{4}$ 41] Obtuse $\mathcal{E}$ kinks	-316.8	-332.2	-318.0	-333.7
[ $\bar{4}$ 41] Obtuse $\mathcal{W}$ kinks	-311.3	-344.5	-312.6	-345.9
[441] Acute $\mathcal{E}$ kinks	-307.7	-345.8	-312.6	-344.6
[441] Acute $\mathcal{W}$ kinks	-305.6	-346.5	-314.7	-345.2
[48 $\bar{1}$ ] Obtuse $\mathcal{E}$ kinks	-312.6	-345.9	-311.3	-344.5
[48 $\bar{1}$ ] Obtuse $\mathcal{W}$ kinks	-318.0	-333.7	-316.8	-332.2
[48 $\bar{1}$ ] Acute $\mathcal{E}$ kinks	-314.7	-345.2	-305.6	-346.5
[48 $\bar{1}$ ] Acute $\mathcal{W}$ kinks	-312.6	-344.6	-307.7	-345.8

## 2.5 Discussion

There is a significant body of literature to identify the PBCs in inorganic solids. Hartman wrote several papers that identify PBCs in inorganic crystals such as - barite [11, 51], sphalerite [52], cadmium iodide [53], tin iodide [54], rutile [55], cotunnite [56], corundum [57], yttrium barium copper oxide (YBCO) [58], gypsum [59], etc. A graph theoretic method was developed by Strom [60, 61] to identify the PBCs in ionic solids based on the Hartman-Perdok rules. Another systematic method has been developed here that can help identify the periodic bond chain structures within any inorganic solid, and can be applied within the framework of a mechanistic crystal growth model.

The original definition of the building unit of a PBC was based on a stoichiometric arrangement of neighboring growth units [16, 62]. For example, in an AB type crystal, each A-B neighboring pair in the solid state was identified as the building unit for the PBC direction parallel to the lattice vector joining the A-B pair. Thus, the structure of a building unit was uniquely defined for every PBC direction and the identification

of one building unit did not provide any information about either the structure of the other building units, or the directions of other PBC vectors. An additional condition is imposed on the structure of the building unit, that its dipole moment must be zero. This condition results in a building unit structure that is identical for all the PBCs, and therefore for the entire crystal. Thus, the identification of the PBC vectors in an inorganic solid is reduced to the identification of a single building unit and then applying the symmetry operators in the unit cell to obtain the crystal packing with building units. The arrangement of building units along a PBC direction may not be equal to the actual structure of the step edge. Therefore, the arrangement of building units along each PBC vector must be decomposed into an arrangement of growth units that follows Hartman-Perdok rules. The identification of PBCs in inorganic solids can now be carried out in a systematic step-by-step methodology, which is discussed in Appendix A.

A more important aspect of our model is the practical implementation of quantum mechanical concepts that govern the electronic properties of the growth units situated on crystal surfaces. The importance of partial charges of surface atoms on thermodynamics and kinetics of crystal growth has been known for some time. Polar morphologies of sodium chlorate [63] and sodium periodate [64] have been explained, using the attachment energy model, on the basis of different partial charges (calculated using quantum mechanics) on the opposite crystal faces. Knowledge of the partial charges in bulk solid combined with the bond valence model allows the calculation of partial charges in surface positions with different solid-state coordination. The effect of the solvent molecules next

to the crystal surface on the partial charges of surface atoms is also captured within the bond valence framework. A space partitioning method allows easy calculation of kink site potential energies while accounting for the different values of surface charges and all the long-range interactions. This model provides a useful engineering solution to the problem of identification of PBC directions on inorganic crystal surfaces and the calculation of interaction energies on the surface that govern the kinetics of layered growth on these crystal surfaces.

## **2.6 Conclusions**

In this chapter, a generalized model capable of capturing the solid-state interactions in inorganic crystals from a crystal growth perspective has been discussed. This approach is based on identifying the directions of strongest intermolecular interactions within the crystal while accounting for long-range electrostatic interactions and stoichiometry. The model can help predict the shape of growth spirals formed on inorganic crystal surfaces such as the calcite ( $10\bar{1}4$ ) surface.

The growth kinetics of inorganic crystals depends on the coulombic interactions of the growth units in the kink site positions on crystal surfaces. The change in the electronic structure of surface atoms from those in the bulk has been captured using the bond valence model and a systematic method is presented to calculate the partial charges of atoms located in different lattice positions on inorganic crystal surfaces. The concept of space partitioning was used to partition a growing crystal into parts that belong to

the bulk crystal or terrace or step edge. This classification simplifies the calculation of the potential energies of growth units in the kink site positions on an inorganic crystal surface. The potential energy calculations for kink sites on the  $(10\bar{1}4)$  calcite surface explains the asymmetric growth of the obtuse and acute edges. This framework lays the foundation for a mechanistic crystal growth model that is capable of predicting the shapes of solution grown inorganic crystals such as calcite, titanium dioxide, barite, etc, which will be discussed in the next chapter.

# Bibliography

- [1] F. C. Frank. *Growth and Perfection of Crystals*, chapter On the Kinematic Theory of Crystal Growth and Dissolution Processes, pages 411–419. New York: Wiley, 1958.
- [2] A. A. Chernov. The kinetics of the growth forms of crystals. *Sov. Phys. Cryst.*, 7:728–730, 1963.
- [3] I. N. Stranski. Zur theorie des kristallwachstums. *Z. Phys. Chem.*, 136:259–278, 1928.
- [4] I. V. Markov. *Crystal Growth for Beginners, Fundamentals of Nucleation, Crystal Growth and Epitaxy*. World Scientific: Singapore, 2003.
- [5] E. Madelung. Das elektrische feld in systemen von regelmässig angeordneten punktladungen. *Phys. Zs.*, 19:524–533, 1918.
- [6] P. P. Ewald. Die berechnung optischer und elektrostatischer gitterpotentiale. *Ann. Phys.*, 64:253, 1921.
- [7] I. D. Brown and R. D. Shannon. Empirical bond-strength-bond-length curves for oxides. *Acta Crystallogr. A*, 29:266–282, 1973.
- [8] I. D. Brown. *The Chemical Bond in Inorganic Chemistry: The Bond Valence Model*. Oxford University Press, 2002.
- [9] P. Hartman and W. G. Perdok. On the relations between structure and morphology of crystals. I. *Acta Crystallogr.*, 8:49–52, 1955.
- [10] L. Pauling. The principles determining the structure of complex ionic crystals. *J. Am. Chem. Soc.*, 51:1010–1026, 1929.
- [11] P. Hartman and W. G. Perdok. On the relations between structure and morphology of crystals. II. *Acta Crystallogr.*, 8:521–524, 1955.
- [12] P. W. Tasker. The stability of ionic crystal surfaces. *J. Phys. C Solid State*, 12:4977, 1979.

- [13] C. Noguera. Polar oxide surfaces. *J. Phys.: Condens. Matter*, 12:R367, 2000.
- [14] U. Diebold, S.-C. Li, and M. Schmid. Oxide surface science. *Annu. Rev. Phys. Chem.*, 61:129–148, 2010.
- [15] W. M. M. Heijnen. The morphology of gel grown calcite. *N. Jb. Miner. Mh.*, 8:357–371, 1985.
- [16] D. Aquilano, M. Calleri, E. Natoli, M. Rubbo, and G. Sgualdino. The {104} cleavage rhombohedron of calcite: theoretical equilibrium properties. *Mater. Chem. Phys.*, 66:159 – 163, 2000.
- [17] M. Miyaka, I. Minato, H. Morikawa, and S. Iwai. Crystal structures and sulphate force constants of barite, celestite and anglesite. *Am. Mineral.*, 63:506–510, 1978.
- [18] W. K. Burton, N. Cabrera, and F. C. Frank. The growth of crystals and the equilibrium structure of their surfaces. *Phil. Trans. Roy. Soc. A*, 243:299–358, 1951.
- [19] C. Kittel. *Introduction to Solid State Physics*. John Wiley & Sons, Inc.: Hoboken, NJ, 2005.
- [20] C. R. A. Catlow, M. Dixon, and W. C. Mackrodt. *Computer Simulation of Solids*, chapter Interionic Potentials in Ionic Solids, pages 130–161. Springer-Verlag: Berlin, 1982.
- [21] J. D. Gale and A. L. Rohl. The general utility lattice program (GULP). *Mol. Simul.*, 29:291–341, 2003.
- [22] J. W. Morse, R. S. Arvidson, and A. Lüttge. Calcium carbonate formation and dissolution. *Chem. Rev.*, 107:342–381, 2007.
- [23] Large crystal of Icelandic Spar (Calcite) on display at the National Museum of Natural History Washington, DC, 2005.
- [24] S. Markgraf and R. Reeder. High-temperature structure refinements of calcite and magnesite. *Am. Mineral.*, 70:590–600, 1985.
- [25] P. Raiteri, J. D. Gale, D. Quigley, and P. M. Rodger. Derivation of an accurate force-field for simulating the growth of calcium carbonate from aqueous solution: A new model for the calcite-water interface. *J. Phys. Chem. C*, 114:5997–6010, 2010.
- [26] P. Raiteri and J. D. Gale. Water is the key to nonclassical nucleation of amorphous calcium carbonate. *J. Am. Chem. Soc.*, 132:17623–17634, 2010.
- [27] H. D. B. Jenkins, K. F. Pratt, and B. T. Smith. Lattice potential energies for calcite, aragonite and vaterite. *J. Inorg. Nucl. Chem.*, 38:371–377, 1976.

- [28] D. Winn and M. F. Doherty. Modeling crystal shapes of organic materials grown from solution. *AIChE J.*, 46:1348–1367, 2000.
- [29] K. J. Davis, P. M. Dove, L. E. Wasylenki, and J. J. De Yoreo. Morphological consequences of differential  $\text{Mg}^{2+}$  incorporation at structurally distinct steps on calcite. *Am. Mineral.*, 89:714–720, 2004.
- [30] H. H. Teng, P. M. Dove, C. A. Orme, and J. J. De Yoreo. Thermodynamics of calcite growth: Baseline for understanding biomineral formation. *Science*, 282:724–727, 1998.
- [31] J. Paquette and R. J. Reeder. Relationship between surface structure, growth mechanism, and trace element incorporation in calcite. *Geochim. Cosmochim. Acta*, 59:735–749, 1995.
- [32] G. Donnay and R. Allmann. How to recognize  $\text{O}^{2-}$ ,  $\text{OH}^-$ , and  $\text{H}_2\text{O}$  in crystal structures determined by X-rays. *Am. Mineral.*, 55:1003–1015, 1970.
- [33] C. Preiser, J. Lösel, I. D. Brown, M. Kunz, and A. Skowron. Long-range coulomb forces and localized bonds. *Acta Crystallogr. B*, 55:698–711, 1999.
- [34] R. S. Mulliken. Electronic Population Analysis on LCAO[Single Bond]MO Molecular Wave Functions. I. *J. Chem. Phys.*, 23:1833–1840, 1955.
- [35] W. Tang, E. Sanville, and G. Henkelman. A grid-based bader analysis algorithm without lattice bias. *J. Phys.: Condens. Matter*, 21:084204, 2009.
- [36] P. Fenter and N. Sturchio. Calcite (104)-water interface structure, revisited. *Geochim. Cosmochim. Acta*, 97:58–69, 2012.
- [37] P. Fenter, S. Kerisit, P. Raiteri, and J. D. Gale. Is the calcite-water interface understood? Direct comparisons of molecular dynamics simulations with specular x-ray reflectivity data. *J. Phys. Chem. C*, 117:5028–5042, 2013.
- [38] M. Wolthers, D. Di Tommaso, Z. Du, and N. H. de Leeuw. Calcite surface structure and reactivity: Molecular dynamics simulations and macroscopic surface modelling of the calcite-water interface. *Phys. Chem. Chem. Phys.*, 14:15145–15157, 2012.
- [39] A. G. Stack, P. Raiteri, and J. D. Gale. Accurate rates of the complex mechanisms for growth and dissolution of minerals using a combination of rare-event theories. *J. Am. Chem. Soc.*, 134:11–14, 2012.
- [40] M. Raju, S.-Y. Kim, A. C. T. van Duin, and K. A. Fichthorn. ReaxFF Reactive Force Field Study of the Dissociation of Water on Titania Surfaces. *J. Phys. Chem. C*, 117:10558–10572, 2013.

- [41] W. L. Jorgensen, J. Chandrasekhar, J. D. Madura, R. W. Impey, and M. L. Klein. Comparison of simple potential functions for simulating liquid water. *J. Chem. Phys.*, 79:926–935, 1983.
- [42] Z. B. Kuvadia and M. F. Doherty. Spiral growth model for faceted crystals of non-centrosymmetric organic molecules grown from solution. *Cryst. Growth Des.*, 11:2780–2802, 2011.
- [43] W. Kossel. Zur theorie des kristallwachstums. *Nachur. Ges. Wiss. Göttingen*, 206:135–143, 1927.
- [44] T. Darden, D. York, and L. Pedersen. Particle mesh ewald: An  $n \log(n)$  method for ewald sums in large systems. *J. Chem. Phys.*, 98:10089–10092, 1993.
- [45] D. Parry. The electrostatic potential in the surface region of an ionic crystal. *Surf. Sci.*, 49:433 – 440, 1975.
- [46] I.-C. Yeh and M. L. Berkowitz. Ewald summation for systems with slab geometry. *J. Chem. Phys.*, 111:3155–3162, 1999.
- [47] J. D. Levine and P. Mark. Theory and observation of intrinsic surface states on ionic crystals. *Phys. Rev.*, 144:751–763, 1966.
- [48] E. Garrone, A. Zecchina, and F. S. Stone. An experimental and theoretical evaluation of surface states in MgO and other alkaline earth oxides. *Philos. Mag. B*, 42:683–703, 1980.
- [49] F. Heberling, T. P. Trainor, J. Lützenkirchen, P. Eng, M. A. Denecke, and D. Bosbach. Structure and reactivity of the calcite-water interface. *J. Colloid Interface Sci.*, 354:843 – 857, 2011.
- [50] S. H. Kim, P. Dandekar, M. A. Lovette, and M. F. Doherty. Kink rate model for the general case of organic molecular crystals. *Cryst. Growth Des.*, 14:2460–2467, 2014.
- [51] P. Hartman and C. Strom. Structural morphology of crystals with the barite ( $\text{BaSO}_4$ ) structure: A revision and extension. *J. Cryst. Growth*, 97:502 – 512, 1989.
- [52] P. Hartman. An approximate calculation of attachment energies for ionic crystals. *Acta Crystallogr.*, 9:569–572, 1956.
- [53] P. Hartman. The Madelung constants of slices and chains, with an application to the  $\text{CdI}_2$  structure. *Acta Crystallogr.*, 11:365–369, 1958.
- [54] P. Hartman. Theoretical morphology of crystals with the  $\text{SnI}_4$  structure. *J. Cryst. Growth*, 2:385 – 394, 1968.

- [55] P. Hartman. *Crystal Growth: An Introduction*, chapter Structure and Morphology, pages 367–402. Amsterdam: North-Holland, 1973.
- [56] C. Woensdregt and P. Hartman. Structural morphology of cotunnite,  $\text{PbCl}_2$ , laurionite,  $\text{Pb}(\text{OH})\text{Cl}$ , and  $\text{SbSI}$ . *J. Cryst. Growth*, 87:561 – 566, 1988.
- [57] P. Hartman. The effect of surface relaxation on crystal habit: Cases of corundum ( $\alpha\text{-Al}_2\text{O}_3$ ) and Hematite ( $\alpha\text{-Fe}_2\text{O}_3$ ). *J. Cryst. Growth*, 96(3):667 – 672, 1989.
- [58] B. Sun, P. Hartman, C. Woensdregt, and H. Schmid. Structural morphology of  $\text{YBa}_2\text{Cu}_3\text{O}_{7-x}$ . *J. Cryst. Growth*, 100:605 – 614, 1990.
- [59] W. Heijnen and P. Hartman. Structural morphology of gypsum ( $\text{CaSO}_4 \cdot 2\text{H}_2\text{O}$ ), brushite ( $\text{CaHPO}_4 \cdot 2\text{H}_2\text{O}$ ) and pharmacolite ( $\text{CaHAsO}_4 \cdot 2\text{H}_2\text{O}$ ). *J. Cryst. Growth*, 108:290 – 300, 1991.
- [60] C. S. Strom. Graph-theoretic construction of periodic bond chains I. General case. *Z. Kristallogr.*, 153:99–113, 1980.
- [61] C. S. Strom. Graph-theoretic construction of periodic bond chains II. Ionic case. *Z. Kristallogr.*, 154:31–43, 1981.
- [62] F. Abbona and D. Aquilano. *Springer Handbook of Crystal Growth*, chapter Morphology of Crystals Grown from Solutions, pages 53–92. Springer-Verlag: Berlin Heidelberg, 2010.
- [63] G. Clydesdale, K. J. Roberts, G. B. Telfer, V. R. Saunders, D. Pugh, R. A. Jackson, and P. Meenan. Prediction of the polar morphology of sodium chlorate using a surface-specific attachment energy model. *J. Phys. Chem. B*, 102:7044–7049, 1998.
- [64] L. J. Soltzberg and E. Madden. Crystal morphology prediction and morphology variation in  $\text{NaIO}_4$  and  $\text{NaIO}_4 \cdot 3\text{H}_2\text{O}$ . *Acta Crystallogr.*, B55:882–885, 1999.

# Chapter 3

## Spiral Growth of Inorganic Crystals

Reproduced in part with permission from: Dandekar, P.; Doherty, M.F. A Mechanistic Growth Model for Inorganic Crystals: Growth Mechanism. *AIChE Journal*, **2014**, (*in press*).

### 3.1 Introduction

In Chapter 2, a mechanistic framework was proposed to model the solid-state interactions in inorganic crystals from a crystal growth and shape evolution point of view. Modeling surface integration-limited crystal growth from solution requires understanding the solid-state interactions as well as the surface growth mechanisms that govern the growth process. The importance of the interactions between the crystal and the solvent in modeling inorganic crystal growth from solution is highlighted by the comparable magnitudes of the lattice energy and the hydration energy for most inorganic solids (both energies have magnitudes typically  $> 100$  kcal/mol). The lattice energy is dominated by the interionic long-range electrostatic interactions in the solid state, while the hydration

energy depends on the interactions between the solvated ions and the water molecules present in the solvation shell. For example, the lattice dissociation enthalpy for cubic NaCl crystal is 188.1 kcal/mol [1] while the combined hydration enthalpy for Na<sup>+</sup> and Cl<sup>-</sup> ions is -187.2 kcal/mol [2, 3]. As a result, the dissolution enthalpy for NaCl crystal in aqueous solution is only 0.9 kcal/mol. Thus, the interactions of the surface growth units with the solvent play a huge role in determining the kinetics of the individual processes involved in growth on inorganic crystal surfaces.

Crystal growth of inorganic crystals, such as calcium carbonate, barium sulfate, potassium dihydrogen phosphate (KDP), etc., from solution has been well studied experimentally. The surface growth mechanisms, such as spiral growth and 2D nucleation, have been experimentally observed using surface characterization techniques such as atomic force microscopy (AFM) [4–8]. Other characterization techniques such as scanning tunneling microscopy (STM), low-energy electron diffraction (LEED), X-ray reflectivity measurements, etc., also provide valuable information about the surface structure and help elucidate the growth mechanism active on the crystal surface [9]. Crystal growth models for inorganic solids that have been developed so far can be divided into two categories - (i) those that study the solid-state interactions on a molecular scale and use the attachment energy model to predict the crystal growth rate and steady-state morphology [10–13] and (ii) those that develop a mechanistic growth model but use experimentally fitted values for nearest-neighbor interactions [14, 15]. A mechanistic crystal growth model that accounts for the solid-state electrostatic interactions as well as the solvent-solute in-

teractions has not yet been developed for inorganic solids. Such a growth model will have predictive capability on a macroscopic scale to prescribe more efficient crystal growth experiments. The challenge here is to study both the solid-state interactions and the effect of the solvent on the growth kinetics in a generalized manner so that the conclusions from the model predictions can be applied to the crystal growth of a broad class of inorganic crystal surfaces. A distinction is being made here between growth on non-polar crystal surfaces and polar crystal surfaces. The stabilization and growth mechanisms on polar inorganic crystal surfaces is not yet fully understood and will not be discussed here (The reader is referred to review articles on polarity of oxide crystal surfaces by Diebold et al. [16] and Goniakowski et al. [17]). The subject of this study is the growth mechanism active on non-polar inorganic crystal surfaces that do not undergo significant surface reconstruction to stabilize themselves.

In this chapter, a generalized methodology is presented to study the spiral growth mechanism on inorganic crystal surfaces. The step velocities of spiral edges on an inorganic crystal surface can be calculated using the kink rate and kink density models discussed here. The density of kink sites along a spiral edge is calculated from the equilibrium distribution of disturbances due to thermal roughening [18, 19]. The rate of kink propagation on an ionic step edge is calculated using steady-state site balances with appropriate expressions for the kink attachment and detachment fluxes that account for solution composition and kink site interaction energies. This mechanistic growth model is applied to the crystal growth on the  $\{10\bar{1}4\}$  family of faces on calcite ( $\text{CaCO}_3$ ) crystals.

Calcite is the most stable and abundant polymorph of calcium carbonate and its crystal growth is well studied from a biomineralization perspective [20]. The surface growth mechanisms in the presence of impurities such as  $\text{Mg}^{2+}$ ,  $\text{Sr}^{2+}$ , biomolecules, etc. that are typically present in the marine ecosystem, are well studied experimentally [21–25]. This model does well in predicting the shape of the growth spirals formed on calcite crystal surfaces, but also the effect of the environmental composition on the step velocities of the spiral edges on the  $(10\bar{1}4)$  calcite surface. The model can be applied to study crystal growth, shape evolution and the steady-state shape achieved by typical inorganic salts grown from aqueous solution.

## 3.2 Growth Mechanism

Growth of crystal surfaces occurs under non-equilibrium conditions when the chemical potential of the growth medium ( $\mu_m$ ) is greater than the chemical potential of the bulk crystal ( $\mu_c$ ). The difference ( $\Delta\mu$ ) between these chemical potentials is the driving force for crystal growth.

$$\Delta\mu = \mu_m - \mu_c \quad (3.1)$$

When the rate of mass transfer between the bulk growth medium and the crystal surface is much faster than the rate of incorporation of the growth units into the crystal lattice, crystal surfaces grow by a layered growth mechanism. The crystal surface grows by the attachment of growth units along steps present on the surface. These steps may originate from either growth spirals or 2D nuclei present on the surface. At low super-

saturation, the activation energy for the formation of 2D nuclei is very high, therefore, the growth rate is dominated by the spiral growth mechanism [26, 27]. A crystal surface contains screw dislocations that act as the source of atomic steps where growth units are preferentially incorporated into the crystal. These steps spread across the surface due to the attachment of growth units and result in a self-perpetuating growth of layers on top of other layers that gives rise to growth hillocks with a spiral pattern [19, 28]. The perpendicular growth rate  $G_{hkl,s}$  of a crystal face with Miller index  $\{hkl\}$ , growing by the spiral growth mechanism, is related to the rotation time  $\tau_s$  of the growth spiral as follows [28]

$$G_{hkl,s} = \left( \frac{h}{\tau_s} \right)_{hkl} \quad (3.2)$$

$$\tau_s = \sum_{i=1}^N \frac{l_{i+1,c} \sin(\alpha_{i,i+1})}{v_i} \quad (3.3)$$

where  $h$  is the height of the spiral edge,  $N$  is the number of edges in the growth spiral,  $l_{i,c}$  is the critical length of spiral edge  $i$ ,  $\alpha_{i,i+1}$  is the angle between edges  $i$  and  $i+1$  and  $v_i$  is the step velocity of edge  $i$ . The critical length  $l_{i,c}$  of edge  $i$  is the minimum length below which the edge does not grow [28]. Since a spiral edge moves by the incorporation of growth units into the kink sites present along the edge, the growth kinetics of the crystal surface depends on the rate of attachment of growth units into kink sites.

The step velocity of each spiral edge on every surface of the crystal must be calculated to predict the growth rates and therefore the steady-state crystal morphology. The step

velocity  $\mathbf{v}_i$  of a spiral edge  $i$  is written as follows [14, 29]

$$\mathbf{v}_i = a_{p,i} \rho_i u_i \quad (3.4)$$

where  $a_{p,i}$  is the perpendicular distance between two rows of the spiral edge  $i$  (units of Å or nm),  $\rho_i$  is the density of kink sites along the edge  $i$  (dimensionless) and  $u_i$  is the net rate of attachment of growth units into the kink sites (units of  $\text{s}^{-1}$ ).  $a_p$  depends on the crystallography and step structure while the kink density is given by the thermodynamics of creating kink sites from a straight step edge [19]. Kink rate  $u$  captures the kinetics of the crystal growth process and combines the rates of the competing processes of attachment and detachment of growth units into and from the kink sites, respectively. The density of kink sites along an edge and the net rate of incorporation into the kink sites depend on the interaction energies of growth units along the edge. Therefore, the first step in crystal growth modeling is the identification of the Periodic Bond Chain (PBC) directions that are parallel to the strongest intermolecular interactions between the growth units in the solid-state. A systematic method to identify the PBC directions in inorganic crystals has been presented in Chapter 2. The interaction energies of growth units present along the spiral edges are calculated while including the surface effect on the partial charges of growth units and the long-range electrostatic interactions. A general method that uses those interaction energies to calculate the kink density and the kink rate for inorganic crystal growth is presented in the following sections.

### 3.3 Kink Density Calculation

The edges on a crystal surface undergo constant thermal fluctuation and are never completely straight at any temperature  $T > 0$  K [19]. These thermal fluctuations provide a finite density of kink sites along the edge where growth units attach. The density of these kink sites or the spacing between two successive kink sites along the edge partially determines the net rate at which the step edge moves due to attachment of growth units (see equation 3.4).

Using the statistical mechanics of fluctuations, Frenkel [18] and Burton et al. [19] developed a method to calculate the density of kink sites along an edge. The probability of finding a kink site along the edge depends on the energy required to rearrange two adjacent growth units from a straight edge to form an edge with four kink sites [19]. If the energy required per kink site for this rearrangement, called the kink energy, is of the order of thermal energy ( $k_B T$ ), the rearrangement occurs on a time scale faster than the attachment/detachment of growth units into the kink sites [30]. Therefore, the edge structure is always in quasi-equilibrium with respect to the growth medium and the kink sites are Boltzmann distributed.

Kuvadia and Doherty proposed a systematic method to calculate the kink density on step edges with multiple types of kink sites on organic crystal surfaces [29]. The probability of observing any type of kink site can be computed by counting all the microstates of edge rearrangements that expose that particular kink type and by calculating the energy for each rearrangement.

The probability of observing any particular rearrangement depends on the change in the potential energy of the system upon the rearrangement of the edge. Therefore, the calculation of kink density on the step edges on an inorganic crystal surface involves computing the change in potential energy of the entire system due to a rearrangement of a straight edge. The system consists of a step edge on a crystal surface as well as the solvent molecules in the immediate vicinity of the step edge. The rearrangement of two adjacent growth units along a straight edge to a step adatom position (Figure 3.1) involves the breaking of solid-solid ‘bonds’ as well as formation of new solid-solvent ‘bonds’. The new solid-solvent interactions are formed because the solvent structure around an edge growth unit is different from that around a growth unit in a kink site [31]. The change in the potential energy of the entire system due to this rearrangement must reflect the changes in both solid-solid and solid-solvent interactions.

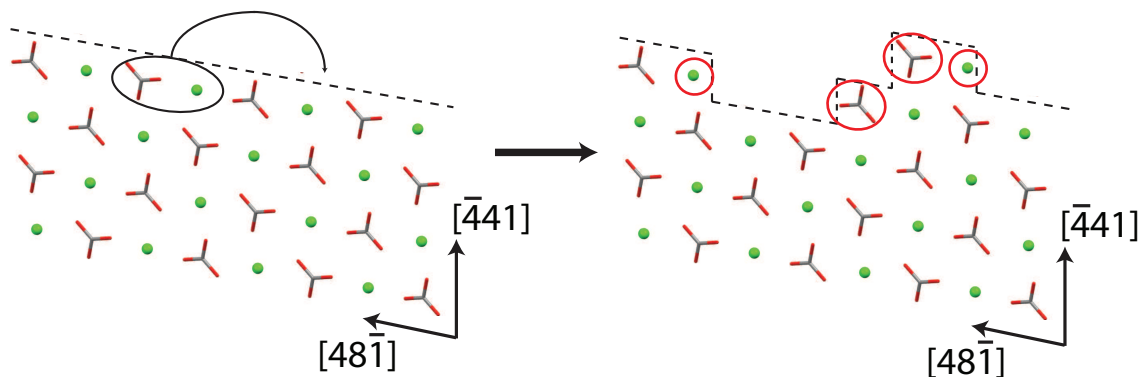


**Figure 3.1:** A representative rearrangement of a Ca and a CO<sub>3</sub> growth unit (within the black circle) from a straight [48 $\bar{1}$ ] edge on (10 $\bar{1}$ 4) surface of calcite to form four kink sites (red circles). The water molecules surrounding the edge and kink sites have not been shown.

At higher supersaturation values ( $S > 1.2$ ), the step rearrangement will compete with kink incorporation attachment such that the step edge structure will no longer be in quasi-equilibrium with the growth medium (see Appendix C). The density of kink sites will then depend on the thermodynamics of edge rearrangement as well as the kinetics of kink incorporation.

The kink densities on the spiral edges of the  $(10\bar{1}4)$  surface of calcite were calculated using this method. As discussed previously, there are two spiral edges -  $[\bar{4}41]$  and  $[48\bar{1}]$  on the  $(10\bar{1}4)$  surface of calcite. Each of these two edges has obtuse and acute orientations depending on the angle that the step edge makes with the plane of the crystal surface. It has been shown in Chapter 2 that either of the orientations on both  $[\bar{4}41]$  and  $[48\bar{1}]$  edges are symmetrically equivalent so only the  $[48\bar{1}]$  edge is discussed henceforth (Figure 3.1).

The  $[48\bar{1}]$  edge has four growth units that repeat along the edge - two calcium and two carbonate ions. The two carbonate growth units differ in their orientations, therefore, the two calcium growth units situated between them have different interaction energies. When considering the rearrangement of a straight  $[48\bar{1}]$  edge, there are four choices to select a pair of adjacent growth units along the edge to be moved. Similarly, there are four choices for the final positions of the earlier selected pair of growth units as step adatoms. Therefore, there are 16 possible rearrangements on each obtuse and acute orientation of the  $[48\bar{1}]$  edge. Also, each of the kink sites on the edge can have two possible orientations -  $\mathcal{E}$  and  $\mathcal{W}$ . The  $\mathcal{E}$  and  $\mathcal{W}$  orientations of the kink sites correspond

**Table 3.1:** Density of kink sites ( $\rho$ ) on the  $[48\bar{1}]$  spiral edges of  $(10\bar{1}4)$  face of calcite

Edge Type	Ca (1)	CO <sub>3</sub> (2)	Ca (3)	CO <sub>3</sub> (4)	Total
$[48\bar{1}]$ Obtuse $\mathcal{E}$ kinks	0.0021	0.0065	0.0021	0.0136	0.0243
$[48\bar{1}]$ Obtuse $\mathcal{W}$ kinks	0.0136	0.0021	0.0065	0.0021	0.0243
$[48\bar{1}]$ Acute $\mathcal{E}$ kinks	0.0139	0.0050	0.0040	0.0092	0.0321
$[48\bar{1}]$ Acute $\mathcal{W}$ kinks	0.0092	0.0139	0.0050	0.0040	0.0321

to the kink site growth unit facing east and west, respectively, when the edge grows in the north direction (Figure 3.2). Therefore, there are a total of 8 kink sites on the  $[48\bar{1}]$  edge on  $(10\bar{1}4)$  surface of calcite.

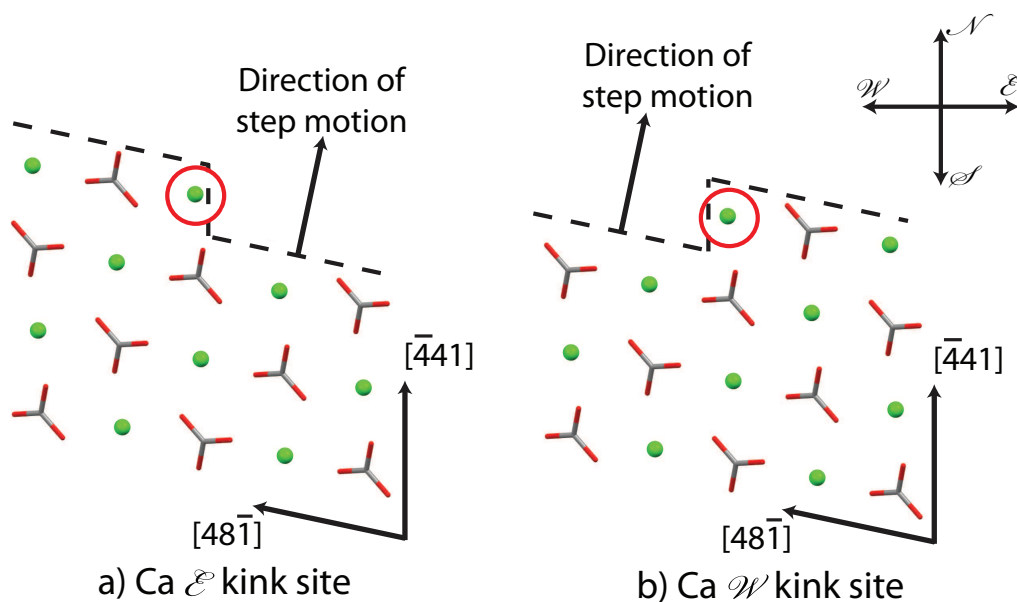

**Figure 3.2:** The two orientations ( $\mathcal{E}$  and  $\mathcal{W}$ ) of kink sites on the  $[48\bar{1}]$  edge on  $(10\bar{1}4)$  surface of calcite.

Table 3.1 shows the kink densities of all the kink sites on both  $[48\bar{1}]$  acute and  $[48\bar{1}]$  obtuse edges. The total density of kink sites is higher on the acute edge than the obtuse edge. Since the step velocity is directly proportional to the kink density along the edge,

the difference in kink densities between the obtuse and acute spiral edges on the  $(10\bar{1}4)$  surface of calcite does explain the asymmetry in the shape of the growth spirals found on the crystal surface. However, the net rate of attachment into the kink sites must also be calculated before predicting the step velocities and the exact shape of the growth spirals.

### **3.4 Kink Rate for Inorganic Crystals**

The net rate of attachment or detachment of growth units from kink sites along a step edge on a crystal surface is called the rate of kink incorporation or the kink rate [32]. Kink rate models have been developed for both organic molecular crystals [29] and ionic crystals [14]. However, these models were limited in their scope of the solid-state interactions and considered only nearest-neighbor interactions. The kinetics of attachment/detachment of ionic growth units will depend on the potential energies of the ions in the kink sites. In Chapter 2, a systematic method has been presented to calculate the kink site potential energies of ions accounting for both long-rang solid-state interactions as well as the solid-solvent interactions.

The kink rate model developed by Zhang and Nancollas [14] is applicable for two types of kink sites along a step edge on the surface of an AB-type ionic crystal. Frequently, the step edges on inorganic crystal surfaces may have different orientations or positions for both cations and anions that result in more than two types of kink sites along a step edge. Therefore, a general kink rate model for inorganic crystals is required that allows for multiple types of kink sites present along the edge.

### 3.4.1 New Kink Rate Model

Kuvadia and Doherty [29] developed a generalized expression for the kink rate  $u$  on a spiral edge on organic crystal surfaces that has  $n$  types of kink sites along the edge

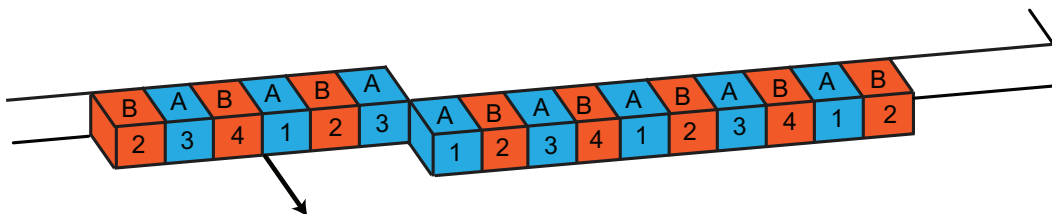
$$u = \frac{(j^+)^n - \prod_{k=1}^n j_k^-}{\sum_{\ell=1}^n (j^+)^{n-\ell} (j^-)^{(\ell-1)}} \quad (3.5)$$

where  $j^+$  is the attachment flux of growth units into the kink site and  $j_k^-$  is the detachment flux from the kink site  $k$ .  $j^+$  is independent of the specific kink site and depends only on supersaturation and solution composition, whereas  $j_k^-$  depends on the solution chemistry and the local bonding energies for the kink site  $k$ . The quantity  $(j^-)^{(\ell-1)}$  in eq 3.5 is given by

$$(j^-)^{(\ell-1)} = \sum_{k=1}^n j_k^- j_{k+1}^- j_{k+2}^- \cdots j_{k+\ell-2}^- \quad (3.6)$$

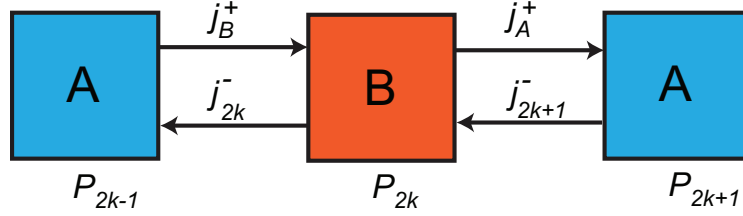
Equation 3.5 holds true for molecular crystals where all the growth units are a single chemical species so that the solvation behavior is the same for all of them. In case of inorganic crystal growth, the growth units are ions (positive and negative) and will exhibit different solvation behavior and attachment kinetics.

Figure 3.3 shows a representative arrangement of multiple types of kink sites along a step edge on the surface of an AB-type ionic crystal where each ion has two distinct orientations. The attachment of a B growth unit into an A-terminated kink site results in the exposure of a B-terminated kink site. Similarly, the detachment from an A-terminated kink site results in the exposure of another B-terminated kink site.



**Figure 3.3:** Representative arrangement of multiple types of kink sites along the edge of an AB-type ionic crystal surface. There are two types of A (cyan) and B (orange) kink sites each that are repeated by symmetry along the edge. The arrow indicates the direction of the growth of the step.

It is assumed that the edge begins with an A-type kink site and alternates between an A type and a B type kink site. Therefore, the odd and even numbered kink sites will be terminated by cationic (A) and anionic (B) species, respectively. If there are  $N$  orientations each of cationic and anionic growth units along the edge, there will be a total of  $2N$  types of kink sites on the edge.  $P_{2k-1}$  and  $P_{2k}$  are defined as the probabilities that the step edge is terminated with an A kink site and a B kink site of type  $(2k-1)$  and  $2k$ , respectively. Therefore,  $k$  takes all the integer values between 1 and  $N$ . The edge is defined to be in state  $2k-1$  if it is terminated with the kink site numbered  $2k-1$ . The transition between any two successive states or types of kink sites is associated with attachment ( $j^+$ ) or detachment ( $j^-$ ) fluxes. Figure 3.4 shows the transition between the  $2k-1$ ,  $2k$  and  $2k+1$  states of the kink site. It is well accepted [30, 33, 34] that the attachment flux  $j^+$  depends on the solvation chemistry of the attaching growth unit and the solution composition but is independent of the kink site location along the edge. The detachment flux  $j^-$  depends on both solution chemistry and the local bonding energies at the kink site location along the edge.



**Figure 3.4:** Transition between A and B kink sites based on the attachment or detachment of A and B growth units and the fluxes associated with these transitions.

The kink incorporation rate on the step edge is given by the net rate at which the edge transitions from one state to the next. The kink rate  $u$  for states  $2k - 1$  and  $2k$  is given by

$$u_{2k-1} = j_B^+ P_{2k-1} - j_{2k}^- P_{2k} \qquad u_{2k} = j_A^+ P_{2k} - j_{2k+1}^- P_{2k+1} \qquad (3.7)$$

A master equation can be written for the time-evolution of every state between  $k = 1$  and  $k = 2N$ . Since a transition can only occur between successive states, the probability of state  $2k$  depends only on the transitions between states  $2k - 1$ ,  $2k$  and  $2k + 1$  as follows

$$\frac{dP_{2k}}{dt} = \left( j_B^+ P_{2k-1} + j_{2k+1}^- P_{2k+1} \right) - \left( j_A^+ + j_{2k}^- \right) P_{2k} \qquad (3.8)$$

Since the time scale for the advancement of a step is at least an order of magnitude greater than the time scale for attachment [30], the probability of the state  $2k$  may be assumed to be in steady state. Therefore, the steady-state solution to the master equation is written as follows

$$j_B^+ P_{2k-1} + j_{2k+1}^- P_{2k+1} = \left( j_A^+ + j_{2k}^- \right) P_{2k} \qquad (3.9)$$

Similar equations can be written for each type of kink site giving rise of  $2N$  such equations. However, due to the cyclic repetition of the arrangement of the kink sites beyond state

$2N$ , there are only  $2N - 1$  independent equations. The condition that the kink state probabilities  $P_k$  must all sum up to 1 provides the  $2N^{th}$  equation to solve for all the probabilities in terms of the attachment and detachment fluxes.

Equation 3.9 can be rearranged as follows

$$j_B^+ P_{2k-1} - j_{2k}^- P_{2k} = j_A^+ P_{2k} - j_{2k+1}^- P_{2k+1} \quad (3.10)$$

From equations 3.10 and 3.7, it implies that, at steady state

$$u_{2k-1} = u_{2k} \quad (3.11)$$

Similar relationships can be derived for the kink rates of other states as well. Therefore, at steady state the net rate of incorporation is exactly equal for each state or kink type.

The kink rate  $u$  can thus be calculated as follows

$$u = \frac{(j_A^+ j_B^+)^N - \prod_{k=1}^{2N} j_k^-}{\sum_{\ell=1}^N (j_A^+ j_B^+)^{N-\ell} \left\{ (j^-)^{(2\ell-1)} + j_A^+ (j_{even}^-)^{(2\ell-2)} + j_B^+ (j_{odd}^-)^{(2\ell-2)} \right\}} \quad (3.12)$$

where

$$\begin{aligned} (j_{odd}^-)^{(\ell)} &= \sum_{k=1}^N j_{2k-1}^- j_{2k}^- j_{2k+1}^- \cdots j_{2k+\ell-2}^- \\ (j_{even}^-)^{(\ell)} &= \sum_{k=1}^N j_{2k}^- j_{2k+1}^- j_{2k+2}^- \cdots j_{2k+\ell-1}^- \\ (j^-)^{(\ell)} &= \sum_{k=1}^{2N} j_k^- j_{k+1}^- j_{k+2}^- \cdots j_{k+\ell-1}^- = (j_{odd}^-)^{(\ell)} + (j_{even}^-)^{(\ell)} \\ (j_{odd}^-)^{(0)} &= N \\ (j_{even}^-)^{(0)} &= N \end{aligned}$$

Equation 3.12 can be used to calculate the kink rate  $u$  on any edge on any crystal surface, provided the attachment and detachment fluxes ( $j^+$  and  $j^-$ , respectively) from kink sites are known. The expressions for the kink state probabilities are discussed in Appendix B. General expressions for these fluxes and a systematic method for their calculation are discussed next.

### 3.4.2 Expressions for Attachment and Detachment Fluxes

Transition state theory (TST) [35] has been used here to calculate the kink site attachment and detachment fluxes. The reaction coordinate is assumed to be the distance from the kink site towards the solution so that the *reactant* state corresponds to the growth unit docked in its kink site and the *product* state corresponds to the growth unit fully solvated in bulk solution (Figure 3.5). The transition state corresponds to a partially broken solvation shell that is also partially bonded to its neighbors around the kink site. In this case, the attachment and detachment fluxes depend on the reverse and forward “reaction rates”, respectively, as shown in eqs 3.13 and 3.14.

A generalized model for the attachment and detachment fluxes must account for the presence of both cationic and anionic growth units in the solution. Additives, impurities, counterions and antisolvents, etc. may also be present in the solution. These species can be classified into three groups - (I) species that can incorporate into the crystal lattice (e.g., chemically similar additives or growth modifiers such as  $\text{Mg}^{2+}$  ions in calcite), (II) species that influence detachment of growth units from kink sites (e.g., antisolvent), and

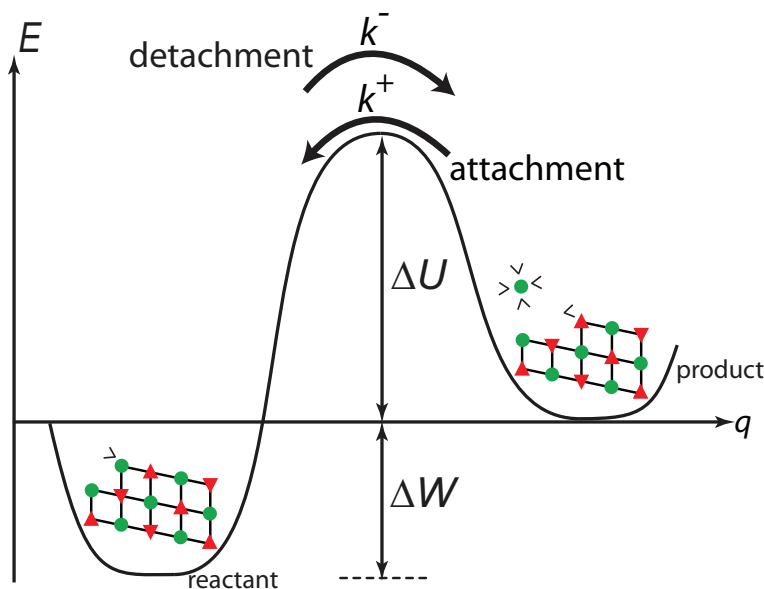


**Figure 3.5:** Representative energy landscape during attachment and detachment from kink sites. The reactant state is the growth unit attached in the kink site. The product state is the unattached kink site and fully solvated growth unit in the solution.  $k^+$  and  $k^-$  are the rate constants for the attachment and detachment processes, respectively.

(III) species that do not participate in any of the steps associated with attachment or detachment of growth units into kink sites (e.g., counterions). The mole fractions of these three types of species in the solution are  $x_I$ ,  $x_{II}$  and  $x_{III}$ , respectively.

The prefactor for the TST rate constant contains partition functions for the solvated growth unit and for the kink site on the crystal surface. The prefactor value will be different for cationic and anionic growth units. The attachment flux of an ionic species into a kink site is proportional to its mole fraction in the adsorption layer [33]. If the bulk transport rate is much faster than the rate of surface integration, the mole fraction of solute molecules in the adsorption layer next to the crystal surface will be the same as the bulk solution mole fraction. Therefore, the attachment flux  $j^+$  for both the ions

is written as

$$\begin{aligned} j_A^+ &= \nu_A \exp\left(-\frac{\Delta U_A}{k_B T}\right) x_A = k_A^+ x_A \\ j_B^+ &= \nu_B \exp\left(-\frac{\Delta U_B}{k_B T}\right) x_B = k_B^+ x_B \end{aligned} \quad (3.13)$$

where  $\nu_A$  and  $\nu_B$  are the vibrational frequencies of attachment and detachment attempts that depend on the temperature and the partition functions of the solute, solvent and the transition state solvated complex. These frequencies are assumed to be the same everywhere on the crystal surface. The attachment energy barriers correspond to the breaking of the solvation shell around the growth units so the barrier heights  $\Delta U_A$  and  $\Delta U_B$  will be constant on all crystal faces.  $x_A$  and  $x_B$  are the respective mole fractions of the cationic and anionic growth units in the solution.  $k_A^+$  and  $k_B^+$  are the first order rate constants for attachment of A and B ions, respectively, into kink sites.

The detachment flux for both types of growth units is proportional to the combined mole fraction of solvent molecules and species of type II in the adsorption layer [33]. The detachment flux  $j^-$  for each of the kink sites is given by

$$\begin{aligned} j_{2k-1}^- &= (1 - x_A - x_B - x_I - x_{III}) \nu_A \exp\left(-\frac{\Delta U_A + \Delta W_{2k-1}}{k_B T}\right) \\ j_{2k}^- &= (1 - x_A - x_B - x_I - x_{III}) \nu_B \exp\left(-\frac{\Delta U_B + \Delta W_{2k}}{k_B T}\right) \quad k = 1, 2, 3, \dots, N \end{aligned} \quad (3.14)$$

where  $\Delta W_{2k-1}$  is the work required to remove the partially solvated growth unit from the  $2k-1$  kink site position to a fully solvated state in the bulk solution.  $\Delta W_{2k-1}$  depends on the interactions between the growth unit which is docked in the  $2k-1$  kink site and the crystal as well as its interactions with the solvent. For vapor grown crystals,  $\Delta W_{2k-1}$  will

be given by the sum of the solid broken bond energies at kink site  $2k - 1$ . As discussed earlier,  $j_{2k-1}^-$  and  $j_{2k}^-$  are the detachment fluxes for the  $2k - 1$  (cationic) and  $2k$  (anionic) kink sites, respectively. The expressions for the attachment and detachment fluxes from eqs 3.13 and 3.14, respectively, can be put into eq 3.12 to calculate the kink propagation rate at any step edge on an inorganic crystal surface. It is convenient to express the mole fractions of A and B ions in the solution ( $x_A$  and  $x_B$ , respectively) in terms of two experimental parameters - supersaturation  $S$ , and ionic activity ratio  $r$ .

Supersaturation or saturation ratio  $S$  of the aqueous solution of a general electrolyte  $A_\alpha B_\beta$  is defined in terms of the difference between the chemical potentials of the solution phase and the crystal as follows [14, 36, 37]

$$\Delta\mu = (\alpha + \beta)k_B T \ln S = k_B T \ln \left( \frac{a_A^\alpha a_B^\beta}{K_{sp}} \right) \quad (3.15)$$

where  $K_{sp}$  is the solubility product of  $A_\alpha B_\beta$  salt. For an AB type salt, the supersaturation  $S$  is defined as

$$S = \left( \frac{a_A a_B}{K_{sp}} \right)^{1/2} = \left( \frac{(M\gamma_A x_A)(M\gamma_B x_B)}{K_{sp}} \right)^{1/2} = \left( \frac{\gamma_A \gamma_B x_A x_B}{K_{sp}/M^2} \right)^{1/2} \quad (3.16)$$

where  $\gamma_A$  and  $\gamma_B$  are the activity coefficients, and  $M$  is the molarity of the solution. For dilute aqueous solutions,  $M = 55.56 \text{ mol.L}^{-1}$ . A supersaturated solution is also quantified by the saturation index ( $SI$ ) in geochemistry literature [38]. In solution growth literature [30, 37], the level of supersaturation is often written as  $\sigma = \frac{C}{C_{eq}} - 1$ , where  $C$  and  $C_{eq}$  are the solute concentrations in the supersaturated and saturated solutions, respectively. The relationship between  $S$ ,  $\sigma$  and saturation index  $SI$  for an AB type

electrolyte is

$$\sigma = S - 1 = \left( \frac{a_A a_B}{K_{sp}} \right)^{1/2} - 1 \quad (3.17)$$

$$SI = \log \left( \frac{a_A a_B}{K_{sp}} \right) = \log S^2 = \log (1 + \sigma)^2 \quad (3.18)$$

$S$  (from eq 3.16) will be used to quantify a supersaturated solution in this chapter. The ionic activity ratio  $r$  is defined as

$$r = \frac{a_A}{a_B} = \frac{\gamma_A x_A}{\gamma_B x_B} \quad (3.19)$$

The relationship between the mole fractions ( $x_A$  and  $x_B$ ), supersaturation  $S$ , and activity ratio  $r$  (from eqs 3.16 and 3.19) is

$$x_A = \frac{S\sqrt{r}}{\gamma_A} \left( \frac{\sqrt{K_{sp}}}{M} \right) \quad x_B = \frac{S}{\gamma_B\sqrt{r}} \left( \frac{\sqrt{K_{sp}}}{M} \right) \quad (3.20)$$

These two experimental parameters ( $S$  and  $r$ ) can be independently manipulated during the crystallization process. The more common experimental cases are when either the supersaturation [39] or the ionic activity ratio is constant [40].

The condition of thermodynamic equilibrium provides a relationship between the attachment and detachment fluxes. At equilibrium, the step velocity is zero so the kink rate must be zero. It follows from eq 3.12 that at equilibrium,

$$\left( j_{A,eq}^+ j_{B,eq}^+ \right)^N = \prod_{k=1}^{2N} j_{k,eq}^- \quad (3.21)$$

The equilibrium attachment and detachment fluxes are obtained by replacing  $x_A$  and  $x_B$  in eqs 3.13 and 3.14 by  $x_{A,eq}$  and  $x_{B,eq}$ , respectively. The expressions for  $j_{eq}^+$  and  $j_{eq}^-$  are

substituted into eq 3.21, which results in

$$-\frac{1}{2N} \sum_{k=1}^{2N} \left( \frac{\Delta W_k}{k_B T} \right) = \ln \left( \frac{\sqrt{x_{A,eq} x_{B,eq}}}{1 - x_{A,eq} - x_{B,eq} - x_I - x_{III}} \right) \quad (3.22)$$

The left-hand side of eq 3.22 contains quantities that are calculated from the intermolecular interactions while the right-hand side contains quantities whose values are experimentally obtained. Therefore, this equation can be used as a consistency check to verify the calculations of the solid-state and solvent interaction energies, so that the calculated values of  $\Delta W_k$  from the model are consistent with the equilibrium mole fractions calculated from the experimentally obtained value of the solubility product  $K_{sp}$  (by putting  $S = 1$  in eq 3.20). If the two sides of eq 3.22 do not match, a local solubility product  $K'_{sp}$  near the crystal surface can be calculated from the  $\Delta W_k$  values as follows

$$K'_{sp} = \frac{\gamma_A \gamma_B M^2 (1 - x_I - x_{III})^2 \exp \left\{ -\frac{1}{N} \sum_{k=1}^{2N} \left( \frac{\Delta W_k}{k_B T} \right) \right\}}{\left[ 1 + \left( \frac{1 + r_{eq} \gamma_B / \gamma_A}{\sqrt{r_{eq} \gamma_B / \gamma_A}} \right) \exp \left\{ -\frac{1}{2N} \sum_{k=1}^{2N} \left( \frac{\Delta W_k}{k_B T} \right) \right\} \right]^2} \quad (3.23)$$

where  $r_{eq}$  is the value of the ionic activity ratio at equilibrium. If the crystallization process occurs at constant ionic activity ratio,  $r_{eq} = r$  and eq 3.23 can be used to calculate the local solubility product and hence the equilibrium mole fractions of A and B (from eq 3.20). However, if the crystallization process occurs at variable  $r$ ,  $r_{eq}$  may be different from the variable values of  $r$ . In that case, eq 3.23 can be solved only if the equilibrium mole fractions of A and B are very small ( $x_{A,eq}, x_{B,eq} \ll 1$ ). Equation 3.23 is then simplified as follows

$$K'_{sp} = \gamma_A \gamma_B M^2 (1 - x_I - x_{III})^2 \exp \left\{ -\frac{1}{N} \sum_{k=1}^{2N} \left( \frac{\Delta W_k}{k_B T} \right) \right\} \quad (3.24)$$

The solubility of several inorganic crystals, such as calcite, barite, rutile, KDP, etc., in water is very low [1, 41]. Therefore, the assumption that  $x_{A,eq}, x_{B,eq} \ll 1$  is quite reasonable for these crystals. For the sake of internal consistency, the value of  $K'_{sp}$  from eq 3.24 is used instead of the experimental value ( $K_{sp}$ ) in the subsequent equations. The mole fractions of A and B in the supersaturated solution ( $x_A$  and  $x_B$ ) are thus calculated by substituting  $K_{sp}$  with  $K'_{sp}$  in eq 3.20. The activity coefficients  $\gamma_A$  and  $\gamma_B$  are calculated using Davies equation [42] that extends the Debye-Hückel theory to high concentration electrolyte solutions. If the mole fraction of the counterions present in the solution ( $x_{III}$ ) is much higher than  $x_A$  and  $x_B$ , the activity coefficients are constant between the saturated and supersaturated solution and do not depend on  $x_A$  and  $x_B$ .

The attachment and detachment fluxes are written in terms of the supersaturation  $S$ , ionic activity ratio  $r$  and the local solubility product  $K'_{sp}$  from eqs 3.13 and 3.14. The calculation of the kink rate  $u$  from eq 3.12 requires that kink detachment work  $\Delta W$  values be known. The detailed expressions for  $j^+$ ,  $j^-$  and  $u$  as functions of  $S$ ,  $r$  and  $\Delta W$  are given in Appendix B.

The kink site potential energies calculated in Chapter 2 are used to calculate the kink detachment work  $\Delta W$ . The species involved in the detachment process are - the growth unit about to be detached, the growth unit that forms the next kink site along the edge, and the solvent molecules that solvate both these growth units. Therefore, calculation of  $\Delta W$  involves computing the kink site energies of the two successive growth units along the edge (Figure 3.6). The information on solvent structure around the kink site is used

along with the space partitioning method to calculate the partial charges on the surface ions and the potential energy of a growth unit in the kink site. Knowledge of the structure of the solvent shell around a growth unit in bulk solution, including the number of solvent molecules in the shell and their distances from the growth unit, is required to calculate the potential energy of the solvated growth unit. The solvation information of  $\text{Ca}^{2+}$  and  $\text{CO}_3^{2-}$  ions for calcite crystal growth was obtained from molecular simulations [31, 43, 44]. The expression for  $\Delta W$  in terms of the kink site potential energy  $U^{kink}$  and potential energy of solvated ion  $U^{solvated}$  is given as follows

$$\Delta W_{2k-1} = U_A^{solvated} + U_{2k}^{kink} - U_{2k-1}^{kink} - U_{2k}^{step} \quad (3.25)$$

$$\Delta W_{2k} = U_B^{solvated} + U_{2k+1}^{kink} - U_{2k}^{kink} - U_{2k+1}^{step} \quad (3.26)$$

where  $U^{step}$  is the potential energy of an ion present along the step edge next to the kink site growth unit.  $U^{step}$  is calculated using the space partitioning method with the partial charges for the atoms in the growth unit corresponding to that for a growth unit situated along the step edge. Figure 3.6 illustrates the kink detachment process and the change in the configuration of a B growth unit that lies next to the A type kink site along the step edge and forms the new kink site (B type) after detachment of the A growth unit.

Table 3.2 shows the values of the kink detachment work ( $\Delta W$ ) for the kink sites on the  $[48\bar{1}]$  spiral edges (acute and obtuse) on a calcite  $(10\bar{1}4)$  surface. As mentioned earlier, the  $\Delta W$  values are the same for the kink sites on the symmetrically equivalent edges along the  $[\bar{4}41]$  direction.

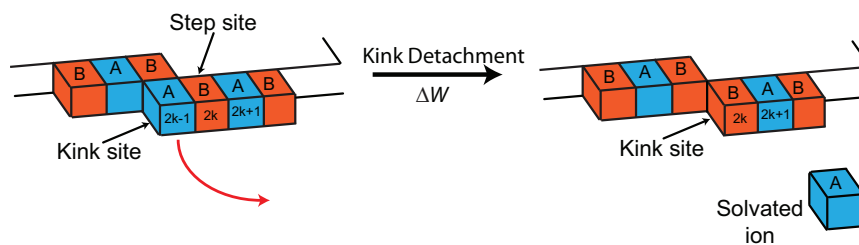


**Figure 3.6:** Illustration of the detachment process of an A type kink site that results in the formation of a B type kink site. The change in the potential energy of the system in this process is given by the kink detachment work  $\Delta W$ . The solvent molecules around the edge are not shown for clarity.

**Table 3.2:** Kink detachment work ( $\Delta W$ ) values in kcal/mol for the kink sites on the  $[48\bar{1}]$  spiral edges of a  $(10\bar{1}4)$  face of calcite

Edge Type	Ca (1)	CO <sub>3</sub> (2)	Ca (3)	CO <sub>3</sub> (4)
$[48\bar{1}]$ Obtuse $\mathcal{E}$ kinks	28.8	24.6	29.2	26.1
$[48\bar{1}]$ Obtuse $\mathcal{W}$ kinks	18.9	36.6	21.0	37.9
$[48\bar{1}]$ Acute $\mathcal{E}$ kinks	21.7	37.9	18.6	36.5
$[48\bar{1}]$ Acute $\mathcal{W}$ kinks	10.9	38.3	28.1	37.5

The  $\Delta W$  values differ between the same type of kink sites on the obtuse and acute spiral edges. From eq B.5 (Appendix B), it is evident that the kink rate, and thus the step velocity, should be different for the obtuse and acute edges on the  $(10\bar{1}4)$  surface of calcite crystals. The model calculates the kink rate to within a multiplicative constant  $k_A^+$ , which is uniform on all crystal surfaces. Therefore, the absolute value of the step velocity of a spiral edge cannot be predicted without using molecular simulations with rare-event methods [43, 45] to estimate the value of  $k_A^+$ .

## 3.5 Step Velocity Predictions on $(10\bar{1}4)$ Surface of Calcite

The step velocity of spiral edges can be measured experimentally using Atomic Force Microscopy (AFM). The step velocity of spiral edges on a  $(10\bar{1}4)$  surface of calcite have been measured using *in situ* AFM under various experimental conditions [5, 39, 40, 46, 47]. De Yoreo and coworkers [7, 40, 48] measured the step velocities of the spiral edges for a wide range of supersaturation ( $1.02 < S < 2.04$ ), while keeping the ionic activity ratio constant at  $r = 1.04$ . Figure 3.7 shows the comparison between the experimentally measured step velocities reported by Teng et al. [48] and predicted values from the model. The predicted step velocities were calculated assuming that no foreign species were present in the solution. The calculated values of step velocities were scaled with the experimental values at  $S = 1.40$ .

The model predictions for the step velocity of the obtuse edge match very well with the experimentally measured values except for very high supersaturation ( $S \geq 1.8$ ). The predictions of the spiral growth model are not reliable at such high supersaturation, where growth by 2D nucleation was also observed in the AFM experiments [40].

Step velocity predictions of the acute edge do not capture the supersaturation trend of the experimental measurements. Teng et al. observed a crossover between the step velocities of obtuse and acute edges at  $S = 1.29$  [48]. This crossover was explained by the effect of ppm level impurities (e.g., Mg,  $\text{SO}_4$ ) present in the experimental reagents, on

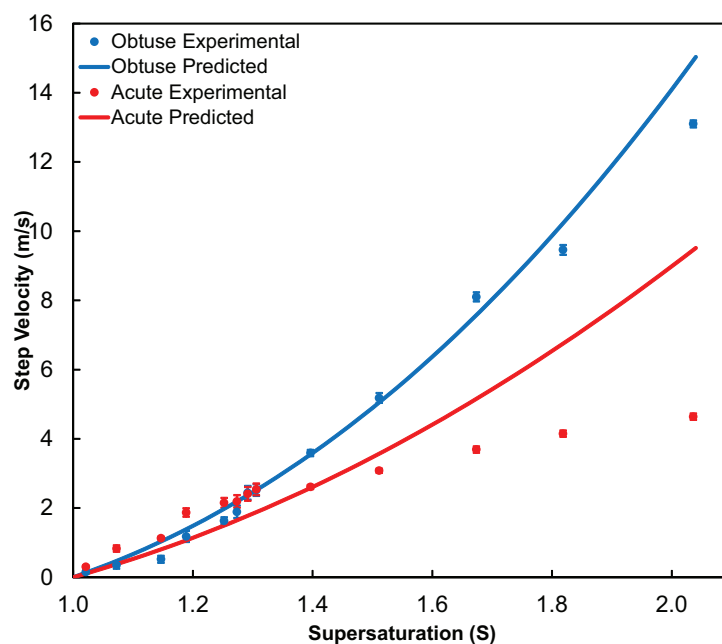


**Figure 3.7:** Comparison of model predictions of the step velocities of obtuse and acute spiral edges with AFM measurements reported by Teng et al. [48] at  $r = 1.04$ .

growth kinetics at the acute edge. These impurities adsorb on the terrace of the crystal surface and slow down the advancing steps, thereby changing the dependence of the step velocity on the supersaturation [49]. Teng et al. [48] showed that a sublinear dependence of the step velocity on the supersaturation fit the experimental data for the acute edge. Impurities such as  $\text{Mg}^{2+}$  ions preferentially adsorb on the acute edges rather than the obtuse edges of  $(10\bar{1}4)$  calcite surface [50]. These ppm level impurities may have affected the step velocity measurement of the acute edges only. The model calculations do not account for the presence of any impurities in the solution or on the terrace. Therefore, the supersaturation trend for the predicted step velocity of the acute edge is not expected to match with the experimental values.

The model does predict asymmetric growth spirals on the  $(10\bar{1}4)$  surface of calcite and a higher step velocity of the obtuse edge than that of the acute edge at close to stoichiometric values of ionic activity ratio, which is consistent with other AFM measurements reported in the literature [5, 39].

The values of the kink detachment work depend strongly on the interaction energies of the kink site ions with the solvent molecules. Figure 3.8 shows the change in the kink detachment work  $\Delta W$  values for the  $\mathcal{E}$  orientation kink sites on the  $[48\bar{1}]$  obtuse edge as the interaction energies between water molecules and the  $\text{Ca}^{2+}$  and  $\text{CO}_3^{2-}$  ions and the water molecules is varied by  $\pm 5\%$ . The  $\Delta W$  values change by at least  $\pm 65\%$  due to a  $\mp 5\%$  change in the interaction energy between the solvent molecules and the kink site ions. The change in the  $\Delta W$  values is consistent for all the kink sites on obtuse and acute edges, therefore, the scaled values of the step velocity do not change with the variation in the solvent interaction energies. High fidelity calculations using transition path sampling [51] to identify the most appropriate reaction coordinate, and rare-event methods to predict the free energy barrier for kink detachment will provide accurate absolute values of the step velocity of both spiral edges.

The activity ratio of  $\text{Ca}^{2+}$  to  $\text{CO}_3^{2-}$  ions,  $r$ , is an important experimental parameter that affects the step velocity of spiral edges. Larsen et al. [47] performed *in situ* AFM experiments to measure the step velocities of the obtuse and acute spiral edges on a  $(10\bar{1}4)$  surface of calcite at different values of  $r$ , while keeping the supersaturation constant at  $S = 2.00$ . 2D nucleation is also expected to be important at this supersaturation value,

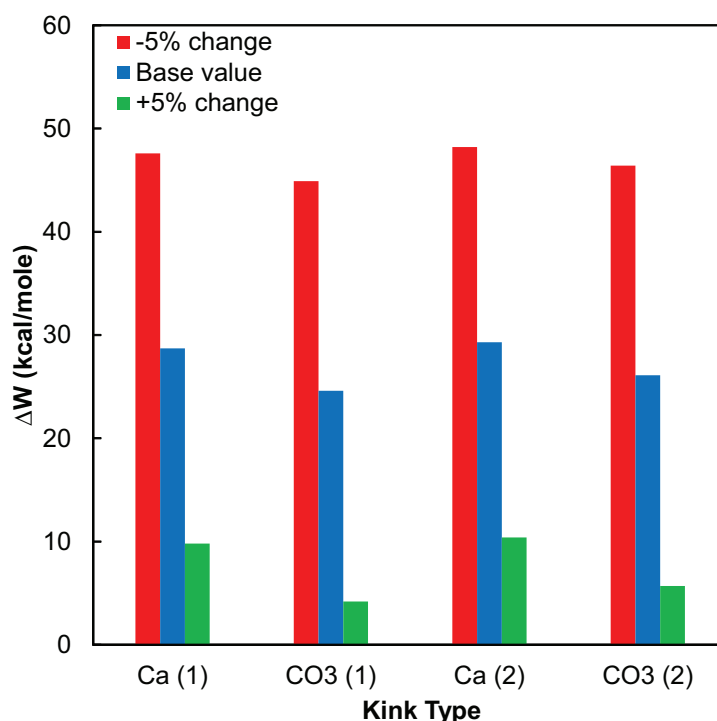


**Figure 3.8:** Sensitivity of the kink detachment work  $\Delta W$  to variations ( $\pm 5\%$ ) in the interaction energies between the kink site ions and the surrounding water molecules for the kink sites with  $\mathcal{E}$  orientation on the  $[\bar{4}41]$  obtuse edge on the  $(10\bar{1}4)$  surface of calcite.

therefore the model predictions cannot be compared with their experiments. Stack and Grantham [39] carried out similar measurements at lower supersaturation ( $S = 1.58$ ). Figure 3.9 shows the observed variation in the shape of the growth spirals on the calcite surface upon increasing  $r$  [39]. The edges of the growth spiral get significantly roughened at very low or very high values of the activity ratio while the growth spiral looks more symmetric at  $r \sim 1$ . At very high or very low values of the activity ratio, the growth kinetics is limited by the availability of one of the two ions in the solution. At close to stoichiometric solution composition, there are plenty of both ions in the solution and the growth is limited only by the attachment/detachment kinetics.

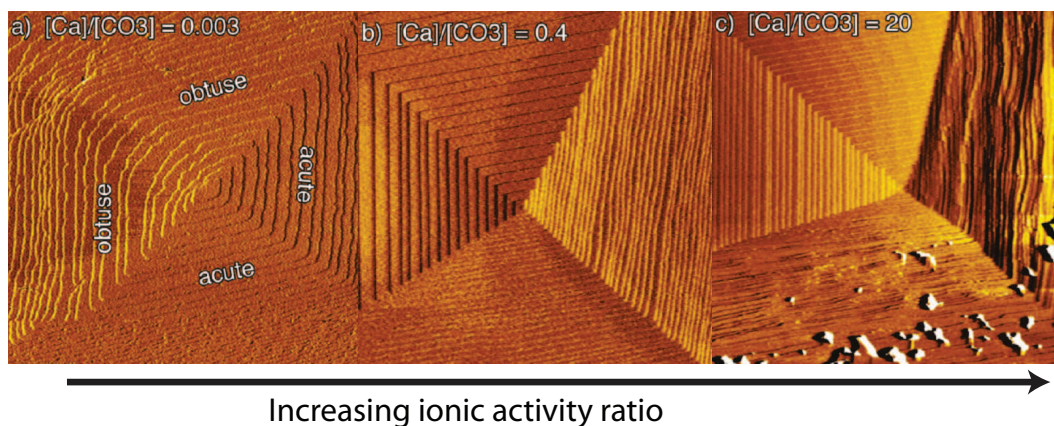


**Figure 3.9:** In situ AFM images of growth spirals on the  $(10\bar{1}4)$  surface of calcite crystal. The activity ratio of  $\text{Ca}^{2+}$  to  $\text{CO}_3^{2-}$  ions increases from panels (a) to (c). Adapted with permission from Stack and Grantham 2010 [39]. Copyright ©2010, American Chemical Society.

Figure 3.10 shows the comparison of the experimentally measured step velocities of both obtuse and acute edges by Stack et al. [39] with the model predictions at different values of  $r$ . The model only predicts relative step velocities and not absolute values, therefore, the model predictions were scaled with an experimental value of step velocity. For obtuse edge, the experimental step velocity value at a value of  $r = 43.7$  was used, while for the acute edge, the step velocity at a value of  $r = 0.015$  was used for scaling. Although the model predictions do not match exactly with the experimental step velocities for both edges, the model accurately captures the step velocity trend for both the edges as the ionic activity ratio is varied. The model also correctly predicts that the maximum step velocity for each of the edges does not occur exactly at  $r = 1$ , which is the stoichiometric composition of the solution. Since the solvation behavior and

attachment rates for  $\text{Ca}^{2+}$  and  $\text{CO}_3^{2-}$  ions are different, the maximum step velocity will not be observed at  $r = 1$ .

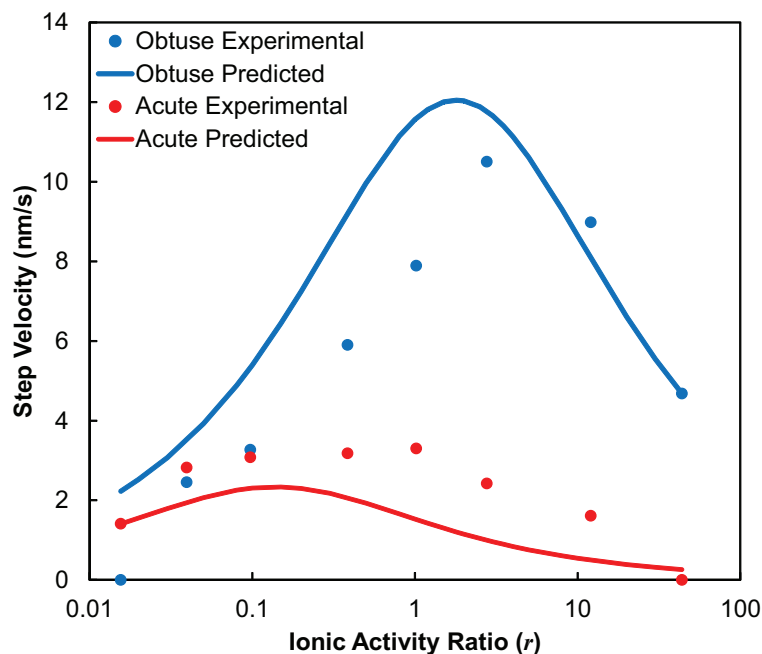


**Figure 3.10:** Comparison of the variation of the step velocities of obtuse and acute spiral edges with increasing activity ratio of  $\text{Ca}^{2+}$  to  $\text{CO}_3^{2-}$  measured by Stack and Grantham [39] with the model predictions. The experiments and the model predictions are at a constant supersaturation of  $S = 1.58$ .

The overall dependence of experimental parameters such as supersaturation ( $S$ ) and ionic activity ratio ( $r$ ) is broadly captured by this mechanistic model for the case of spiral growth on the  $(10\bar{1}4)$  surface of calcite crystals. The model shows a more complex relationship between step velocity  $v$  and the driving force  $(S - 1)$  than the simple linear relationship that was assumed by traditional models [19, 52] and shown experimentally for large protein molecules [53, 54]. This complex dependence on  $S$  is consistent with the model developed by Zhang and Nancollas for an edge on an ionic crystal surface with 2

types of kink sites [14]. The scaling of the step velocity with the ionic activity ratio  $r$  is also correctly captured by this model.

## 3.6 Critical Length of a Spiral Edge

The rotation time of a growth spiral  $\tau_s$  depends on step velocities as well as the critical lengths of the spiral edges. The original definition of critical length was given as the length of the edge below which its step velocity is zero [55]. The velocity of an advancing spiral edge is assumed to have a heaviside (“on-off”) functionality such that the velocity is zero for edges with lengths smaller than the critical length and the edge advances with a constant velocity at all lengths above the critical length. One definition of the critical length is that it is the length above which the free energy required for 1D nucleation of an edge becomes negative. For crystal growth of centrosymmetric molecules, the free energy change on 1D nucleation of an edge of length  $l$  is given as follows [28, 56]

$$\Delta G(l) = -\Delta\mu \frac{l}{a_e} + 2\gamma A \quad (3.27)$$

where  $\Delta\mu$  is the chemical potential difference between solution and crystal per growth unit,  $a_e$  is the distance between successive growth units along the edge,  $A$  is the cross sectional area of the edge and  $\gamma$  is the surface energy per unit area between the edge and the solvent molecules. In equation 3.27, the first term on the right hand side indicates the lowering of free energy due to the creation of a new phase and the second term is the free energy penalty for the creation of a new surface area (Figure 3.11a). The function

$\Delta G(l)$  is a discrete function since the length of the edge increases in discrete amounts equal to  $a_e$  corresponding to each additional growth unit (Figure 3.11b).

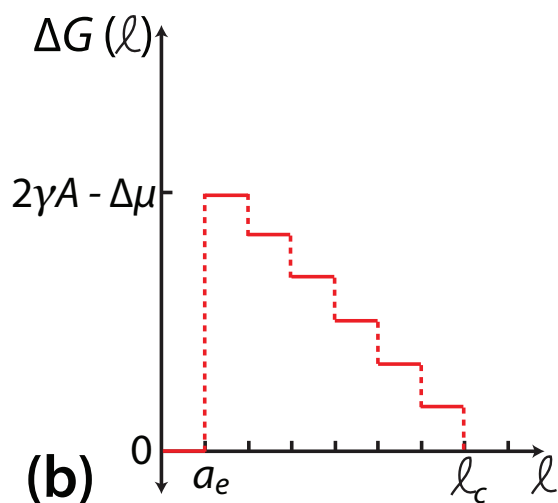
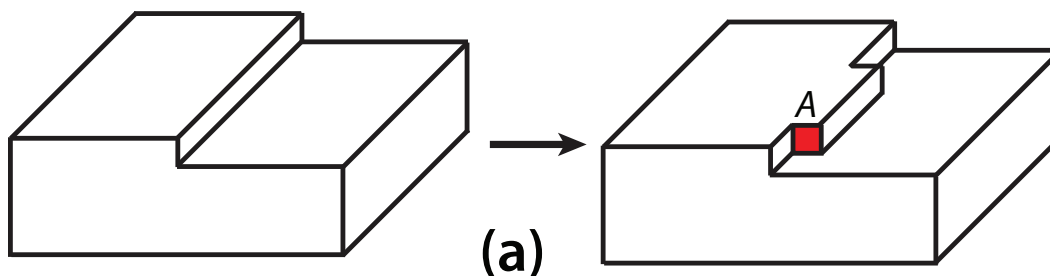


**Figure 3.11:** (a) 1D nucleation of a new edge and the creation of new surface area (colored in red). (b)  $\Delta G$  variation with length of the edge for a hypothetical centrosymmetric molecular crystal.

The critical length  $l_c$  is obtained by putting  $\Delta G(l)$  in equation 3.27 equal to zero at  $l = l_c$ . The expression for the critical length is as follows

$$l_c = \frac{2a_e\gamma A}{k_B T \ln S^2} \quad (3.28)$$

where  $S$  is the supersaturation of the solution.

The bonding structure for noncentrosymmetric molecular crystals and inorganic crystals is highly asymmetric, therefore, the surface area term in equation 3.27 may not have the same value ( $2\gamma A$ ) for every value of  $l$ . For example, on the  $[48\bar{1}]$  edge of  $(10\bar{1}4)$  calcite surface, the ion terminating the edge varies as a function of the length of the edge (see Figure 3.12 (b) to (e)). Therefore, the surface energy term  $2\gamma A$  also varies with the length of the edge (via both  $\gamma$  and  $A$ ). Since the structure of the edge repeats in a periodic fashion, the  $2\gamma A$  term will also be a periodic function of  $l$ .

Let the four growth units along the  $[48\bar{1}]$  edge be numbered 1 to 4 as shown in Figure 3.12(a). If the spiral edge is advancing in the North direction, the 1D nucleated edge is defined to ‘begin’ from the West direction towards the East direction. A new edge can begin and terminate with any of the four ions. The free energy of a new edge  $\Delta G_{ij}$  is given as follows

$$\Delta G_{ij}(l_{ij}) = - (k_B T \ln S^2) \frac{l_{ij}}{a_e} + (\gamma_i A_i + \gamma_j A_j) \quad i = 1, 2, 3, 4; \quad j = 1, 2, 3, 4 \quad (3.29)$$

where  $i$  and  $j$  are the numbers for the growth unit that the new edge begins and ends with, respectively, and  $l_{ij}$  is the length of the edge between these two growth units. The distance between successive growth units along the  $[48\bar{1}]$  obtuse edge,  $a_e$ , is the same (3.212 Å) between all four growth units. For each value of  $i$ , there will be a free energy curve  $\Delta G_{ij}(l_{ij})$  and a corresponding value of critical length  $l_{i,c}$  such that  $\Delta G_{ij}(l_{ij} = l_{i,c}) = 0$ . Figure 3.13 shows the free energy curve as a function of edge length for a 1D nucleated edge that begins with a Ca ion ( $i = 1$ ) at supersaturation  $S = 1.5$ . Since the free energy curve has a sawtooth-like shape, there are multiple values of the

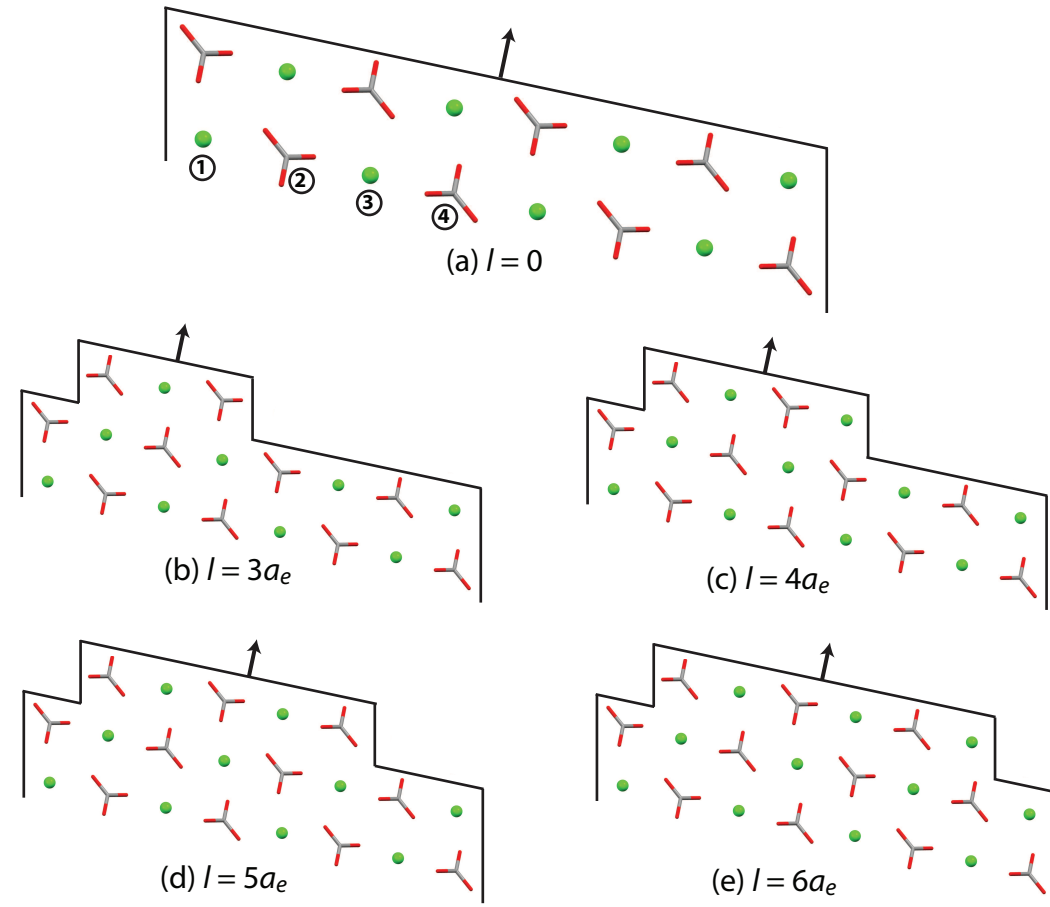


**Figure 3.12:** Structure of 1D nucleated edge along  $[48\bar{1}]$  direction on the  $(10\bar{1}4)$  surface of calcite as a function of length of the edge.

edge length at which  $\Delta G_{ij} = 0$ . The largest value of  $l_{ij}$  for which the free energy change goes to zero was selected as the critical length. The edge will start advancing beyond this length since  $\Delta G_{ij} < 0$  for all values of  $l_{ij}$  larger than this particular value of edge length.

The surface energy term  $\gamma_i A_i$  for every growth unit  $i$  was calculated from the interaction energy between the same growth unit in a kink site position and a neighboring

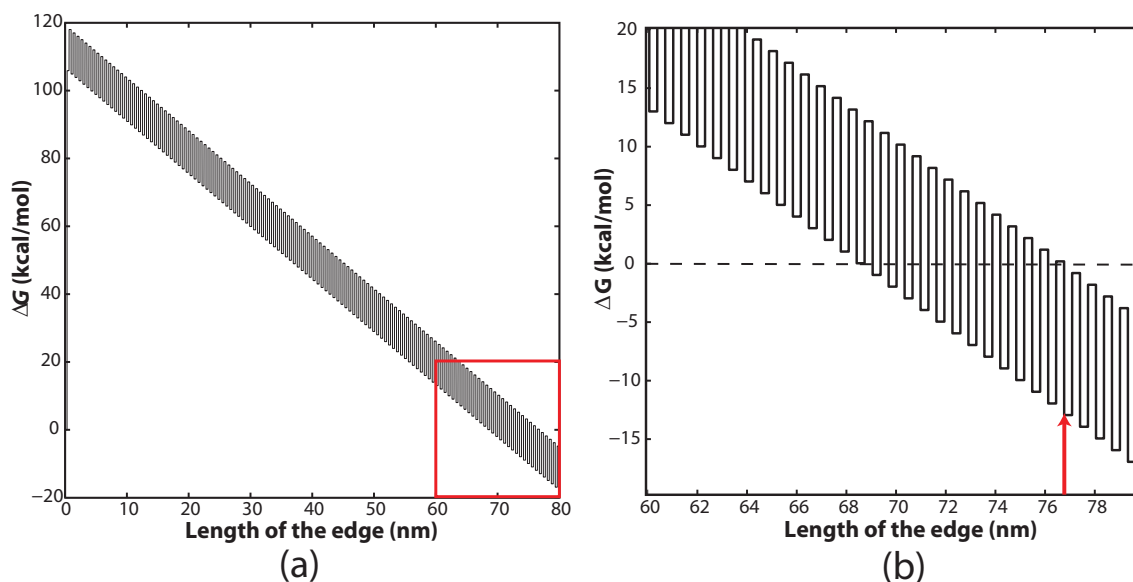


**Figure 3.13:** (a) and (b)  $\Delta G$  variation with the length of the  $[48\bar{1}]$  obtuse spiral edge on the  $(10\bar{1}4)$  surface of calcite crystals at  $S = 1.5$ . The edge begins with a Ca ion ( $i = 1$ , see Figure 3.12a). (b) shows an enlarged version of the inset within the red rectangle in (a). The black dashed line in (b) signifies  $\Delta G = 0$  while the red vertical arrow shows the value of the critical length  $l_{1,c} = 76.8$  nm.

**Table 3.3:** Critical lengths ( $l_c$ ) in nm of the  $[48\bar{1}]$  spiral edges on the  $(10\bar{1}4)$  face of calcite crystals at  $S = 1.5$

Edge Type	Edge begins with growth unit				Maximum Value (nm)
	Ca (1)	CO <sub>3</sub> (2)	Ca (3)	CO <sub>3</sub> (4)	
$[48\bar{1}]$ Obtuse	76.8	64.6	76.8	70.4	76.8
$[48\bar{1}]$ Acute	76.8	70.4	76.8	67.1	76.8

water molecule. Table 3.3 shows the values of the critical lengths of both obtuse and acute spiral edges on the  $(10\bar{1}4)$  surface of calcite crystals grown at  $S = 1.5$ . Since a 1D nucleated edge may begin with either of the four growth units, choosing a maximum of the four  $l_{i,c}$  values as the critical length will ensure that the step starts advancing at this value of the edge length. The model predicts equal values of the critical length for the obtuse and acute spiral edges on the  $(10\bar{1}4)$  surface of calcite, which does not agree

with the measured critical lengths (46 and 32 nm, respectively) determined from *in situ* AFM [7]. This discrepancy might be resolved in one (or more) of the following ways

- A higher-fidelity solvent structure information using molecular dynamics may provide more accurate values of the  $\gamma A$  term.
- Instead of a maximum of the four critical lengths, the calculation of the critical length might involve a weighted average of the four values, where the weighting factors would depend on the probability that the edge begins with one of the four growth units.
- The aforementioned definition of the critical length of a spiral edge is based on the free energy change due to 1D nucleation of an edge [7, 19, 28]. A stochastic definition for the critical length was recently proposed, where the critical length of a spiral edge was defined as the smallest length beyond which a growth unit situated along the edge cannot diffuse parallel to the edge across its entire length [30].
- Another possible definition for the critical length is the length at which a 1D nucleated edge is equally likely to grow or dissolve. A systematic comparison of the critical length predictions from these various definitions for several crystal chemistries will be required to identify the most suitable definition to be applied within the spiral growth model.

### 3.6.1 Morphology of Calcite Crystals

The growth rate of the  $(10\bar{1}4)$  calcite crystal face can be calculated by putting the values of the step velocities and critical lengths of the obtuse and acute edges in the  $[\bar{4}41]$  and  $[48\bar{1}]$  directions into eqs 3.3 and 3.2 to calculate  $\tau_s$  and the relative growth rate  $G$ , respectively. There is a single family of F faces present in calcite -  $\{10\bar{1}4\}$ . There are 6 faces in the  $\{10\bar{1}4\}$  family of F faces, each growing at the same perpendicular growth rate. These six faces enclose the entire crystal resulting in a regular rhombohedron morphology (Figure 3.14 as observed in the Icelandic Spar calcite crystals [57]).

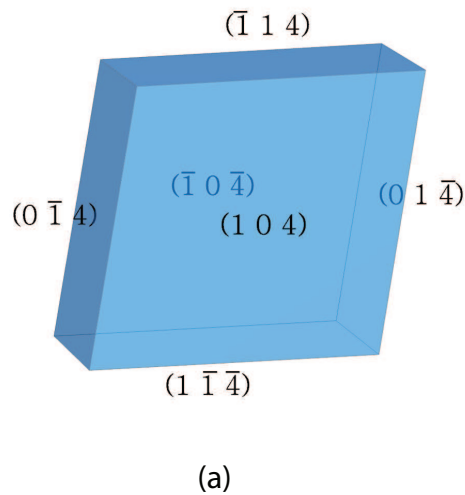


**Figure 3.14:** (a) The predicted morphology of calcite crystals dominated by the  $\{10\bar{1}4\}$  family of faces. (b) Morphology of the Icelandic Spar calcite crystal on exhibition at the National Museum of Natural History in Washington, DC.

## 3.7 Conclusions

A mechanistic growth model has been developed that can predict the relative growth rate of a crystal face and the steady-state morphology of inorganic crystals grown from solution. The model has been used to study the spiral growth mechanism which dominates the surface growth at low supersaturation. A generalized framework was developed to calculate the kink incorporation rate on every spiral edge on the face of an AB-type ionic crystal, irrespective of the number of kink sites exposed along each edge. The expressions for the attachment and detachment fluxes from the kink sites account for the effect of the solution composition and the kink detachment work on the kinetics of attachment and detachment processes.

The asymmetry in the step velocities on the obtuse and acute spiral edges on the  $(10\bar{1}4)$  surface of calcite crystals is captured by the model. The difference in the electronic properties of the carbonate ions situated on these edges results in different kinetics of attachment and detachment from the kink sites along the edge, which is reflected in the kink detachment work ( $\Delta W$ ) values calculated for the obtuse and acute edges. The model captures accurately the variation of the step velocity with supersaturation. The predictions match closely with the experimentally measured step velocities for the obtuse edge [48]. The ratio of the activities of  $\text{Ca}^{2+}$  to  $\text{CO}_3^{2-}$  ions is also an important experimental parameter with profound effect on the kinetics of step advancement of the spiral edges on calcite  $(10\bar{1}4)$  surface. The model predicts the scaling of the step velocity with the activity ratio and the deviation in the maxima for the step velocities of both obtuse

and acute spiral edges from the stoichiometric solution composition. The model is well suited to calculate relative step velocities of the spiral edges that can be used to predict the relative growth rates and the steady-state morphology of inorganic crystals.

The interaction energies of the surface ions with solvent (water) significantly impact the growth kinetics of inorganic crystal surfaces. This necessitates use of molecular simulations or experiments that can accurately characterize the local solvent structure and density around kink sites present on inorganic crystal surfaces. Molecular simulations coupled with rare-event methods such as transition path sampling [51] and metadynamics [58] are being used to map out the free energy landscape and to calculate the absolute rates of attachment and detachment from kink sites on inorganic crystal surfaces [45]. These advances can be used to identify the exact rate determining step among the several steps involved in the growth process on inorganic crystal surfaces and to refine the kinetic expressions used in the mechanistic growth models to make them more accurate.

# Bibliography

- [1] W. M. Haynes, editor. *CRC Handbook of Chemistry and Physics*. CRC Press: Boca Raton, FL, 2013.
- [2] J. Burgess. *Metal Ions in Solution*. Ellis Horwood: Chichester, UK, 1986.
- [3] D. R. Rosseinsky. Electrode potentials and hydration energies. theories and correlations. *Chem. Rev.*, 65:467–490, 1965.
- [4] A. J. Gratz, S. Manne, and P. K. Hansma. Atomic force microscopy of atomic-scale ledges and etch pits formed during dissolution of quartz. *Science*, 251:1343–1346, 1991.
- [5] A. Gratz, P. Hillner, and P. Hansma. Step dynamics and spiral growth on calcite. *Geochim. Cosmochim. Acta*, 57:491 – 495, 1993.
- [6] J. J. DeYoreo, T. A. Land, and B. Dair. Growth morphology of vicinal hillocks on the {101} face of  $\text{KH}_2\text{PO}_4$ : From step-flow to layer-by-layer growth. *Phys. Rev. Lett.*, 73:838–841, 1994.
- [7] H. H. Teng, P. M. Dove, C. A. Orme, and J. J. De Yoreo. Thermodynamics of calcite growth: Baseline for understanding biomineral formation. *Science*, 282:724–727, 1998.
- [8] C. M. Pina, U. Becker, P. Risthaus, D. Bosbach, and A. Putnis. Molecular-scale mechanisms of crystal growth in barite. *Nature*, 395:483–486, 1998.
- [9] J. A. Venables. Atomic processes in crystal growth. *Surf. Sci.*, 299/300:798 – 817, 1994.
- [10] P. Hartman. *Crystal Growth: An Introduction*, chapter Structure and Morphology, pages 367–402. Amsterdam: North-Holland, 1973.
- [11] S. C. Parker, J. O. Titiloye, and G. W. Watson. Molecular modelling of carbonate minerals: studies of growth and morphology. *Phil. Trans. R. Soc. A*, 344:37–48, 1993.

- [12] L. J. Soltzberg, O. Carneiro, G. S. Joseph, Z. Khan, T. D. Meretsky, M. M. Ng, and S. A. Ofek. Prediction of Early- and Late-Growth Morphologies of Ionic Crystals. *Acta Crystallogr. B*, 54:384–390, 1998.
- [13] C. Schmidt and J. Ulrich. Crystal habit prediction - including the liquid as well as the solid side. *Cryst. Res. Technol.*, 47:597–602, 2012.
- [14] J. Zhang and G. H. Nancollas. Kink density and rate of step movement during growth and dissolution of an AB crystal in a nonstoichiometric solution. *J. Colloid Interface Sci.*, 200:131 – 145, 1998.
- [15] D. J. DePaolo. Surface kinetic model for isotopic and trace element fractionation during precipitation of calcite from aqueous solutions. *Geochim. Cosmochim. Acta*, 75:1039 – 1056, 2011.
- [16] U. Diebold, S.-C. Li, and M. Schmid. Oxide surface science. *Annu. Rev. Phys. Chem.*, 61:129–148, 2010.
- [17] J. Goniakowski, F. Finocchi, and C. Noguera. Polarity of oxide surfaces and nanostructures. *Rep. Prog. Phys.*, 71:016501, 2008.
- [18] J. Frenkel. On the surface motion of particles in crystals and the natural roughness of crystalline faces. *J. Phys. U.S.S.R.*, 9:392, 1945.
- [19] W. K. Burton, N. Cabrera, and F. C. Frank. The growth of crystals and the equilibrium structure of their surfaces. *Phil. Trans. Roy. Soc. A*, 243:299–358, 1951.
- [20] J. W. Morse, R. S. Arvidson, and A. Lüttge. Calcium carbonate formation and dissolution. *Chem. Rev.*, 107:342–381, 2007.
- [21] K. J. Davis, P. M. Dove, and J. J. De Yoreo. The role of  $Mg^{2+}$  as an impurity in calcite growth. *Science*, 290:1134–1137, 2000.
- [22] G. Fu, S. R. Qiu, C. A. Orme, D. E. Morse, and J. J. De Yoreo. Acceleration of calcite kinetics by abalone nacre proteins. *Adv. Mater.*, 17:2678–2683, 2005.
- [23] S. Elhadj, J. J. De Yoreo, J. R. Hoyer, and P. M. Dove. Role of molecular charge and hydrophilicity in regulating the kinetics of crystal growth. *Proc. Natl. Acad. Sci. U.S.A*, 103:19237–19242, 2006.
- [24] A. E. Stephenson, J. J. DeYoreo, L. Wu, K. J. Wu, J. Hoyer, and P. M. Dove. Peptides enhance magnesium signature in calcite: Insights into origins of vital effects. *Science*, 322:724–727, 2008.

- [25] J. N. Bracco, M. C. Grantham, and A. G. Stack. Calcite Growth Rates As a Function of Aqueous Calcium-to-Carbonate Ratio, Saturation Index, and Inhibitor Concentration: Insight into the Mechanism of Reaction and Poisoning by Strontium. *Cryst. Growth Des.*, 12:3540–3548, 2012.
- [26] M. A. Lovette, A. R. Browning, D. W. Griffin, J. P. Sizemore, R. C. Snyder, and M. F. Doherty. Crystal shape engineering. *Ind. Eng. Chem. Res.*, 47:9812–9833, 2008.
- [27] P. Dandekar, Z. B. Kuvadia, and M. F. Doherty. Engineering crystal morphology. *Annu. Rev. Mater. Res.*, 43:359–386, 2013.
- [28] R. C. Snyder and M. F. Doherty. Predicting crystal growth by spiral motion. *Proc. R. Soc. A*, 465:1145–1171, 2009.
- [29] Z. B. Kuvadia and M. F. Doherty. Spiral growth model for faceted crystals of non-centrosymmetric organic molecules grown from solution. *Cryst. Growth Des.*, 11:2780–2802, 2011.
- [30] J. P. Sizemore and M. F. Doherty. A stochastic model for the critical length of a spiral edge. *J. Cryst. Growth*, 312:785–792, 2010.
- [31] M. Wolthers, D. Di Tommaso, Z. Du, and N. H. de Leeuw. Calcite surface structure and reactivity: Molecular dynamics simulations and macroscopic surface modelling of the calcite-water interface. *Phys. Chem. Chem. Phys.*, 14:15145–15157, 2012.
- [32] J. Zhang and G. H. Nancollas. Kink densities along a crystal surface step at low temperatures and under nonequilibrium conditions. *J. Cryst. Growth*, 106:181–190, 1990.
- [33] I. V. Markov. *Crystal Growth for Beginners, Fundamentals of Nucleation, Crystal Growth and Epitaxy*. World Scientific: Singapore, 2003.
- [34] S. H. Kim, P. Dandekar, M. A. Lovette, and M. F. Doherty. Kink rate model for the general case of organic molecular crystals. *Cryst. Growth Des.*, 14:2460–2467, 2014.
- [35] H. Eyring. The activated complex in chemical reactions. *J. Chem. Phys.*, 3:107–115, 1935.
- [36] A. E. Nielsen. Theory of electrolyte crystal growth: The parabolic rate law. *Pure Appl. Chem.*, 53:2025–2039, 1981.
- [37] J. Mullin. *Crystallization*. Butterworth-Heinemann: Oxford, UK, 2001.
- [38] D. Langmuir. The geochemistry of some carbonate ground waters in central Pennsylvania. *Geochim. Cosmochim. Acta*, 35:1023 – 1045, 1971.

- [39] A. G. Stack and M. C. Grantham. Growth rate of calcite steps as a function of aqueous calcium-to-carbonate ratio: Independent attachment and detachment of calcium and carbonate ions. *Cryst. Growth Des.*, 10:1409–1413, 2010.
- [40] H. H. Teng, P. M. Dove, and J. J. De Yoreo. Kinetics of calcite growth: surface processes and relationships to macroscopic rate laws. *Geochim. Cosmochim. Acta*, 64:2255–2266, 2000.
- [41] A. D. Visscher and J. Vanderdeelen. IUPAC-NIST Solubility Data Series. 95. Alkaline Earth Carbonates in Aqueous Systems. Part 2. Ca. *J. Phys. Chem. Ref. Data*, 41:023105, 2012.
- [42] C. W. Davies. *Ion Association*. Butterworths, 1962.
- [43] S. Kerisit and S. C. Parker. Free energy of adsorption of water and metal ions on the  $\{10\bar{1}4\}$  calcite surface. *J. Am. Chem. Soc.*, 126:10152–10161, 2004.
- [44] V. Vchirawongkwin, C. Kritayakornupong, A. Tongraar, and B. M. Rode. Symmetry breaking and hydration structure of carbonate and nitrate in aqueous solutions: A study by ab initio quantum mechanical charge field molecular dynamics. *J. Phys. Chem. B*, 115:12527–12536, 2011.
- [45] A. G. Stack, P. Raiteri, and J. D. Gale. Accurate rates of the complex mechanisms for growth and dissolution of minerals using a combination of rare-event theories. *J. Am. Chem. Soc.*, 134:11–14, 2012.
- [46] Y. Liang, D. R. Baer, J. M. McCoy, and J. P. LaFemina. Interplay between step velocity and morphology during the dissolution of  $\text{CaCO}_3$  surface. *J. Vac. Sci. Technol. A*, 14:1368–1375, 1996.
- [47] K. Larsen, K. Bechgaard, and S. L. S. Stipp. The effect of the  $\text{Ca}^{2+}$  to  $\text{CO}_3^{2-}$  activity ratio on spiral growth at the calcite  $\{10\bar{1}4\}$  surface. *Geochim. Cosmochim. Acta*, 74:2099–2109, 2010.
- [48] H. Teng, P. M. Dove, and J. J. DeYoreo. Reversed calcite morphologies induced by microscopic growth kinetics: insight into biomineralization. *Geochim. Cosmochim. Acta*, 63:2507–2512, 1999.
- [49] V. V. Voronkov and L. N. Rashkovich. Influence of a mobile adsorbed impurity on the motion of steps. *Sov. Phys. Cryst.*, 37:289–295, 1992.
- [50] K. J. Davis, P. M. Dove, L. E. Wasylenki, and J. J. De Yoreo. Morphological consequences of differential  $\text{Mg}^{2+}$  incorporation at structurally distinct steps on calcite. *Am. Mineral.*, 89:714–720, 2004.

- [51] B. Peters. Recent advances in transition path sampling: accurate reaction coordinates, likelihood maximisation and diffusive barrier-crossing dynamics. *Mol. Simul.*, 36:1265–1281, 2010.
- [52] A. A. Chernov. *Modern Crystallography III. Crystal Growth*. Berlin: Springer-Verlag, 1984.
- [53] D. N. Petsev, K. Chen, O. Gliko, and P. G. Vekilov. Diffusion-limited kinetics of the solution-solid phase transition of molecular substances. *Proc. Natl. Acad. Sci. USA*, 100:792–796, 2003.
- [54] P. G. Vekilov. What determines the rate of growth of crystals from solution? *Cryst. Growth Des.*, 7:2796–2810, 2007.
- [55] V. V. Voronkov. The movement of an elementary step by means of the formation of one-dimensional nuclei. *Sov. Phys. Cryst.*, 15:8–13, 1970.
- [56] M. A. Lovette and M. F. Doherty. Reinterpreting edge energies calculated from crystal growth experiments. *J. Cryst. Growth*, 327:117–126, 2011.
- [57] Large crystal of Icelandic Spar (Calcite) on display at the National Museum of Natural History Washington, DC, 2005.
- [58] A. Laio and M. Parrinello. Escaping free-energy minima. *Proc. Natl. Acad. Sci. U.S.A.*, 99:12562–12566, 2002.

# Chapter 4

## Crystal Growth and Morphology Prediction of Aragonite

### 4.1 Introduction

Calcium carbonate ( $\text{CaCO}_3$ ) occurs in nature in three different anhydrous polymorphic forms - calcite, aragonite and vaterite. Calcite is the thermodynamically stable polymorph at room temperature and pressure. However, aragonite occurs naturally in biological organisms found in marine and freshwater environment, such as mollusk shells. The native crystal habit of aragonite is usually prismatic or acicular [1], but aragonite crystals present in mollusk shells have a tabular habit with hexagonal plate-like shape [2]. Aragonite crystallization has been well studied in the biomineralization literature [3] to understand the biological processes that create plate-like aragonite crystals that constitute a high strength organic-inorganic composite material known as nacre [4].

Calcite is a high-symmetry crystal structure with a single family of F-faces, which made the spiral growth model relatively easy to implement. Applying the model devel-

oped in Chapters 2 and 3 to crystal growth of aragonite would help validate the generality of the mechanistic growth modeling framework that is the centerpiece of this dissertation. A systematic understanding of aragonite crystal growth would also allow the design of aragonite crystals with hexagonal plate-like shape that mimic high strength materials found in nature.

## 4.2 Periodic Bond Chains in Aragonite Crystals

Aragonite crystallizes in an orthorhombic lattice with a Pmcn space group ( $a = 4.9614$  Å,  $b = 7.9671$  Å,  $c = 5.7404$  Å) [5]. Figure 4.1 shows the crystallographic unit cell of aragonite. Four  $\text{CaCO}_3$  molecules lie inside the unit cell ( $Z = 4$ ). The C-O bond lengths for the carbonate group are not all equal; they are 1.278 Å for one oxygen (O1) and 1.284 Å for the remaining two oxygen atoms (O2). Therefore, there are two different oxygen atoms present in the asymmetric unit of aragonite unit cell (Figure 4.1). Similar to calcite crystal structure, each Ca atom in aragonite is surrounded by six carbonate groups and each carbonate group has six neighboring Ca atoms. However, unlike calcite, the surrounding carbonates or calcium atoms are not at the same distance.

Figure 4.2 shows the packing of the aragonite lattice with building units. The stoichiometry and zero dipole moment properties were considered to identify the building units of periodic bond chains within the aragonite unit cell. Two types of building units with the same stoichiometry ( $\text{Ca}_2\text{C}_2\text{O}_6$ ) were identified within the unit cell and are represented by cyan and black ellipses in Figure 4.2. The centroids of the black building

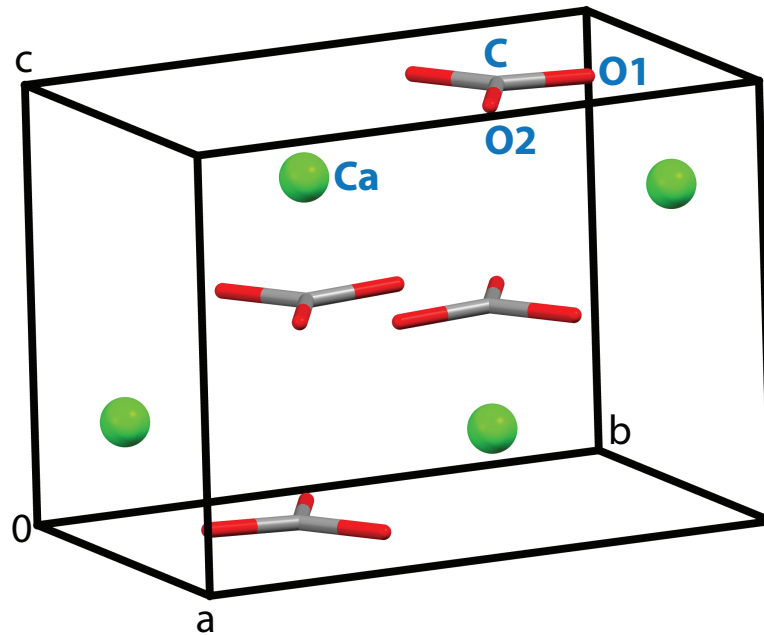


**Figure 4.1:** Aragonite unit cell with the Ca atoms (green sphere) and  $\text{CO}_3$  groups (grey and red capped sticks). The contents of the asymmetric unit of the unit cell are labeled in blue.

units are located at fractional coordinates  $(0.5, 0.5, 0)$  and  $(0.5, 0.5, 1)$  while the centroids of the cyan building units are located at  $(0, 0, 0.5)$ ,  $(1, 0, 0.5)$ ,  $(0, 1, 0.5)$  and  $(1, 1, 0.5)$ . The cyan and black building units are related to each other by a diagonal glide plane perpendicular to the  $[001]$  direction at  $z = 0.25$ , with the translational component equal to  $\frac{1}{2}(\vec{a} + \vec{b})$ . This diagonal glide plane is a part of the list of symmetry operators present for the Pmcn space group. Therefore, there is a single symmetrically-independent building unit in aragonite crystal.

Lattice translational operators were applied to the centroids of the building units to identify continuous chains of building units along the  $[100]$ ,  $[010]$ ,  $[001]$ ,  $[11\bar{1}]$ ,  $[1\bar{1}1]$ ,  $[\bar{1}11]$ ,  $[111]$ ,  $[110]$  and  $[\bar{1}10]$  directions. The reflection/extinction conditions for the Pmcn space

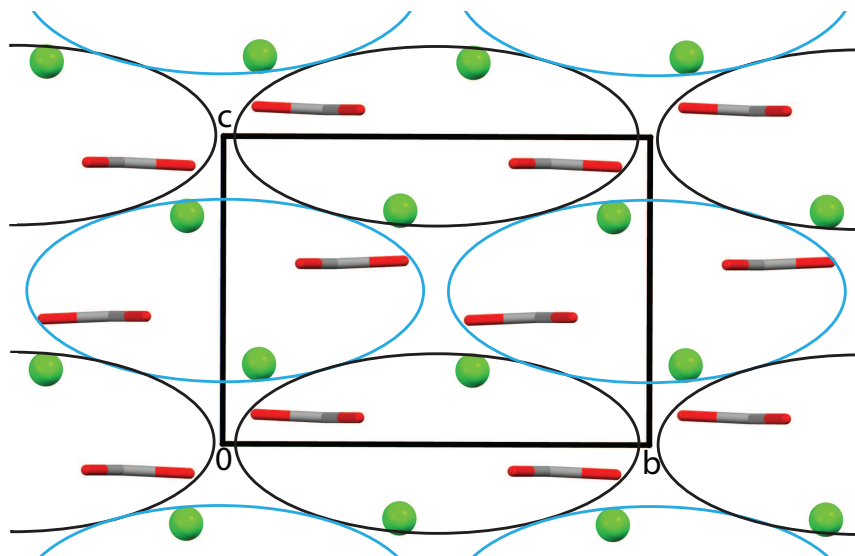


**Figure 4.2:** A view of the crystal packing in aragonite along the  $[100]$  direction with building units enclosed within cyan and black ellipses. Each building unit consists of two Ca and two  $\text{CO}_3$  groups.

group allow the reflections of the following faces to be present on the crystal surface -  $(110)$ ,  $(020)$ ,  $(011)$  and  $(002)$ . On each of these crystal faces, periodic bond chains that lie within a slice of thickness  $d_{hkl}$  must be identified from chains of building units.

On the  $(020)$  aragonite crystal face ( $d_{020} = 3.988 \text{ \AA}$ ), there are two continuous chains of building units along  $[100]$  and  $[001]$  directions that satisfy the stoichiometry and dipole moment properties for periodic bond chains in inorganic crystals. However, these chains of building units are not contained within the thickness of the  $(020)$  slice. As Figure 4.3 shows, the  $(020)$  slice contains only half of the cyan and half of the black building units.

The contents of the building units that lie within the  $(020)$  slice create a continuous chain of growth units along the  $[001]$  direction as shown in Figure 4.4a, but the chain

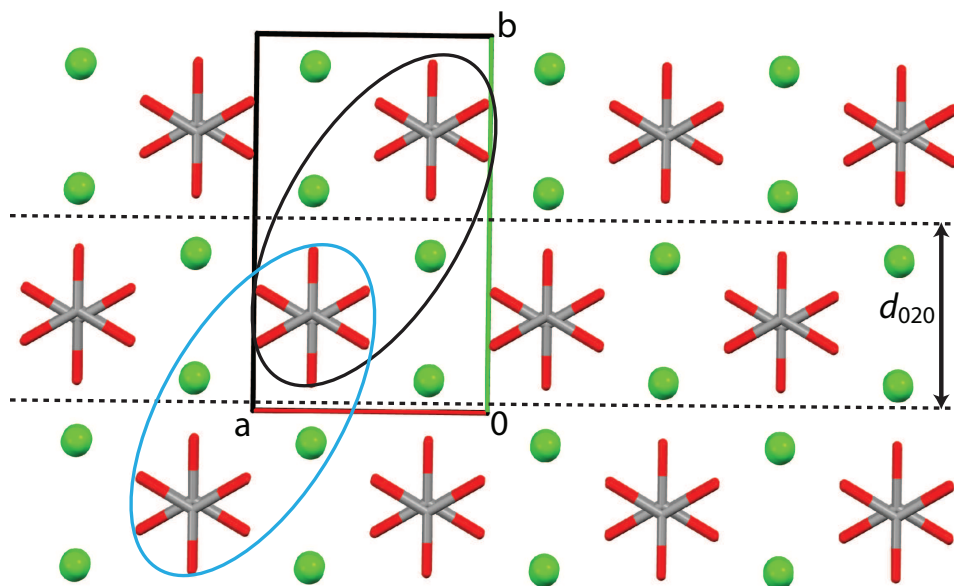


**Figure 4.3:** A view of the crystal packing in aragonite along the  $[001]$  direction with the boundaries of a  $(020)$  slice shown with broken black lines. The blue and black ellipses represent the contents of the two types of building units.

of growth units in the  $[100]$  direction shares half of its interactions with the  $[001]$  PBC, and is no longer continuous. If the arrangement of the growth units along  $[201]$  and  $[\bar{2}01]$  directions were considered (Figure 4.4b), the step edges or chains of growth units formed along these two directions are continuous, and they satisfy the stoichiometry and dipole moment properties as well. Therefore,  $[201]$  and  $[\bar{2}01]$  were chosen as the periodic bond chains in the  $(020)$  face of aragonite crystals.

The  $(110)$  crystal face ( $d_{110} = 4.213 \text{ \AA}$ ) contains  $[001]$ ,  $[\bar{1}10]$ ,  $[1\bar{1}1]$  and  $[\bar{1}\bar{1}1]$  chains of building units within the thickness of a single slice (Figure 4.5a). Similar to the aforementioned case of the  $[100]$  PBC in  $(020)$  face, growth units in the  $(110)$  face do form continuous chains along the  $[001]$  direction, but the chain in the  $[\bar{1}10]$  direction is not continuous. However, the arrangement of growth units along  $[\bar{1}\bar{1}1]$  and  $[1\bar{1}1]$  do

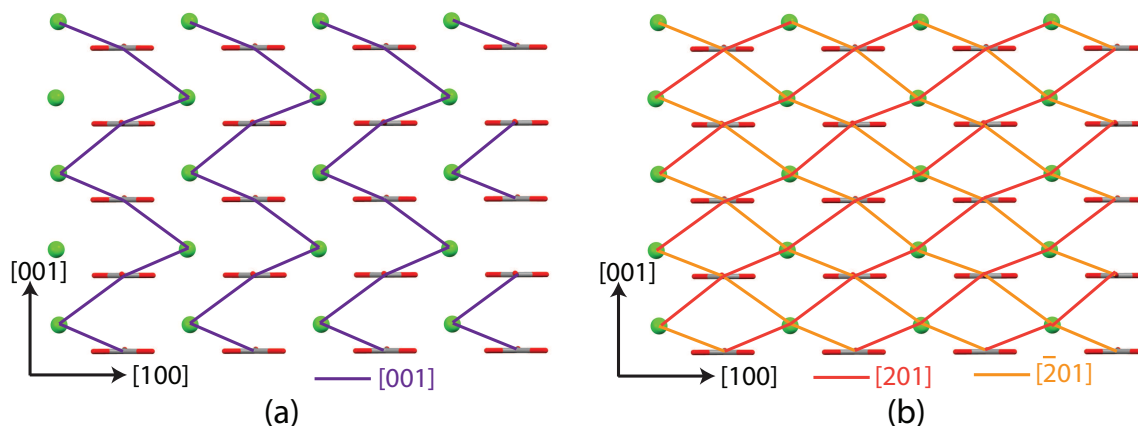


**Figure 4.4:** A plan view of the (020) slice of aragonite crystal. (a) shows the periodic bond chains along the [001] direction (purple). (b) shows the periodic bond chains along [201] (red) and  $[\bar{2}01]$  (mustard) directions.

form a pair of continuous periodic bond chains that satisfy the stoichiometry and dipole moment properties as well (Figure 4.5b). Therefore,  $[\bar{1}11]$  and  $[1\bar{1}1]$  were chosen as the PBCs present in the (110) face of aragonite crystals.

The PBCs on the (002) and (011) faces are also identified in a similar manner. The (002) face has two PBCs along  $[\bar{1}10]$  and  $[310]$  directions, while the (011) face has two PBCs along the  $[11\bar{1}]$  and  $[3\bar{1}1]$  directions (Figure 4.6).

Hartman, in his doctoral dissertation [6], proposed that periodic bond chains in a crystal be identified under the constraint that two periodic bond chains must never share any intermolecular interactions. However, there are some instances found in his dissertation where two or more PBCs shared the same intermolecular interaction in inorganic crystals such as barite and aragonite [6]. Hartman also proposed that a periodic bond chain must not consist of periods of other chains [6]. The period of a PBC is defined as the structural (or energetic) fundamental unit of the bond chain, such that the entire

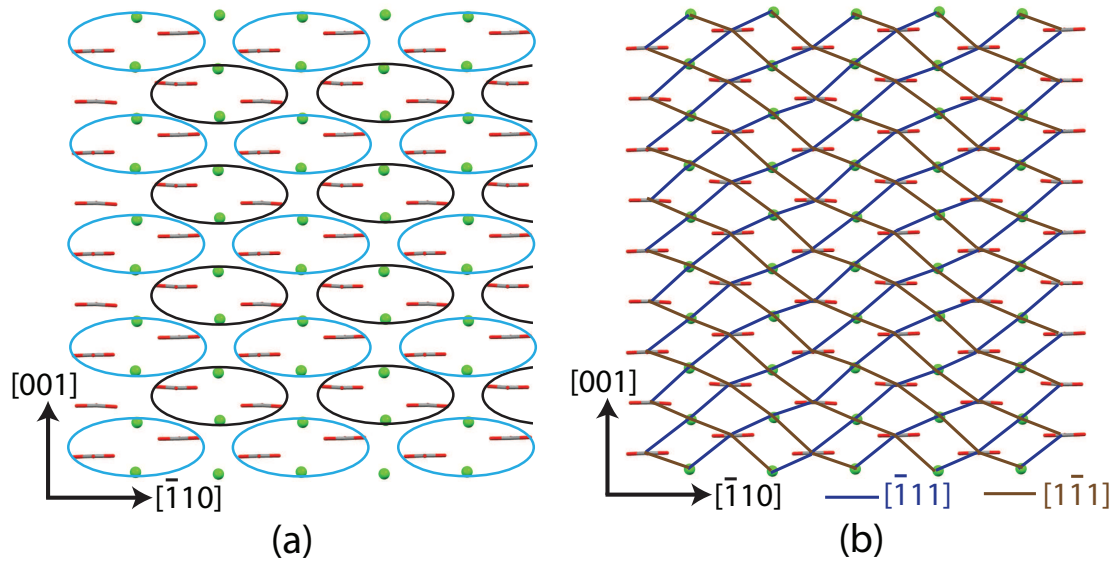


**Figure 4.5:** A plan view of the (110) slice of aragonite crystal. (a) shows the arrangement of the building units (black and cyan ellipses). (b) shows the periodic bond chains along the  $[\bar{1}11]$  (blue) and  $[1\bar{1}1]$  (brown) directions.

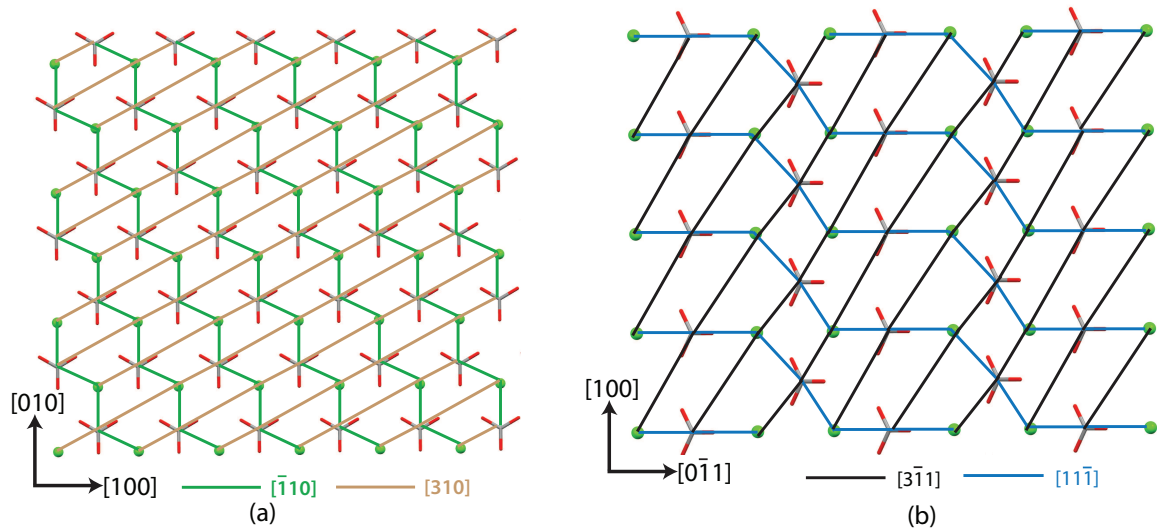


**Figure 4.6:** Plan views of the (a) (002) and (b) (011) slice of aragonite crystals.

chain is obtained by translation along the PBC vector of the atomic arrangement within the period. In this dissertation, the interpretation of the two aforementioned properties of PBCs is that two periodic bond chains that do not lie within the same F-face of a

crystal, may share intermolecular interactions if the shared interactions do not form the entire period of either PBCs. If two PBCs in the same crystal face were to share an interaction, the two growth units that interact via the particular intermolecular interaction will be shared between two spiral edges on the crystal surface. As a result, one of the edges may not grow, depending on the strength of the remaining intermolecular interactions along the periods of the two edges. The edge with the higher strength of the remaining interactions will grow preferentially, and the crystal face could behave as an S-face.

In aragonite crystals, the chains of building units along the  $\langle 111 \rangle$  family of directions do not share any interactions, but the step edges formed along these directions do share some interactions. Figure 4.7a shows a view of aragonite crystal along the  $[001]$  direction with only the slices of  $(110)$  and  $(\bar{1}10)$  faces visible. The  $(110)$  crystal face contains  $[\bar{1}11]$  and  $[1\bar{1}1]$  PBCs while the  $(\bar{1}10)$  face contains  $[11\bar{1}]$  and  $[111]$  PBCs. Figure 4.7b shows twice the length of the period of these four PBC directions passing through a common  $\text{Ca}^{2+}$  ion. The  $\text{Ca}^{2+}-\text{CO}_3^{2-}$  interactions shared between the  $[\bar{1}11]$  &  $[111]$  edges, and between the  $[\bar{1}11]$  &  $[\bar{1}11]$  edges are highlighted. There are no interactions shared between the step edges that are present either on the  $(110)$  or the  $(\bar{1}10)$  faces.

The partial charges and Buckingham potential parameters for bulk aragonite crystal were obtained from the force field reported by Raiteri et al. [7]. The original force field was optimized for all crystalline phases of calcium carbonate [7], and the same potential parameters were used to model calcite growth in Chapters 2 and 3. The force field

parameters accurately reproduced the crystal structure of calcite, with about 1.5% error in the prediction of aragonite lattice parameters [7]. Specifically, the force field does not account for the asymmetry of the carbonate group and the presence of two types of O atoms (O1 and O2, Figure 4.1) in the crystal structure. Therefore, the partial charge of the oxygen atoms in aragonite were recalculated using the bond valence model. The normalized values of the bond valences between Ca-O and C-O atom pairs were calculated from the partial charges of Ca (+2.0) and C (+1.123) atoms as reported by Raiteri et al. [7]. The summation of the bond valences around O1 and O2 atoms in bulk aragonite provided the values of their partial charges as -0.980 and -1.071, respectively. These values were used for the partial charges of O1 and O2 oxygen atoms in this chapter.

The lattice energy of aragonite was calculated by building a supercell of size  $60 \times 60 \times 60$  along the three lattice directions and performing a Madelung-type summation of the long-range electrostatic interactions. A 10 Å cutoff was applied for the short-range interactions. The calculated value of aragonite lattice energy is -644.0 kcal/mol which matches well with the reported value of -651.4 kcal/mol calculated using the Born-Fajans-Haber thermodynamic cycle [8]. Table 4.1 shows the values of the attachment energy  $E^{att}$  for the four F-faces on aragonite crystal surface.

The long-range interaction energies of growth units along a PBC direction ( $E_{PBC}$ ) were calculated for each PBC that lies within an F-face on aragonite crystal surface. These interaction energies were calculated with bulk partial charges for each atom present along the periodic bond chain. Table 4.1 shows the  $E_{PBC}$  values for the periodic bond

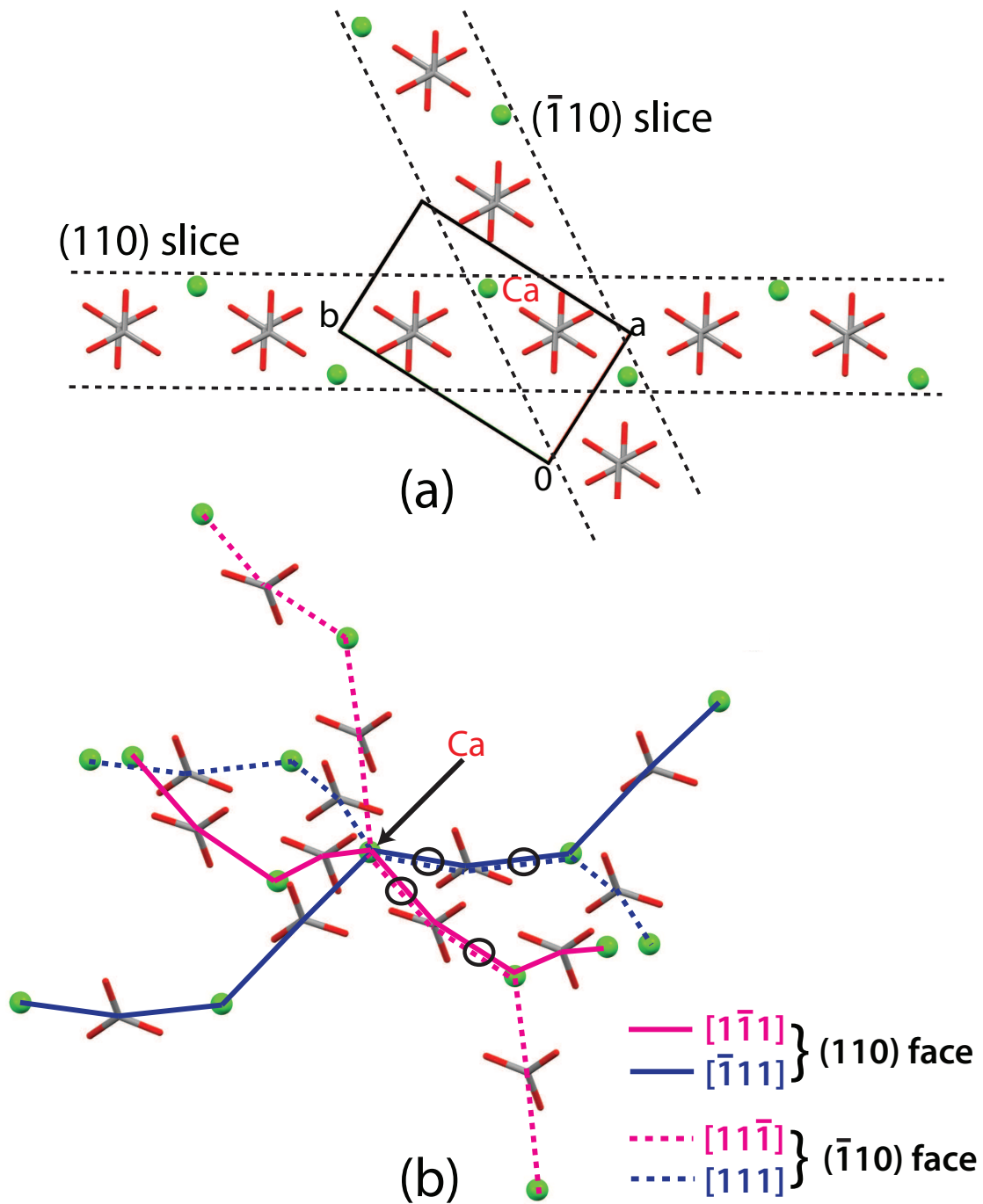


**Figure 4.7:** (a) View along the  $[001]$  direction of  $(110)$  and  $(\bar{1}10)$  slices of aragonite crystals. (b) Step edges along the  $\langle 111 \rangle$  family of PBCs passing through the Ca atom labeled in red. The shared intermolecular interactions are highlighted using black circles.

**Table 4.1:**  $E^{att}$  and  $E_{PBC}$  values for the F-faces on aragonite crystal surface

Crystal Face	$E^{att}$ (kcal/mol)	PBC vectors	$E_{PBC}$ (kcal/mol)
(110)	-47.6	$[\bar{1}11]$	-139.2
		$[1\bar{1}1]$	-139.2
(020)	-48.5	$[\bar{2}01]$	-138.7
		$[201]$	-138.7
(011)	-62.8	$[11\bar{1}]$	-139.2
		$[3\bar{1}1]$	-99.4
(002)	-51.6	$[\bar{1}10]$	-141.2
		$[310]$	-113.5

chains present within the four F-faces. The PBCs within the (020) face -  $[201]$  &  $[\bar{2}01]$ , and the (110) face -  $[\bar{1}11]$  &  $[1\bar{1}1]$ , are symmetric and have the same values of  $E_{PBC}$ . Therefore, only one spiral edge from each of these two faces will be considered for the spiral growth calculations in the subsequent sections. The magnitudes of both the  $E^{att}$  and the  $E_{PBC}$  for the edges present within a face suggest that the (110) and (020) faces may be more prominent on the aragonite crystal morphology than the (011) and (002) faces because the PBCs with stronger intermolecular interactions are present in the former pair of F-faces.

### 4.3 Step Velocity of Edges with Multiple Structures

The calculation of kink incorporation rate and step velocity of spiral edges has been discussed previously in Section 3.4. However, this framework assumed that there is a single step edge structure for each spiral edge. Figure 4.8 shows two different views of aragonite crystal packing along the  $[\bar{1}11]$  and the  $[\bar{3}\bar{1}0]$  directions. There are two types of

structures for the  $[\bar{1}11]$  spiral edge that lies within the (110) slice. The arrangement of growth units along the  $[\bar{1}11]$  edge is similar for the two structures (Figure 4.8b) except for the inversion of the carbonate group orientation.

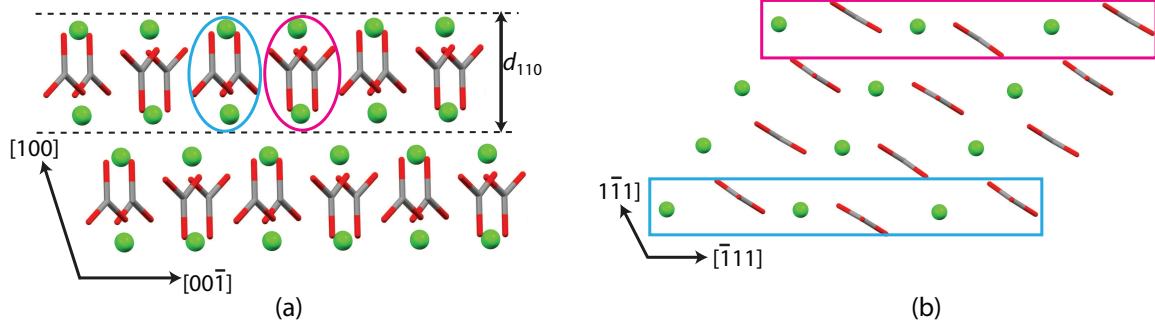


**Figure 4.8:** View of aragonite crystal packing along (a)  $[\bar{1}11]$  and (b)  $[\bar{3}\bar{1}0]$  lattice directions highlighting the two different structures (cyan and magenta) of the  $[\bar{1}11]$  PBC edge.

A spiral edge that consists of multiple edge structures growing at different step velocities will affect the rotation time of the growth spiral. The rotation time of a growth spiral depends on the time it takes for each spiral edge  $i + 1$  to reach its critical length  $l_{i+1,c}$ . Edge  $i + 1$  increases in length due to its tangential step velocity,  $\mathbf{v}_{i+1}^t$  (see Figure 4.9). If  $t'_i$  is the time required by edge  $i$  to advance in its normal direction by a distance  $a_{p,i}$ , in this same period of time the edge  $i + 1$  will increase in length by  $a_{e,i+1}$  due to its tangential velocity  $\mathbf{v}_{i+1}^t$ . A relationship between  $\mathbf{v}_{i+1}^t$  and the normal step velocity  $\mathbf{v}_i$  is obtained as follows

$$t'_i = \frac{a_{p,i}}{\mathbf{v}_i} = \frac{a_{e,i+1}}{\mathbf{v}_{i+1}^t} \quad (4.1)$$

$$\mathbf{v}_{i+1}^t = \mathbf{v}_i \left( \frac{a_{e,i+1}}{a_{p,i}} \right) = \frac{\mathbf{v}_i}{\sin(\alpha_{i,i+1})} \quad (4.2)$$

where  $\alpha_{i,i+1}$  is the angle between edges  $i$  and  $i + 1$ . The time required for edge  $i + 1$  to reach its critical length is given by  $l_{i+1,c}/v_{i+1}^t$ . The rotation time,  $\tau_s$ , of a growth spiral with  $N$  edges is equal to the total time required for all the spiral edges to achieve their critical lengths as follows [9]

$$\tau_s = \sum_{i=1}^N \frac{l_{i+1,c} \sin(\alpha_{i,i+1})}{v_i} \quad (4.3)$$

Figure 4.9 shows a hypothetical crystal surface with two types of edge structures along edge 1 that grows with a normal step velocity  $v_1$ . The second edge growing with step velocity  $v_2$  has a single edge structure with two types of growth units along the edge (red and green). It is assumed that the distance between the growth units along the edge ( $a_{e,1}$ ) is the same for both edge structures ( $I$  and  $II$ ) along edge 1. Similarly, the distance of propagation ( $a_{p,1}$ ) is assumed to be the same for both the edge structures.

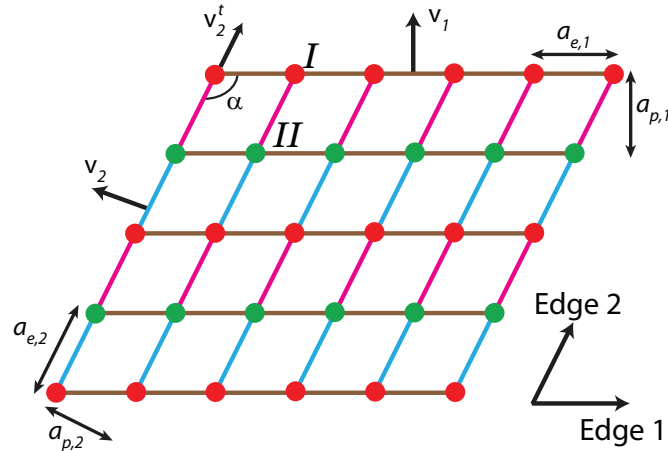


**Figure 4.9:** Plan view of a hypothetical crystal face with two types for edge 1. The growth units along the two types of edge structures are represented by red ( $I$ ) and green ( $II$ ) circles.

Let  $t'_I$  and  $t'_{II}$  be the time required for the red and green growth units along edge 1 to advance by a distance  $a_{p,1}$ . In time  $t'_I + t'_{II}$ , the length of edge 2 increases by a distance  $2a_{e,2}$  due to the tangential velocity of edge 2. As a result, the following equations can be written

$$t'_I = \frac{a_{p,1}}{v_{1,I}} \quad (4.4)$$

$$t'_{II} = \frac{a_{p,1}}{v_{1,II}} \quad (4.5)$$

$$t'_I + t'_{II} = \frac{2a_{e,2}}{v_2^t} = a_{p,1} \left( \frac{1}{v_{1,I}} + \frac{1}{v_{1,II}} \right) \quad (4.6)$$

The relationship between the tangential velocity of edge 2 and the normal step velocities of both edge 1 structures are obtained as follows

$$\frac{2}{v_2^t} = \left( \frac{a_{p,1}}{a_{e,2}} \right) \left( \frac{1}{v_{1,I}} + \frac{1}{v_{1,II}} \right) \quad (4.7)$$

$$\therefore v_2^t = \frac{v_1^{HM}}{\sin \alpha} \quad (4.8)$$

where  $v_1^{HM}$  is the harmonic mean (normal) step velocity for the two types of edge 1 structures, given by

$$v_1^{HM} = \frac{2v_{1,I}v_{1,II}}{v_{1,I} + v_{1,II}} \quad (4.9)$$

Therefore, the time required for edge 2 to reach its critical length is given by  $l_{2,c}/v_2^t = l_{2,c} \sin \alpha / v_1^{HM}$ . This expression is substituted into the expression for the spiral rotation time to calculate  $\tau_s$  and therefore the growth rate of the crystal face. Thus, if multiple types of edge structures are present for a spiral edge, the overall (normal) step velocity for that edge must be calculated as the harmonic mean of the individual step velocities

of each type of edge structure. The overall step velocity of the  $[\bar{1}11]$  spiral edge on the (110) aragonite crystal face can therefore be calculated as the harmonic mean of the step velocities of the two edge structures (cyan and magenta in Figure 4.8).

From equation 4.9, a connection may be made with the concept of stable and unstable edges proposed by Kuvadia and Doherty for modeling growth of noncentrosymmetric molecular crystals [10]. An unstable edge was defined as an edge with a negative work for edge rearrangement. This results in an unusually high density of kink sites along the edge. Therefore, an unstable edge grows with a much larger step velocity than a stable edge. In the limiting case where  $v_{1,II} \gg v_{1,I}$ , the harmonic mean step velocity becomes  $v_1^{HM} \approx 2v_{1,I}$ . Therefore, the time required for edge 2 to reach its critical length is equal to  $l_{2,c} \sin \alpha / 2v_{1,I}$ . This is exactly equal to the time required for edge 2 to reach a length  $l_{2,c}/2$  if edge 1 consisted of only the structure  $I$ . It takes effectively zero time for edge 2 to attain the remaining  $l_{2,c}/2$  length due to the large value of the normal step velocity of the structure  $II$  of edge 1.

In the limit of large kink densities ( $\rho \sim 0.1$ ), every thermal disturbance may not create a kink site. A multi-site model is required to account for the density of various intermediate sites created along an edge as a result of thermal disturbances [11]. A comprehensive framework needs to be developed that incorporates a multi-site kink density model for unstable edges that expose a large number of kink sites on any crystal surfaces.

## 4.4 Space Partitioning in Aragonite Crystals

The step velocity of a spiral edge on an inorganic crystal depends on the work required to remove a kink site growth unit [10, 12]. The interaction energy between a kink site growth unit and its neighbors (in both solid-state and solution) determines the kink detachment work,  $\Delta W$ . The calculation of the potential energy of kink site growth units was carried out using the space partitioning method (see Section 2.4.1). The long-range electrostatic interactions and the variation in the partial charges in various surface coordinations is accurately captured by dividing up the three-dimensional space into partitions within which all the chemically identical growth units have the same partial charges.

The space partitioning method requires that a growth unit must always belong to only one partition of space. As discussed in Section 4.2, some periodic bond chains in aragonite crystals share certain intermolecular interactions. If an intermolecular interaction was shared between two of the three cardinal directions, both the growth units between which that particular interaction exists, will belong to more than one partitions of space. Therefore, for crystals such as aragonite, the PBC directions that share interactions cannot both be cardinal directions.

The (110) face of aragonite crystals contains two PBCs -  $[\bar{1}11]$  and  $[1\bar{1}1]$ , while the  $(\bar{1}10)$  face contains PBCs along the  $[111]$  and  $[11\bar{1}]$  directions. The  $[\bar{1}11]$  and  $[111]$  PBC directions share two intermolecular interactions (see Figure 4.7). If, for example,  $[\bar{1}11]$ ,  $[1\bar{1}1]$  and  $[111]$  were chosen as the cardinal directions, the space partitioning for the

**Table 4.2:** The cardinal directions used for space partitioning on aragonite crystal faces

Crystal Face	Cardinal Directions	
	In plane	Out of plane
(110)	$[\bar{1}11], [1\bar{1}1]$	$[0\ 1\ 0]$
(020)	$[\bar{2}01], [201]$	$[0\ 0.5\ 0]$
(011)	$[11\bar{1}], [3\bar{1}1]$	$[0\ 0\ 0.5]$
(002)	$[\bar{1}10], [310]$	$[0\ 0\ 0.5]$

(110) aragonite crystal face will become unworkable. One of the spiral edges, namely  $[\bar{1}11]$ , on the (110) face shares interactions with the out-of-plane cardinal direction,  $[111]$ . Therefore, a growth unit that lies in the 1D partition (or axis) along the  $[\bar{1}11]$  spiral edge must also lie in a partition whose growth units have bulk character. But the atoms within such a growth unit cannot be assigned two different values of partial charges at the same time. Similar problems arise from the choice of  $[111]$ ,  $[11\bar{1}]$  and  $[\bar{1}11]$  as the cardinal directions for the space partitioning of the  $(\bar{1}10)$  face.

A common choice of the three cardinal directions for all faces of aragonite crystals will surrender the benefits of using space partitioning to calculate the potential energy of kink site growth units. If the three cardinal directions are chosen separately for every crystal face, the choice of the out-of-plane cardinal direction ( $Z$  in Section 2.4.1) can be made such that no intermolecular interactions are shared with the other two cardinal directions for that particular crystal face.

Table 4.2 shows the list of the three cardinal directions for the four faces on aragonite crystals. The first two cardinal directions for each crystal face lie within the plane, while the third vector is the out-of-plane cardinal direction.

If the cardinal directions are chosen separately for every crystal face, there is no requirement for the out-of-plane cardinal direction to satisfy the stoichiometry and dipole moment properties of PBCs. The chain of bonds (or intermolecular interactions) between the growth units along this direction must be continuous, but this chain need not be a periodic bond chain. However, the two cardinal directions that lie within the crystal face must be parallel to PBC directions and those chains must satisfy the stoichiometry, the dipole moment, and the “no common bond” properties. In Table 4.2, only the  $[0\ 0.5\ 0]$  cardinal direction for the (020) face forms a stoichiometric chain with zero dipole moment perpendicular to the chain direction. The other three out-of-plane cardinal directions listed in Table 4.2 are not stoichiometric.

The solvent structure information for aragonite crystal growth from aqueous solution is not readily available in the literature. Ruiz-Hernandez et al. [13] performed molecular dynamics simulation to quantify the incorporation of  $\text{Mg}^{2+}$  ions on aragonite crystal surfaces. However, they report the radial distribution function of water molecules around only  $\text{Mg}^{2+}$  ions incorporated within the crystal surface. Since the values of the distances between surface  $\text{Ca}^{2+}$  and  $\text{CO}_3^{2-}$  ions and the neighboring water molecules could not be obtained for aragonite crystal surfaces, solvent structure data from crystal growth of calcite was used. The solvation structure of the  $\text{Ca}^{2+}$  and  $\text{CO}_3^{2-}$  ions in bulk water must be exactly the same for both aragonite and calcite crystal growth. The average distance between the aragonite surface growth units and nearest neighbor water molecules, i.e., an average of  $\text{Ca-O}(\text{water})$  and  $\text{O}(\text{carbonate})\text{-H}(\text{water})$  distances, was estimated from

calcite molecular simulations [14] as 2.435 Å. Since the values of these distances are not available for every aragonite edge and kink site, those distances were assumed to be all equal to 2.435 Å.

The coordination of a  $\text{Ca}^{2+}$  ion or a carbonate O atom with its solid-state neighbors decreases as the respective ions go from bulk crystalline sites to surface, edge or kink sites. This change in the solid-state coordination was assumed to have a 1:1 correlation with the number of solvent molecules that surround the ions in the surface layer, which is consistent with molecular simulation data for some other inorganic crystals such as calcite [14], barite [15], etc. Therefore, a  $\text{Ca}^{2+}$  site would coordinate with one additional water molecule for the loss of every neighboring carbonate oxygen atom, and so on. The partial charges of the calcium and carbonate ions in various surface sites were calculated using the bond valence model [16, 17], while also accounting for the presence of the water molecules surrounding the ions.

The potential energies of the growth units were calculated in kink site and step positions for each spiral edge on the four crystal faces of aragonite crystals. The work done for kink detachment,  $\Delta W$ , was calculated from the potential energy and solvation energy values using equation 3.26. Table 4.3 shows the  $\Delta W$  values calculated for the spiral edges on aragonite crystal surfaces. Each spiral edge contains four growth units in series - two  $\text{Ca}^{2+}$  and two  $\text{CO}_3^{2-}$ . The average  $\Delta W$  for each spiral edge is also listed in Table 4.3.

**Table 4.3:**  $\Delta W$  values (in kcal/mol) for the 112 types of kink sites on the spiral edges of aragonite crystal surfaces

(011) face		Ca (1)	CO <sub>3</sub> (2)	Ca (3)	CO <sub>3</sub> (4)	Avg
[11 $\bar{1}$ ] growing in [3 $\bar{1}$ 1]	$\mathcal{W}$	201.5	172.7	31.3	71.7	119.3
	$\mathcal{E}$	161.2	112.2	68.0	153.3	123.7
[11 $\bar{1}$ ] growing in [ $\bar{3}$ 1 $\bar{1}$ ]	$\mathcal{W}$	192.9	77.8	127.8	119.8	129.6
	$\mathcal{E}$	160.2	151.7	147.4	25.5	121.2
[3 $\bar{1}$ 1] growing in [11 $\bar{1}$ ]	$\mathcal{W}$	232.8	103.7	91.2	64.8	123.1
	$\mathcal{E}$	305.6	107.6	34.0	14.5	115.4
[3 $\bar{1}$ 1] growing in [ $\bar{1}$ 1 $\bar{1}$ ]	$\mathcal{W}$	188.3	93.8	93.7	58.0	108.4
	$\mathcal{E}$	47.5	81.1	218.2	100.8	111.9
(002) face		Ca (1)	CO <sub>3</sub> (2)	Ca (3)	CO <sub>3</sub> (4)	Avg
[ $\bar{1}$ 10] growing in [310]	$\mathcal{W}$	174.0	165.2	72.5	30.9	110.6
	$\mathcal{E}$	160.9	158.1	81.0	67.6	116.9
[ $\bar{1}$ 10] growing in [ $\bar{3}$ 10]	$\mathcal{W}$	141.8	127.2	96.6	79.8	111.3
	$\mathcal{E}$	130.5	163.0	64.4	66.2	106.0
[310] growing in [ $\bar{1}$ 10]	$\mathcal{W}$	104.4	107.5	129.4	54.2	98.9
	$\mathcal{E}$	26.4	171.8	52.8	125.0	94.0
[310] growing in [1 $\bar{1}$ 0]	$\mathcal{W}$	43.4	257.9	38.1	55.4	98.7
	$\mathcal{E}$	171.5	64.0	95.8	46.5	94.4
(110) face		Ca (1)	CO <sub>3</sub> (2)	Ca (3)	CO <sub>3</sub> (4)	Avg
[ $\bar{1}$ 11] magenta growing in [1 $\bar{1}$ 1]	$\mathcal{W}$	295.7	57.8	328.2	47.5	182.3
	$\mathcal{E}$	362.4	34.1	439.8	24.9	215.3
[ $\bar{1}$ 11] magenta growing in [ $\bar{1}$ 1 $\bar{1}$ ]	$\mathcal{W}$	312.6	194.8	488.2	104.1	274.9
	$\mathcal{E}$	251.6	95.8	508.5	118.1	243.5
[ $\bar{1}$ 11] cyan growing in [1 $\bar{1}$ 1]	$\mathcal{W}$	251.6	68.4	355.7	32.9	177.1
	$\mathcal{E}$	338.1	145.5	279.7	54.4	204.4
[ $\bar{1}$ 11] cyan growing in [ $\bar{1}$ 1 $\bar{1}$ ]	$\mathcal{W}$	294.4	157.3	439.5	168.4	264.9
	$\mathcal{E}$	207.2	77.7	505.6	168.7	239.8
(020) face		Ca (1)	CO <sub>3</sub> (2)	Ca (3)	CO <sub>3</sub> (4)	Avg
[ $\bar{2}$ 01] growing in [201]	$\mathcal{W}$	57.7	61.7	98.0	36.1	63.4
	$\mathcal{E}$	81.3	28.6	84.7	86.1	70.2
[ $\bar{2}$ 01] growing in [ $\bar{2}$ 0 $\bar{1}$ ]	$\mathcal{W}$	53.4	84.6	113.4	137.4	97.2
	$\mathcal{E}$	59.4	122.1	52.2	149.9	95.9

The  $\Delta W$  values for the kink sites along the two edge structures of  $[\bar{1}11]$  spiral edge (cyan and magenta, Fig 4.8) on the (110) face are not equal for any of the four growth units. Therefore, the two edge structures will have different values of the kink incorporation rate. The effective step velocity of the  $[\bar{1}11]$  edge is calculated using the harmonic mean expression from equation 4.9. It must be noted that the kink density of the  $[\bar{1}11]$  edge is calculated for both the edge structures together. Since the kink sites are formed due to thermal rearrangement of a straight edge, the equilibrium structure of the edge will be independent of the initial configuration of the straight edge. The equilibrium structure of an edge is determined by free energy minimization alone and could expose kink sites from both type of edge structures. Therefore, there is a single value of the kink density on the  $[\bar{1}11]$  edge, which is calculated from the Boltzmann distribution of all the microstates that expose kink sites belonging to the two types of edge structures (cyan and magenta).

## 4.5 Spiral Growth Calculations

Crystal growth of aragonite grown from aqueous solution is studied using the spiral growth model discussed in Chapters 2 and 3. The quantities required to predict the relative growth rates and the steady-state morphology of aragonite crystals include the density of kink sites along the spiral edges ( $\rho$ ), the kink incorporation rate ( $u$ ), and the critical length of each spiral edge ( $l_c$ ). The details of the spiral growth calculations can be found in Sections 3.3, 3.4, 3.6 and 4.3.

**Table 4.4:** Results of spiral growth calculations on the edges of aragonite crystal surfaces at  $S = 1.2$ ,  $r = 1.0$

(011) face	$l_c$ (nm)	$\rho$	$u$	$v$	$R$
$[11\bar{1}]$ growing in $[3\bar{1}1]$	162.2	2.5E-9	8.4E-140	9.3E-149	1.0E+176
$[11\bar{1}]$ growing in $[\bar{3}1\bar{1}]$	166.7	1.3E-4	3.1E-141	1.8E-145	
$[3\bar{1}1]$ growing in $[11\bar{1}]$	162.2	0.0423	2.6E-170	3.1E-172	
$[3\bar{1}1]$ growing in $[\bar{1}\bar{1}1]$	165.4	3.07E-13	6.9E-138	5.8E-151	
(002) face	$l_c$ (nm)	$\rho$	$u$	$v$	$R$
$[\bar{1}10]$ growing in $[310]$	183.4	0.0049	5.1E-148	1.1E-150	4.1E+197
$[\bar{1}10]$ growing in $[\bar{3}\bar{1}0]$	179.5	6.38E-5	1.2E-115	3.3E-120	
$[310]$ growing in $[\bar{1}10]$	178.3	0.0028	1.9E-105	1.3E-108	
$[310]$ growing in $[1\bar{1}0]$	183.4	0.0284	1.2E-125	8.1E-128	
(110) face	$l_c$ (nm)	$\rho$	$u$	$v$	$R$
$[\bar{1}11]$ magenta growing in $[1\bar{1}\bar{1}]$	150.6	0.0681	8.3E-240	2.8E-241	1.0
$[\bar{1}11]$ cyan growing in $[1\bar{1}\bar{1}]$			5.5E-193		
$[\bar{1}11]$ magenta growing in $[\bar{1}\bar{1}\bar{1}]$	149.4	8.5E-6	1.6E-340	2.7E-348	
$[\bar{1}11]$ cyan growing in $[\bar{1}\bar{1}\bar{1}]$			6.4E-343		
(020) face	$l_c$ (nm)	$\rho$	$u$	$v$	$R$
$[\bar{2}01]$ growing in $[201]$	139.7	0.0257	4.0E-172	2.6E-174	1.0E+174
$[\bar{2}01]$ growing in $[\bar{2}0\bar{1}]$	135.9	3.75E-5	6.6E-110	6.2E-115	

The model calculations were carried out at a supersaturation of  $S = 1.2$  with spiral growth as the dominant growth mechanism, as is the case for crystal growth of calcite [18]. The ionic activity ratio  $r = a_{Ca}/a_{CO_3}$  was assumed to be 1.0. The solution temperature was assumed to be 25 °C with the assumption that no foreign species were present in the solution. Table 4.4 shows the results of the spiral growth calculations performed on the (110), (020), (011) and (002) faces of aragonite crystals.  $R$  in Table 4.4 is defined as the perpendicular growth rate of a crystal face relative to a reference face. For aragonite, the (110) face was designated as the reference face, so its relative growth rate is 1.0.

Figure 4.10 shows the predicted steady-state morphology of aragonite crystals. The morphology is dominated by the  $\{110\}$ , and to a lesser extent, the  $\{011\}$  family of faces. The other two families of faces are not present on the steady-state morphology. The crystal shape is needle-like with extremely high aspect ratio ( $\gg 100$ ). Although several experimental papers report needle-like or acicular morphology of aragonite crystals [1, 19, 20], the measured aspect ratios are typically in the range of 10-50. Therefore, the model correctly predicts the crystal habit but completely overestimates the aspect ratio of acicular aragonite crystals.

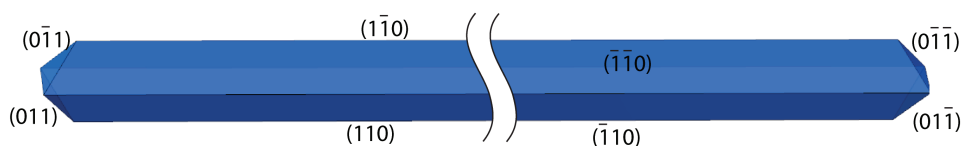


**Figure 4.10:** Predicted morphology of aragonite crystals grown from aqueous solution at  $S = 1.2$  and  $r = 1.0$ . The crystal shape is needle-like with an aspect ratio  $\gg 100$ .

From Table 4.4, it is evident that the  $\{110\}$  family of F-faces are the slowest growing faces on the aragonite surface. The order of morphological importance is  $\{110\} > \{020\} > \{011\} > \{002\}$ . However, the predicted growth rates of the other three families of faces are several ( $\sim 170$ ) orders of magnitude larger than that of the  $\{110\}$  family of faces, which is consistent with the values of the kink detachment work ( $\Delta W$ ) listed in Table 4.3. The values of  $\Delta W$  reported in Table 4.3 for all the faces are typically much larger than those predicted for calcite crystal growth (Table 3.2). The average  $\Delta W$  values listed in Table 4.3 are especially large for the spiral edges of the (110) face. The step velocity and therefore the growth rate, has an exponential dependence on the kink

detachment work. As a result, a 100 kcal/mol difference in  $\Delta W$  results in growth rates that are about 70 orders of magnitude larger. Table 4.4 shows that the step velocities of spiral edges within the same crystal face may also vary by several orders of magnitude. Since the growth rate of a crystal face is dominated by the slowest growing spiral edge, an exceptionally larger value of  $\Delta W$  for one spiral edge (such as for the  $[\bar{1}11]$  edge growing in the  $[\bar{1}1\bar{1}]$  direction on the (110) face) forces the crystal face to grow at a very slow rate. This accounts for another 100 orders of magnitude difference between the growth rates of the (110) face and the other crystal faces.

The spiral growth calculations are extremely sensitive to the accuracy in the estimation of the kink detachment work.  $\Delta W$  depends on the long-range electrostatic interaction energy between the kink site growth unit and its solid-state neighbors, which is calculated using the space partitioning method. The partial charges of the growth units in the surface layer are calculated using the bond valence model [17]. The interatomic distances between the growth units in the surface layer affect the electrostatic interaction energy of kink site growth units in two different ways – (i) as the interionic separation distance in the denominator of the expression for columbic energy, and (ii) as the partial charges (or summation of bond valences) that have an exponential dependence on interatomic distance (equation 2.4).

Information about surface relaxation in the presence of water molecules will provide the correct atomic positions of both solute and solvent species, and therefore, the correct interatomic distances. No experimental or simulation studies were found in the litera-

ture that report values of surface relaxation and solvent structure near aragonite crystal surfaces. Therefore, the solvent structure information for calcite growth was used here to perform the calculations for aragonite crystal growth. Accurate structural information of the crystal-solution interface is necessary to correctly predict the aspect ratios of needle-like aragonite crystals. This model presents a systematic methodology that correctly captures the overall crystal shape of aragonite crystals grown from aqueous solution, despite the absence of solvent structure information. However, a more accurate prediction of the relative growth rates requires complementary efforts to specify the structure of the crystal surface and its surroundings using molecular dynamics simulations or measurement techniques such as neutron scattering, electron diffraction, etc.

## **4.6 Conclusions**

The spiral growth model was applied to study aragonite crystal growth from aqueous solutions. Lower symmetry of aragonite crystal structure (as compared to calcite) presented new challenges for the mechanistic modeling framework and helped make it more general. A consequence of the sharing of intermolecular interactions between two PBCs in a crystal is that, in the space partitioning method, the cardinal directions must be chosen anew for each crystal face. With this modification, the space partitioning method can still be applied to calculate the kink site potential energies and the kink detachment work.

The spiral edges on the (110) face of aragonite exhibit multiple structures that have different rates of kink incorporation. A suitable modification to the spiral growth model has been proposed that accounts for multiple edge structures advancing at dissimilar velocities. The harmonic mean of the step velocities of the various edge structures is used as the overall step advancement rate in the expression for the spiral rotation time.

The spiral growth model correctly predicts needle-like shape for aragonite crystals, but the aspect ratio of the needles is overestimated by several orders of magnitude. The overestimation is caused by the absence of the correct solvent structure information that results in the loss of accuracy in the calculation of the kink detachment work ( $\Delta W$ ). Molecular simulations can provide more precise radial distribution functions for solvent molecules near surface growth units on aragonite crystal surfaces. This will allow accurate predictions of the crystal morphology as well as the shapes of growth spirals on each crystal face. The latter predictions could be validated with *in situ* Atomic Force Microscopy (AFM) measurement techniques that have been implemented to observe the growth of some inorganic crystals such as calcite [21], zeolites [22], etc.

# Bibliography

- [1] L. Wang, I. Sondi, and E. Matijevic. Preparation of uniform needle-like aragonite particles by homogeneous precipitation. *J. Colloid Interface Sci.*, 218:545–553, 1999.
- [2] F. Nudelman, B. A. Gotliv, L. Addadi, and S. Weiner. Mollusk shell formation: Mapping the distribution of organic matrix components underlying a single aragonitic tablet in nacre. *J. Struct. Biol.*, 153:176 – 187, 2006.
- [3] S. Weiner and L. Addadi. Crystallization pathways in biomineralization. *Annu. Rev. Mater. Res.*, 41:21–40, 2011.
- [4] A. P. Jackson, J. F. V. Vincent, and R. M. Turner. The mechanical design of nacre. *Proc. R. Soc. Lond. B Biol. Sci.*, 234:415–440, 1988.
- [5] J. P. R. De Villiers. Crystal structures of aragonite, strontianite, and witherite. *Am. Mineral.*, 56:758–767, 1971.
- [6] P. Hartman. *Relations between Structure and Morphology of Crystals*. PhD thesis, University of Groningen, 1953.
- [7] P. Raiteri, J. D. Gale, D. Quigley, and P. M. Rodger. Derivation of an accurate force-field for simulating the growth of calcium carbonate from aqueous solution: A new model for the calcite-water interface. *J. Phys. Chem. C*, 114:5997–6010, 2010.
- [8] H. D. B. Jenkins, K. F. Pratt, and B. T. Smith. Lattice potential energies for calcite, aragonite and vaterite. *J. Inorg. Nucl. Chem.*, 38:371–377, 1976.
- [9] R. C. Snyder and M. F. Doherty. Predicting crystal growth by spiral motion. *Proc. R. Soc. A*, 465:1145–1171, 2009.
- [10] Z. B. Kuvadia and M. F. Doherty. Spiral growth model for faceted crystals of non-centrosymmetric organic molecules grown from solution. *Cryst. Growth Des.*, 11:2780–2802, 2011.
- [11] M. A. Lovette and M. F. Doherty. Multisite models to determine the distribution of kink sites adjacent to low-energy edges. *Phys. Rev. E*, 85:021604, 2012.

- [12] P. Dandekar and M. F. Doherty. A mechanistic growth model for inorganic crystals: Growth mechanism. *AIChE J.*, (in press), 2014.
- [13] S. E. Ruiz-Hernandez, R. Grau-Crespo, N. Almora-Barrios, M. Wolthers, A. R. Ruiz-Salvador, N. Fernandez, and N. H. de Leeuw. Mg/Ca partitioning between aqueous solution and aragonite mineral: A molecular dynamics study. *Chem. Eur. J.*, 18:9828–9833, 2012.
- [14] M. Wolthers, D. Di Tommaso, Z. Du, and N. H. de Leeuw. Calcite surface structure and reactivity: Molecular dynamics simulations and macroscopic surface modelling of the calcite-water interface. *Phys. Chem. Chem. Phys.*, 14:15145–15157, 2012.
- [15] A. G. Stack. Molecular Dynamics Simulations of Solvation and Kink Site Formation at the {001} Barite-Water Interface. *J. Phys. Chem. C*, 113:2104–2110, 2009.
- [16] I. D. Brown and R. D. Shannon. Empirical bond-strength-bond-length curves for oxides. *Acta. Crystallogr. A*, 29:266–282, 1973.
- [17] I. D. Brown. *The Chemical Bond in Inorganic Chemistry: The Bond Valence Model*. Oxford University Press, 2002.
- [18] H. Teng, P. M. Dove, and J. J. DeYoreo. Reversed calcite morphologies induced by microscopic growth kinetics: insight into biomineralization. *Geochim. Cosmochim. Acta*, 63:2507–2512, 1999.
- [19] Z. Hu and Y. Deng. Supersaturation control in aragonite synthesis using sparingly soluble calcium sulfate as reactants. *J. Colloid Interface Sci.*, 266:359–365, 2003.
- [20] N. Koga, D. Kasahara, and T. Kimura. Aragonite crystal growth and solid-state aragonite-calcite transformation: A physico-geometrical relationship via thermal dehydration of included water. *Cryst. Growth Des.*, 13:2238–2246, 2013.
- [21] H. H. Teng, P. M. Dove, C. A. Orme, and J. J. De Yoreo. Thermodynamics of calcite growth: Baseline for understanding biomineral formation. *Science*, 282:724–727, 1998.
- [22] A. I. Lupulescu and J. D. Rimer. In situ imaging of silicalite-1 surface growth reveals the mechanism of crystallization. *Science*, 344:729–732, 2014.

# Chapter 5

## Crystal Growth of Anatase from Hydrothermal Synthesis

### 5.1 Introduction

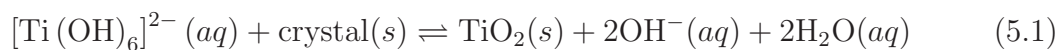
Titanium dioxide ( $\text{TiO}_2$ ) exists in nature in three polymorphic forms - rutile, anatase, brookite. Rutile is the thermodynamically stable polymorph at room temperature and pressure, and is widely used as a white pigment in paints and cosmetic products. Anatase finds applications in areas such as photocatalysis [1] and dye-sensitized solar cells [2, 3]. The (001) crystal face of anatase shows higher catalytic activity towards water dissociation than the (101) face [4]. Additives such as hydrofluoric acid have been used to tailor the shapes of anatase crystals to maximize the surface area of the (001) face [5]. A systematic understanding of the crystal growth process will allow design of functionally desirable anatase crystals.

Titanium dioxide is sparingly soluble in water at room temperature and pressure, therefore anatase crystals cannot be grown by traditional solution synthesis techniques.

The solubility in water increases at higher temperatures, therefore, hydrothermal synthesis techniques can be used to grow anatase crystals at high temperature ( $> 100^{\circ}\text{C}$ ) and high pressure ( $> 1$  bar).

### 5.1.1 Growth Unit for Anatase Crystal Growth

In an aqueous solution,  $\text{Ti}^{4+}$  ions are octahedrally coordinated with  $\text{H}_2\text{O}$  or  $\text{OH}^-$  species, depending on the pH of the solution [6]. It is well known that  $\text{TiO}_6$  octahedra are the growth units in the hydrothermal synthesis of anatase crystals [7–9]. Depending on the composition and pH of the solution, the oxygen atoms in the  $\text{TiO}_6$  octahedra may form chemical bonds with hydrogen atoms or other species, and the actual chemical composition of these octahedral growth units will vary. The  $\text{TiO}_6$  octahedral species are referred to as the solution phase growth units in this chapter. A dehydration step, such as the one shown below, may follow before these species incorporate into the stoichiometric crystal lattice [9].



The effect of the solution chemistry on crystal growth of anatase remains an area of active research [10]. In a high-pH solution, the surface incorporated  $\text{TiO}_2$  species may themselves be coordinated with  $\text{OH}^-$  ions. Therefore, the dehydration step may not yield stoichiometric and charge neutral species that have incorporated into the crystal lattice [6]. However, to identify the periodic bond chains within the crystal under a mechanistic growth modeling framework, it is assumed that the dehydration step is fast

and it is not the rate determining step. The  $\text{TiO}_2$  species that have incorporated into the crystal surface are referred to as the solid-state growth units in this chapter.

## 5.2 Periodic Bond Chains in Anatase Crystals

Anatase crystallizes in a tetragonal lattice with a  $I4_1/amd$  space group ( $a = b = 3.7842 \text{ \AA}$ ,  $c = 9.5146 \text{ \AA}$ ,  $\alpha = \beta = \gamma = 90^\circ$ ) [11]. Figure 5.1a shows the crystallographic unit cell of anatase. There are four formula units (or molecules) of  $\text{TiO}_2$  in the unit cell with each Ti atom coordinated with six O atoms while each O atom is surrounded by three Ti atoms. The crystal structure can also be visualized as a framework of distorted  $\text{TiO}_6$  octahedra (Figure 5.1b). Each octahedron shares four corners and four edges with its surrounding octahedra. The distortion in the shape of the  $\text{TiO}_6$  octahedron is the result of two different values of the nearest neighbor Ti-O distances –  $1.934 \text{ \AA}$  and  $1.98 \text{ \AA}$ .

Figure 5.2 shows the packing of anatase crystal lattice with building units. The stoichiometry and zero dipole moment properties were considered to identify building units of periodic bond chains within the anatase unit cell. A single type of building unit with the stoichiometry  $\text{Ti}_2\text{O}_4$  was identified within the unit cell and is represented by cyan ellipses in Figure 5.2. The unit cell contains two building units with their centers of mass at  $(0, 0, 0)$  and  $(\frac{1}{2}, \frac{1}{2}, \frac{1}{2})$  lattice coordinates. As discussed earlier, the solid-state growth unit for anatase crystal growth is  $\text{TiO}_2$ . Therefore, each building unit in anatase crystal structure contains two solid-state growth units. The asymmetric unit of anatase unit cell

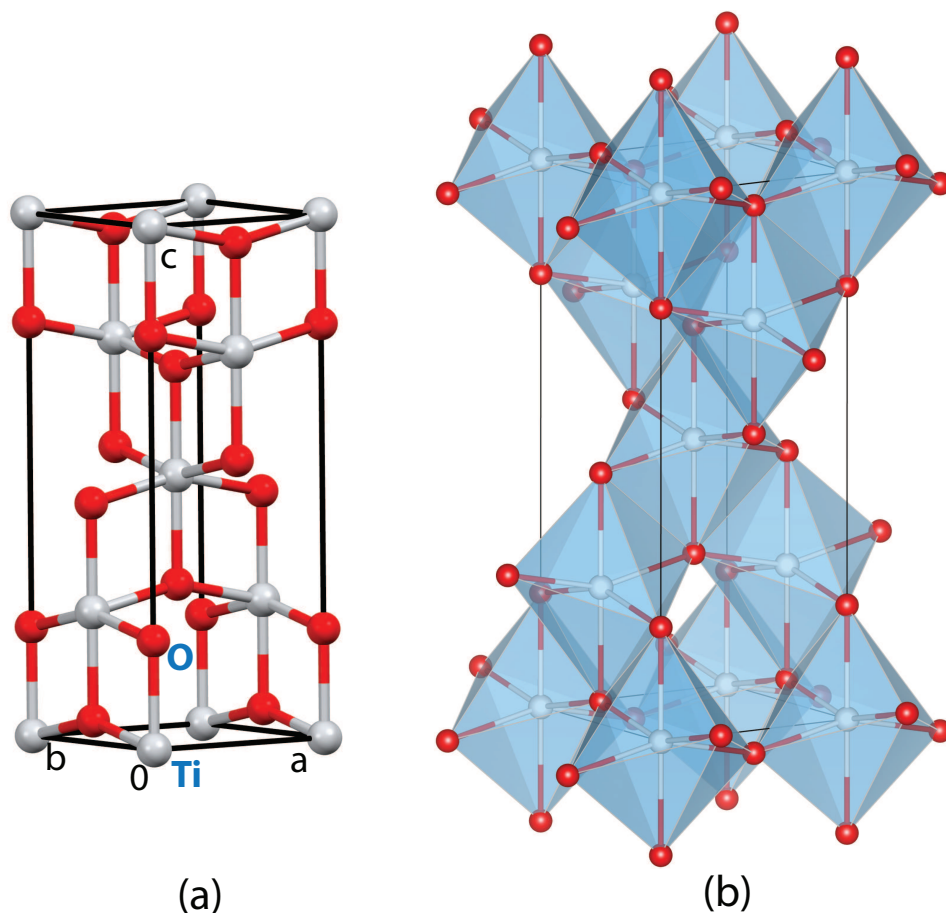


**Figure 5.1:** (a) Anatase (TiO<sub>2</sub>) unit cell with the contents of the asymmetric unit labeled in blue. Ti and O atoms are represented by silver and red spheres respectively. (b) Packing of the coordination octahedra (TiO<sub>6</sub>) within the unit cell.

has the composition TiO, the solid-state growth unit and the molecular stoichiometry is TiO<sub>2</sub>, the building unit has the composition Ti<sub>2</sub>O<sub>4</sub>, and the contents of the unit cell have the stoichiometry Ti<sub>4</sub>O<sub>8</sub>.

The PBC directions in anatase lattice were obtained by identifying continuous chains of building units within the crystal. Since the building unit is stoichiometric and has zero dipole moment, chains of building units will satisfy the stoichiometry and dipole

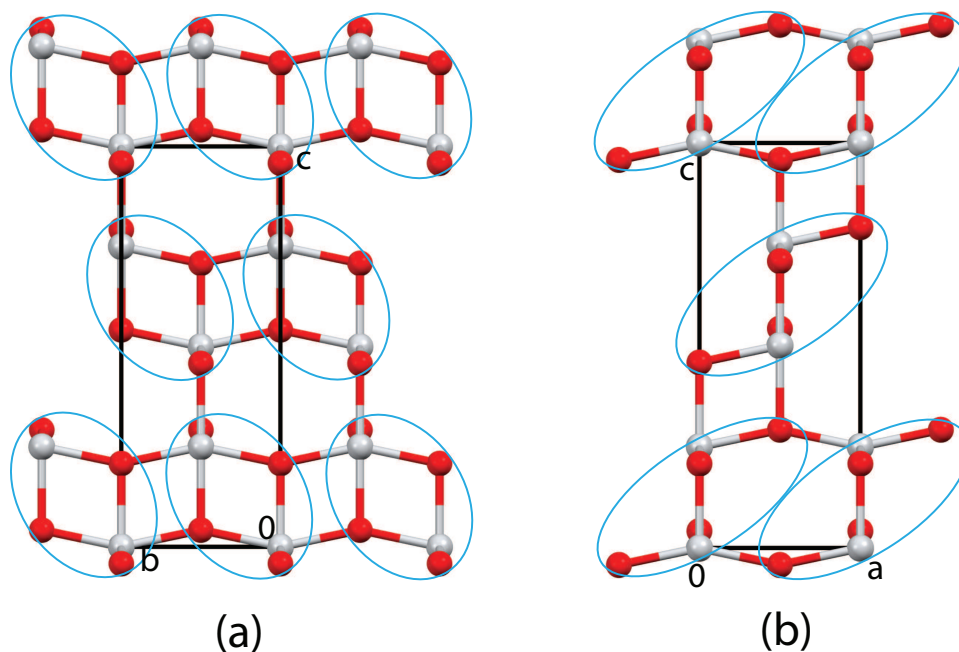


**Figure 5.2:** View along (a) [100] and (b) [010] lattice directions of the crystal packing around the anatase unit cell with building units enclosed within cyan ellipses.

moment properties specified under the Hartman-Perdok rules [12]. Continuous chains of building units were found along [100], [010], [111],  $[\bar{1}\bar{1}1]$ ,  $[1\bar{1}\bar{1}]$  and  $[11\bar{1}]$ .

There are two families of F-faces on anatase crystal surface -  $\{101\}$  and  $\{004\}$ . (220) is an S-face because only the  $[1\bar{1}\bar{1}]$  periodic bond chain lies within its slice thickness. Figure 5.3a shows the packing of the (101) surface with building units while Figure 5.3b shows the step edges along the [010] and  $[\bar{1}\bar{1}1]$  PBC directions. The chain of solid-state growth units along the  $[\bar{1}\bar{1}1]$  direction is not a continuous chain of bonds (or intermolecular interactions), therefore, it cannot be considered as a periodic bond chain.

Figure 5.4a shows a side view of the (004) slice of anatase crystals. Since the inversion center (black circles) is not at the center of the (004) slice, the dipole moment of the (004)

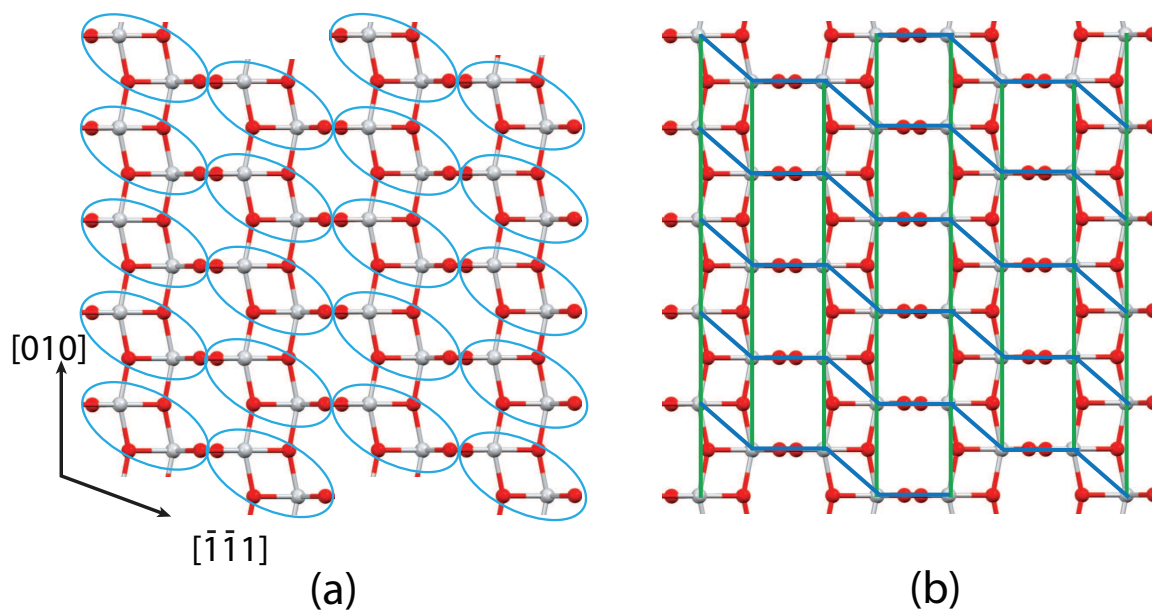


**Figure 5.3:** Plan view of the (101) anatase crystal surface. (a) shows the packing of the surface with building units (cyan ellipses). (b) shows the periodic bond chains along the [010] (green) and  $[\bar{1}\bar{1}1]$  (blue) step edges.

slice is not zero. The residual dipole moment lies along a direction parallel to the (004) slice. The dipole moment of successive (004) layers are aligned in opposite directions, therefore the slice thickness of  $2 \times d_{004}$  has a zero dipole moment. The definition of unstable crystal surfaces proposed by Tasker [13] was based on the presence of a dipole moment perpendicular to the crystal surface. Therefore, the (004) anatase crystal surface is not unstable. However, the structure of the PBC edges within the (004) slice does differ from that in other faces. Figure 5.4b shows the step edges present within the (004) surface of anatase crystals. The two PBCs along the [100] and [010] directions are equivalent due to the symmetry of the tetragonal lattice. However, the structure of the [010] edge in the (004) face is different from that in the (101) face. The nearest neighbor Ti-O distances

for the  $\text{TiO}_2$  solid-state growth unit in the (101) face are 1.934 Å and 1.980 Å, whereas in the (004) face both Ti-O distances are 1.934 Å.

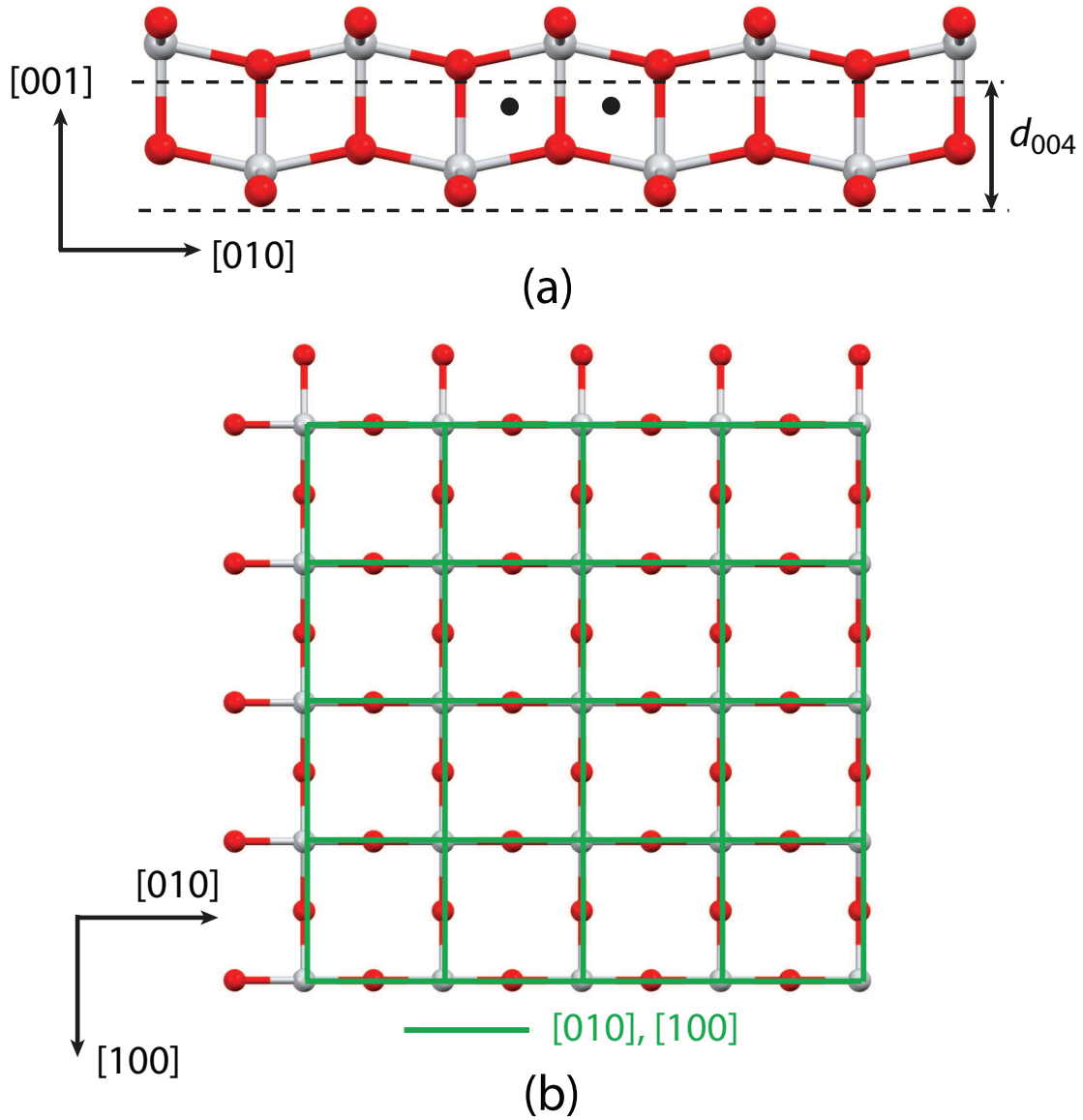


**Figure 5.4:** (a) View of anatase crystal packing along the  $[\bar{1}00]$  direction showing the boundaries of the (004) slice and the inversion centers (black circles). (b) Plan view of the (004) anatase crystal surface showing the periodic bond chains along  $[010]$  and  $[100]$  (green) edges.

**Table 5.1:**  $E_{PBC}$  values for the F-faces on the anatase crystal surface

Crystal Face	$E^{att}$ (kcal/mol)	PBC vectors	$E_{PBC}$ (kcal/mol)
(101)	-36.5	[010]	-47.9
		[11 $\bar{1}$ ]	-59.9
(004)	-45.1	[010]	-41.1
		[100]	-41.1

The interaction energies of the  $\text{TiO}_2$  solid-state growth units along each of the periodic bond chains in bulk anatase were calculated while accounting for the long-range electrostatic interactions (Table 5.1). The pairwise interatomic interactions within anatase crystals were calculated using a force field containing both coulombic and Buckingham potential, that was developed for all the polymorphs of  $\text{TiO}_2$  [14]. The partial charges of Ti and O atoms in the bulk crystal were reported as +2.196 and -1.098, respectively. The lattice energy of anatase crystals was calculated by a Madelung-type summation in three dimensions for a supercell of dimensions  $80 \times 80 \times 32$ . The calculated value of -902.5 kcal/mol matches well with the experimental lattice energy of -889.7 kcal/mol [15, 16].

The attachment energy model for growth in vacuum predicts a bipyramidal morphology (dominated by the {101} family of faces) truncated by {004} faces (Figure 5.5a). However, the native morphology of hydrothermally grown anatase crystals usually does not exhibit the {004} faces (Figure 5.5b) [7, 17]. Since the attachment energy model is based on an empirical relationship between the growth rate of a crystal face and its attachment energy, it can be used to make predictions of anatase crystal morphology with limited accuracy.

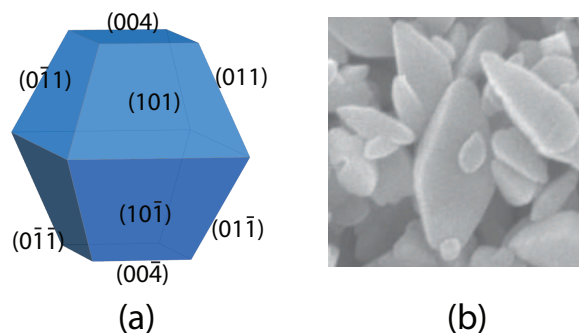


**Figure 5.5:** (a) Predicted morphology of anatase crystals using the attachment energy model. (b) A typical morphology of anatase crystals grown by hydrothermal synthesis. Adapted with permission from Deng et al. [17]. Copyright ©2009 Elsevier B.V.

### 5.3 Hydrothermal Synthesis

Hydrothermal synthesis of anatase crystals was performed to obtain large single crystals of anatase. The characterization of anatase crystal surfaces provided valuable insights into the growth mechanism by which anatase crystallizes under hydrothermal conditions. Several hydrothermal techniques have been reported in the literature for the synthesis of anatase crystals [5, 7–9, 18]. The typical size of anatase crystals reported was in the range of 10–100 nm. Thermodynamic analysis suggested that anatase crystal larger than 14 nm in size would transform into rutile [19]. However, large ( $\sim 1\mu\text{m}$ ) single crystals of anatase are required to perform surface characterization using electron microscopy and atomic force microscopy to elucidate the growth mechanism. Recently, Deng et al. [17] reported a hydrothermal synthesis method that yielded large ( $> 1\mu\text{m}$ ) single crystals of anatase. Their methodology was applied here to synthesize large ( $1–2\mu\text{m}$ ) single crystals of anatase.

### **5.3.1 Synthesis Procedure**

The hydrothermal synthesis procedure for anatase crystals consists of two steps [8, 17]. The first step involves the synthesis of a titanate precursor. 0.5 g of anatase TiO<sub>2</sub> powder (from Sigma Aldrich) was dissolved into 50 mL of 10 M NaOH solution at room temperature and then transferred into a 125 mL Teflon-lined pressure vessel (Parr Instruments). The reaction vessel was placed in a drying oven at a temperature of 200 °C and was kept for 72 hours. The vessel was allowed to cool down to room temperature, after which the precipitate was filtered (0.45µm Durapore membrane filter) and washed with sufficient amount of 0.1 M HCl solution until the desired pH of 10.5 was reached for the precipitate-HCl solution. The resulting slurry is composed of layered titanate (Na<sub>2</sub>Ti<sub>2</sub>O<sub>7</sub>) which is the precursor to anatase single crystals.

In the second step of the synthesis procedure, the precursor was dispersed into 50 mL millipore water. This mixture was transferred into a Teflon-lined vessel of 125 mL volume and kept in an oven at 200 °C for 48 hours. The final product was cooled to room temperature, filtered and washed with millipore water. The crystalline precipitate was dried at 70 °C for three hours. Three different batches were created - the first batch exactly followed the above procedure while the second batch was conducted with exactly half the amount of all reagents in a 45 ml Teflon-lined pressure vessel. The third batch had the same amount of reactants as the first batch but the second step in the synthesis procedure was carried out for 72 hours instead of 48 hours. The longer duration for the

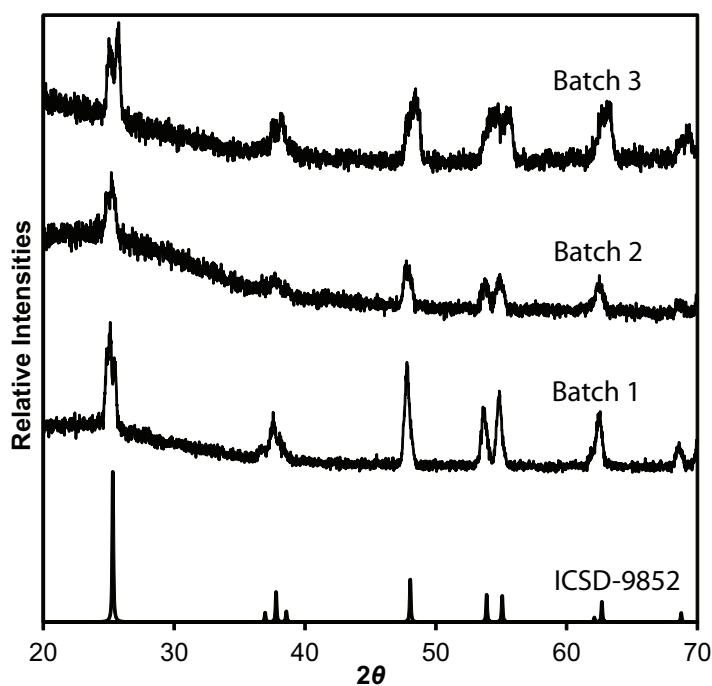
crystallization step for the third batch was introduced to obtain anatase crystals with larger sizes.

### 5.3.2 Characterization

Various characterization techniques were used to verify the crystal structure, size and morphology of the anatase crystals obtained from hydrothermal synthesis. The degree of crystallinity and the specific polymorph of  $\text{TiO}_2$  was identified with powder X-ray diffraction (XRD) using a Philips X'Pert diffractometer ( $\text{Cu K}\alpha$  radiation). Figure 5.6 shows the comparison between the diffraction patterns for the three batches and the pattern for pure anatase crystals reported in the Inorganic Crystal Structure Database (ICSD-9852).

The diffraction patterns in Figure 5.6 show peaks at identical  $2\theta$  values ( $25^\circ$ ,  $37^\circ$ ,  $48^\circ$ ,  $54^\circ$ ,  $55^\circ$ ,  $63^\circ$ ) as the diffraction pattern for pure anatase crystals. Therefore, the XRD analysis confirms that the hydrothermal synthesis produces anatase crystals, and not rutile.

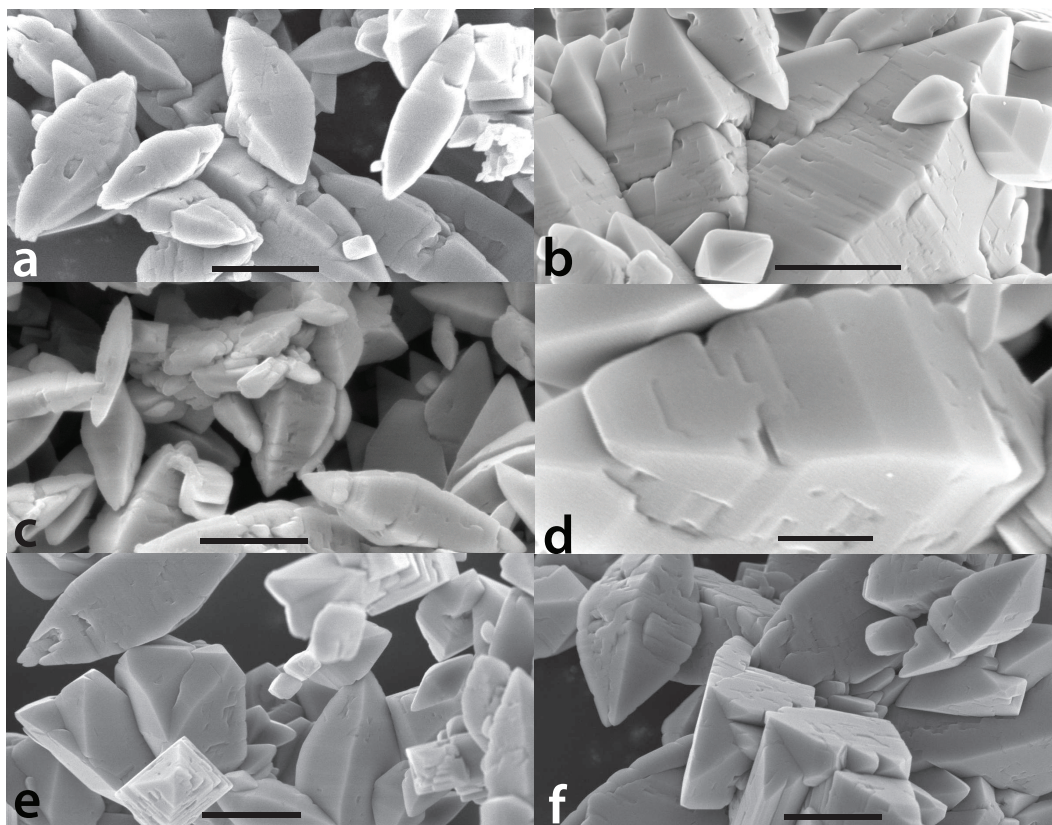
Scanning electron microscopy (SEM) was used to characterize the size and morphology of anatase crystals. Samples from the three batches were sputter-coated with Pd under Ar atmosphere, then imaged with an XL40 Sirion electron microscope with a 5 kV beam. Figure 5.7 shows some SEM images of samples taken from the three batches. Tetragonal bipyramidal-shaped anatase crystals of  $\gtrsim 1 \mu\text{m}$  size were obtained from all the batches. The crystal surfaces were highly roughened which may be attributed to surface dissolution



**Figure 5.6:** X-ray diffraction patterns of  $\text{TiO}_2$  crystals synthesized using the hydrothermal synthesis technique reported by Deng et al [17].

at such high pH values [17]. Some of the anatase crystals in the sample taken from batch 3 show twinning (Figure 5.7e and f). Crystal twinning on the  $\{112\}$  anatase crystal surfaces has been observed previously using transmission electron microscopy (TEM) [20]. Therefore, the size of anatase crystals cannot be further increased by extending the time for the second step in the synthesis procedure. Further experiments are needed to explore other options to develop a synthesis method that yields anatase crystals larger than  $10 \mu\text{m}$  in size, so that their crystal surfaces can be characterized using atomic force microscopy (AFM).

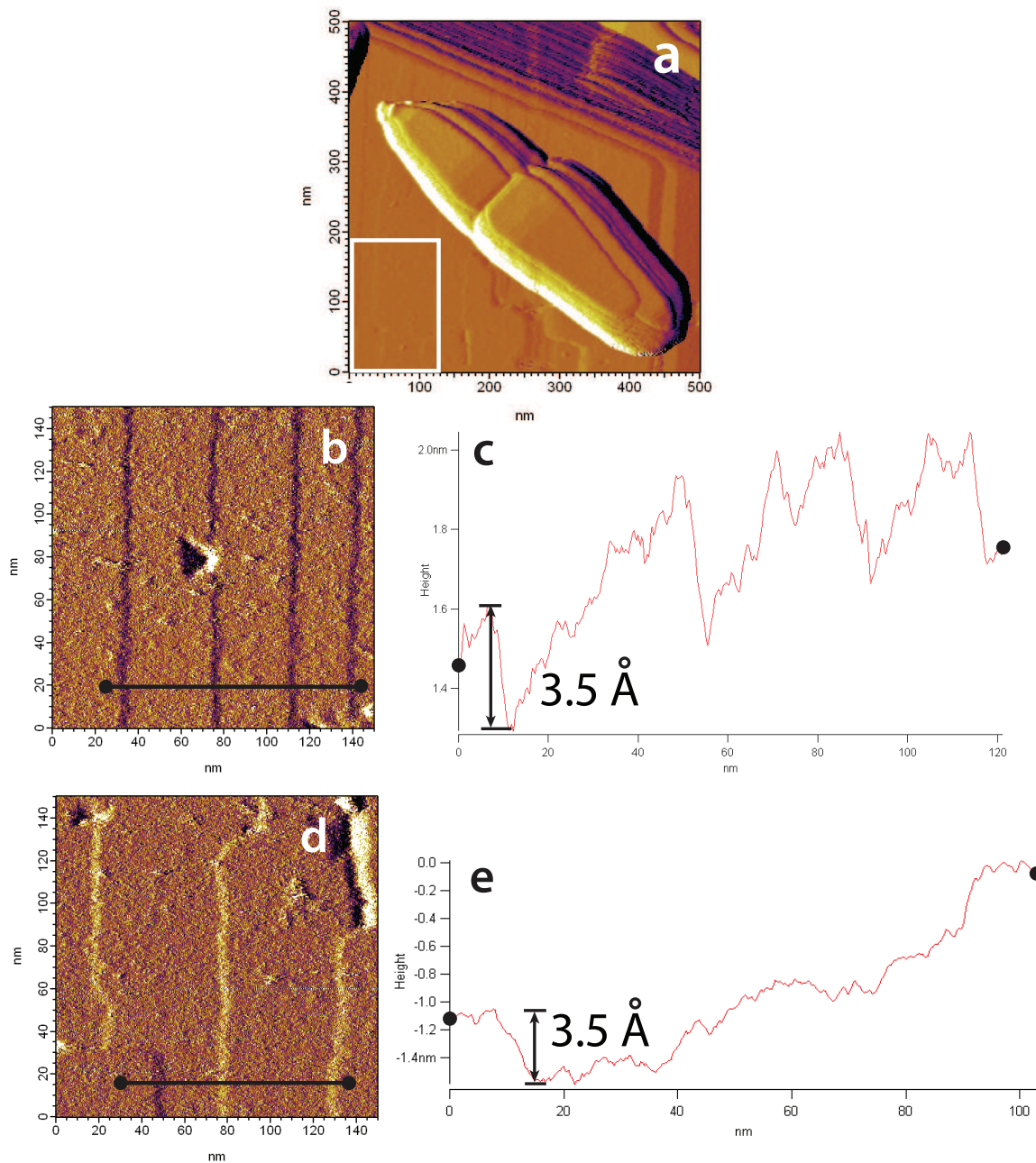
The surfaces of anatase crystals were characterized with an atomic force microscope (MFP-3D, Asylum Research). Figure 5.8 shows the AFM images of a sample from batch 2



**Figure 5.7:** SEM images of hydrothermally grown anatase crystals. (a) and (b) are samples from batch 1, (c) and (d) are samples from batch 2, and (e) and (f) are samples from batch 3. The scale bar on all the figures except (d) is 1  $\mu\text{m}$ . The scale bar on (d) is 200 nm.

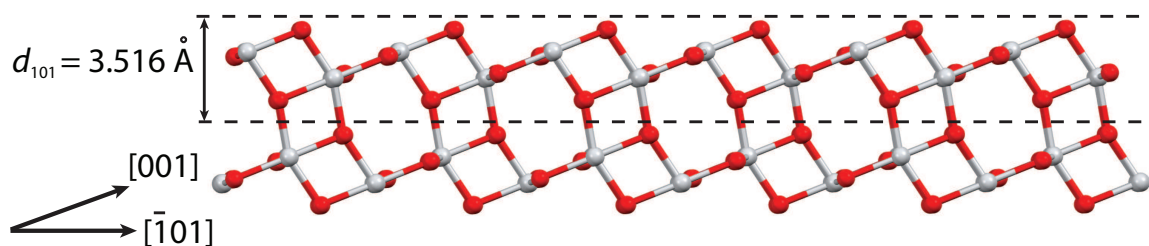
that was imaged in air. The crystal surfaces were scanned using Si cantilevers (AC240TS, Olympus). Figures 5.8b and d show monomolecular steps with roughly equal spacing ( $\sim 40\text{-}60$  nm). The height profiles in Figures 5.8c and e show that the steps are roughly 3.5  $\text{\AA}$  in height.

Figure 5.9 shows the side view of the (101) slice of anatase crystals. The height of a layer of  $\text{TiO}_2$  solid-state growth units on the (101) surface is 3.516  $\text{\AA}$ , which matches with the height of the steps found from the AFM images of anatase crystals. Therefore,



**Figure 5.8:** *Ex situ* AFM images of hydrothermally grown anatase crystal surfaces of a sample taken from batch 2. (a) shows a part of an anatase crystal in the background. The object in the foreground could be another anatase crystal. (b) and (d) are amplitude images from an area shown within white rectangle in (a). (c) and (e) are the height profiles of the black lines in (b) and (d).

it is concluded that it was the (101) anatase crystal surface that was scanned with the AFM. The spacing between the monomolecular steps shown in Figures 5.8b and d is roughly equal, which is suggestive of spiral growth [21, 22]. However, the entire crystal surface could not be scanned, so it cannot be conclusively stated that anatase crystals grow by a spiral growth mechanism. But they do grow by a layered growth mechanism, which contradicts the hypothesis that anatase crystal growth is governed by an oriented attachment mechanism [7, 23].



**Figure 5.9:** Side view of the (101) slice of anatase crystals. The height of monomolecular steps on the (101) surface is equal to the slice thickness,  $d_{101} = 3.516 \text{ \AA}$ .

## 5.4 Discussion

Crystal growth of anatase presents several challenges. Anatase is a metastable polymorph of titanium dioxide, and Ostwald's step rule suggests that during the course of solution crystallization, the thermodynamically stable polymorph (rutile) will be formed. Traditionally, anatase crystals have been synthesized only in the nanometer size range [2, 7, 10, 20]. In this size range, crystals cannot grow by the spiral growth mechanism since the surface area is too small to sustain screw dislocations [23]. The low solubil-

ity of titanium dioxide in water necessitates the use of hydrothermal synthesis at high temperatures and pressures. *in situ* AFM imaging of the crystal growth process provides valuable insight into the growth mechanism of certain inorganic crystals such as calcite [21], barite [24], zeolites [25], etc. Due to the extreme conditions required for anatase crystal growth, *in situ* imaging is currently a technological challenge.

The growth of faceted anatase nanocrystals has been proposed to proceed by a non-classical growth mechanism, namely the oriented attachment mechanism, wherein nanoparticles aggregate along specific crystallographic orientations [7]. The driving force behind crystal growth by oriented attachment has been suggested to be interatomic columbic interactions [26]. Penn and Banfield [7] showed using TEM that anatase nanocrystals preferentially aggregated along the [001] direction than the [101] direction. The periodic bond chain theory [12] can be applied to test this hypothesis. The PBC interaction energy in inorganic crystals is dominated by the electrostatic interactions. Table 5.1 shows that the periodic bond chains in the (004) surface of anatase crystals have lower interaction energy than the ones in the (101) crystal surface. Specifically, the  $[11\bar{1}]$  PBC lies within the (101) anatase face while it is nearly perpendicular to the (004) face. Therefore, the electrostatic interaction energy perpendicular to the (004) surface, or along the [001] direction, is higher than the interaction energy along the [101] direction. Therefore, the PBC theory is consistent with the hypothesis that the electrostatic interactions are the driving force behind the oriented attachment growth mechanism [26].

The presence of monomolecular steps on the  $\{101\}$  anatase crystal surface (Figure 5.8) is not consistent with the oriented attachment growth mechanism. The attachment of anatase nanocrystals onto a larger crystal cannot result in monomolecular steps on the crystal surface. A similar dilemma has been resolved recently in the field of zeolite crystal growth. Lupulescu and Rimer performed *in situ* AFM imaging of real-time growth on a zeolite crystal surface [25]. They observed the attachment of both monomer molecules and nanocrystals on the zeolite surface, and concluded that the growth proceeds by simultaneous deposition of both types of species. Such co-existence of the classical and non-classical growth mechanisms could explain the presence of molecular steps on anatase crystal surfaces and also be consistent with the oriented attachment growth mechanism. However, conclusive evidence of the growth mechanism is contingent upon overcoming the technology barrier associated with *in situ* AFM imaging of hydrothermal growth of anatase crystals.

A mechanistic growth model could be applied to anatase crystal growth if layered growth mechanisms (spiral growth or 2D nucleation) were assumed to be dominant on anatase crystal surfaces. However, these calculations require accurate solvent structure information from molecular simulations. Raju et al. [27] have recently developed a reactive force field to study the dissociation of water on  $\text{TiO}_2$  surfaces. The number of water molecules around growth units located in various surface sites and the distance between the water molecules and the crystal surface would allow the calculation of the potential energies of the surface growth units and the estimation of the growth kinetics on anatase

crystal surfaces. An accurate growth model might also need to account for the kinetics of the dehydration reaction that precedes the incorporation of the  $\text{TiO}_6$  solution phase growth units into anatase crystal.

## 5.5 Conclusions

Hydrothermal synthesis of anatase crystals was performed to obtain large single crystals of anatase. Surface characterization techniques such as SEM and AFM provided some insight into the synthesis process and the growth mechanism. There may be a thermodynamic limit to the size of anatase crystals that can be obtained by hydrothermal synthesis, beyond which either polymorph transformation or crystal twinning takes place. *Ex situ* AFM images showed the presence of monomolecular steps on the (101) surface of anatase, which suggests a classical layered growth mechanism.

The periodic bond chain theory predicts that the electrostatic interaction energy along the [001] direction is higher than along the [101] direction. This is consistent with the hypothesis that the electrostatic interactions are the driving force for the oriented attachment mechanism, which is a non-classical growth mechanism.

The exact growth mechanism that governs anatase crystal growth may be a combination of classical and non-classical mechanisms, and could also be a function of the crystal size [10]. The design of micrometer sized anatase crystals with higher proportion of the catalytically active {001} faces [5] requires a better understanding of the growth process.

Future efforts in both theoretical modeling and *in situ* AFM imaging should be geared towards solving this mystery.

# Bibliography

- [1] A. Linsebigler, G. Lu, and J. T. Yates Jr. Photocatalysis on TiO<sub>2</sub> surfaces: Principles, mechanisms, and selected results. *Chem. Rev.*, 95:735–758, 1995.
- [2] A. Hagfeldt and M. Gratzel. Light-induced redox reactions in nanocrystalline systems. *Chem. Rev.*, 95:49–68, 1995.
- [3] M. Grätzel. Photoelectrochemical cells. *Nature*, 414:338–344, 2001.
- [4] X.-Q. Gong and A. Selloni. Reactivity of anatase TiO<sub>2</sub> nanoparticles: The role of the minority (001) surface. *J. Phys. Chem. B*, 109:19560–19562, 2005.
- [5] H. G. Yang, C. H. Sun, S. Z. Qiao, J. Zou, G. Liu, S. C. Smith, H. M. Cheng, and G. Q. Lu. Anatase TiO<sub>2</sub> single crystals with a large percentage of reactive facets. *Nature*, 453:638–641, 2008.
- [6] D. Bahnemann, A. Henglein, and L. Spanhel. Detection of the Intermediates of Colloidal TiO<sub>2</sub>-catalysed Photoreactions. *Faraday Discuss. Chem. Soc.*, 78:151–163, 1984.
- [7] R. Penn and J. F. Banfield. Morphology development and crystal growth in nanocrystalline aggregates under hydrothermal conditions: insights from titania. *Geochim. Cosmochim. Acta*, 63:1549–1557, 1999.
- [8] J.-N. Nian and H. Teng. Hydrothermal synthesis of single-crystalline anatase TiO<sub>2</sub> nanorods with nanotubes as the precursor. *J. Phys. Chem. B*, 110:4193–4198, 2006.
- [9] N. M. Kinsinger, A. Wong, D. Li, F. Villalobos, and D. Kisailus. Nucleation and crystal growth of nanocrystalline anatase and rutile phase TiO<sub>2</sub> from a water-soluble precursor. *Cryst. Growth Des.*, 10:5254–5261, 2010.
- [10] S. G. Kumar and K. S. R. K. Rao. Polymorphic phase transition among the titania crystal structures using a solution-based approach: from precursor chemistry to nucleation process. *Nanoscale*, (in press), 2014.
- [11] M. Horn and C. Schwerdtfeger. Refinement of the structure of anatase at several temperatures. *Z. Krist.*, 136:273–281, 1972.

- [12] P. Hartman and W. G. Perdok. On the relations between structure and morphology of crystals. I. *Acta Crystallogr.*, 8:49–52, 1955.
- [13] P. W. Tasker. The stability of ionic crystal surfaces. *J. Phys. C Solid State*, 12:4977, 1979.
- [14] P. M. Oliver, G. W. Watson, E. Toby Kelsey, and S. C. Parker. Atomistic simulation of the surface structure of the TiO<sub>2</sub> polymorphs rutile and anatase. *J. Mater. Chem.*, 7:563–568, 1997.
- [15] L. Glasser. Lattice energies of crystals with multiple ions: A generalized Kapustinskii equation. *Inorg. Chem.*, 34:4935, 1995.
- [16] H. Jenkins. *Handbook of Chemistry and Physics*, chapter Lattice Energies, page 27. CRC Press, 1992.
- [17] Q. Deng, M. Wei, X. Ding, L. Jiang, K. Wei, and H. Zhou. Large single-crystal anatase TiO<sub>2</sub> bipyramids. *J. Cryst. Growth*, 312:213–219, 2010.
- [18] A. A. Gibb and J. F. Banfield. Particle size effects on transformation kinetics and phase stability in nanocrystalline TiO<sub>2</sub>. *Am. Mineral.*, 82:717–728, 1997.
- [19] H. Zhang and J. F. Banfield. Thermodynamic analysis of phase stability of nanocrystalline titania. *J. Mater. Chem.*, 8:2073–2076, 1998.
- [20] R. L. Penn and J. F. Banfield. Oriented attachment and growth, twinning, polytypism, and formation of metastable phases: Insights from nanocrystalline TiO<sub>2</sub>. *Am. Mineral.*, 83:1077–1082, 1998.
- [21] H. H. Teng, P. M. Dove, C. A. Orme, and J. J. De Yoreo. Thermodynamics of calcite growth: Baseline for understanding biomineral formation. *Science*, 282:724–727, 1998.
- [22] P. Cubillas, M. A. Holden, and M. W. Anderson. Crystal growth studies on microporous zincophosphate-faujasite using atomic force microscopy. *Cryst. Growth Des.*, 11:3163–3171, 2011.
- [23] R. L. Penn and J. F. Banfield. Imperfect oriented attachment: Dislocation generation in defect-free nanocrystals. *Science*, 281:969–971, 1998.
- [24] C. M. Pina, U. Becker, P. Risthaus, D. Bosbach, and A. Putnis. Molecular-scale mechanisms of crystal growth in barite. *Nature*, 395:483–486, 1998.
- [25] A. I. Lupulescu and J. D. Rimer. In situ imaging of silicalite-1 surface growth reveals the mechanism of crystallization. *Science*, 344:729–732, 2014.

- [26] H. Zhang and J. F. Banfield. Interatomic coulombic interactions as the driving force for oriented attachment. *CrystEngComm*, 16:1568–1578, 2014.
- [27] M. Raju, S.-Y. Kim, A. C. T. van Duin, and K. A. Fichthorn. ReaxFF Reactive Force Field Study of the Dissociation of Water on Titania Surfaces. *J. Phys. Chem. C*, 117:10558–10572, 2013.

# Chapter 6

## Stabilization and Growth of Polar Crystal Surfaces

### 6.1 Introduction

Crystal growth occurs near the interface of a crystal surface and the growth medium (vapor, solution or melt). When the overall growth kinetics is limited by the kinetics of surface integration, the structure of the crystal surface plays an important role in determining the growth kinetics. Several experimental (such as electron diffraction, x-ray scattering, etc.) and theoretical methods (such as molecular dynamics simulations) are used to characterize the structure of the crystal surface under various growth conditions.

The stability of an ionic crystal surface based on its surface energy has been studied since the 1950s [1]. If the crystal surface has a non-zero component of the electrostatic dipole moment perpendicular to the surface, its surface energy will diverge with increasing size of the crystal [2]. An ionic crystal surface can be characterized as stable or unstable

on the basis of the presence or absence, respectively, of a dipole moment perpendicular to the surface [3].

A repeat unit of a crystal surface packing is defined as the set of growth units that are repeated in the direction perpendicular to the surface (Figure 6.1). The electrostatic dipole moment of the repeat unit of a crystal surface is calculated as follows

$$\vec{\mu}_{repeat} = \sum_i q_i \vec{r}_i \quad (6.1)$$

where  $q_i$  and  $\vec{r}_i$  are the atomic charge and the position vector of atom  $i$ , respectively, and the index  $i$  runs over all the atoms that are part of the repeat unit. The dipole moment perpendicular to the crystal surface  $\vec{\mu}_\perp$  is calculated as follows

$$\vec{\mu}_\perp = (\vec{\mu}_{repeat} \cdot \hat{n}) \hat{n} = \left( \left[ \sum_i q_i \vec{r}_i \right] \cdot \hat{n} \right) \hat{n} \quad (6.2)$$

where  $\hat{n}$  is the unit vector perpendicular to the crystal surface.

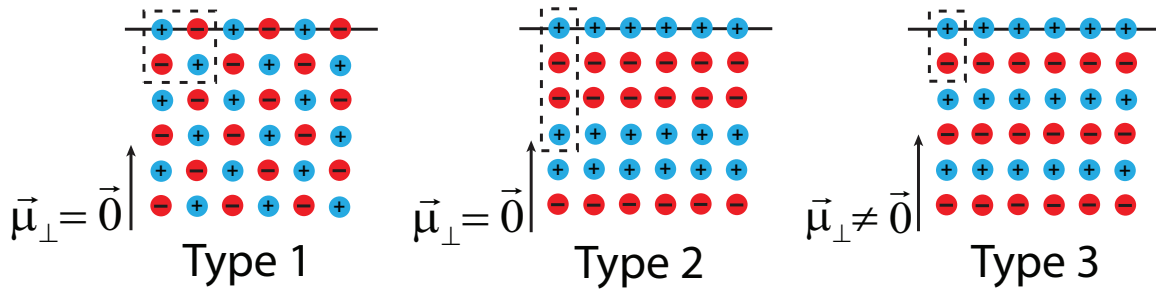


**Figure 6.1:** The classification of ionic crystal surfaces based on the value of the electrostatic dipole moment perpendicular to the crystal surface (denoted by the black horizontal line). The contents of the repeat unit for the crystal packing perpendicular to the surface are enclosed within broken black rectangles. The three crystal surfaces with different ionic arrangements are labeled based on Tasker’s classification [3].

Figure 6.1 shows the three different types of crystal surfaces that were characterized by Tasker [3] on the basis of the arrangement of ions within the surface layers. Type 1

surfaces have both positive and negative ions within each layer, which is charge neutral. The perpendicular component of the dipole moment,  $\vec{\mu}_\perp$ , is zero for such crystal surfaces. Examples of Tasker type 1 surfaces include (100) NaCl surface, (10 $\bar{1}$ 4) calcite surface, etc. Type 2 surfaces have either positive or negative ions within each layer. However, the repeat unit of the stacking of these layers has a zero dipole moment perpendicular to the surface (Figure 6.1). Examples of Tasker type 2 surfaces include (111) surface of fluorite (CaF<sub>2</sub>), (002) aragonite surface, etc. Type 3 surfaces have alternate layers of positively and negatively charged ions, resulting in a non-zero perpendicular dipole moment. Tasker type 3 surfaces are polar crystal surfaces and are unstable in their native structure. These surfaces undergo reconstruction to reduce the perpendicular dipole moment and stabilize themselves. Quantum mechanical calculations have shown that various reconstructions of the (111) NaCl surface yield structures with finite surface energy values [4, 5].

Polar crystal surfaces of inorganic oxides find relevance in areas such as catalysis [6], semiconductors [7] and gas sensing systems [8]. The symmetrically related polar crystal surfaces ( $hkl$ ) and ( $\bar{h}\bar{k}\bar{l}$ ) grow at different rates, leading to asymmetric crystal morphologies (Figure 6.2). The asymmetric growth of polar crystal surfaces of organic molecular crystals such as urea [9, 10] and  $\alpha$ -resorcinol [11–13] has also been studied in some detail. However, the larger question about the stabilization and the growth mechanisms of polar crystal surfaces remains unanswered. This chapter focuses on finding an answer to the same question for the polar surfaces of wurtzite zinc oxide (ZnO) crystals.

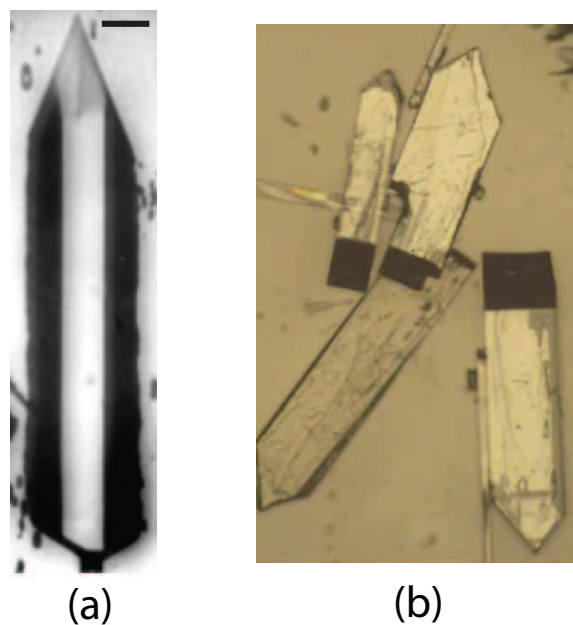


**Figure 6.2:** (a) Asymmetric shape of an  $\alpha$ -resorcinol crystal grown from aqueous solution. Scale bar is  $10\ \mu\text{m}$ . Adapted with permission from Srinivasan et al [11]. Copyright ©2005, American Chemical Society. (b) Asymmetric shapes of urea crystals grown from methanol. Adapted with permission from Piana et al [14]. Copyright ©2005, Nature Publishing Group.

## 6.2 Crystal Structure of Wurtzite Zinc Oxide

Zinc oxide crystallizes in two different polymorphs that are commonly known by their respective crystal structures - wurtzite and zinc blende. The wurtzite structure of zinc oxide is more stable at ambient temperatures and pressures. It belongs to the hexagonal lattice system and the  $P6_3mc$  space group ( $a = b = 3.2494\ \text{\AA}$ ,  $c = 5.2038\ \text{\AA}$ ,  $\alpha = \beta = 90^\circ$ ,  $\gamma = 120^\circ$ ) [15]. Figure 6.3 shows the unit cell of zinc oxide in the wurtzite crystal structure. The unit cell contains two molecules of  $\text{ZnO}$  ( $Z = 2$ ). Each Zn atom is surrounded by four O atoms in a distorted tetrahedron (vice versa for the coordination around O atom). The nearest neighbor Zn-O interatomic distances  $1.974\ \text{\AA}$  and

1.988 Å are denoted as the equatorial and axial ‘bonds’, respectively. The coordination tetrahedron around Zn atoms contains three equatorial and one axial Zn-O bonds.

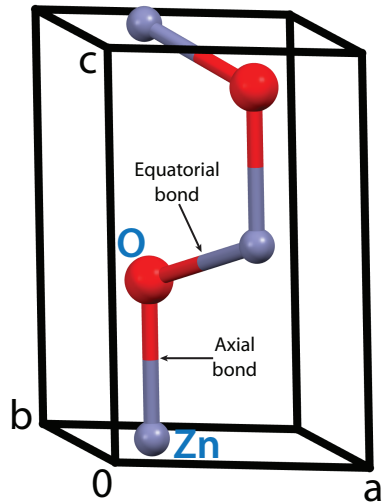


**Figure 6.3:** The crystallographic unit cell of wurtzite zinc oxide structure with the contents of the asymmetric unit labeled in blue. Zn and O atoms are represented by the blue-grey and the red spheres, respectively.

Most dielectric materials undergo polarization, or separation of charges, due to the influence of an external electric field. In polar crystals, the separation of charges is observed even in the absence of an external electric field. The collection of all the atoms within the wurtzite ZnO unit cell has a residual electrostatic dipole moment parallel to the *c* direction. Therefore, there is a separation of charges along the *c* direction in ZnO wurtzite, which is a polar crystal with the polar axis parallel to the *c* direction.

A crystal structure that does not have an inversion center within the unit cell is called noncentrosymmetric. The absence of an inversion center or center of symmetry in the unit cell is a necessary but not sufficient condition for a crystal to be polar. Several inorganic oxides crystallize in noncentrosymmetric nonpolar crystal structures, e.g. -

$\gamma$ -LiAlO<sub>2</sub> [16]. The reader is referred to an article by Halasyamani and Poeppelmeier [17] for more examples of inorganic oxides that crystallize in either polar or nonpolar noncentrosymmetric crystal structures.

In a hexagonal lattice system, the  $(hkl)$  Miller indices of a crystal face are often written in a four index notation as  $(hkil)$ , where  $i = -h - k$ . A lattice direction  $[uvw]$  is written in the four index notation as  $[\frac{2u-v}{3} \frac{2v-u}{3} \frac{-u-v}{3} w]$  [18]. A lattice direction  $[uvjw]$  can be written back in the three index notation as  $[u - j v - j w]$ . For example, the  $[120]$  lattice direction in wurtzite crystal structure is also written as  $[\frac{2-2}{3} \frac{4-1}{3} \frac{-1-2}{3} 0]$  or  $[01\bar{1}0]$  in the four index notation. The  $[01\bar{1}0]$  direction can be converted back to the three index notation as the  $[0 - (-1) 1 - (-1) 0]$  or the  $[120]$  direction. The four index notation is more popular for the Miller indices of crystal faces than for the lattice directions. In this chapter, the four index notation is used for the crystal faces, but the three index notation is used to denote the lattice directions.

The reflection/extinction conditions for the  $P6_3mc$  space group allow the reflections of the following crystal faces -  $(0002)$ ,  $(10\bar{1}0)$  and  $(11\bar{2}0)$ . Figure 6.4 shows a view along the  $[010]$  direction of the packing in wurtzite ZnO crystals. The arrangement of atoms along the  $[001]$  direction or the polar axis is the same as that of Tasker type 3 surfaces (see Figures 6.1 and 6.4). Therefore, the  $(0002)$  and the  $(000\bar{2})$  are the polar surfaces of zinc oxide crystals in the wurtzite structure. The other two families of faces -  $\{10\bar{1}0\}$  and  $\{11\bar{2}0\}$  are non-polar Tasker type 1 crystal surfaces. Figure 6.5 shows that the  $(hkil)$  and  $(\bar{h}\bar{k}\bar{i}\bar{l})$  surfaces have the same atomic structure for the two families of non-polar faces.

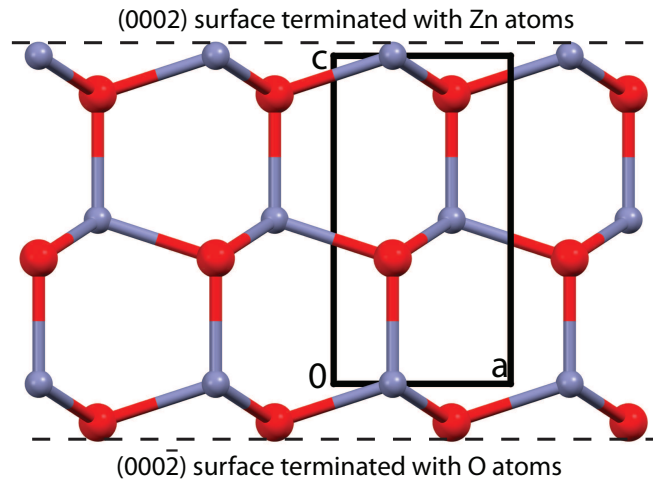


**Figure 6.4:** A view of the crystal packing in wurtzite ZnO along the  $b$  lattice direction. The dashed lines indicate the  $(0002)$  and  $(000\bar{2})$  planes that terminate with Zn and O atoms, respectively.

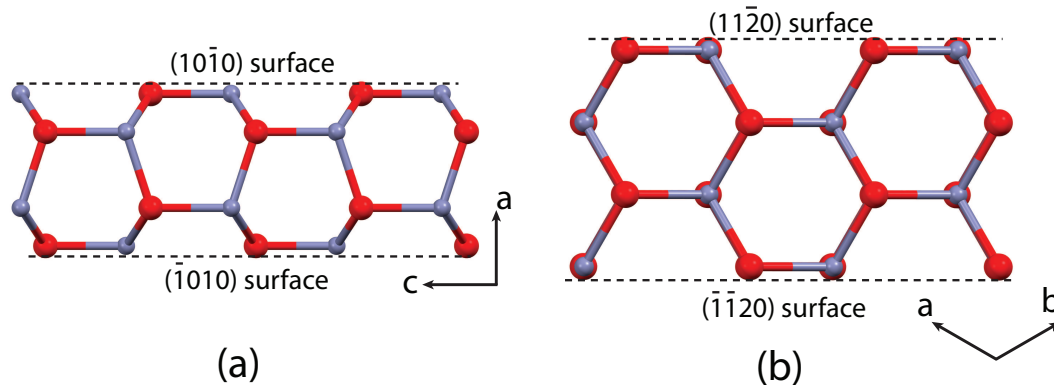


**Figure 6.5:** View of wurtzite zinc oxide crystal packing along (a)  $b$  and (b)  $c$  lattice directions showing the arrangement of Zn and O atoms in the layers of the non-polar crystal surfaces -  $(10\bar{1}0)$  and  $(11\bar{2}0)$ .

### 6.3 Building Unit and PBCs in Zinc Oxide Crystals

Hartman and Perdok established that periodic bond chains in inorganic crystals must not have a dipole moment perpendicular to the PBC direction [19]. This rule cannot be satisfied by each PBC in polar crystals due to the presence of the polar axis in the unit

cell. Except for a PBC that is parallel to the polar axis, every other PBC in a polar crystal will have a net dipole moment perpendicular to the PBC direction. This perpendicular dipole moment will be parallel to the polar axis direction.

A systematic method to identify the building unit of periodic bond chains (PBCs) in inorganic crystals was discussed in Section 2.2.1. This method is limited to the PBCs in non-polar crystals only. As mentioned above, the PBCs in polar crystals must have a residual dipole moment along the polar axis direction. Therefore, the definition of the building unit of the PBCs in polar crystals must be revised so that the collection of atoms within a building unit has a non-zero dipole moment, which must be parallel to the polar axis direction.

The modified definition of the building unit will allow the identification of the building units in ZnO wurtzite crystals. Figure 6.6 shows two choices (*I* and *II*) for the building unit within ZnO wurtzite crystals. Since the two sets of atoms share three atoms between them, only one of the sets is the unique building unit for the PBCs in ZnO crystals. Both *I* and *II* have stoichiometric composition of  $\text{Zn}_2\text{O}_2$ , and both have a net dipole moment along the *c* direction. As discussed in Section 2.2.1, if two candidates for the building unit have the same number of atoms, the one with the smallest radius of gyration may be used as the building unit. The radius of gyration ( $R_g$ ) for candidates *I* and *II* was calculated as the root mean square distance between the centroid of each candidate building unit and the atoms that constitute that candidate building unit.  $R_g$  for *II* is 1.633 Å, whereas

$R_g$  for  $I$  is equal to 1.887 Å. Therefore, the set  $II$  was chosen as the building unit for the PBCs in ZnO wurtzite crystal.

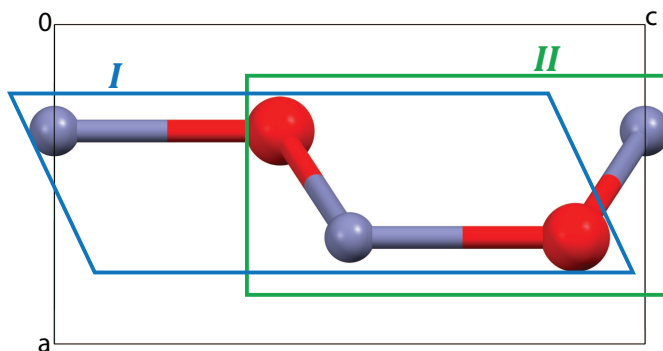
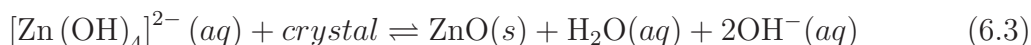


**Figure 6.6:** Two choices for the building unit of PBCs in ZnO wurtzite crystals.  $I$  and  $II$  have radii of gyration equal to 1.887 Å and 1.633 Å, respectively.

The building unit and the unit cell have the same stoichiometric composition,  $Zn_2O_2$ . Therefore, there is only one building unit present within the unit cell of wurtzite ZnO crystals, with the fractional coordinates of its centroid as  $(0.5, 0.5, 0.691)$ . Translations along the three lattice vector directions  $a$ ,  $b$ , and  $c$  provides continuous chains of building units along the  $[100]$ ,  $[010]$ ,  $[110]$  and  $[001]$  directions. The structural period of the chain of building units along the  $[001]$  direction is actually  $\frac{1}{2}[001]$ , but for the sake of simplicity  $[001]$  will be used to denote this chain.

Similar to the hydrothermal synthesis of anatase ( $TiO_2$ ) crystals discussed in Chapter 5, the growth unit for the solution synthesis of zinc oxide crystals is Zn tetrahedra. It is well known that  $[Zn(OH)_4]^{2-}$  ions are the solution phase growth units for zinc oxide synthesis from aqueous solutions at high pH (9 to 12) [20–22]. A dehydration step precedes the incorporation of the solution phase growth units into the crystal surface.

The solid-state growth unit is ZnO, which is formed due to the following reaction at the crystal surface



The building unit of ZnO wurtzite crystals contains two solid-state growth units (ZnO). Figure 6.7a shows that the slice thickness of the (0002) face contains only one solid-state growth unit (ZnO), which is equal to half the contents of the building unit. The (0002) slice containing the equatorial Zn-O bonds is more stable than the one containing the axial Zn-O bond. The periodic bond chains within the (0002) slice are shown in Figure 6.7b. The PBCs along the [100] and the [010] directions are symmetric. There are periodic bond chains that lie along the  $[\bar{1}10]$  directions as well.

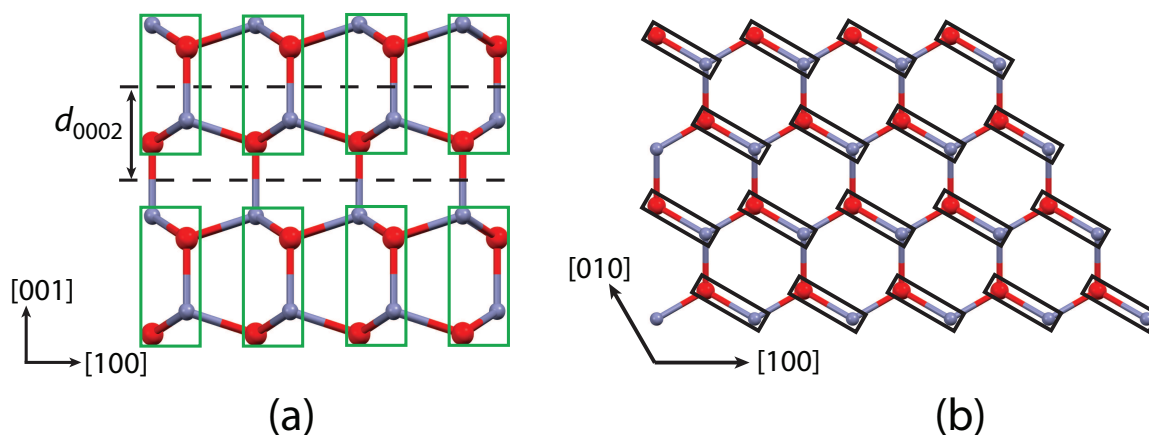


**Figure 6.7:** (a) A view of the crystal packing in wurtzite ZnO along the [010] direction. The dashed lines indicate the boundaries of the (0002) slice. The green rectangles show the contents of the building unit for wurtzite ZnO crystals. (b) Plan view of the (0002) face showing the periodic bond chains along the [100] and [010] directions. The solid-state growth units (ZnO) are shown within the black rectangles.

Figure 6.8 shows the periodic bond chain networks on the  $(10\bar{1}0)$  and the  $(11\bar{2}0)$  faces of ZnO wurtzite crystals. The PBC networks are similar for both the faces, and the  $[001]$  PBC is common to them. The  $(10\bar{1}0)$  contains  $[010]$  as the second PBC within the face, while the  $(11\bar{2}0)$  face contains  $[\bar{1}10]$  as the second PBC.

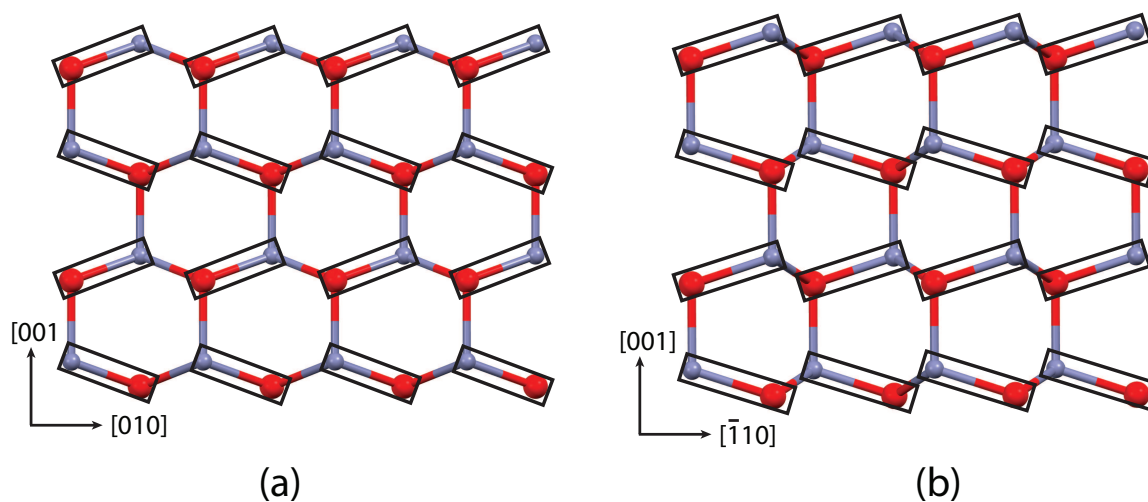


**Figure 6.8:** Plan view of the (a)  $(10\bar{1}0)$  and (b)  $(11\bar{2}0)$  faces on ZnO wurtzite crystals. The solid-state growth units ZnO are shown within black rectangles. The PBCs on the  $(10\bar{1}0)$  face are  $[010]$  and  $[001]$ , while the PBCs on the  $(11\bar{2}0)$  face are parallel to the  $[\bar{1}10]$  and  $[001]$  directions.

The interatomic interactions within the ZnO wurtzite crystal were modeled by a pairwise interaction force field that contains coulombic and Buckingham potentials [23]. It is known from density functional theory calculations that the partial charges of Zn and O atoms in bulk inorganic ZnO crystals are  $\pm 1.335$ , respectively [24]. However, force fields with full oxidation state charges ( $\pm 2.0$ ) for the Zn and O atoms have accurately reproduced the crystal structure and elastic constants of ZnO wurtzite crystals [25, 26]. Therefore, the partial charges on Zn and O atoms in the bulk crystal were assumed to

be  $\pm 2.0$  for the calculation of the interatomic interaction energies in this chapter. The lattice energy was calculated using the Madelung summation method for a supercell of size  $40 \times 40 \times 100$ . The calculated value of  $-895.0$  kcal/mol was within 5% of the lattice energy value of  $-933.4$  kcal/mol calculated from the Born-Haber-Fajans cycle [27].

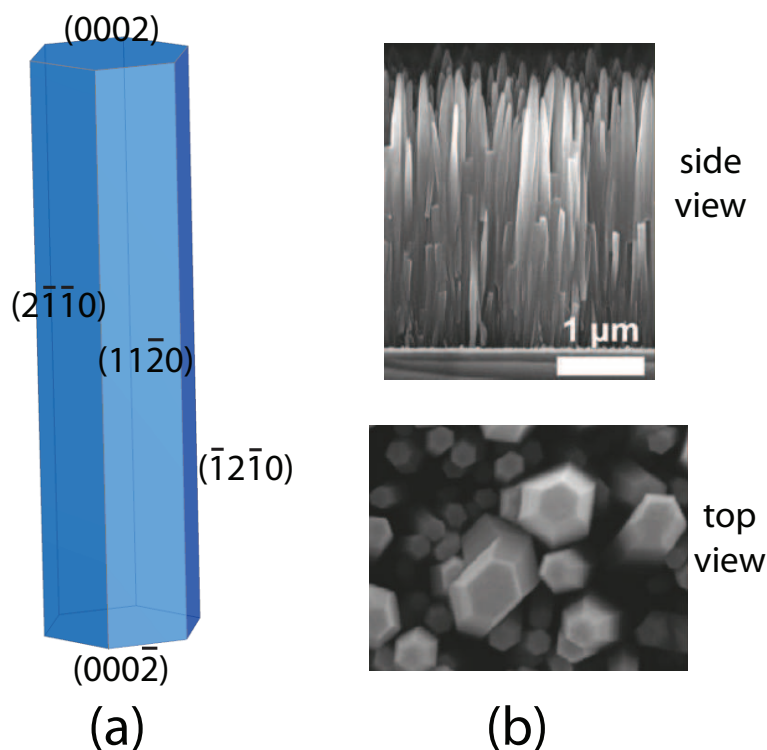
The interaction energies of the solid-state ZnO growth units along the PBC directions in wurtzite crystals were calculated while accounting for the long-range electrostatic interactions (Table 6.1). The [001] PBC has the largest magnitude of intermolecular interaction energy, which is also reflected in the high attachment energy value of the (0002) face. The attachment energies reported in Table 6.1 are averaged between the  $E_{hkl,+}^{att}$  and  $E_{hkl,-}^{att}$  values. For a polar crystal surface such as the (0002) ZnO face, the  $E_{hkl,+}^{att}$  and  $E_{hkl,-}^{att}$  may not be equal to each other, and each of these two values diverge as a function of the slice thickness. However, the average attachment energy of the (0002) face converges to a value of  $-109.4$  kcal/mol.

Figure 6.9a shows the predicted crystal morphology of ZnO wurtzite crystals using the attachment energy model. The morphology prediction is for growth under vacuum conditions without any solvent. The attachment energy model predicts rod-like crystals oriented along the [001] direction with aspect ratio  $\sim 5$ . The side faces are predicted to belong to the  $\{11\bar{2}0\}$  family of faces. ZnO crystals have been grown, from both solution and vapor, in the shape of long rods or nanowires [22, 28–31]. The attachment energy model accurately predicts the crystal habit, but the predicted morphology is symmetric along the [001] direction. Asymmetric crystal shapes with dissimilar growth rates along

**Table 6.1:**  $E_{PBC}$  values for the periodic bond chains on the ZnO wurtzite crystal surfaces

Crystal Face	$E^{att}$ (kcal/mol)	PBC vectors	$E_{PBC}$ (kcal/mol)
(0002)	-109.4	[100], [010], [110]	-51.4
		$[\bar{1}10]$ , [120], [210]	-31.8
(10 $\bar{1}0$ )	-28.8	[001]	-95.2
		[010]	-51.4
(11 $\bar{2}0$ )	-21.4	[001]	-95.2
		$[\bar{1}10]$	-77.6

the (0002) and (000 $\bar{2}$ ) faces have been reported in the literature [20, 31, 32]. Since the attachment energy of the (0002) face is the same as that of the (000 $\bar{2}$ ), the attachment energy model cannot predict asymmetric growth shapes of zinc oxide crystals.



**Figure 6.9:** (a) Morphology of ZnO wurtzite crystals predicted under vacuum growth using the attachment energy model. (b) SEM images showing the morphology of ZnO crystals grown from zinc nitrate and hexamethylenetetramine (HMT). Adapted with permission from McPeak and Baxter [31]. Copyright ©2009, American Chemical Society.

## 6.4 Stabilization of Polar {0002} ZnO surfaces

Figure 6.4 shows the stacking of atomic layers perpendicular to the polar axis direction, [001], in ZnO wurtzite crystals. Conventionally, the (0002) face is assumed to be terminated by Zn atoms and the (000 $\bar{2}$ ) face is terminated by O atoms. Tasker type 3 surfaces could be stabilized by canceling out the dipole moment perpendicular to the surface. Appendix D shows how the modification of the charges in the two outermost layers of a crystal surface could stabilize the divergent electrostatic potential above a type 3 crystal surface, and thereby stabilize the polar surface. For the (0002) surfaces of ZnO crystals, the magnitude of the surface charge needs to be reduced by 24% to quench the perpendicular dipole moment [33].

Several experimental and theoretical papers have been written that discuss the mechanism for the surface charge reduction on the polar ZnO crystal surfaces. There are three principal mechanisms for the reduction of surface charges on {0002} faces of ZnO wurtzite crystals

1. Creation of surface states and transfer of negative charge from the (000 $\bar{2}$ ) face to the (0002) face
2. Removal of surface atoms
3. Adsorption of charged impurity or foreign species on the crystal surfaces

Mechanism 1 has been well studied from a theoretical standpoint using quantum mechanics and density functional theory (DFT). Slabs of {0002} ZnO surfaces are allowed to relax and the electronic structure of the atoms in the surface layers is quantified using various functionals for the electron density. A charge transfer ranging in value from

0.17 $e$  to 0.3 $e$  was reported between the (000 $\bar{2}$ ) and the (0002) faces [34, 35], where  $e$  is the magnitude of the charge on an electron. The amount of charge transfer between the two polar surfaces was found to depend on the thickness of the {0002} slab that was considered for the DFT calculations, and a residual perpendicular dipole moment existed even after the charge transfer had taken place [36]. A transfer of charge from the O-terminated (000 $\bar{2}$ ) surface to the Zn-terminated (0002) surface must result in surface Zn atoms with lower charge density. The electronic structure of these surface Zn atoms should resemble that of metallic Zn atoms. The evidence of metallic surface states was not found in photoemission [37] and scanning tunneling spectroscopy [38] experiments performed on the (0002) ZnO crystal surface. However, metallic surface states were found on the (000 $\bar{2}$ ) surface from angle-resolved photoemission spectroscopy (ARPES) [39]. Conclusive evidence for charge transfer as the governing mechanism for the stabilization of both polar crystal surfaces of ZnO wurtzite is yet to be found.

Mechanism 3 has been used to explain the stabilization of the polar surfaces of ZnO crystals under oxygen and hydrogen-rich environments. X-ray photoelectron spectroscopy (XPS) measurements revealed that the Zn-terminated surface was stabilized by the adsorption of hydroxyl (OH) species at high partial pressures of hydrogen gas [40, 41]. The amount of surface coverage of water was also found to govern the structure of the Zn-terminated surface [42, 43]. On the O-terminated (000 $\bar{2}$ ) ZnO surface, XPS measurements showed 0.5 monolayer coverage of H atoms to form hydroxyl species [44], which

is consistent with the electrostatic concept of surface charge reduction by  $\sim 25\%$  for polarity stabilization.

The polar crystal surfaces of zinc oxide crystals have also been observed under ultra high vacuum (UHV) conditions which are typically deficient in O and H atoms. The Zn-terminated surface was found to be stabilized by triangular reconstructions observed using scanning tunneling microscopy (STM) [38, 43, 45, 46]. Figure 6.10 shows STM images of the triangular structures on the (0002) surface reported by Dulub et al. [38] and Onsten et al. [43]. Both triangular islands and pits are visible in these images, and the pits and islands are rotated by  $180^\circ$  with respect to each other. The height/depth of these triangular features was measured as about  $2.6 \text{ \AA}$  [45], which is equal to the distance between successive Zn (or O) layers along the [001] direction.

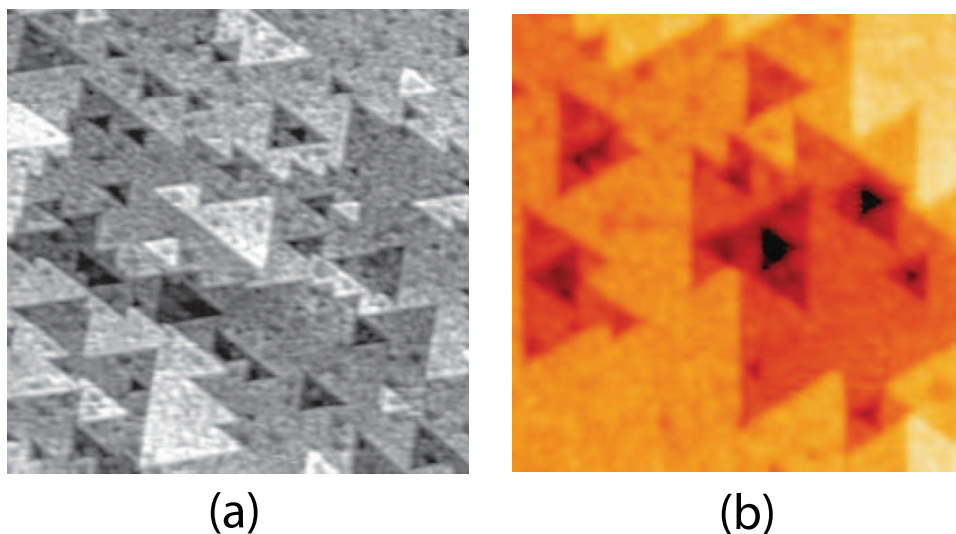


**Figure 6.10:** Scanning tunneling microscopy (STM) images of triangular islands and pits formed on clean Zn-terminated (0002) ZnO surface under UHV conditions. (a) Adapted with permission from Dulub et al [38]. Copyright ©2002 Elsevier Science B.V. Image size is  $50 \text{ nm} \times 50 \text{ nm}$ . (b) Adapted with permission from Onsten et al [43]. Copyright ©2010, American Chemical Society. Image size is  $30 \text{ nm} \times 30 \text{ nm}$ .

The edges of the triangular islands and pits are parallel to the  $[100]$ ,  $[010]$  and  $[110]$  directions. Due to the crystal structure along these directions, these islands or pits will contain more O atoms than Zn [45]. This is consistent with the second mechanism for polarity stabilization where the surface charge is reduced by the net removal of 25% Zn atoms [33]. A triangular island with 7 O atoms along its edges contains a total of 28 O atoms and 21 Zn atoms (Figure 6.11). Therefore, there are 25% less Zn atoms within the island than the number of O atoms. The size of such an island is about 20 Å, which is about the same size as some of the islands visible in the STM images (Figure 6.10). It was also reported that a 75% occupancy in the surface layers of the (0002) face provided a better fit to the results from surface x-ray diffraction experiments [47]. Therefore, the mechanism of removal of surface atoms seems to explain the stabilization of the (0002) polar surface of ZnO crystals under conditions that are deficient in O and H.

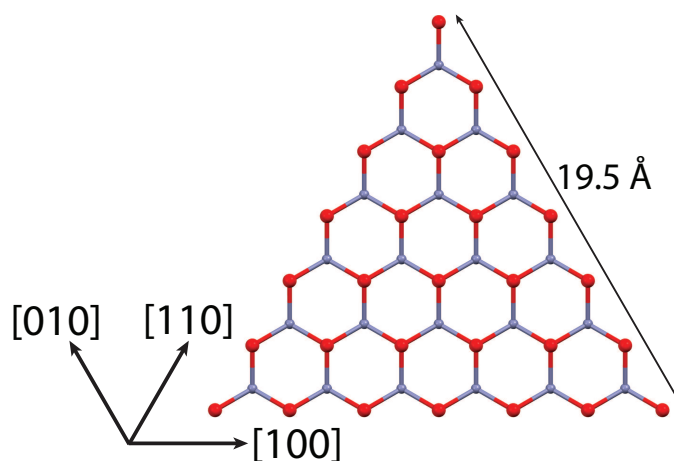


**Figure 6.11:** A hypothetical structure of a triangular island on the (0002) surface of wurtzite zinc oxide crystals. The edges of the triangular island are parallel to the  $[100]$ ,  $[010]$  and  $[110]$  directions. There are 28 O atoms and 21 Zn atoms within the island.

The STM measurements on the  $(000\bar{2})$  did not reveal any triangular islands or pits that were deficient in O atoms, therefore, mechanism 2 (removal of surface atoms) may not govern the stabilization of this polar surface. Large flat terraces interspersed with steps of hexagonal symmetry were observed [38, 44]. The stabilization of the  $(000\bar{2})$  face has been proposed to proceed by the adsorption of H atoms (mechanism 3) even under UHV conditions [44].

DFT calculations have been performed to create phase diagrams for both polar surfaces as a function of the chemical potentials of O and H [42, 45, 48, 49]. At each value of  $\mu_{\text{O}}$  and  $\mu_{\text{H}}$ , free energy minimization is carried out to predict the most probable surface structure (triangular reconstructions, adsorption overlayer, etc.). These phase diagrams agree well with experimental observations [42, 45], therefore, DFT could be used to predict the surface structure that stabilizes a polar crystal surface. However, the large amount of computational time required for these calculations to create such phase diagrams make them a more suitable tool for ‘offline’ predictions.

A simpler thermodynamic model was sought to be developed that would predict the free energy minimizing reconstruction of a polar crystal surface. Knowledge of the periodic bond chain energies would allow the model to predict the surface reconstruction with the lowest edge energy, for a fixed size of the islands/pits. The shape of these reconstructions should be governed by the Wulff construction [50], with the edge energies replacing the surface energies [51].

The periodic bond chain theory predicts that the Zn and O atoms in the (0002) slice experience the strongest intermolecular interactions along the  $\langle 100 \rangle$  family of PBCs, which includes the [100], the [010] and the [110] directions (Table 6.1). The triangular island shown in Figure 6.11 has edges parallel to the  $\langle 100 \rangle$  family of PBCs. The edge energy of such a triangular island depends on the  $E_{PBC}$  values along the  $[\bar{1}10]$ , the [120] and the [210] directions. From Table 6.1, the  $E_{PBC}$  value for the  $\langle \bar{1}10 \rangle$  family of directions is much smaller than that of the other PBCs in the (002) face. The edge energy, and therefore the free energy penalty for reconstruction, will be minimum for the triangular island with edges parallel to the  $\langle 100 \rangle$  family of directions. As a result, the PBC theory predicts a Wulff-shape of the reconstruction islands that is consistent with the shape of the triangular reconstructions observed from STM measurements [38, 43].

## 6.5 Conclusions

The stabilization of polar crystal surfaces is one of the most difficult problems in the fields of surface science and crystal growth. The electrostatic argument for stabilization is based on reducing the surface charge density on the outermost Zn and O layers by 24% to get rid of the macroscopic dipole moment perpendicular to the {0002} surfaces. Several stabilization mechanisms have been studied both theoretically and from an experimental point of view. The removal of about 25% atoms in the surface layer may be the most credible stabilization mechanism for pure ZnO crystal surfaces, although the evidence of this mechanism stabilizing the O-terminated surface is not conclusive.

Surface reconstructions that relieve the perpendicular dipole moment by the formation of triangular islands and pits with non-stoichiometric quantities of Zn and O atoms have been reported from scanning tunneling microscopy experiments. The fundamentals of a thermodynamic model have been discussed that predicts the shape of the surface reconstructions on the basis of minimizing the edge energy of the islands and pits. The periodic bond chain theory is consistent with the shape of the triangular reconstructions observed from STM measurement and the edge directions that bound the islands and pits.

A mechanistic growth model for zinc oxide wurtzite crystals requires an understanding of the kinetics of the surface reconstruction process. In presence of water, the polar surfaces are often reported to be covered by a hydroxyl (OH) overlayer [42–44]. Therefore, the growth kinetics on the polar crystal surfaces of zinc oxide will be significantly impacted by the structure and dynamics of this adsorption layer. Molecular dynamics simulations could provide valuable quantitative information about the kinetics of adsorption and reconstruction. A comprehensive crystal growth model that accounts for the dissociative adsorption of water molecules on the crystal surface and the surface reconstruction to form non-stoichiometric islands/pits will have a fighting chance of solving the mystery of how polar crystal surfaces stabilize and grow.

# Bibliography

- [1] F. Bertaut. L'Energie Electrostatique De Reseaux Ioniques. *J. Phys. et le Radium*, 13:499–505, 1952.
- [2] F. Bertaut. Physique Du Cristal - Le terme electrostatique de l'energie de surface. *Compt. Rendu.*, 246:3447–3450, 1958.
- [3] P. W. Tasker. The stability of ionic crystal surfaces. *J. Phys. C Solid State*, 12:4977, 1979.
- [4] M. Bruno, D. Aquilano, L. Pastero, and M. Prencipe. Structures and surface energies of (100) and octopolar (111) faces of halite (NaCl): an ab initio quantum-mechanical and thermodynamical study. *Cryst. Growth Des.*, 8:2163–2170, 2008.
- [5] M. Bruno, D. Aquilano, and M. Prencipe. Quantum-mechanical and thermodynamical study on the (110) and reconstructed (111) faces of NaCl crystals. *Cryst. Growth Des.*, 9:1912–1916, 2009.
- [6] V. E. Henrich and P. A. Cox. *The Surface Science of Metal Oxides*. Cambridge University Press, Cambridge, U.K., 1996.
- [7] A. Janotti and C. G. V. de Walle. Fundamentals of zinc oxide as a semiconductor. *Rep. Prog. Phys.*, 72:126501, 2009.
- [8] C. Woll. The chemistry and physics of zinc oxide surfaces. *Prog. Surf. Sci.*, 82:55, 2007.
- [9] R. Docherty, K. J. Roberts, V. Saunders, S. Black, and R. J. Davey. Theoretical analysis of the polar morphology and absolute polarity of crystalline urea. *Faraday Discuss.*, 95:11–25, 1993.
- [10] M. K. Singh and A. Banerjee. Growth and dissolution mechanism at the opposite and hemihedral faces of polar crystals. *CrystEngComm*, 15:4143–4152, 2013.
- [11] K. Srinivasan and J. N. Sherwood. Asymmetric growth of  $\alpha$ -Resorcinol crystals: Comparison of growth from the vapor phase and from aqueous solution. *Cryst. Growth Des.*, 5:1359–1370, 2005.

- [12] K. Srinivasan and J. N. Sherwood. Asymmetric growth of  $\alpha$ -Resorcinol crystals: In situ studies of crystal growth from the vapor phase. *Cryst. Growth Des.*, 11:5010–5018, 2011.
- [13] M. K. Singh, S. K. Sharma, and A. Banerjee. Asymmetrical growth and dissolution along polar axis of  $\alpha$ -resorcinol crystal: role of solvent and external environment. *CrystEngComm*, 15:8493–8503, 2013.
- [14] S. Piana, M. Reyhani, and J. D. Gale. Simulating micrometre-scale crystal growth from solution. *Nature*, 438:70–73, 2005.
- [15] K. Kihara and G. Donnay. Anharmonic thermal vibrations in ZnO. *Can. Mineral.*, 23:647–654, 1985.
- [16] M. Marezio. The crystal structure and anomalous dispersion of  $\gamma$ -LiAlO<sub>2</sub>. *Acta Crystallogr.*, 19:396–400, 1965.
- [17] P. S. Halasyamani and K. R. Poeppelmeier. Noncentrosymmetric oxides. *Chem. Mater.*, 10:2753–2769, 1998.
- [18] C. Giacobozzo, H. L. Monaco, D. Viterbo, F. Scordari, G. Gilli, G. Zanotti, and M. Catti. *Fundamentals of Crystallography*. Oxford University Press, New York, 1992.
- [19] P. Hartman and W. G. Perdok. On the relations between structure and morphology of crystals. I. *Acta Crystallogr.*, 8:49–52, 1955.
- [20] W. J. Li, E. W. Shi, W. Z. Zhong, and Z. W. Yin. Growth mechanism and growth habit of oxide crystals. *J. Cryst. Growth*, 203:186–196, 1999.
- [21] H. Zhang, D. Yang, D. Li, X. Ma, S. Li, and D. Que. Controllable growth of ZnO microcrystals by a capping-molecule-assisted hydrothermal process. *Cryst. Growth Des.*, 5:547–550, 2005.
- [22] J. J. Richardson and F. F. Lange. Controlling low temperature aqueous synthesis of ZnO. 1. Thermodynamic analysis. *Cryst. Growth Des.*, 9:2570–2575, 2009.
- [23] A. J. Kulkarni, M. Zhou, and F. J. Ke. Orientation and size dependence of the elastic properties of zinc oxide nanobelts. *Nanotechnology*, 16:2749, 2005.
- [24] F. Labat, I. Ciofini, and C. Adamo. Modeling ZnO phases using a periodic approach: From bulk to surface and beyond. *J. Chem. Phys.*, 131:044708, 2009.
- [25] L. Whitmore, A. A. Sokol, and C. A. Catlow. Surface structure of zinc oxide (10 $\bar{1}$ 0), using an atomistic, semi-infinite treatment. *Surf. Sci.*, 498:135–146, 2002.

- [26] C. R. A. Catlow, S. A. French, A. A. Sokol, A. A. Al-Sunaidi, and S. M. Woodley. Zinc oxide: A case study in contemporary computational solid state chemistry. *J. Comput. Chem.*, 29:2234–2249, 2008.
- [27] H. Jenkins. *Handbook of Chemistry and Physics*, chapter Lattice Energies, page 27. CRC Press, 1992.
- [28] S. C. Lyu, Y. Zhang, C. J. Lee, H. Ruh, and H. J. Lee. Low-temperature growth of ZnO nanowire array by a simple physical vapor-deposition method. *Chem. Mater.*, 15:3294–3299, 2003.
- [29] K. Govender, D. S. Boyle, P. B. Kenway, and P. O’Brien. Understanding the factors that govern the deposition and morphology of thin films of ZnO from aqueous solution. *J. Mater. Chem.*, 14:2575–2591, 2004.
- [30] A. M. Peiro, J. A. Ayllon, J. Peral, X. Domenech, and C. Domingo. Microwave activated chemical bath deposition (MW-CBD) of zinc oxide: Influence of bath composition and substrate characteristics. *J. Cryst. Growth*, 285:6–16, 2005.
- [31] K. M. McPeak and J. B. Baxter. ZnO nanowires grown by chemical bath deposition in a continuous flow microreactor. *Cryst. Growth Des.*, 9:4538–4545, 2009.
- [32] L. Xu, Y.-L. Hu, C. Pelligra, C.-H. Chen, L. Jin, H. Huang, S. Sithambaram, M. Aindow, R. Joesten, and S. L. Suib. ZnO with different morphologies synthesized by solvothermal methods for enhanced photocatalytic activity. *Chem. Mater.*, 21:2875–2885, 2009.
- [33] C. Noguera. Polar oxide surfaces. *J. Phys.: Condens. Matter*, 12:R367, 2000.
- [34] J. M. Carlsson. Electronic structure of the polar ZnO{0001}-surfaces. *Comput. Mater. Sc.*, 22:24–31, 2001.
- [35] A. Wander, F. Schedin, P. Steadman, A. Norris, R. McGrath, T. S. Turner, G. Thornton, and N. M. Harrison. Stability of polar oxide surfaces. *Phys. Rev. Lett.*, 86:3811–3814, 2001.
- [36] B. Meyer and D. Marx. Density-functional study of the structure and stability of ZnO surfaces. *Phys. Rev. B*, 67:035403, 2003.
- [37] R. Girard, O. Tjernberg, G. Chiaia, S. Soderholm, U. Karlsson, C. Wigren, H. Nylén, and I. Lindau. Electronic structure of ZnO(0001) studied by angle-resolved photoelectron spectroscopy. *Surf. Sci.*, 373:409–417, 1997.
- [38] O. Dulub, L. A. Boatner, and U. Diebold. STM study of the geometric and electronic structure of ZnO(0001)-Zn, (000 $\bar{1}$ )-O, (10 $\bar{1}$ 0), and (11 $\bar{2}$ 0) surfaces. *Surf. Sci.*, 519:201–217, 2002.

- [39] L. F. J. Piper, A. R. H. Preston, A. Fedorov, S. W. Cho, A. DeMasi, and K. E. Smith. Direct evidence of metallicity at ZnO (000 $\bar{1}$ )-(1  $\times$  1) surfaces from angle-resolved photoemission spectroscopy. *Phys. Rev. B*, 81:233305, 2010.
- [40] M. Valtiner, S. Borodin, and G. Grundmeier. Preparation and characterisation of hydroxide stabilised ZnO(0001)-Zn-OH surfaces. *Phys. Chem. Chem. Phys.*, 9:2406–2412, 2007.
- [41] E. D. Batyrev and J. C. van den Heuvel. Modification of the ZnO(0001)-Zn surface under reducing conditions. *Phys. Chem. Chem. Phys.*, 13:13127–13134, 2011.
- [42] M. Valtiner, M. Todorova, G. Grundmeier, and J. Neugebauer. Temperature stabilized surface reconstructions at polar ZnO(0001). *Phys. Rev. Lett.*, 103:065502, 2009.
- [43] A. Onsten, D. Stoltz, P. Palmgren, S. Yu, M. Gothelid, and U. O. Karlsson. Water adsorption on ZnO(0001): Transition from triangular surface structures to a disordered hydroxyl terminated phase. *J. Phys. Chem. C*, 114:11157–11161, 2010.
- [44] J. V. Lauritsen, S. Porsgaard, M. K. Rasmussen, M. C. R. Jensen, R. Bechstein, K. Meinander, B. S. Clausen, S. Helveg, R. Wahl, G. Kresse, and F. Besenbacher. Stabilization principles for polar surfaces of ZnO. *ACS Nano*, 5:5987–5994, 2011.
- [45] O. Dulub, U. Diebold, and G. Kresse. Novel stabilization mechanism on polar surfaces: ZnO(0001)-Zn. *Phys. Rev. Lett.*, 90:016102, 2003.
- [46] F. Ostendorf, S. Torbrügge, and M. Reichling. Atomic scale evidence for faceting stabilization of a polar oxide surface. *Phys. Rev. B*, 77:041405, 2008.
- [47] N. Jedrecy, M. Sauvage-Simkin, and R. Pinchaux. The hexagonal polar ZnO (0001) - (1  $\times$  1) surfaces: structural features as stemming from X-ray diffraction. *Appl. Surf. Sci.*, 162-163:69–73, 2000.
- [48] B. Meyer. First-principles study of the polar O-terminated ZnO surface in thermodynamic equilibrium with oxygen and hydrogen. *Phys. Rev. B*, 69:045416, 2004.
- [49] R. Wahl, J. V. Lauritsen, F. Besenbacher, and G. Kresse. Stabilization mechanism for the polar ZnO(000 $\bar{1}$ )-O surface. *Phys. Rev. B*, 87:085313, 2013.
- [50] G. Wulff. Zur frage der geschwindigkeit des wachsthums und der auflösung der krystallflächen. *Z. Kristallogr.*, 34:449, 1901.
- [51] M. A. Lovette and M. F. Doherty. Predictive modeling of supersaturation-dependent crystal shapes. *Cryst. Growth Des.*, 12:656–669, 2012.

# Chapter 7

## Conclusions and Future Work

### 7.1 Overview and Summary

In this dissertation, a predictive model for the crystal shapes of inorganic solids grown from solution has been developed. The model unifies a detailed description of the solid-state interactions within inorganic crystals with a molecular level understanding of the effect of the growth medium on the kinetics of inorganic crystal growth.

A systematic method has been developed for the identification of the periodic bond chain (PBC) directions in inorganic crystals by using the concept of a building unit of a PBC. The long-range electrostatic interactions between the ionic growth units are accounted for, to calculate the energy values relevant to the crystal growth model. The variation of the partial charges of the surface growth units is captured using an easy-to-implement method which is based on the bond valence model [1]. Accurate information of the surface relaxation and solvent structure from molecular simulations is used as input for the partial charge calculations. A space partitioning method is applied to calculate

the potential energy of a growth unit situated in the kink site position. The interaction energies with the solid-state neighbors are calculated by assigning the correct partial charges to the atoms in the surface layer.

A steady-state master equation is used to derive a general expression for the kink incorporation rate in terms of the attachment and detachment fluxes. These fluxes depend on the solution composition as well as the kink site potential energies, the latter calculated using the space partitioning method. Thus, the step velocity of spiral edges, and the growth rates of crystal faces under the spiral growth regime are calculated within a mechanistic framework that accounts for the solid-state and the solution phase chemistry. The model correctly predicts the steady-state morphologies of inorganic crystals such as calcite and aragonite grown from solution at ambient conditions.

The PBC theory has also been applied to identify the directions of strongest intermolecular interactions in metal oxides such as  $\text{TiO}_2$  (anatase) and  $\text{ZnO}$  (wurtzite structure). *Ex situ* AFM experiments on the anatase crystal surfaces grown using hydrothermal synthesis suggest that in addition to the oriented attachment mechanism [2], a layered growth mechanism could also be active. The shape of the triangular reconstructions believed to stabilize the polar crystal surfaces in  $\text{ZnO}$  wurtzite is found to be consistent with the shape obtained from the Wulff condition.

## 7.2 Directions for Future Work

### 7.2.1 Modeling

#### Effect of Additives

This dissertation focuses on predicting the steady-state growth morphology of inorganic crystals. However, the native or ‘typical’ crystal morphology may not be the most functionally desirable morphology. For example, the native morphology of TiO<sub>2</sub> anatase crystals is tetragonal bipyramidal dominated by the {101} family of faces (see Figure 5.5b). However, the {004} family of faces show higher catalytic activity towards water dissociation reaction [3]. Therefore, the desired morphology of anatase crystals should expose higher surface area of the {004} surfaces. Thus, one of the future directions within the modeling framework is to extend this mechanistic growth model to predict the effect of various growth modifiers or additives on the crystal growth rates and the steady-state morphology of inorganic crystals.

There is a considerable body of work on predicting the effect of impurities or additive species on the spiral growth on crystal surfaces [4–6]. Cabrera and Vermilyea [4] developed a model, which has since been referred to as the “step-pinning” model, which suggested that additive molecules block the attachment of new growth units to the step edge and slow down the growth kinetics. There is a minimum supersaturation below which the step does not advance [7]. ‘Spiral-pinning’ [5, 6] is another mechanism that focuses on the effect of impurities/additives on spiral growth. This mechanism suggests

that the growth retardation is due to an increase in the critical length of a spiral edge in the presence of the additive species along the edge. There are some other mechanisms by which additive species can disrupt the crystal growth process and the reader is referred to an article by De Yoreo and Vekilov [7] that discusses those mechanisms in further detail.

The mechanistic model presented in this dissertation could be adapted to account for the effect of the additive species on the crystal growth process. The composition of the solution in the expressions for the kink attachment and detachment fluxes (Equations 3.13 and 3.14) will reflect the presence of the additive species in the solution. The solvation structure of an ionic impurity, such as  $\text{Mg}^{2+}$  in calcite growth, will determine the kinetics of attachment and detachment of the impurity ions into the kink sites (Equation 3.26).

### **Free Energy Barriers for Kink Attachment/Detachment**

The expressions for the attachment and detachment fluxes into the kink sites in Section 3.4.2 were derived based on the assumption that there is a single free energy barrier between a completely solvated growth unit situated close to the crystal-solution interface and the growth unit incorporated into a kink site along the edge (Figure 3.5). The free energy landscape of the kink attachment/detachment process on several inorganic crystal surfaces has been mapped using molecular simulations and multiple intermediate steps were found to exist in the kink attachment/detachment process [8–10].

Depending on the intermediate step with the highest free energy barrier, the attachment/detachment fluxes may not depend on the mole fraction of solute ions in the bulk solution, as shown in equations 3.13 and 3.14. For example, if the rate-limiting step was the kink site attachment of a growth unit from a surface adatom position, the mole fraction prefactor in equation 3.13 would be equal to the mole fraction of the growth unit species adsorbed on the crystal surface [11]. Moreover, if the rate-limiting step is not the same for each growth unit along a spiral edge, the surface adsorbed mole fractions cannot be estimated from the model by calculating a local solubility product  $K'_{sp}$  from equation 3.24. In such cases, molecular dynamics simulations could be used to calculate the adsorbed mole fractions [12].

Therefore, molecular dynamics simulations coupled with rare-event methods such as transition path sampling [13] or metadynamics [14], that correctly identify the rate-limiting step, the free energy barriers for the kink attachment and detachment processes, and the appropriate mole fraction prefactors for the attachment/detachment fluxes, could be used as inputs to the mechanistic growth model to obtain accurate expressions for the kink incorporation rate on the spiral edges of inorganic crystal surfaces.

### **Dynamics of the Step Edge Structure**

The model developed in this dissertation assumes that the time scale for the thermal rearrangement of a step edge is much smaller than the time scale for kink attachment. Therefore, the edge structure is assumed to be in quasi-equilibrium with the solution and

the density of kink sites is governed by the Boltzmann distribution for the rearrangement of microstates that expose kink sites. Appendix C makes a quantitative estimation of the time scales for the edge rearrangement and kink incorporation, and concluded that for growth on inorganic crystal surfaces at high supersaturation values  $S > 1.2$ , the kink incorporation may happen simultaneously with edge rearrangement.

At high supersaturation values, 1D nucleation may also contribute to the creation of kink sites along the edge. 1D nucleation involves the attachment of a growth unit in a step adatom position (Figure 7.1), and is a source of additional kink sites where kink incorporation could subsequently occur. In an ongoing work, the density of kink sites created due to 1D nucleation has been proposed to be a function of supersaturation  $S$  and the density of step adatom growth units at equilibrium [15].

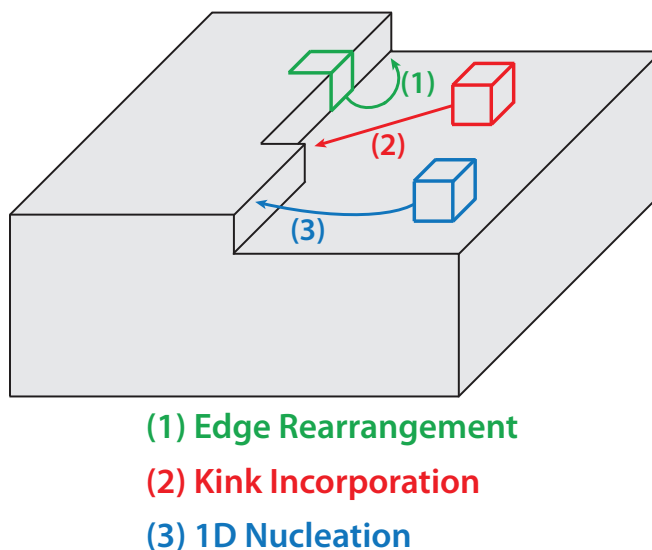


**Figure 7.1:** An illustrative representation of the following molecular processes occurring near a step edge of a crystal surface - (1) edge rearrangement, (2) kink incorporation, and (3) 1D nucleation.

The structure of a step edge exposed to a supersaturated solution will be a function of the relative rates of three processes - edge rearrangement, kink incorporation and 1D nucleation. The steady-state master equation (Equation 3.9) may need to be modified to allow the kinetics of 1D nucleation or edge rearrangement to govern the transition rates between any two kink types or states.

### **Molecular Design of Intergrown Mullite Crystals**

Mullite refers to a class of aluminosilicate minerals with an alumina ( $\text{Al}_2\text{O}_3$ ) to silica ( $\text{SiO}_2$ ) stoichiometric ratio that typically varies from 5:4 to 3:1 [16]. Acicular or rod-like mullite crystals exhibit favorable material properties such as low density, high porosity and mechanical strength at high temperatures [17]. These properties have facilitated the development of diesel particulate filters that contain crystalline films of mullite [18].

Intergrowth of rod-shaped mullite crystals provides a honeycomb-like microstructure with high mechanical strength [16]. The design of such honeycomb structures with a large fraction of intergrown mullite crystals requires a mechanistic understanding of the growth conditions, including the effect of additives, which could yield crystals with non-convex shapes. The reported synthesis of non-convex shapes of Engelhard Titanium Silicate (ETS) [19, 20] and MnO [21] crystals could provide mechanistic insights into the causality of non-convex crystal morphologies. A possible change in the rate-limiting step from surface integration to diffusion-controlled kinetics may also result in a higher fraction of crystals with non-convex shapes. A crystal growth modeling effort for the

design of intergrown mullites with application as composite structural materials [22], could begin with studying the growth of sillimanite ( $\text{Al}_2\text{SiO}_5$ ) crystals, which has the simplest mullite composition of 1:1 stoichiometric ratio of alumina to silica.

### 7.2.2 Experiments

The characterization of growth features on crystal surfaces using *ex situ* atomic force microscopy (AFM) was described in Chapter 5 of this dissertation. *In situ* AFM experiments must be carried out to obtain conclusive evidence of the mechanisms that govern the growth of hydrothermally grown crystals (e.g., anatase). *In situ* AFM techniques have been developed to observe crystal growth at room temperature [23–26] as well as higher temperatures [27, 28]. These techniques allow accurate measurement of the step velocities, critical lengths, and spacing between adjacent steps along the spiral edges of crystal surfaces [29–31]. The measured values of these quantities could be compared with the model predictions to validate the mechanistic growth model for inorganic crystal systems other than calcite. The specific action of an additive species on the step velocity of spiral edges can also be observed using *in situ* AFM experiments [32, 33]. With the advent of commercial AFM instruments that can operate at high temperatures (up to  $300^\circ$ ) [34], there is an exciting opportunity to carry out *in situ* AFM experiments that elucidate the relevant growth mechanism on crystal surfaces of inorganic oxides such as  $\text{TiO}_2$ ,  $\text{ZnO}$ , etc.

The structure and the stoichiometry of the solution phase growth unit in the hydrothermal synthesis of inorganic crystals provides valuable insights into the structure of the solid-state growth unit. Solution characterization techniques such as *in situ* Raman spectroscopy [35], solution phase nuclear magnetic resonance (NMR) [36], neutron scattering [37], etc., provide information about the structure of the growth unit in the solution, and of the solvation shell around it. Measurements of the solvation shell coordination and the distances between the solute and the solvent molecules from these experimental techniques could be used by the mechanistic model as an input to calculate the kink detachment work ( $\Delta W$ ) from equation 3.26. Alternatively, such measurements could be used to check the predictions of such quantities from molecular dynamics simulations.

# Bibliography

- [1] I. D. Brown. *The Chemical Bond in Inorganic Chemistry: The Bond Valence Model*. Oxford University Press, 2002.
- [2] R. Penn and J. F. Banfield. Morphology development and crystal growth in nanocrystalline aggregates under hydrothermal conditions: insights from titania. *Geochim. Cosmochim. Acta*, 63:1549–1557, 1999.
- [3] X.-Q. Gong and A. Selloni. Reactivity of anatase TiO<sub>2</sub> nanoparticles: The role of the minority (001) surface. *J. Phys. Chem. B*, 109:19560–19562, 2005.
- [4] N. Cabrera and D. Vermilyea. *Growth and Perfection of Crystals*, chapter The Growth of Crystals from Solution, pages 393–410. New York: Wiley, 1958.
- [5] J. P. Sizemore and M. F. Doherty. A new model for the effect of molecular imposters on the shape of faceted molecular crystals. *Cryst. Growth Des.*, 9:2637–2645, 2009.
- [6] Z. B. Kuvadia and M. Doherty. Effect of structurally similar additives on crystal habit of organic molecular crystals at low supersaturation. *Cryst. Growth Des.*, 13:1412–1428, 2013.
- [7] J. J. DeYoreo and P. G. Vekilov. *Biomineralization*, chapter Principles of Crystal Nucleation and Growth, pages 57–93. Washington, DC: Mineralogical Society of America, 2003.
- [8] S. Kerisit and S. C. Parker. Free energy of adsorption of water and metal ions on the {10 $\bar{1}$ 4} calcite surface. *J. Am. Chem. Soc.*, 126:10152–10161, 2004.
- [9] S. Piana, F. Jones, and J. D. Gale. Assisted desolvation as a key kinetic step for crystal growth. *J. Am. Chem. Soc.*, 128:13568–13574, 2006.
- [10] A. G. Stack, P. Raiteri, and J. D. Gale. Accurate rates of the complex mechanisms for growth and dissolution of minerals using a combination of rare-event theories. *J. Am. Chem. Soc.*, 134:11–14, 2012.
- [11] X. Y. Liu, E. S. Boek, W. J. Briels, and P. Bennema. Prediction of crystal growth morphology based on structural analysis of the solid-fluid interface. *Nature*, 374:342–345, 1995.

- [12] X. Y. Liu, E. S. Boek, W. J. Briels, and P. Bennema. Analysis of morphology of crystals based on identification of interfacial structure. *J. Chem. Phys.*, 103:3747–3754, 1995.
- [13] B. Peters. Recent advances in transition path sampling: accurate reaction coordinates, likelihood maximisation and diffusive barrier-crossing dynamics. *Mol. Simul.*, 36:1265–1281, 2010.
- [14] A. Laio and M. Parrinello. Escaping free-energy minima. *Proc. Natl. Acad. Sci. U.S.A.*, 99:12562–12566, 2002.
- [15] M. N. Joswiak, M. F. Doherty, and B. Peters. Is 1D nucleation important in kink site generation? (*manuscript in preparation*), 2014.
- [16] A. J. Pyzik, C. S. Todd, and C. Han. Formation mechanism and microstructure development in acicular mullite ceramics fabricated by controlled decomposition of fluorotopaz. *J. Eur. Ceram. Soc.*, 28:383 – 391, 2008.
- [17] C.-H. Hsiung, A. Pyzik, F. D. Carlo, X. Xiao, S. Stock, and K. Faber. Microstructure and mechanical properties of acicular mullite. *J. Eur. Ceram. Soc.*, 33:503–513, 2013.
- [18] A. J. Pyzik and C. G. Li. New design of a ceramic filter for diesel emission control applications. *Int. J. Appl. Ceram. Technol.*, 2:440–451, 2005.
- [19] B. Yilmaz, P. Q. Miraglia, J. Warzywoda, and A. Sacco. Synthesis of titanosilicate ETS-4 with controlled morphology and investigation of its crystallization kinetics. *Microporous Mesoporous Mater.*, 71:167–175, 2004.
- [20] Y.-Q. Zhang, W. Zhou, S. Liu, and A. Navrotsky. Controllable Morphology of Engelhard Titanium Silicates ETS-4: Synthetic, Photocatalytic, and Calorimetric Studies. *Chem. Mater.*, 23:1166–1173, 2011.
- [21] T. Ould-Ely, D. Prieto-Centurion, A. Kumar, W. Guo, W. V. Knowles, S. Asokan, M. S. Wong, I. Rusakova, A. Luttge, and K. H. Whitmire. Manganese(II) Oxide Nanohexapods: Insight into Controlling the Form of Nanocrystals. *Chem. Mater.*, 18:1821–1829, 2006.
- [22] H. Fujita, G. Jefferson, R. M. McMeeking, and F. W. Zok. Mullite/Alumina Mixtures for Use as Porous Matrices in Oxide Fiber Composites. *J. Am. Ceram. Soc.*, 87:261–267, 2004.
- [23] G. T. Palocz, B. L. Smith, P. K. Hansma, D. A. Walters, and M. A. Wendman. Rapid imaging of calcite crystal growth using atomic force microscopy with small cantilevers. *Appl. Phys. Lett.*, 73:1658–1660, 1998.

- [24] C. M. Pina, U. Becker, P. Risthaus, D. Bosbach, and A. Putnis. Molecular-scale mechanisms of crystal growth in barite. *Nature*, 395:483–486, 1998.
- [25] H. H. Teng, P. M. Dove, C. A. Orme, and J. J. De Yoreo. Thermodynamics of calcite growth: Baseline for understanding biomineral formation. *Science*, 282:724–727, 1998.
- [26] J. D. Rimer, Z. An, Z. Zhu, M. H. Lee, D. S. Goldfarb, J. A. Wesson, and M. D. Ward. Crystal Growth Inhibitors for the Prevention of L-Cystine Kidney Stones Through Molecular Design. *Science*, 330:337–341, 2010.
- [27] A. I. Lupulescu and J. D. Rimer. In situ imaging of silicalite-1 surface growth reveals the mechanism of crystallization. *Science*, 344:729–732, 2014.
- [28] J. D. Rimer, M. Kumar, R. Li, A. I. Lupulescu, and M. D. Oleksiak. Tailoring the physicochemical properties of zeolite catalysts. *Catal. Sci. Technol.*, (in press), 2014.
- [29] H. Teng, P. M. Dove, and J. J. DeYoreo. Reversed calcite morphologies induced by microscopic growth kinetics: insight into biomineralization. *Geochim. Cosmochim. Acta*, 63:2507–2512, 1999.
- [30] M. Kowacz, C. Putnis, and A. Putnis. The effect of cation:anion ratio in solution on the mechanism of barite growth at constant supersaturation: Role of the desolvation process on the growth kinetics. *Geochim. Cosmochim. Acta*, 71:5168–5179, 2007.
- [31] K. Larsen, K. Bechgaard, and S. L. S. Stipp. The effect of the  $\text{Ca}^{2+}$  to  $\text{CO}_3^{2-}$  activity ratio on spiral growth at the calcite  $\{10\bar{1}4\}$  surface. *Geochim. Cosmochim. Acta*, 74:2099–2109, 2010.
- [32] J. J. De Yoreo and P. M. Dove. Shaping crystals with biomolecules. *Science*, 306:1301–1302, 2004.
- [33] P. Dandekar and M. F. Doherty. Imaging crystallization. *Science*, 344:705–706, 2014.
- [34] J. Li and M. Rutgers. Asylum Research. Private Communication, 2014.
- [35] F. Fan, Z. Feng, G. Li, K. Sun, P. Ying, and C. Li. In Situ UV Raman Spectroscopic Studies on the Synthesis Mechanism of Zeolite X. *Chem. Eur. J.*, 14:5125–5129, 2008.
- [36] C. A. Hunter, J. F. McCabe, and A. Spitaleri. Solvent effects of the structures of prenucleation aggregates of carbamazepine. *CrystEngComm*, 14:7115–7117, 2012.
- [37] R. C. Burton, E. S. Ferrari, R. J. Davey, J. L. Finney, and D. T. Bowron. Relationship between solution structure and phase behavior: A neutron scattering study of concentrated aqueous hexamethylenetetramine solutions. *J. Phys. Chem. B*, 113:5967–5977, 2009.

# Appendix A

## Step-by-step Methodology for Crystal Morphology Prediction of Inorganic Solids

1. **Input crystallography of the inorganic solid:** The crystal structure and unit cell information is obtained as an input from single crystal X-ray diffraction data available in commonly used databases such as - Cambridge Structural Database, Inorganic Crystal Structure Database (ICSD), American Mineralogist Crystal Structure Database, etc. The list of symmetry operators from the crystallographic information file (CIF) must be checked to ensure that there is an inversion symmetry operator within the unit cell. If the inversion operator is not present, an intrinsic dipole moment is present within the unit cell and the subsequent steps cannot be applied to model crystal growth for such systems. This method works only for crystals with non-polar unit cells.
2. **Input the force field and partial charges:** An intermolecular force field that is appropriate to study the crystal growth of this particular inorganic solid is required.

Buckingham potential is commonly used to describe the short range interactions in typical inorganic solids. The parameters of the Buckingham potential and the bulk partial charges of all the atoms are needed as an input to the crystal growth model. Molecular simulations or quantum mechanical calculations may be carried out to obtain the partial charges and short range interaction parameters by fitting to structural and mechanical properties of the bulk crystal that are experimentally known. The parameter values from an existing force field may be utilized if that force field accurately predicts the experimentally obtained properties of the solid. A molecular simulation package such as GULP [1] is extremely useful to fit force field parameters for inorganic solids.

- 3. Identify the building unit of PBCs:** The unit cell packing is constructed from the asymmetric unit information and all the symmetry operators that are present in the unit cell. In some cases, an entire building unit may be spread across two adjacent unit cells. Therefore, a supercell is created that is 1.5 times the length of the lattice constants in each of three directions. A stoichiometric arrangement of atoms with zero dipole moment is identified from the contents of this supercell.

The dipole moment of any arrangement of  $n$  atoms is calculated as follows

$$\vec{\mu} = \sum_{i=1}^n q_i \vec{r}_i \quad (\text{A.1})$$

where  $q_i$  is the partial charge and  $\vec{r}_i$  is the position vector of atom  $i$ . Amongst all the stoichiometric groups of atoms with zero dipole moment, choose the groups with fewest number of atoms such that the atoms are located ‘close’ to each other.

- 4. Pack the entire unit cell with building units:** If multiple stoichiometric arrangements of atoms are found that have zero dipole moment and the same number of atoms, the symmetry relationship between these arrangements must be checked. If a single symmetry operator (from the list of all symmetry operators in the space group table) can be applied to each atom in an arrangement to obtain a second stoichiometric arrangement, the two arrangements are related to each other by that particular symmetry operator and only one of the building units is independent. Once an independent building unit within the unit cell is identified, the remaining symmetry operators are applied to each atom within the building unit to obtain the remaining building unit arrangements within the unit cell.
- 5. Identification of PBC directions:** Translational operators are applied to the unit cell contents along the three crystallographic axes to create a large supercell (e.g.,  $4 \times 4 \times 4$  times the unit cell). Any building unit inside the central unit cell is considered as a central building unit and all the building units surrounding it are accounted for to identify chains of building units that run continuously throughout the supercell packing. The crystallographic direction of each of these chains is obtained by joining the centers of mass of all the building units present along the chain. Each of these directions is a Periodic Bond Chain (PBC) vector. The actual PBC vector is multiplied by the lowest common multiple of the denominators of its fractional coordinates to create a vector of the form  $[uvw]$  such that  $u$ ,  $v$ ,  $w$  are all integers.

6. **Identify step edge structures on every face:** A list of all possible  $(hkl)$  values for the faces present on the crystal surface is obtained from the extinction conditions listed in the crystallography tables for the specific space group. The PBC vectors that are perpendicular to the  $[hkl]$  vector are short listed from the list of PBC vectors obtained in step 5. The PBCs that will be present in the crystal face  $(hkl)$  are thus obtained. Let  $(hkl)$  be a face with two PBC vectors,  $\vec{v}_1$  and  $\vec{v}_2$ , present on it. The chain of building units is constructed along both  $\vec{v}_1$  and  $\vec{v}_2$  directions. The length of the kink sites along each of the chains is calculated as the distance between the adjacent growth units along the respective PBC directions. If the thickness of the  $\vec{v}_1$  chain along  $\vec{v}_2$  direction is more than the length of the kink site along the  $\vec{v}_2$  direction, the chain of building units along  $\vec{v}_1$  must be further decomposed into a chain of growth units (also known as the step edge) along  $\vec{v}_1$ . If the thickness of the chain is exactly equal to the length of the kink site, then the chain of building units is exactly identical to the step edge structure. If there is another PBC vector  $\vec{v}_3$  present on the  $(hkl)$  face, the thickness of the  $\vec{v}_1$  chain along  $\vec{v}_3$  must be similarly compared with the size of the kink site along  $\vec{v}_3$  chain to determine the step edge structure along  $\vec{v}_1$ . The step edge structure thus obtained must result in a stoichiometric chain of growth units that has zero dipole moment perpendicular to  $\vec{v}_1$  direction. The step edge must not share any interactions with another step edge within that face. Similarly, a decomposition of the chain of

building units along every other PBC direction will result in identification of chains of growth units along each of the PBC vectors present in the  $(hkl)$  face.

**7. Identify all the F faces:** The  $(hkl)$  slice is constructed of thickness equal to the interplanar spacing  $d_{hkl}$ . The slice boundaries may be shifted in the  $[hkl]$  direction to obtain a slice that is stoichiometric and has zero dipole moment along the  $[hkl]$  direction. If a continuous chain of growth units along a PBC vector is contained within the slice, then that PBC vector is said to be present within the slice. All the PBCs contained within the slice  $(hkl)$  are thus obtained. The  $(hkl)$  crystal face is classified as an F, S or K face depending on if there are two (or more), one or zero PBCs are present within the  $(hkl)$  slice, respectively.

**8. Calculate solid state bond valences from bulk partial charges:** Bond valence parameters are required to calculate the partial charges of atoms in various surface positions. The bond valence parameters  $R_0$  and  $b$  for every pair of atoms are obtained from a database available online at

[http://www.ccp14.ac.uk/ccp/web-mirrors/i\\_d\\_brown/bond\\_valence\\_param/bvparam2006.c](http://www.ccp14.ac.uk/ccp/web-mirrors/i_d_brown/bond_valence_param/bvparam2006.c)

The interatomic distances between all the pairs of atoms in the bulk crystal are calculated from the fractional coordinate information using the crystal structure. For atoms in the surface layer, the exact atomic positions are calculated from the surface relaxation information that is an input to the growth model. The relaxation of the surface layer atoms (in presence of the solvent) can be measured experimentally or predicted using molecular simulations. The amount of surface relaxation

is used to recalculate the distances between atoms in the surface and in the underneath layers. The bond valence  $s_{ij}$  shared between atoms  $i$  and  $j$  is calculated from equation 2.4. The oxidation state  $q_{i,OS}$  on the atoms  $i$  is calculated from equation 2.3. Equation 2.6 is used to obtain the normalized bond valence  $s'_{ij}$  from  $s_{ij}$ ,  $q_{i,OS}$  and the partial charge  $q_{i,actual}$  of atom  $i$  in the bulk crystal obtained in step 2.

9. **Input solvent structure information around surface sites:** The solvent structure next to the crystal surface and near the spiral edges (parallel to the PBC vectors) is required as an input to the model. There are three types of surface sites (surface, edge and kink) that are relevant for the energy calculations. The number of solvent molecules surrounding each type of surface site and their interatomic distances from all the atoms in that surface site is needed to calculate the bond valence shared between the surface site atoms and the atoms of the solvent molecule, as well as the interaction energy between the surface growth unit and the solvent molecules. Molecular simulations provide the solvent structure information (e.g., radial distribution function) around every type of surface site. Molecular simulation packages such as LAMMPS [2] or DL\_POLY [3] can be used to obtain the solvent structure information around a crystal surface. The bond valence parameters ( $R_0$  and  $b$ ) for the atoms in the solvent molecule and the atoms in the crystalline solid are also obtained from the bond valence parameter database. The bond valences  $s'_{ij}$  between the growth unit atoms and atoms of solvent molecules are also calculated using step 8. The solvent structure information around a fully solvated growth

unit in bulk solution is also required for kink detachment work calculations. The number of solvent molecules and their average distances from a fully solvated ion can be obtained from molecular simulations or neutron diffraction experiments.

10. **Calculate the partial charges for every surface species:** The actual partial charge on every atom in each surface site is calculated from equation 2.7 using the bond valences calculated in steps 8 and 9.
11. **Calculate kink site interaction energy with solid state neighbors:** The potential energy of a growth unit situated in a kink site on a step edge is calculated using the space partitioning method discussed in Section 2.4.1. The space partitioning method allows easy calculation of the long-range electrostatic potential energy of the kink site growth unit, while assigning different partial charges to the atoms in bulk, surface or edge sites in the crystal lattice.
12. **Calculate kink site interaction energy with solvent molecules:** Only the nearest neighbor interactions are considered for the calculation of the interaction energy between the kink site growth unit and the solvent. A more accurate energy calculation can be performed if the radial distribution function of all the atoms within the solvent molecules is known (from molecular simulations or neutron scattering measurements) for large distances away from the kink site. The number of solvent molecules surrounding the kink site growth unit and their average distances from the atoms within the kink site growth unit are known from step 9.

13. **Calculate the kink detachment work  $\Delta W_k$  for every kink site:** The work done to remove a growth unit from a kink site and solvate it is calculated from equation 3.26. The kink site energies ( $U^{kink}$ ) are calculated using steps 11 and 12. The potential energy of a growth unit on the step edge located next to the kink site position ( $U^{step}$ ) is calculated in the same way except that the partial charges appropriate for atoms situated at the edge site are used for the central growth unit. The potential energy of a fully solvated ion ( $U^{solvated}$ ) is calculated from the information about the solvation shell structure, i.e., the number of solvent molecules around the solvated ion and their average distances from the atoms within the ion).
14. **Input experimental growth conditions:** The parameters relevant to the growth experiments such as the solubility product  $K_{sp}$ , supersaturation  $S$ , the ratio of the ionic activities  $r$ , and the solution composition  $x_I$ ,  $x_{II}$  and  $x_{III}$  (see Section 3.4.2) are needed as input to the crystal growth model. If the exact concentration of the growth units in the solution is known, the activity coefficients  $\gamma_{A,B}$  of an AB type ionic solid is calculated from ionic strength calculation and Davies equation as follows

$$I = \frac{1}{2} (c_A z_A^2 + c_B z_B^2) \quad (\text{A.2})$$

$$-\log \gamma_{A,B} = 0.5 z_A z_B \left( \frac{\sqrt{I}}{1 + \sqrt{I}} - 0.15 I \right) \quad (\text{A.3})$$

where  $I$  is the ionic strength in moles per liter,  $c_i$  is the molar concentration of ion  $i$  in the growth medium in moles per liter,  $z_i$  is the dimensionless charge on the ion

$i$  ( $i = A, B$ ). If the exact concentrations ( $c_A, c_B$ ) are not known and only  $K_{sp}$  and  $S$  are specified, the mole fractions of the ions in the growth medium are estimated from equation 3.20 by putting the activity coefficient as 1. The actual values of the activity coefficients is then obtained iteratively by solving the above equations along with equation 3.20.

15. **Calculate kink rate on every spiral edge:** The actual solubility product  $K'_{sp}$  near a spiral edge is calculated from equations 3.23 or 3.24. The quantities  $x_{eq}$  and  $Sx'$  are calculated from equation B.4. An accurate estimation of the ratio of the kink attachment rate constant of the cation to that of the anion ( $\xi$ ) is also required to calculate the kink rate. The kink attachment rate constants may be calculated either from a molecular simulation using rare event methods, or by fitting the measured step velocity to empirical rate laws. The kink rate  $u$  is calculated from equation B.5 using the values of  $\xi, \Delta W_k, x_{eq}, Sx'$  and  $S$ .
16. **Calculate kink density on every spiral edge:** For every PBC step edge on any F face, the work required for thermal rearrangement of the step edge that creates kink sites is calculated. The kink sites created from thermal fluctuations follow Boltzmann distribution where the density of a kink site depends on the work done for each rearrangement that creates that particular kink site. Work done in rearrangement of a straight step edge involves the change in the potential energy of four growth units as their configuration changes from edge sites to kink sites. The partial charges of the atoms of each growth unit in these two configurations along

with the change in the solvent structure is accounted for to calculate the change in the potential energy of each growth unit. The density of each kink site along a spiral edge is calculated by counting all the microstates of edge rearrangements that expose that particular kink site.

**17. Calculate step velocity, critical length and spiral growth rate:** The step velocity  $v$  of a spiral edge is calculated using the kink rate  $u$  and kink density  $\rho$  from equation 3.4. The critical length  $l_c$  of a spiral edge is calculated using the Gibbs-Thomson law, which dictates that  $l_c$  is the minimum length of the edge beyond which the addition of a growth unit to the edge makes the free energy change negative. The critical length  $l_c$  is calculated using the equation 3.29. Other definitions of critical length have been suggested in the literature [4] and may be used in step 17 as appropriate. The spiral growth rate  $G$  of that crystal face is calculated from equations 3.3 and 3.2.

**18. Predict the crystal shape:** The steady-state growth shape of the crystal is predicted from the growth rates of all the F faces (normalized with respect to the slowest growing face) using the Frank-Chernov condition

$$\frac{R_1}{x_1} = \frac{R_2}{x_2} = \dots = \frac{R_{N-1}}{x_{N-1}} = 1 \quad (\text{A.4})$$

where  $R_i$  is the growth rate of face  $i$  relative to a reference (slowest growing) face,  $x_i$  is the normalized perpendicular distance from the center of the crystal to the

face  $i$  and  $N$  is the total number of F faces. The  $x$  values are used to construct the steady state growth shape of the crystal.

# Bibliography

- [1] J. D. Gale and A. L. Rohl. The general utility lattice program (GULP). *Mol. Simul.*, 29:291–341, 2003.
- [2] S. Plimpton. Fast parallel algorithms for short-range molecular dynamics. *J. Comput. Phys.*, 117:1 – 19, 1995.
- [3] I. Todorov and W. Smith. *The DL-POLY\_4 User Manual*. STFC Daresbury Laboratory, UK, 2013.
- [4] J. P. Sizemore and M. F. Doherty. A stochastic model for the critical length of a spiral edge. *J. Cryst. Growth*, 312:785–792, 2010.

## Appendix B

# Detailed Expression for the Kink Rate

The mole fractions of A and B species in a supersaturated solution are written as a function of the local solubility product  $K'_{sp}$  from eqs 3.20 and 3.24 as

$$x_A = \frac{S\sqrt{r}}{\gamma_A} \left( \frac{\sqrt{K'_{sp}}}{M} \right) \quad x_B = \frac{S}{\gamma_B\sqrt{r}} \left( \frac{\sqrt{K'_{sp}}}{M} \right) \quad (\text{B.1})$$

The attachment and detachment fluxes on the kink sites from a supersaturated solution are written from eqs 3.13 and 3.14 as follows

$$j_A^+ = \frac{Sx_{eq}\sqrt{r}}{\gamma_A} \nu_A \exp\left(-\frac{\Delta U_A}{k_B T}\right) \quad j_B^+ = \frac{Sx_{eq}}{\gamma_B\sqrt{r}} \nu_B \exp\left(-\frac{\Delta U_B}{k_B T}\right) \quad (\text{B.2})$$

$$j_{2k-1}^- = (1 - Sx') \nu_A \exp\left(-\frac{\Delta U_A + \Delta W_{2k-1}}{k_B T}\right) \quad j_{2k}^- = (1 - Sx') \nu_B \exp\left(-\frac{\Delta U_B + \Delta W_{2k}}{k_B T}\right) \quad (\text{B.3})$$

where

$$Sx' = Sx_{eq} \left( \frac{\sqrt{r}}{\gamma_A} + \frac{1}{\gamma_B\sqrt{r}} \right) + x_I + x_{III} \quad x_{eq} = \left( \frac{\sqrt{K'_{sp}}}{M} \right) \quad (\text{B.4})$$

The kink rate is calculated from eq 3.12 as

$$u = \frac{x_{eq}^{2N} (S^{2N} - 1)}{\sum_{\ell=1}^N \left\{ (1 - Sx')^{2\ell-2} (Sx_{eq})^{2N-2\ell} \left[ (1 - Sx') (O_{\ell} + \xi P_{\ell}) + (Sx_{eq}) \left( \sqrt{\frac{r\gamma_B}{\gamma_A}} \xi Z_{\ell} + \sqrt{\frac{\gamma_A}{r\gamma_B}} Y_{\ell} \right) \right] \right\}} \quad (\text{B.5})$$

where

$$\begin{aligned} O_{\ell} &= \sum_{k=1}^N \left\{ \exp \left( - \sum_{m=0}^{2\ell-2} \frac{\Delta W_{2k+m-1}}{k_B T} \right) \right\} & P_{\ell} &= \sum_{k=1}^N \left\{ \exp \left( - \sum_{m=0}^{2\ell-2} \frac{\Delta W_{2k+m}}{k_B T} \right) \right\} \\ Y_{\ell} &= \sum_{k=1}^N \left\{ \exp \left( - \sum_{m=0}^{2\ell-3} \frac{\Delta W_{2k+m-1}}{k_B T} \right) \right\} & Z_{\ell} &= \sum_{k=1}^N \left\{ \exp \left( - \sum_{m=0}^{2\ell-3} \frac{\Delta W_{2k+m}}{k_B T} \right) \right\} \\ Y_1 &= N & Z_1 &= N \\ \xi &= \frac{\nu_A}{\nu_B} \exp \left( - \frac{\Delta U_A - \Delta U_B}{k_B T} \right) \end{aligned}$$

The solubility of inorganic crystals in water is often extremely low ( $x_{eq} \ll 1$ ) so that the term  $(1 - Sx')$  may be approximated as  $(1 - x_I - x_{III})$ . From eq B.5, the leading order term for the kink rate, and therefore the step velocity, scales linearly with the concentration driving force  $(S - 1)$ . The Taylor series for calcite spiral edges is reported in equations B.11 and B.12. Also, the kink rate scales as  $(r^{1/2} + r^{-1/2})^{-1}$  with the ionic activity ratio  $r$ . Both these scalings are consistent with the simplified models reported in the literature [1, 2]. Equation B.5 is used to calculate the kink rate to within a multiplicative factor  $\nu_A \exp(-\Delta U_A/k_B T)$  that is constant everywhere on the crystal surface and will therefore drop out of the relative growth rate expressions.

$\xi$  is the ratio of the kink attachment rate constants of the cation to the anion. If the cation and anion are of similar sizes,  $\xi$  can be assumed to be  $\mathcal{O}(1)$  and will not affect the

scaling of other quantities in eq B.5. The value of  $\xi$  for calcite growth was calculated from the estimates of the rate constants from fitting to the step velocity measurement data as reported by Bracco et al. [3]. The value of  $\xi$  was calculated as 0.19 for the obtuse spiral edge and 1.36 for the acute spiral edge on the  $(10\bar{1}4)$  calcite surface. Although the value of  $\xi$  is not the same for the two spiral edges, they are both close to  $\mathcal{O}(1)$  in magnitude, and are relatively insignificant in determining the kink rate. Molecular simulations along with rare event methods can provide accurate values of the individual attachment rate constants for both ions, and therefore of  $\xi$ .

The kink rate expression for the spiral edges on the  $(10\bar{1}4)$  surface of calcite can be written by putting  $N = 2$  into eqn B.5 as follows

$$u(S) = \frac{x_{eq}^4 (S^4 - 1)}{b_1 S^3 + b_2 S^2 + b_3 S + b_4} \quad (\text{B.6})$$

where  $b_i$  are coefficients that depend on  $r$ ,  $\xi$ ,  $\Delta W$ ,  $x_{eq}$ , etc. ( $i = 1, 2, 3, 4$ ). The expressions for  $b_i$  are as follows

$$b_1 = x_{eq}^3 \left[ \left( \sqrt{\frac{r\gamma_B}{\gamma_A}} \xi Z_1 + \sqrt{\frac{\gamma_A}{r\gamma_B}} Y_1 \right) + \left( \frac{\sqrt{r}}{\gamma_A} + \frac{1}{\gamma_B \sqrt{r}} \right)^2 \left( \sqrt{\frac{r\gamma_B}{\gamma_A}} \xi Z_2 + \sqrt{\frac{\gamma_A}{r\gamma_B}} Y_2 \right) - \left( \frac{\sqrt{r}}{\gamma_A} + \frac{1}{\gamma_B \sqrt{r}} \right) (O_1 + \xi P_1) - \left( \frac{\sqrt{r}}{\gamma_A} + \frac{1}{\gamma_B \sqrt{r}} \right)^3 (O_2 + \xi P_2) \right] \quad (\text{B.7})$$

$$b_2 = x_{eq}^2 \left[ O_1 + \xi P_1 + 3 \left( \frac{\sqrt{r}}{\gamma_A} + \frac{1}{\gamma_B \sqrt{r}} \right)^2 (O_2 + \xi P_2) - 2 \left( \frac{\sqrt{r}}{\gamma_A} + \frac{1}{\gamma_B \sqrt{r}} \right) \left( \sqrt{\frac{r\gamma_B}{\gamma_A}} \xi Z_2 + \sqrt{\frac{\gamma_A}{r\gamma_B}} Y_2 \right) \right] \quad (\text{B.8})$$

$$b_3 = x_{eq} \left[ \left( \sqrt{\frac{r\gamma_B}{\gamma_A}} \xi Z_2 + \sqrt{\frac{\gamma_A}{r\gamma_B}} Y_2 \right) + 3 \left( \frac{\sqrt{r}}{\gamma_A} + \frac{1}{\gamma_B \sqrt{r}} \right) (O_2 + \xi P_2) \right] \quad (\text{B.9})$$

$$b_4 = O_2 + \xi P_2 \quad (\text{B.10})$$

*Appendix B. Detailed Expression for the Kink Rate*

---

The expression for the kink rate from equation B.6 can be simplified in a Taylor series in powers of  $(S - 1)$  expanded around  $S = 1$ . For the obtuse and acute edges on the (10 $\bar{1}$ 4) surface of calcite, the expansion for the kink rate (at  $r = 1.04$ ) is as follows

$$u_{obtuse} = 33.73(S - 1) + 7.53(S - 1)^2 + 7.39(S - 1)^3 + 5.9(S - 1)^4 + \dots \quad (\text{B.11})$$

$$u_{acute} = 5.31(S - 1) - 0.42(S - 1)^2 + 1.45(S - 1)^3 - 0.91(S - 1)^4 + \dots \quad (\text{B.12})$$

Equations B.11 and B.12 show that the kink rate, and therefore, the step velocity of calcite spiral edges has a nonlinear dependence on the concentration driving force  $(S - 1)$ . This nonlinear dependence on  $(S - 1)$  is different from the classical crystal growth models [4, 5] that assumed the step velocity is linearly dependent on  $(S - 1)$ .

Detailed expressions can be obtained for the probability  $P_{2k}$  of finding the edge in a kink site of type  $2k$  by writing steady-state balances (similar to eqn 3.9) for  $2N - 1$  sites. The  $2N^{th}$  equation is that the sum of all probabilities equals 1. The resulting system of  $2N$  linearly independent equations can be solved to obtain the probabilities of the  $2N$  kink sites as follows

$$\begin{bmatrix} P_1 \\ P_2 \\ P_3 \\ \vdots \\ \vdots \\ P_{2N} \end{bmatrix} = \begin{bmatrix} -(j_B^+ + j_1^-) & j_2^- & 0 & \dots & 0 & j_A^+ \\ j_B^+ & -(j_A^+ + j_2^-) & j_3^- & 0 & \dots & 0 \\ 0 & j_A^+ & -(j_B^+ + j_3^-) & j_4^- & 0 & \vdots \\ \vdots & 0 & j_B^+ & \ddots & \ddots & 0 \\ 0 & \dots & 0 & j_A^+ & -(j_B^+ + j_{2N-1}^-) & j_{2N}^- \\ 1 & 1 & 1 & 1 & 1 & 1 \end{bmatrix}^{-1} \begin{bmatrix} 0 \\ 0 \\ \vdots \\ \vdots \\ 0 \\ 1 \end{bmatrix} \quad (\text{B.13})$$

*Appendix B. Detailed Expression for the Kink Rate*

---

For the case of  $N = 2$ , which applies to crystal growth on the  $(10\bar{1}4)$  surface of calcite, the probabilities of the four kink sites are as follows

$$\begin{aligned}
 P_1 &= \frac{j_A^{+2}j_B^+ + j_A^+j_B^+j_2^- + j_A^+j_2^-j_3^- + j_2^-j_3^-j_4^-}{j_A^+j_B^+ \left( 2j_A^+ + 2j_B^+ + \sum_{k=1}^4 j_k^- \right) + \left( \sum_{k=1}^4 j_k^- j_{k+1}^- j_{k+2}^- \right) + \left( \sum_{k=1}^2 j_B^+ j_{2k-1}^- j_{2k}^- + j_A^+ j_{2k}^- j_{2k+1}^- \right)} \\
 P_2 &= \frac{j_A^+j_B^{+2} + j_A^+j_B^+j_3^- + j_B^+j_3^-j_4^- + j_1^-j_3^-j_4^-}{j_A^+j_B^+ \left( 2j_A^+ + 2j_B^+ + \sum_{k=1}^4 j_k^- \right) + \left( \sum_{k=1}^4 j_k^- j_{k+1}^- j_{k+2}^- \right) + \left( \sum_{k=1}^2 j_B^+ j_{2k-1}^- j_{2k}^- + j_A^+ j_{2k}^- j_{2k+1}^- \right)} \\
 P_3 &= \frac{j_A^{+2}j_B^+ + j_A^+j_B^+j_4^- + j_A^+j_4^-j_1^- + j_1^-j_2^-j_4^-}{j_A^+j_B^+ \left( 2j_A^+ + 2j_B^+ + \sum_{k=1}^4 j_k^- \right) + \left( \sum_{k=1}^4 j_k^- j_{k+1}^- j_{k+2}^- \right) + \left( \sum_{k=1}^2 j_B^+ j_{2k-1}^- j_{2k}^- + j_A^+ j_{2k}^- j_{2k+1}^- \right)} \\
 P_4 &= \frac{j_A^+j_B^{+2} + j_A^+j_B^+j_1^- + j_B^+j_1^-j_2^- + j_1^-j_2^-j_3^-}{j_A^+j_B^+ \left( 2j_A^+ + 2j_B^+ + \sum_{k=1}^4 j_k^- \right) + \left( \sum_{k=1}^4 j_k^- j_{k+1}^- j_{k+2}^- \right) + \left( \sum_{k=1}^2 j_B^+ j_{2k-1}^- j_{2k}^- + j_A^+ j_{2k}^- j_{2k+1}^- \right)}
 \end{aligned}$$

# Bibliography

- [1] J. Zhang and G. H. Nancollas. Kink density and rate of step movement during growth and dissolution of an AB crystal in a nonstoichiometric solution. *J. Colloid Interface Sci.*, 200:131 – 145, 1998.
- [2] A. Chernov, E. Petrova, and L. Rashkovich. Dependence of the  $\text{CaO}_x$  and  $\text{MgO}_x$  growth rate on solution stoichiometry. Non-Kossel crystal growth. *J. Cryst. Growth*, 289:245 – 254, 2006.
- [3] J. N. Bracco, M. C. Grantham, and A. G. Stack. Calcite Growth Rates As a Function of Aqueous Calcium-to-Carbonate Ratio, Saturation Index, and Inhibitor Concentration: Insight into the Mechanism of Reaction and Poisoning by Strontium. *Cryst. Growth Des.*, 12:3540–3548, 2012.
- [4] W. K. Burton, N. Cabrera, and F. C. Frank. The growth of crystals and the equilibrium structure of their surfaces. *Phil. Trans. Roy. Soc. A*, 243:299–358, 1951.
- [5] A. A. Chernov. *Modern Crystallography III. Crystal Growth*. Berlin: Springer-Verlag, 1984.

## Appendix C

# Time Scale Comparison between Edge Rearrangement and Kink Incorporation

The model developed here to calculate the step velocity assumes that the rearrangement of the step edge structure happens on a time scale that is much faster than the rate at which growth units incorporate into the kink sites present along the step edge. Therefore, the edge structure is governed by the most probable equilibrium distribution (i.e., Boltzmann distribution) and the density of kink sites along the edge depends only on the energy required for edge rearrangement. To verify this assumption, a comparison of characteristic time scales for edge rearrangement ( $\tau_{rea}$ ) and kink incorporation ( $\tau_{inc}$ ) was carried out. The time scale estimation is performed for a simpler case of a single type of kink site present along the edge, which corresponds to the crystal growth of centrosymmetric molecules. This simplification allows us to make useful predictions, with relative ease, of the time scales of the two processes involved. The inferences drawn from

this time scale analysis can be also applied to predict the rates of edge rearrangement and kink incorporation on the surfaces of inorganic crystals.

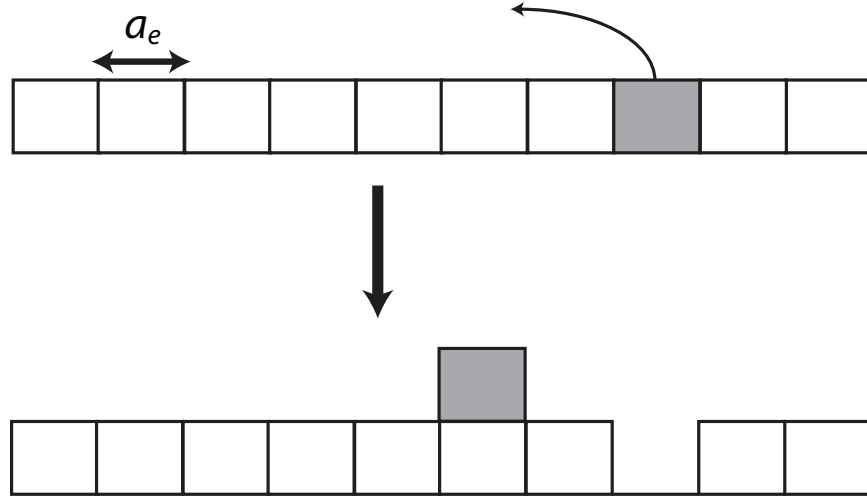


**Figure C.1:** Representative rearrangement of a straight edge on a crystal surface that involves the detachment of an edge growth unit to a step adatom position.

The characteristic time for rearrangement,  $\tau_{rea}$ , depends on the diffusivity of a growth unit along the edge  $D$  as follows

$$\tau_{rea} = \frac{a_e^2}{2D} \quad (\text{C.1})$$

where  $a_e$  is the length of the growth unit along the edge (Figure C.1). The rearrangement process is modeled by considering the detachment of a growth unit situated in a step edge position and its subsequent attachment into a step adatom position. The diffusivity of growth units along the edge is written as follows

$$D = \frac{a_e^2}{2} \left( j_{edge}^- + j_{adatom}^+ \right) \quad (\text{C.2})$$

### Appendix C. Time Scale Comparison between Edge Rearrangement and Kink Incorporation

---

where  $j_{edge}^-$  and  $j_{adatom}^+$  are the detachment and attachment fluxes from the edge and step adatom positions, respectively.  $a_e$  has units of nm or Å,  $D$  has units of nm<sup>2</sup>.s<sup>-1</sup> and the fluxes have units of s<sup>-1</sup>.

The characteristic time for kink incorporation,  $\tau_{inc}$ , depends on the net rate of attachment into a kink site.

$$\tau_{inc} = \frac{1}{j_{kink}^+ - j_{kink}^-} \quad (C.3)$$

The ratio of the two time scales is written as follows

$$\frac{\tau_{rea}}{\tau_{inc}} = \frac{j_{kink}^+ - j_{kink}^-}{j_{edge}^- + j_{adatom}^+} \quad (C.4)$$

The kink site attachment and detachment fluxes for centrosymmetric growth units are written as follows

$$j_{kink}^+ = Sx_{eq}\nu \exp\left(-\frac{\Delta U}{k_B T}\right) \quad j_{kink}^- = (1 - Sx_{eq})\nu \exp\left(-\frac{\Delta U + \Delta W}{k_B T}\right) \quad (C.5)$$

At equilibrium, supersaturation  $S = 1$ , and the attachment and detachment fluxes from the kink site must be equal. This results in a relationship between solubility  $x_{eq}$  and the kink detachment work  $\Delta W$  as follows

$$x_{eq} = \frac{1}{1 + \exp(\Delta W/k_B T)} \quad (C.6)$$

The ratio  $j_{kink}^+/j_{kink}^-$  is written as follows

$$\frac{j_{kink}^+}{j_{kink}^-} = \frac{S e^{\Delta W/k_B T}}{1 - S + e^{\Delta W/k_B T}} \quad (C.7)$$

The attachment fluxes to any surface site depends primarily upon the supersaturation and an energy barrier that depends on the desolvation of the incoming growth unit [1, 2].

Appendix C. Time Scale Comparison between Edge Rearrangement and Kink Incorporation

Therefore, the attachment flux to the step adatom can be approximated as  $j_{adatom}^+ \approx j_{kink}^+$ .

The detachment flux from an edge position must be smaller in magnitude than the detachment flux from a kink site. A scaling factor,  $\lambda \ll 1$ , is defined as

$$\lambda = \frac{j_{edge}^-}{j_{kink}^-} \quad (C.8)$$

Using eqs C.7 and C.8, the ratio of time scales from eq C.4 is rewritten as

$$\begin{aligned} \frac{\tau_{rea}}{\tau_{inc}} &= \frac{j_{kink}^+ / j_{kink}^- - 1}{j_{kink}^+ j_{kink}^- + \lambda} \\ \frac{\tau_{rea}}{\tau_{inc}} &= \frac{(S-1) \left(1 + e^{\Delta W / k_B T}\right)}{\lambda(1-S) + (\lambda + S)e^{\Delta W / k_B T}} \end{aligned} \quad (C.9)$$

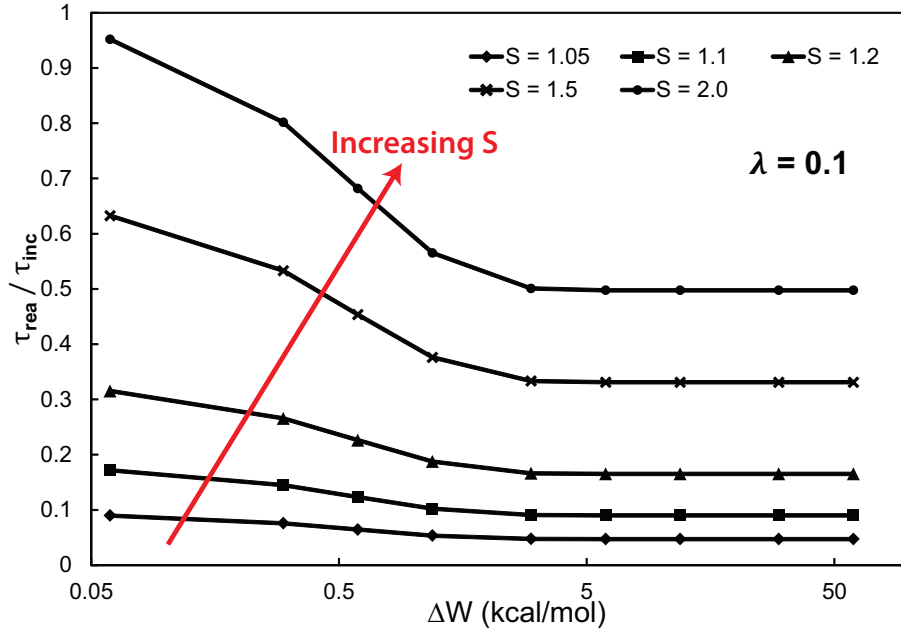


**Figure C.2:** The ratio of characteristic time scales of edge rearrangement ( $\tau_{rea}$ ) to kink incorporation ( $\tau_{inc}$ ) at different  $S$  and  $\Delta W$  values.

The value of  $\lambda$  for a Kossel crystal in equilibrium with a vacuum was reported as 0.18 [3]. Figure C.2 shows the variation of the ratio of time scales from eq C.9 as a

*Appendix C. Time Scale Comparison between Edge Rearrangement and Kink Incorporation*

---

function of the kink detachment work ( $\Delta W$ ) at  $\lambda = 0.1$  for different values of  $S$ . At low supersaturations ( $S \leq 1.2$ ), the time required for the edge to rearrange is much smaller than the time required for a growth unit to be incorporated into a kink site. This is true for all values of  $\Delta W$ . However, at larger supersaturations ( $S > 1.2$ ), the rate of kink incorporation becomes faster and starts competing with the rearrangement process such that the edge structure is no longer in quasi-equilibrium with a vacuum.

It is well known that for solution grown crystals, growth units in a kink site position are solvated to a greater extent than those in an edge site [4, 5]. Therefore, the process of dissolution and complete solvation should occur at a faster rate from a kink site position than from an edge site. Hence, the assumption that  $\lambda \ll 1$  should also hold for solution grown crystals. For calcite crystals grown from an aqueous solution, the values of  $\Delta W$  on the spiral edges of the  $(10\bar{1}4)$  surface are in the range 10-40 kcal/mol (Table 3.2). At low supersaturations ( $S \leq 1.2$ ), the rearrangement is 5-10 times faster than kink incorporation on those spiral edges. However, the spiral edges on a calcite crystal surface will not undergo fast rearrangement at  $S > 1.2$ . The step velocity model derived in Chapters 2 and 3 will need to be modified in this supersaturation range to account for the two processes - edge rearrangement and kink incorporation, occurring simultaneously.

# Bibliography

- [1] I. V. Markov. *Crystal Growth for Beginners, Fundamentals of Nucleation, Crystal Growth and Epitaxy*. World Scientific: Singapore, 2003.
- [2] P. G. Vekilov. What determines the rate of growth of crystals from solution? *Cryst. Growth Des.*, 7:2796–2810, 2007.
- [3] B. Mutaftschiev. *The Atomistic Nature of Crystal Growth*. Springer-Verlag: Berlin, 2001.
- [4] A. G. Stack. Molecular Dynamics Simulations of Solvation and Kink Site Formation at the {001} Barite-Water Interface. *J. Phys. Chem. C*, 113:2104–2110, 2009.
- [5] M. Wolthers, D. Di Tommaso, Z. Du, and N. H. de Leeuw. Calcite surface structure and reactivity: Molecular dynamics simulations and macroscopic surface modelling of the calcite-water interface. *Phys. Chem. Chem. Phys.*, 14:15145–15157, 2012.

# Appendix D

## Modification of Surface Charges for Polarity Stabilization

A polar crystal surface is defined to possess a non-zero dipole moment perpendicular to the plane of the surface [1, 2]. This dipole moment results in the divergence of the surface energy of a polar crystal surface [3], thereby destabilizing the surface. This appendix discusses the instability caused by the arrangement of ions in the surface layers using the fundamentals of electrostatics.

The electrostatic potential or electric field at any point P above a Tasker type 3 [1] crystal surface can be calculated by making certain assumptions about the arrangement of the ions within the layers parallel to the surface. If the distance between the ions within each layer is much smaller than the distance between the point P and the layers, each atomic layer can be approximated by an infinitely long flat plane with a uniform charge density  $\sigma$  (Figure D.1).  $\sigma$  has units of Coulombs per  $\text{m}^2$  or  $\text{C}\cdot\text{m}^{-2}$ . The charge density  $\sigma$  will depend on the partial charges of the ions that lie within each layer and the distances between the ions.

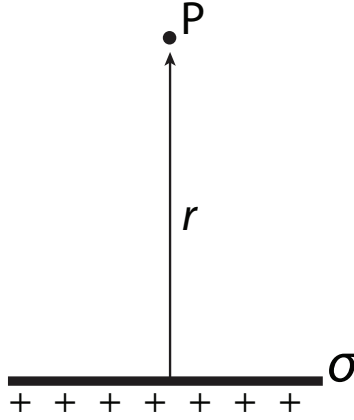


**Figure D.1:** The electric field and potential at a point P at a distance  $r$  from an infinitely long flat plane with a uniform surface charge per unit area,  $+\sigma$ .

The electrostatic field,  $\mathbb{E}$ , at any point P near an infinitely long plane (Figure D.1) is given from Gauss' law as follows

$$\mathbb{E} = \frac{\sigma}{2\epsilon_0} \quad (\text{D.1})$$

where  $\sigma$  is the charge per unit area on the infinite plane and  $\epsilon_0$  is the vacuum permittivity. It should be noted that the electric field from equation D.1 is independent of the distance between the point P and the infinite plane. Therefore, the electrostatic potential at the point P can be written as follows

$$\int_{\mathbb{V}(0)}^{\mathbb{V}(r)} d\mathbb{V} = - \int_{\ell=0}^{\ell=r} \mathbb{E} d\ell = - \frac{\sigma}{2\epsilon_0} \int_{\ell=0}^{\ell=r} d\ell \quad (\text{D.2})$$

By choosing  $\mathbb{V}$  at  $r = 0$  to be zero, the electrostatic potential at a point P which is at a distance  $r$  from the infinite plane is given as follows

$$\mathbb{V}(r) = - \frac{\sigma r}{2\epsilon_0} \quad (\text{D.3})$$

Figure D.2a shows the arrangement of layers for a Tasker type 3 surface [1]. The electric potential at point P due to all the charged layers is written from equation D.3 as follows

$$\begin{aligned} \mathbb{V}(r) &= -\frac{-\sigma r}{2\epsilon_0} - \frac{\sigma(r + R_2)}{2\epsilon_0} - \frac{-\sigma(r + R_2 + R_1)}{2\epsilon_0} - \frac{\sigma(r + 2R_2 + R_1)}{2\epsilon_0} + \dots \\ &= -\frac{\sigma}{2\epsilon_0}(R_2 + R_2 + \dots) \\ \mathbb{V}(r) &= -\frac{\sigma N R_2}{2\epsilon_0} \end{aligned} \tag{D.4}$$

where the total number of ionic layers beneath the surface is  $2N$ . The number of layers must be even to maintain charge neutrality. The electrostatic potential  $\mathbb{V}(r)$  is independent of the distance,  $r$ , between the surface layer and the point P. The magnitude of the potential increases linearly with the number of layers ( $N$ ) below the surface. Therefore, the electrostatic potential above a macroscopic crystal surface diverges for a Tasker type 3 surface.

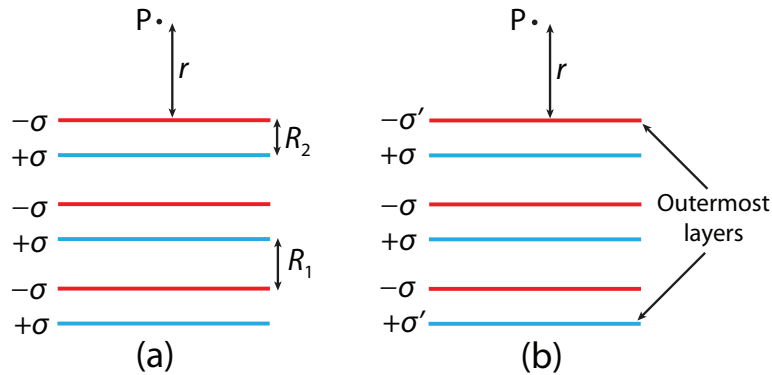


**Figure D.2:** A simplified view of the arrangement of ions in the layers beneath a Tasker type 3 ionic crystal surface [1]. (a) shows the crystal surface with native charge density ( $\sigma$ ) on the ionic layers. (b) shows the crystal surface with modified charge densities ( $\sigma'$ ) on the two outermost layers. Green and blue lines represent layers containing negative and positive charged ions, respectively.

The surface charge on the two outermost layers can be modified to cancel out the perpendicular dipole moment and to prevent the divergence of the electrostatic potential and the surface energy. Let the modified surface charge density on the outer layers be  $\sigma'$ . The requirement for the electrostatic potential at the point P to converge is that  $\mathbb{V}(r)$  must be independent of the total number of atomic layers ( $2N$ ) present below the crystal surface.

The electrostatic potential at the point P with the modified charge density  $\sigma'$  for the outermost layers (Figure D.2b) is written as follows

$$\begin{aligned}
 \mathbb{V}(r) &= -\frac{-\sigma' r}{2\epsilon_0} - \frac{\sigma(r+R_2)}{2\epsilon_0} - \frac{-\sigma(r+R_2+R_1)}{2\epsilon_0} - \frac{\sigma(r+2R_2+R_1)}{2\epsilon_0} \\
 &\quad - \dots - \frac{-\sigma(r+(N-1)(R_2+R_1))}{2\epsilon_0} - \frac{\sigma'(r+NR_2+(N-1)R_1)}{2\epsilon_0} \\
 &= \frac{-1}{2\epsilon_0} [-\sigma' r - \sigma R_1(N-1) + \sigma'(r+NR_2+(N-1)R_1)] \\
 &= \frac{-1}{2\epsilon_0} [\sigma' NR_2 - (\sigma - \sigma')(N-1)R_1] \\
 &= \frac{-\sigma}{2\epsilon_0} \left[ \frac{\sigma'}{\sigma} (NR_2) - \left(1 - \frac{\sigma'}{\sigma}\right) (N-1)R_1 \right] \\
 \mathbb{V}(r) &= \frac{-\sigma}{2\epsilon_0} N \left\{ \frac{\sigma' R_2}{\sigma} - \left(1 - \frac{\sigma'}{\sigma}\right) R_1 \right\} + \left(1 - \frac{\sigma'}{\sigma}\right) R_1 \tag{D.5}
 \end{aligned}$$

The first term on the right hand side of equation D.5 is the only term that is dependent on  $N$ . If  $\mathbb{V}(r)$  is independent of  $N$ , the coefficient of  $N$  in equation D.5 must be zero.

$$\begin{aligned}
 \frac{\sigma' R_2}{\sigma} &= \left(1 - \frac{\sigma'}{\sigma}\right) R_1 \\
 \therefore \sigma' &= \frac{\sigma R_1}{R_1 + R_2} \tag{D.6}
 \end{aligned}$$

Equation D.6 is the condition for stability of the Tasker type 3 crystal surface with charge density  $\sigma$ . If the charge density of the outermost layers is modified to  $\sigma'$  from equation D.6, the electrostatic potential above the crystal surface will not diverge. The converged value of the electrostatic potential is obtained by substituting the value of  $\sigma'$  from equation D.6 into equation D.5 as follows

$$\mathbb{V}(r) = -\frac{\sigma R_1 R_2}{2\epsilon_0 (R_1 + R_2)} \quad (\text{D.7})$$

The modified charge density ( $\sigma'$ ) depends on the original charge density ( $\sigma$ ) and the distances between successive ionic layers ( $R_1, R_2$ ), that are calculated from knowledge of the crystal structure. For the (0001) ZnO surface in the wurtzite crystal structure,  $R_1 = 1.988 \text{ \AA}$ , and  $R_2 = 0.614 \text{ \AA}$  [4]. Therefore, the magnitude of the new charge density on the outermost Zn and O layers is  $\sigma' = 0.76\sigma$ . A 24% reduction in the charge densities on the outermost layers of the (0001) surface of wurtzite ZnO will stabilize the electrostatic potential above the surface.

# Bibliography

- [1] P. W. Tasker. The stability of ionic crystal surfaces. *J. Phys. C Solid State*, 12:4977, 1979.
- [2] C. Noguera. Polar oxide surfaces. *J. Phys.: Condens. Matter*, 12:R367, 2000.
- [3] F. Bertaut. L'Energie Electrostatique De Reseaux Ioniques. *J. Phys. et le Radium*, 13:499–505, 1952.
- [4] K. Kihara and G. Donnay. Anharmonic thermal vibrations in ZnO. *Can. Mineral.*, 23:647–654, 1985.

# Appendix E

## Force Field Parameters for Some Inorganic Crystals

**Table E.1:** Force field parameters for calcite and aragonite crystals [1]

Atom Pair	$A$ (eV)	$\rho$ (Å)	$C$ (eV Å <sup>6</sup> )
Ca - Oc (carbonate)	3161.6335	0.271511	0.0
Ca - Ow (water)	1186.4929	0.2970	0.0
Ca - C	1.20E+8	0.120	0.0
Oc - Oc	63840.199	0.1989	27.899
Oc - Ow	12534.4551	0.2152	12.090
Oc - Hw	396.321	0.230	0.0

The partial charges for Ca, C and O atoms in bulk calcite are  $+2.0e$ ,  $+1.123e$  and  $-1.041e$ , respectively [1]. The partial charges of the O atoms in bulk aragonite were recalculated using the bond valence model [2] as  $-0.980e$  and  $-1.071e$  for the O1 and O2 atoms, respectively (see Figure 4.1). The partial charges of O and H atoms in TIP3P water are  $+0.8e$  and  $-0.4e$ , respectively [3].

**Table E.2:** Force field parameters for anatase crystals [4]

Atom Pair	$A$ (eV)	$\rho$ ( $\text{\AA}$ )	$C$ (eV $\text{\AA}^6$ )
Ti - Ti	31120.2	0.154	5.25
Ti - O	16957.53	0.194	12.59
O - O	11782.76	0.234	30.22

The partial charges for Ti and O atoms in bulk calcite are  $+2.196e$  and  $-1.098e$ , respectively [4].

**Table E.3:** Force field parameters for ZnO wurtzite crystals [5]

Atom Pair	$A$ (eV)	$\rho$ ( $\text{\AA}$ )	$C$ (eV $\text{\AA}^6$ )
Zn - Zn	0.0	0.0	0.0
Zn - O	529.7	0.3581	0.0
O - O	9547.96	0.2192	32.0

The partial charges for Zn and O atoms in bulk wurtzite are  $+2.0e$  and  $-2.0e$ , respectively [5].

# Bibliography

- [1] P. Raiteri, J. D. Gale, D. Quigley, and P. M. Rodger. Derivation of an accurate force-field for simulating the growth of calcium carbonate from aqueous solution: A new model for the calcite-water interface. *J. Phys. Chem. C*, 114:5997–6010, 2010.
- [2] I. D. Brown. *The Chemical Bond in Inorganic Chemistry: The Bond Valence Model*. Oxford University Press, 2002.
- [3] W. L. Jorgensen, J. Chandrasekhar, J. D. Madura, R. W. Impey, and M. L. Klein. Comparison of simple potential functions for simulating liquid water. *J. Chem. Phys.*, 79:926–935, 1983.
- [4] P. M. Oliver, G. W. Watson, E. Toby Kelsey, and S. C. Parker. Atomistic simulation of the surface structure of the TiO<sub>2</sub> polymorphs rutile and anatase. *J. Mater. Chem.*, 7:563–568, 1997.
- [5] A. J. Kulkarni, M. Zhou, and F. J. Ke. Orientation and size dependence of the elastic properties of zinc oxide nanobelts. *Nanotechnology*, 16:2749, 2005.